Temporal and Geographical Variation in Martian Surface Dust Lifting Processes

Thesis

Temporal and Geographical Variation in Martian Surface Dust Lifting Processes

Rhian Chapman

MPhys Astrophysics

Submitted for the degree of

Doctor of Philosophy

School of Physical Sciences

The Open University

June 2018

Abstract

Numerical experiments were completed examining the variability of key aspects of the Martian dust cycle and investigating their importance in predicting conditions for spacecraft atmospheric descent and landing.

The dust cycle – lifting, transportation and deposition – is a significant Martian climate cycle. The geographical and temporal variation in dust lifting processes were investigated using a Martian Global Circulation Model.

The geographical representation of Martian dust lifting by wind stress was used to explore the experimental impact of changes in model resolution. It was found that increasing the resolution improved the model's geographical representation of observed dust lifting regions, such as resolving important storm-forming regions in the northern hemisphere. This improvement was unanticipated in the case of changes in vertical resolution, and the horizontal resolution work identified an important length scale for dust lifting (of the order of 100 kilometres).

The temporal variation of a dust lifting process was investigated through experiments focusing on the diurnal variability of Martian dust devils (small-scale convective vortices). This research compared results with published lander and rover observations and found that dust devils were more active during morning hours than anticipated, suggesting that the generally accepted description of dust devil behaviour on Mars is incomplete.

Predictions were made of the atmospheric and near-surface environment encountered by the ESA ExoMars Schiaparelli landing module. The experiments produced a reasonable representation of atmospheric quantities along the descent trajectory and were able to generate similar low-altitude wind fields to those reported by the spacecraft. The global-scale model also out-performed a higher resolution mesoscale model.

These findings are significant in the field of Martian climate modelling, are important for the planning of Martian dust devil observation campaigns and future missions to the planet‘s surface, and will also be relevant to researchers operating atmospheric models for other planetary bodies.

Acknowledgements

I want to thank my supervisors, Stephen Lewis, Matt Balme and Liam Steele, firstly for giving me the opportunity to undertake this PhD, and secondly for advising me and supporting me through it. I genuinely believe that my supervision team was the best I could have had.

Thank you to Vic Pearson, for our cheerful coffee-and-catch-up meetings. Thank you to the wider members of the OU School of Physical Sciences – particularly the administration and support staff in Robert Hooke for their willingness to provide assistance whenever I needed it, and to the Linux support team for fixing the system whenever it broke. Thank you to Lori-Ann for her excellent proof-reading.

Thank you to my parents, for their never-ending support, and to my sister, all our lives. Thank you to my 'grown-up' friends, for not teasing me more than was appropriate through my return sojourn in studentdom: Russ, Siân, Adam, Rob and Anna, Robert and Lucy (and Iris), Lydia and Beckie; Katie, Jon and Alex; Lee (and Joshua).

Thank you to the new friends I have made upon becoming a student again, including – but not limited to – Ashley, Jimmy, Peter W, Amy, Jack, Frances, Alex, Rachael, Pegg, Shannon, Paul G, Paul S, Chris, Peter and Leanne, Stacy. You all helped me through.

This thesis is dedicated to Emily, who was always working to better herself.

Contents

List of Figures

List of Tables

List of Abbreviations

AMELIA	Atmospheric Mars Entry and Landing Investigations and Analysis
AMR	Above MOLA Radius
AOPP	Atmospheric, Oceanic and Planetary Physics department, Oxford
AR-WRF	Advanced Research Weather Research and Forecasting
CaSSIS	Colour and Stereo Surface Imaging System
CBL	Convective Boundary Layer
CFL	Courant-Friedrichs-Lewy
DREAMS	Dust characterization, Risk assessment and Environment Analyzer on the Martian Surface
EDM	Entry Demonstrator Module
ESA	European Space Agency
GCM	Global Circulation Model
GFDL	Geophysical Fluid Dynamics Laboratory
HiRISE	High Resolution Imaging Science Experiment
HRSC	High Resolution Stereo Camera
IQR	Interquartile range
JPL	Jet Propulsion Laboratory
LMD	Laboratoire de Météorologie Dynamique
LTE	Local Thermal Equilibrium
MARCI	Mars Color Imager
MCD	Mars Climate Database
MCS	Mars Climate Sounder
MER	Mars Exploration Rover
MEx	Mars Express

MGCM	Mars Global Circulation Model
MGS	Mars Global Surveyor
MMM	Mars Mesoscale Model
MOC	Mars Orbital Camera
MOLA	Mars Orbital Laser Altimeter
MRO	Mars Reconnaisance Orbiter
MSL	Mars Science Laboratory
MY	Mars Year
NASA	National Aeronautic and Space Administration
NCAR	National Center for Atmospheric Research
NH	Northern Hemisphere
NSWS	Near-surface wind stress
RMSD	Root Mean Square Deviation
SH	Southern Hemisphere
SI	Système International (d'unité) / International System of Units
TES	Thermal Emission Spectrometer
TGO	Trace Gas Orbiter
UKSA	UK Space Agency
VL2	Viking Lander 2

List of Publications

Journal Publications

Chapman, R. M.; Lewis, S. R.; Balme, M. and Steele, L. J. (2017), **Diurnal Variation in Martian Dust Devil Activity**. *Icarus*, 292, pp.154-167. DOI 10.1016/j.icarus.2017.01.003.

Conference Items

Chapman, R. M.; Lewis, S. R.; Balme, M. and Steele, L. J. (2018), **Comparison of Global-Scale and Mesoscale Modelling of Vertical Profiles in the Martian Atmosphere: How Does Model Resolution Impact Predictions of Conditions at Mission Landing Sites?** *49th Lunar and Planetary Science Conference*, 19-23 March 2018, Texas, USA.

Chapman, R. M.; Lewis, S. R.; Balme, M. and Steele, L. J. (2017), **Wind-Stress Dust Lifting in a Mars Global Circulation Model: Representation across Resolutions.** *AGU Fall Meeting 2017*, 11-15 December 2017, New Orleans, LA, USA.

Chapman, R. M.; Lewis, S. R.; Balme, M. and Steele, L. J. (2017), **Impact of Global Model Resolution on the Representation of Martian Wind-Stress Dust Lifting.** *1st British Planetary Science Congress*, 3-5 December 2017, Glasgow, UK.

Chapman, R. M.; Lewis, S. R.; Balme, M. and Steele, L. J. (2016), **The Effect of Model Resolution on Wind-Stress Dust Lifting Within the LMD/UK Mars Global Circulation Model.** *6th International Workshop*

on the Mars Atmosphere: Modelling and Observations, 17-20 January 2017, Granada, Spain.

Chapman, R. M.; Lewis, S. R.; Balme, M. and Steele, L. J. (2016), **How Do Martian Dust Devils Vary Throughout the Sol?** *AGU Fall Meeting 2016*, 12-17 December 2016, San Francisco, CA, USA.

Chapman, R. M.; Lewis, S. R.; Balme, M. and Steele, L. J. (2016), **Martian Dust Devils: When to Watch for Them.** *UKPF 13th Annual Early Career Scientists' Meetings*, 22 January 2016, Leicester, UK.

Chapman, R. M.; Lewis, S. R.; Balme, M. and Steele, L. J. (2015), **Investigating the Martian atmosphere using the ExoMars 2016 lander.** *4th UK in Aurora Programme Meeting*, 15 May 2015, London, UK.

Chapter 1

Introduction

Martian atmospheric dust is a crucial component in the climate cycles of Mars (e.g. *Gierasch and Goody*, 1971; *Haberle et al.*, 1982; *Kahn et al.*, 1992; *Zurek et al.*, 1992; *Lewis et al.*, 1999; *Read and Lewis*, 2004; *Kahre et al.*, 2017). Understanding the dust cycle of lifting, transportation and deposition, is key to understanding Martian long-term weather and climate patterns (e.g. *Zurek*, 1978; *Zurek et al.*, 1992; *Pankine and Ingersoll*, 2004; *Fenton et al.*, 2007). One strong driver behind the desire to improve our knowledge of the dust cycle, and its impact on the planet's climate, is the importance of being able to predict the atmospheric environment that will be encountered by future missions to the surface of Mars (e.g. *Petrosyan et al.*, 2011; *Vasavada et al.*, 2012).

The phenomena that lift dust from the surface into the Martian atmosphere are fundamental to the dust cycle. Observations of Martian dust lifting events are currently constrained either in space or time – or both. Surface observations from landers and rovers are necessarily restricted in geographical scope, the amount of information that can be returned is constrained by data transmission rates, and missions have a limited life-span[1]. Orbital observations are often limited temporally: while an orbiting spacecraft may have a longer nominal mission than a lander, platform orbits and instrument pointing affect the timing of data capture (such as the polar orbit of the Mars Global Surveyor spacecraft restricting Mars Orbiter Camera images to afternoon hours, *Cantor et al.* 2006),

[1] With the possible exception of NASA's Opportunity rover.

and these spacecraft are at a great distance from any surface processes being studied and their ability to resolve those processes is consequently constrained.

Variations in the behaviour of dust lifting phenomena can therefore currently be most comprehensively explored through numerical computer experiments. The output of any such experiments must be compared with local observations made by landers and rovers, and with regional and global observations made by orbiting spacecraft, to test the fidelity of the model, the reliability of the experiments, and the accuracy of the results. The better the representation of dust lifting within a model, the better the representation of the dust cycle and of the consequent impact the dust has on the planet's climate, and the more pertinent the results of any experiments completed with that model.

This work uses the parameterisations of dust lifting processes embedded within a global atmospheric model to: (i) investigate the temporal variation of those processes, (ii) test the geographical fidelity of this aspect of the modelled dust cycle, (iii) explore the robustness of the model, (iv) test predictions of the atmospheric conditions and near-surface dust events likely to be encountered by a spacecraft during the mission's entry, descent and landing.

1.1 Research Questions

This thesis will discuss the variability in the dust lifting processes of the Martian dust cycle, and the impact of atmospheric dust on model predictions of local conditions during spacecraft descent and landing. This work will answer three research questions:

1. Does the model exhibit an accurate geographical representation of dust lifting, and is this representation robust?

2. Can the temporal variability of Martian dust lifting be deduced by comparison with terrestrial processes?

3. Is the model's prediction of the atmospheric and near-surface environment at a selected landing site accurate enough to aid mission planning?

The questions were approached through three research topics:

1. **Geographical Representation of Martian Dust Lifting**

   To test the robustness of the model's geographical representation of dust lifting, experiments were completed with a focus on the lifting process associated closely with dust storms: dust lifting by the near-surface wind stress induced by large scale winds (Section 2.3). These experiments were designed to test the model's response to changes in the experimental setup rather than changes in the physics of the process being modelled. Simulations were completed across a range of model resolutions, exploring the impact upon results of changes to both horizontal and vertical resolutions.

   While it has been reported that the resolution at which global experiments are completed will affect results (e.g. *Toigo et al.*, 2012; *Mulholland et al.*, 2015), few published studies have considered how dust lifting parameterisations are specifically affected, particularly with regard to the geographical representation of dust lifting: such studies consider only a limited portion of the year, or consider the total area affected without detailing the geographical distribution (*Takahashi et al.*, 2008, 2011b). In addition, studies exploring how varying model resolution can impact results often change the horizontal resolution while keeping the vertical resolution constant (e.g. *Takahashi et al.*, 2011a; *Toigo et al.*, 2012). Understanding precisely how changes to model resolution affect the representation of this key aspect of the dust cycle is important for improving model fidelity, and hence for running accurate experiments and obtaining valid and useful results, with the aim of furthering Martian atmospheric science.

   The hypothesis tested herein was that more dust would be lifted as horizontal resolution is increased, but that changes to the vertical resolution would only minimally impact the amount of dust lifted. An increase in modelled horizontal resolution allows a more detailed representation of the planet's surface properties, including topography and small-scale variations in albedo and thermal inertia, which provides an improved representation of local variability within the near-surface wind and a better

capture of small-scale circulations. Increasing the model's vertical dimension was not expected to provide the same improvement, as the Martian atmosphere has not generally been observed to exhibit the same detailed variation as seen on the planet's surface. The goal of this test was to quantify any change in the amount of dust lifted, and to assess the fidelity of the geographical patterns of modelled dust lifting against observations of an associated atmospheric phenomena: dust storms.

2. **Temporal Representation of Martian Dust Lifting**

To explore the model's representation of the temporal variability of dust lifting, experiments were completed with a focus on dust lifting by small-scale convective events: 'dust devils' (*Balme and Greeley*, 2006; *Fenton et al.*, 2016). Dust devils are known to vary seasonally and diurnally (e.g. *Fisher et al.* 2005 and see Section 2.4). The diurnal timescale was selected for experimentation in this work, as there is little published data concentrating on this aspect of modelled Martian dust devil behaviour, compared to seasonal variation. The experiments were designed to test the variability in diurnal dust devil behaviour.

The expectation was that the diurnal pattern of Martian dust devil behaviour should match that of terrestrial dust devils, which are most active in the afternoon (e.g. *Sinclair*, 1969; *Snow and McClelland*, 1990; *Oke et al.*, 2007; *Lorenz and Lanagan*, 2014). The timing of the diurnal maximum in modelled dust devil activity was evaluated against orbital and surface observations of Martian dust devil activity and compared with terrestrial observations.

3. **Landing Site Case Study**

To investigate the accuracy of the model's prediction of the environment of a specific landing site, a case study was completed on the modelled atmosphere and near-surface environment encountered by the ESA ExoMars Schiaparelli mission. Experiments were completed using two models of different scale: a global-scale model and a mesoscale model. The model

results were compared against data returned by the Schiaparelli landing module during its descent.

Previous comparisons of results from different scale models often focus on areas of varying terrain (e.g. *Rafkin et al.*, 2001; *Spiga and Forget*, 2009), rather than the relatively flat, low-latitude location chosen for the Schiaparelli landing site. It was anticipated that the higher resolution mesoscale model should produce results that match more accurately the data received from the spacecraft. Predictions were also made of the near-surface dust lifting environment that the lander would have experienced during its brief surface mission; no previously published studies have directly compared surface dust lifting across global-scale and mesoscale models.

1.2 Document Preliminaries

This work adopts the following conventions:

- The Martian calendar proposed within *Clancy et al.* (2000), in which Mars Year 1 (MY1) began on 11th April 1955. At the moment of writing we are approximately midway through MY34.

- A Martian year lasts 668.6 sols. Moments and periods in the year are identified by the associated Solar Longitude, L_S, which describes the position of Mars in its orbit, shown in Figure 1.1.

- A Martian sol is 88,775 seconds long, using the standard (SI) unit of seconds (as a reference point, an Earth day is 86,400 seconds long). A Martian 'hour' is defined as 1/24th of a sol, following *Lewis et al.* (1999), and a Martian 'minute' is 1/60th of that hour.

- All times herein that refer to surface-level phenomena relate to local times for the locations in question.

- Surface locations are identified using the 'planetocentric' coordinate system (*Seidelmann et al.*, 2002), with latitude given in degrees north, and

longitude given in degrees east from the prime meridian that passes through the crater Airy-0 (*de Vaucouleurs et al.*, 1973).

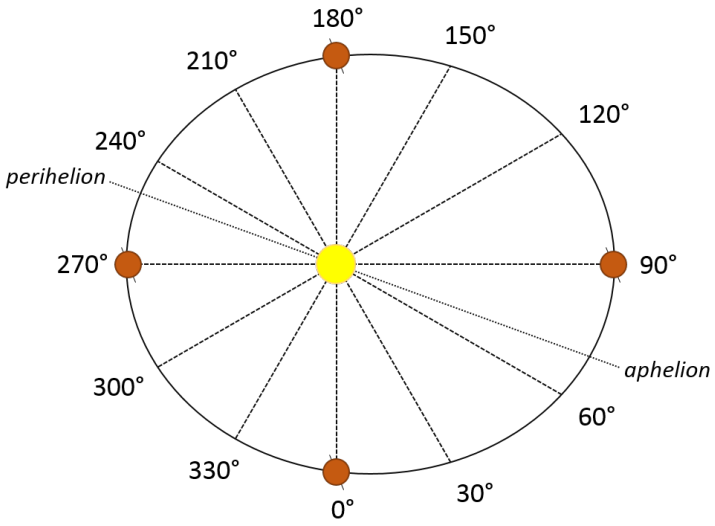

Figure 1.1: Diagram of Solar Longitude, L_S, as it is used to describe moments and periods during the Martian year. The year begins at $L_S = 0°$, the northern hemisphere spring equinox; Martian 'seasons' are defined as being $90° L_S$ long, starting from this equinox. Aphelion occurs at $L_S = 71°$ and perihelion occurs at $L_S = 251°$.

1.3 Document Guide

- Chapter 2 explains the importance of dust in the Martian atmosphere, and describes the major dust-lifting phenomena that have been observed on Mars: dust storms and dust devils.
- Chapter 3 details the global atmospheric model that has been used to complete the experiments presented in this work.
- Chapter 4 presents the investigation into a geographical aspect of the model's representation of dust lifting: the model's response to changes in horizontal and vertical resolution.
- Chapter 5 details the investigation into a temporal aspect of the model's representation of dust lifting: the diurnal variability of dust devils.
- Chapter 6 presents the case study of the selected mission landing site, comparing *in situ* data returned by the ESA ExoMars Schiaparelli module with the results of experiments completed at different model scales.
- Chapter 7 contains the summary and conclusions of this research and identifies future research opportunities.

Chapter 2

Martian Atmospheric Dust

This chapter discusses dust in the Martian atmosphere and its importance in the field of Martian climate modelling. A brief overview is given of the dust particles, the dust-lifting events that have been observed on Mars and incorporated into atmospheric models, and the relevance of atmospheric dust to spacecraft landing on Mars.

2.1 The Importance of Martian Dust

Dust has been observed in the Martian atmosphere since modern studies began (although it was not always appreciated as such) (*Schiaparelli*, 1882; *Lowell*, 1907; *Hess*, 1950; *Ryan*, 1964), and investigated as soon as was practicable (e.g. *Gierasch and Goody*, 1971; *Hanel et al.*, 1972). The presence of this dust affects the atmosphere: the dust absorbs incident solar radiation and re-radiates at thermal wavelengths, warming its surroundings (*Gierasch and Goody*, 1971; *Zurek*, 1978; *Cantor et al.*, 2001). This effect is amplified in regions containing a very high density of dust, such as within dust storms, and the general warming effect of dust in the atmosphere can have an impact on larger circulation patterns (*Zurek et al.*, 1992; *Zalucha*, 2014; *Guzewich et al.*, 2016). The effect of atmospheric dust on local temperature and pressure gradients is complex, as changes in local atmospheric gradients affect the strengths and patterns of local winds, which then affect the transport of dust (and other aerosols) within the

atmosphere. Dust particles also act as nucleation points for condensing CO_2 and water ice clouds (*Määttänen et al.*, 2005), which in turn can have a large effect on the wider atmosphere (*Wilson et al.*, 2008; *Madeleine et al.*, 2012).

The long-term climate of Mars could be expected to be a consistent annual cycle with limited variability: without oceans or a thick atmosphere that warms in response to incident solar radiation, and then transports and slow-releases that stored heat, the planet's response to incident solar radiation should be predictable and repeatable (*Pankine and Ingersoll*, 2004). While annual atmospheric patterns and circulations are indeed seen, such as seasonal thermal gradients (*Read et al.*, 2015), regular variations in dust optical depth[1] (*Smith*, 2009; *Lemmon et al.*, 2015), and the annual low-latitude through-aphelion cloud belt (*Smith*, 2004), a degree of interannual variability in the atmosphere is also observed, particularly through the 'storm season' around perihelion (*Clancy et al.*, 2000; *Smith*, 2004). The most striking examples of long-term variability in the Martian climate are the global dust storms, which have been observed on multiple occasions but are not annual events (*Zurek and Martin*, 1993) and their re-occurence cannot yet be predicted accurately (*Shirley*, 2015; *Montabone and Forget*, 2017); global storms are discussed further below.

Understanding the properties of the atmospheric dust, and the geographical and temporal patterns within the cycle of lifting, transport and deposition, is a key component to understanding the entire Martian climate. Studying – and modelling – the various parts of the Martian dust cycle expands our knowledge of the planet's current climate, the potential past climate (enabling better-informed investigations into geologically long-term climate studies of both Mars and other terrestrial planets, *Haberle* 2003), and improves our ability to predict more accurately future conditions on Mars. Predicting the behaviour of the future Martian atmosphere and climate is crucial during planning and completion of missions to the surface of the planet.

[1]The optical depth of a material is the logarithm of the ratio of the incident radiant flux to the transmitted radiant flux: $\tau = \ln(\Phi_e^i/\Phi_e^t)$.

2.2 Dust Particles and Distribution

Few *in situ* samples of Martian atmospheric dust particles have been obtained, although samples of Martian surface particulate have been studied by landers and rovers. One example is the NASA Phoenix lander, which carried a microscope station that was used to determine the particle size distribution of the Martian soil. *Pike et al.* (2011) found that, for particle sizes below 10 μm, the soil at the Phoenix landing site was more comparable to fine-grained lunar regolith than to any terrestrial soil.

The particle size and composition of atmospheric dust can be estimated from observations of the optical properties of the atmosphere. The size of the dust particles is typically explored using distribution functions that can be defined using a limited set of free parameters, which are then used to describe the scattering properties of a given particle population. To facilitate comparison of their results, most studies into the Martian atmospheric dust population assume a log-normal size distribution, where the number density of particles with radius r is given by

$$n(r) = \frac{N}{(2\pi)^{1/2}\sigma_0 r} \exp\big(-\frac{\ln^2(r/r_0}{2\sigma_0}\big), \tag{2.1}$$

where N is the total number of particles per mass of atmosphere (i.e. the number mixing ratio), r_0 is the geometric mean radius of the particles in the distribution, and σ_0 is the standard deviation (*Hansen and Travis*, 1974).

Values for the 'effective radius' of a log-normal distribution, r_{eff}, which is the particle mean scattering radius, and the 'effective variance', v_{eff}, which defines the spread of the distribution, can be found spectroscopically, and used to calculate r_0:

$$r_0 = \frac{r_{\text{eff}}}{(1 + v_{\text{eff}})^{5/2}}. \tag{2.2}$$

Orbital and surface observations of atmospheric dust have been used to estimate particle sizes: *Toon et al.* (1977) used Mariner 9 infrared obervations and calculated a mean particle radius $\sim$1 μm; *Pollack et al.* (1995) calculated particle sizes from Viking lander images both during the aphelion low dust season ($r_{\text{eff}} = 1.85$ μm) and during a dust storm ($r_{\text{eff}} = 1.52$ μm), resulting in mean radii of 0.68 μm and 0.55 μm; *Tomasko et al.* (1999) derived $r_{\text{eff}} = 1.6$

μm from Pathfinder images, giving a mean radius of 0.76 μm; *Wolff and Clancy* (2003) used MGS Thermal Emission Spectrometer (TES) data to calculate the average $r_{\text{eff}} = 1.85$ μm, producing a mean radius of 0.67 μm, but the spatial range of their data encompassed varying population distributions, including areas exhibiting mean particle radii of 0.76-1.03 μm. More recently, *Komguem et al.* (2013) used Phoenix observations to calculate $r_{\text{eff}} = 1.2$-1.4 μm, resulting in a mean particle radius range of 0.76-0.89 μm.

Combining size distribution models and spectroscopic observations allows absorption and scattering properties of the dust particle population to be calculated, see *Ockert-Bell et al.* (1997); *Wolff et al.* (2006, 2009, 2010). Consequently, the material that composes the dust particles can be estimated: Martian surface and atmospheric dust is believed to be largely basaltic in origin (*Morris et al.*, 2000; *McSween and Keil*, 2000), consisting primarily of related montmorillonite-like (*Toon et al.*, 1977) and/or palagonite-like (*Clancy et al.*, 1995) materials.

The distribution of dust in the Martian atmosphere varies through the year, as shown in Figure 2.1. Broadly speaking, through $L_S = 0$-$180°$, i.e. during the northern hemisphere spring and summer, the Martian atmosphere experiences 'low dust loading' (e.g. *Smith*, 2004; *Montabone et al.*, 2017). This aphelion season is relatively cool, and displays highly repeatable cycles of atmospheric temperature and optical depth through multiple years (e.g. *Smith and Lemmon*, 1999; *Liu et al.*, 2003; *Smith*, 2009; *Montabone et al.*, 2015b). Typical optical depths[2] of $\sim$0.4-0.6 (*Colburn et al.*, 1989; *Smith and Lemmon*, 1999; *Lemmon et al.*, 2015) are reported through this period.

Through $L_S = 180$-$360°$ – southern hemisphere spring and summer – the Martian atmosphere experiences higher dust loading. Generally higher optical depths are observed through the season, $\tau \sim$0.7-1.2 (*Colburn et al.*, 1989; *Martin*, 1986; *Liu et al.*, 2003; *Smith*, 2004), punctuated by sharp rises in τ during large dust storms (*Pollack et al.*, 1979; *Lemmon et al.*, 2015). The sporadic occurrence of large dust storms through this period drives a much higher degree of interannual variability than during the aphelion period (*Clancy et al.*, 2000;

[2]Unless otherwise noted, (absorption) optical depths given herein refer to values related to the visible portion of the spectrum, with any necessary conversions made using $\tau_{\text{visible}}/\tau_{\text{IR}} \approx 2$ (*Clancy et al.*, 1995).

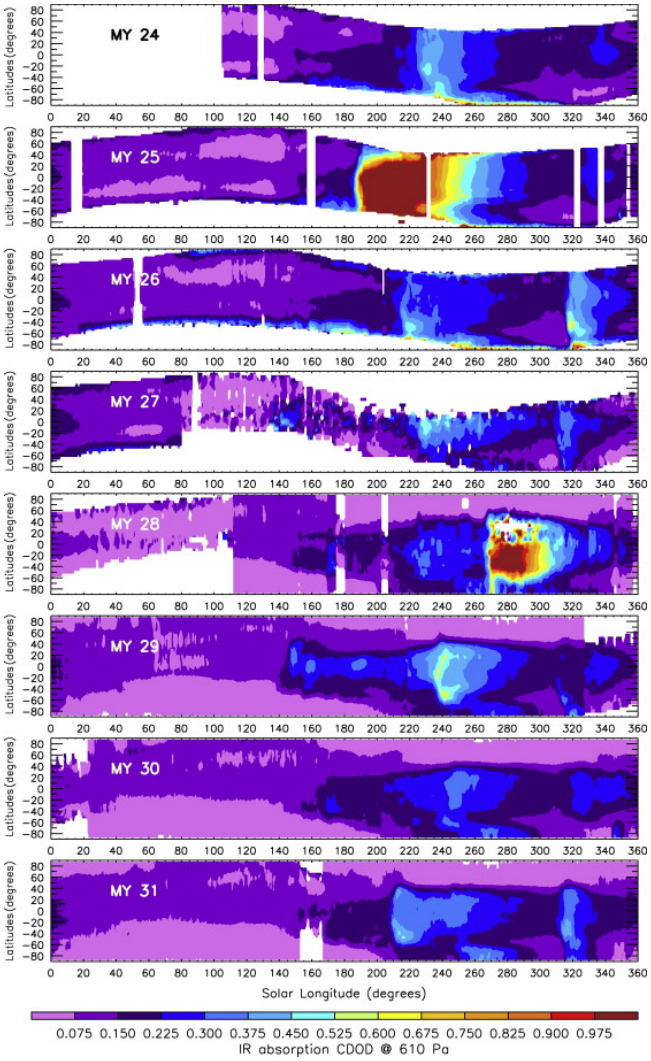

Figure 2.1: Zonal mean absorption column dust optical depth (at a thermal wavelength of 9.3 μm) by time, across multiple Martian Years. It is easy to see similar 'low dust loading' across aphelion seasons and the varibility during the perihelion 'high dust loading' seasons. From *Montabone et al.* (2015b), Fig. 16.

Liu et al., 2003).

With regard to the vertical distribution of dust, there is more dust in the lower atmosphere, and this amount decreases with altitude (*Conrath*, 1975) – but the detail of this description is complex. Dust is relatively well-mixed in the lowest few kilometres of the atmosphere, within the convective boundary layer (CBL) (*Whiteway et al.*, 2009; *Petrosyan et al.*, 2011). Larger particles

fall more quickly (*Kahre et al.*, 2006), so both dust particle size and dust density decrease with altitude. Seasonally, dust tends to rise to higher altitudes during the perihelion season, with the atmosphere exhibiting a faint dust haze up to 50-70 km (*McCleese et al.*, 2010; *Määttänen et al.*, 2013), Figure 2.2, but recently 'high altitude dust layers' have been observed through aphelion seasons at heights of 15-25 km (*Heavens et al.*, 2011a), 30 km and 60 km (*Guzewich et al.*, 2013a), although subsequent investigations have not confirmed these observations (*Kleinböhl et al.*, 2015).

The geographical dust cycle of lifting, transportation and deposition is not yet understood to the point at which it can be predicted successfully. Regions which seem to regularly produce dust storms must presumably be resupplied with surface dust at some point, in order to maintain the multi-year cycles observed in recent decades. Studies have been able to develop maps of the surface dust coverage (*Ruff and Christensen*, 2002; *Szwast et al.*, 2006), and proposed climatological maps of atmospheric dust distibution (*Montabone et al.*, 2017), but the full removal-resupply dust cycle – and the timescales involved in such a cycle – is still an active area of research (*Basu et al.*, 2004; *Szwast et al.*, 2006; *Kahre et al.*, 2006; *Wilson*, 2011; *Mulholland et al.*, 2013; *Newman and Richardson*, 2015).

2.3 Dust Storms

Dust storms are common phenomena in the Martian atmosphere, see Figures 2.3 and 2.4. Through decades of capturing images of the surface of Mars – from terrestrial telescopes, from orbiting spacecraft, and recently from surface missions – dust storms have been counted, catalogued and studied. Recent data have allowed multiple surveys of their sizes, timings, locations and behaviour.

Dust storms can be roughly categorised by their physical scale (*Zurek and Martin*, 1993): local storms are the smallest, covering areas starting from a few dozen square kilometres upwards and lasting for only a sol or so (*Cantor et al.*, 2001); regional storms span an area greater than 1.6×10^6 km^2, last for more than two sols, and develop to cover a geographical area beyond the originating region (*Cantor et al.*, 2001; *Wang and Richardson*, 2015); 'planet-encircling'

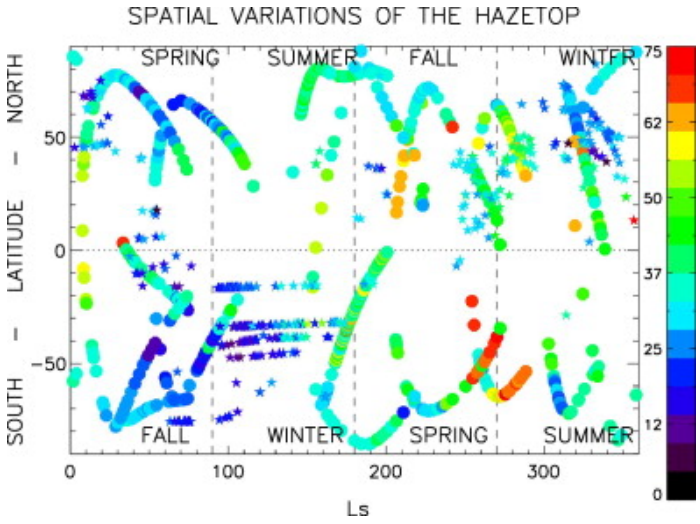

Figure 2.2: The variation in altitude of the top of the dust haze, obtained using solar (circles) and stellar (stars) occulations. The colour scale identifies the altitude of the observed dust. The period around perihelion (L_S ≈210-300°) exhibits generally higher haze-top altitudes, particularly in the southern hemisphere. From *Määttänen et al.* (2013), Fig. 4.

storms encompass very large dust events that span an entire latitudinal band of the planet's surface (*Zurek*, 2017) up to global-scale dust storms, and can be weeks or months long (*Cantor*, 2007). Local storms are most common – one study observed local storms occurring ∼60 times more often than regional storms (*Cantor et al.*, 2001) – and global storms are the most infrequent.

The height to which dust is lifted in a storm also varies. Observations have been made of dust plumes above storm centres reaching heights of 20-30 km (*Cantor*, 2007), although a recent study suggests that the majority of a regional storm's dust remains within the CBL, below an altitude of ∼8 km (*Heavens*, 2017). In contrast, global dust storms can lift dust up to altitudes of ∼60 km (*Anderson and Leovy*, 1978; *Clancy et al.*, 2010). Optical depths within dust storms have been observed by the Viking landers and Spirit and Opportunity rovers, reaching τ ∼5 (*Pollack et al.*, 1979; *Lemmon et al.*, 2015); note that in a typical summer atmosphere, without a dust storm present, $\tau \lesssim 1.5$.

Dust storm activity is seasonal in nature: the perihelion 'dust storm season' is generally defined as spanning L_S ≈160-350° (*Zurek and Martin*, 1993), as the majority of storms are observed through this period. The eccentricity in Mars'

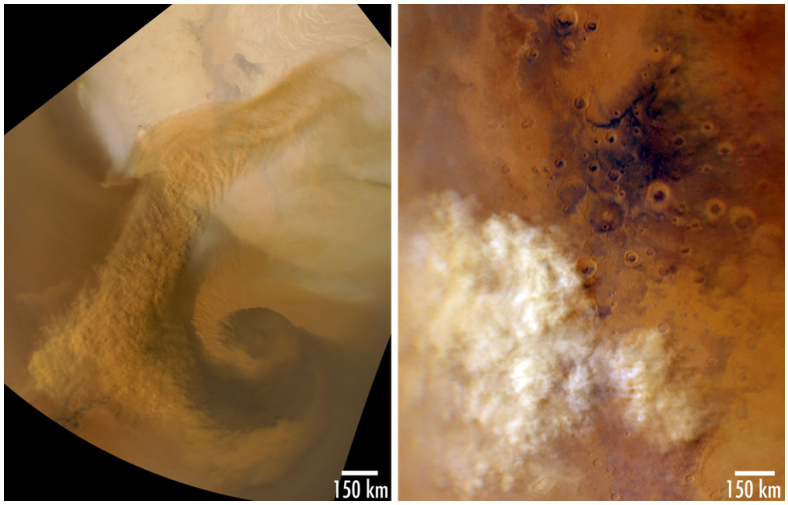

Figure 2.3: Mars Color Imager (MARCI) captures: a spiral storm over the north pole (left), dust clouds nearing the NASA Opportunity rover site (right). Image credit: NASA/JPL-Caltech/Malin Space Science Systems.

orbit (0.093, more than 5 times greater than that of Earth) results in the planet being closer to the sun when the southern hemisphere experiences summer. Southern hemisphere summers therefore receive greater insolation than northern summers, which drives higher temperature and pressure gradients within the atmosphere through this period, impacting large-scale atmospheric circulation and weather patterns, including higher near-surface wind speeds (*Cantor et al.*, 2001). These higher wind speeds facilitate surface dust lifting, a neccessary occurrence for the formation of dust storms.

Martian dust storm formation is still not fully understood. The atmospheric dust that populates a storm is lifted from the surface by strong winds (*Wilson*, 2011), rather than by convective phenomena (*Cantor et al.*, 2006), and the trigger for the formation of a storm is believed to be related to the interaction of these winds with large-scale systems: it is the addition of local wind stress (and associated dust lifting) onto large scale circulations (*Kahn et al.*, 1992), weather fronts (*Hinson and Wang*, 2010; *Wang and Richardson*, 2015) or atmospheric tides (*Wang et al.*, 2003) that drives storm development.

The presence of a dust storm creates a positive feedback loop within the Martian atmosphere: wind-lifted dust raises the local atmospheric temperature (*Gierasch and Goody*, 1973), which drives a reduction in near-surface pressure,

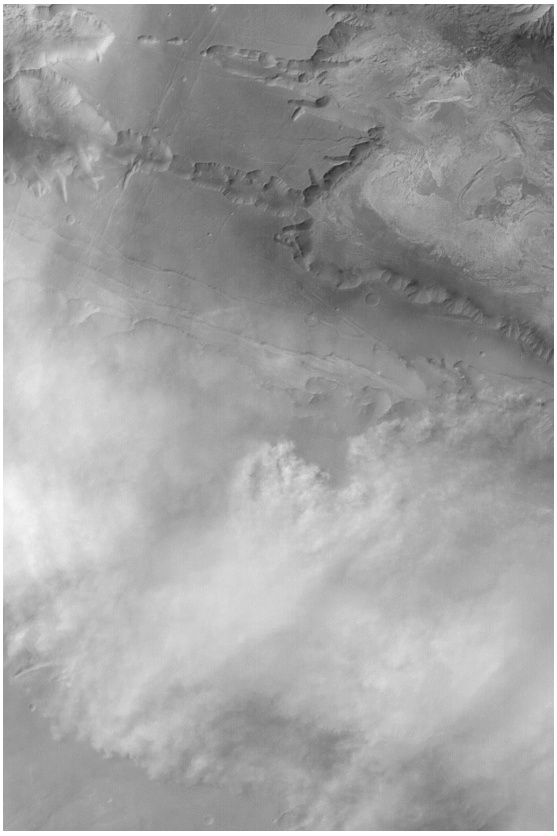

Figure 2.4: A large dust storm captured by the Mars Orbital Camera (MOC) on NASA's Mars Global Surveyor (MGS) orbiter. The topographic features at the top of the image are Melas Chasma and Ius Chasma in the Valles Marineris system; the width of the area imaged is 246 km. Image credit: NASA/JPL-Caltech/Malin Space Science Systems.

so horizontal temperature and pressure gradients are enhanced, resulting in stronger winds that lift more dust (*Rafkin*, 2009). However, this feedback is limited to the area within – or immediately adjacent to – the storm (*Rafkin*, 2009; *Toigo et al.*, 2018), and will be restricted to near-surface altitudes (*Heavens*, 2017).

A thickening storm reduces the amount of insolation reaching the planet's surface. This reduced level of surface heating, combined with the increasing atmospheric temperature, reduces the surface-atmosphere temperature difference (potentially by 10-20 K, *Toigo et al.* 2018). This leads to an inhibition of small-scale convective processes within the region of the storm, and is considered to

be one potential process that causes storms to weaken and disperse (*Gierasch and Goody*, 1973; *Cantor et al.*, 2001). A storm may also begin to weaken if it exhausts the amount of surface dust in the immediate area (*Rafkin*, 2009).

Storms are seen to form in both the northern and southern hemispheres during the dust storm season. Geographical regions in which storms have been observed repeatedly include Elysium, Acidalia, Arcadia, Utopia, Chryse, Hellas, Argyre, Noachis, Cimmeria and Sirenum (*Cantor et al.*, 2001; *Wang et al.*, 2005; *Hinson and Wang*, 2010; *Wang and Richardson*, 2015), with some storm-forming regions associated with areas that experience strong topographically-related wind patterns (particularly in the northern hemisphere) such as slope winds, and some associated with areas experiencing strong horizontal temperature gradients (e.g. the edge of the southern polar cap) (*Cantor et al.*, 2001).

Local storms do not last long and do not travel far, but regional storms can travel great distances. Storms have been observed travelling south in both northern and southern hemispheres (*Cantor et al.*, 2001; *Wang and Richardson*, 2015) and many southern hemisphere storms also travel laterally (*Wang and Richardson*, 2015). A type of Martian dust storm termed a 'flushing' storm forms at high northern latitudes before travelling southwards over the course of a number of sols and crossing the equator (*Cantor et al.*, 2001; *Hinson and Wang*, 2010), following channels through Acidalia-Chryse (longitude ≈-20° E) or south of Utopia (longitude ≈110° E) (*Wang et al.*, 2005; *Wang and Richardson*, 2015). The reverse migration has been observed less frequently (*Wang and Richardson*, 2015).

Predicting individual dust storms is not yet possible, but trends in storm timings through the dust storm season have been identified. *Kass et al.* (2016) report observations through six Martian years of an approximately repeating three-regional-storms cycle in the southern hemisphere through the dust storm season: the first storm occurring through L_S =205-270°, the second occurring through the period L_S =245-290°, usually associated with the edge of the south polar cap, and the third – and most variable within the study – tending to occur through L_S =305-335°. *Liu et al.* (2003) completed a wide survey of long term observations of dust phenomena, and identify a period around L_S =225° that annually exhibits high levels of atmospheric dust associated with storm activity,

and there is often a subsequent repeatable lull in storm activity through the perihelion-solstice period, L_S ≈250-270° (*Wang*, 2007).

While the dust lifted by any local or regional storm will affect the properties of the immediate atmosphere, modelling studies suggest that only long-lasting (>10 sols) regional storms will have an impact on the more distant atmosphere (*Toigo et al.*, 2018). Global dust storms are the exception, as the increased dust loading throughout the entire atmosphere during a global-scale storm creates widespread warming that affects large-scale circulations (*Wilson*, 1997; *Shirley*, 2015), see Figure 2.5. These global dust events appear to arise from conglomerations of local and/or regional storms that suddenly expand in size (*Strausberg et al.*, 2005; *Cantor*, 2007), although the mechanism for this rapid expansion is not yet understood fully.

An early thorough assessment of global dust storm patterns was completed by *Zurek and Martin* (1993), who identified an approximate periodicity of three Mars years between global dust storms. This estimate has held roughly true since that study (*Montabone and Forget*, 2017), although the global dust storm of mid-2018 (L_S ∼190°, MY34) was overdue by this approximation, being statistically anticipated in MY32 or MY33 (*Shirley*, 2015).

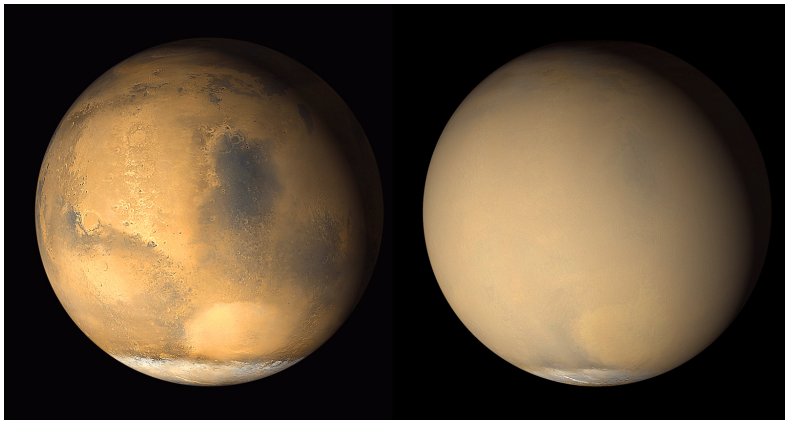

Figure 2.5: Two images of Mars taken by the MGS MOC. Captured only a month apart in 2001, these images illustrate the occasional extent of dust in the Martian atmosphere. Left, Mars with an atmosphere containing a 'typical' dust loading for this time of year, L_S ∼180°; right, a planet entirely enveloped by a global-scale dust storm. Image credit: NASA/JPL-Caltech/Malin Space Science Systems.

2.4 Dust Devils

Martian dust devils are named after the apparently similar features observed on Earth (*Sinclair*, 1969; *Kanak et al.*, 2000; *Balme and Greeley*, 2006; *Fenton et al.*, 2016). These are near-surface atmospheric vortices, visible because of the particles they lift from the ground and entrain in a vertical, upwardly-spiraling column of air. The core of a dust devil is commonly at a lower pressure than the surrounding vortex (*Sinclair*, 1964; *Balme and Greeley*, 2006). Dust devils are able to lift surface dust particles due to the wind shear stress present within the walls of the vortex (*Murphy and Nelli*, 2002; *Balme et al.*, 2003a). The lower central pressure within the column may also contribute to dust lifting by providing an upwards force that assists the shear stress in overcoming interparticle cohesion forces (*Greeley et al.*, 2003; *Balme and Greeley*, 2006), although it is likely only the smallest particles that can be lifted solely by the reduced core pressure (*Neakrase and Greeley*, 2010).

Dust devils were first identified on Mars in Viking Orbiter images (*Thomas and Gierasch*, 1985) and have since been observed in a large number of images captured by orbiting spacecraft (*Fisher et al.*, 2005; *Stanzel et al.*, 2006), as well as in multiple images returned from rovers on the surface (*Ferri et al.*, 2003; *Greeley et al.*, 2006), see Figure 2.6. The tracks left behind by the passage of dust devils – visible as dark streaks against the higher albedo surface – have also been observed in many orbiter images (*Cantor et al.*, 2006), see Figure 2.7.

Martian dust devil speeds and directions of travel have been studied (*Reiss et al.*, 2011, 2014b), their heights calculated (*Fenton and Lorenz*, 2015), potential radial wind speeds evaluated (*Choi and Dundas*, 2011), and estimates have been attempted regarding the amount of dust that they entrain (*Reiss et al.*, 2014a).

While dust storms are large, highly visible phenomena that lift and transport large amounts of dust, the Martian atmosphere still contains 'background' levels of dust throughout the aphelion half of the year, outside the dust storm season. It is believed that the frequent, small-scale lifting performed by dust devils is what sustains this low-level dust loading in the atmosphere through this period (*Basu et al.*, 2004; *Fisher et al.*, 2005). Dust devils therefore play a key role in

433 the annual Martian dust cycle. Indeed, albedo decreases have been recorded for
434 regions over which large numbers of dust devil tracks have been seen (*Cantor*
435 *et al.*, 2006) and lander observations reported diurnal variations in dust opacity
436 associated with the diurnal observations of dust devils (*Smith and Lemmon*,
437 1999). The actual flux of dust lifted into the atmosphere by dust devils is
438 unknown and difficult to calculate due to the large number of uncertainties that
439 exist in the system, including wind speeds internal to the dust devils, the precise
440 structure of the column, the area of the surface from which it draws particles,
441 and how much material is carried to the top of the column before being dispersed
442 compared to how much is redeposited quickly upon the surface (*Balme et al.*,
443 2003b).

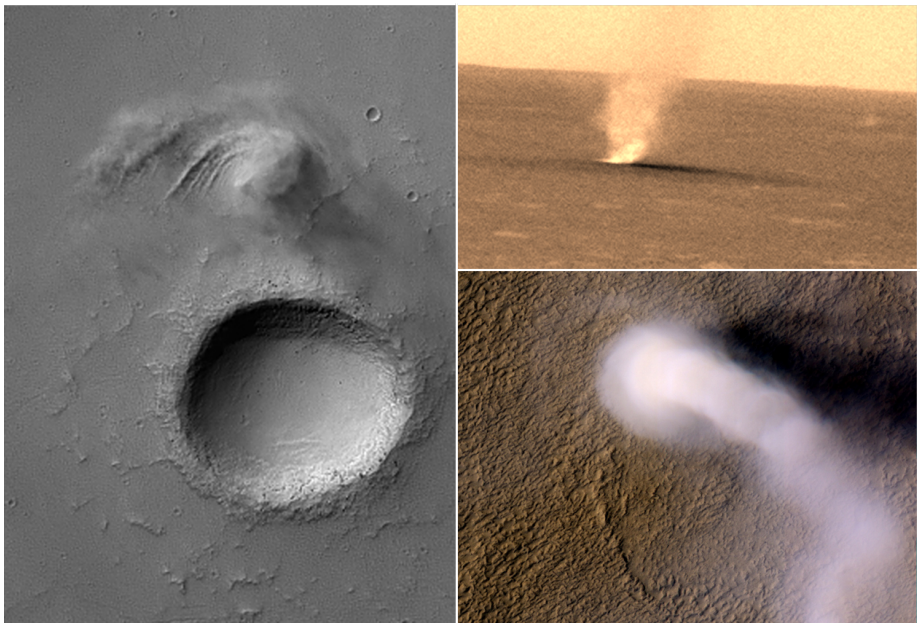

Figure 2.6: Dust devils imaged from orbit and the surface. Clockwise from left: MGS MOC image of a large dust devil in Syria Planum (image credit: NASA/JPL/Malin Space Science Systems); a dust devil captured by NASA's Spirit rover on Sol 486 (during the Northern Hemisphere winter) (image credit: NASA); HiRISE (High Resolution Imaging Science Experiment) image of a dust devil in Amazonis Planitia with a column estimated to be around 70 metres wide but 20 kilometres high (image credit: NASA/JPL-Caltech/University of Arizona).

444 The morphology of Martian and terrestrial dust devils is similar, but Martian
445 dust devils can grow into much larger atmospheric features. The smallest dust

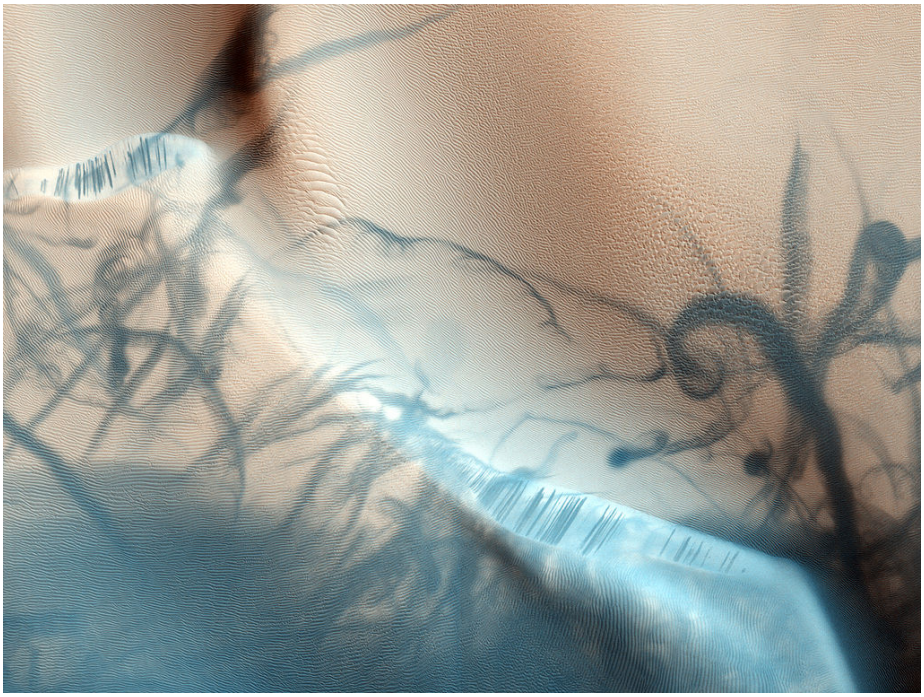

Figure 2.7: A HiRISE image of dust devil tracks across a Nili Fossae sand dune field. The dark tracks indicate a passing dust devil has lifted the surface layer of light-coloured dust from the underlying darker sand (image credit: NASA/JPL/University of Arizona).

devils observed on both Earth and Mars are only a few metres in diameter (*Sinclair*, 1969; *Ferri et al.*, 2003). Large terrestrial dust devils have been observed with diameters of tens of metres (*Snow and McClelland*, 1990; *Balme and Greeley*, 2006) and heights between a few metres and a few hundred metres (*Balme and Greeley*, 2006). In contrast, Martian dust devils have been observed with diameters of up to ∼500 m and heights of up to ∼8 km (*Fisher et al.*, 2005). A possible explanation for this disparity is the lower pressure atmosphere on Mars, which could allow for more frequent and larger dust devils (*Lorenz and Radebaugh*, 2016).

Dust devil activity on Mars is highly variable between regions and seasons (*Fisher et al.*, 2005). Dust devil observations are widespread across the surface of Mars, and they have been seen to move with the ambient wind (*Ferri et al.*, 2003; *Reiss et al.*, 2014b; *Stanzel et al.*, 2008). Particularly active dust devil regions include Amazonis Planitia, Casius, Argyre Planitia, Cimmerium,

Sinai, and Solis (*Cantor et al.*, 2006; *Fisher et al.*, 2005). Observations of dust devils on Earth have identified key local environmental factors that facilitate their formation: (i) arid, rocky terrain, (ii) frequent, strong insolation of the ground, (iii) gently sloping topography. Dust devils arise due to heating of the ground by strong insolation, a vertical instability in the atmosphere in a region that provides a source of vorticity, a superadiabatic lapse rate, and a supply of particulate debris (e.g. *Sinclair*, 1969; *Murphy and Nelli*, 2002).

Martian dust devils are observed to be most frequent in the spring and summer months in each hemisphere (*Thomas and Gierasch*, 1985; *Balme et al.*, 2003b; *Cantor et al.*, 2006), and are rarely observed during local winter (*Balme et al.*, 2003b). The diurnal behaviour of dust devils is discussed in Chapter 5.

2.5 Other Dust Lifting Phenomena

Smaller-scale dust phenomena that can affect dust lifting could be present at the Martian surface. For example, dust particles entrained in the atmosphere can carry electrical charge, arising through collisional (triboelectric) charging (*Rennó et al.*, 2003). This charge can be transmitted to the surface by saltating particles, resulting in an electric force on surface dust particles that is in the opposite direction to the gravitational force (*Kok and Rennó*, 2006). The presence of such a force can weaken the cohesive forces that bind particles to a surface, potentially facilitating more extensive dust lifting by other processes, such as dust devils. However, this effect has been observed at the Earth's surface, which generally contains a high enough fraction of water molecules that it acts as a good conductor (*Kok and Rennó*, 2006); the electrostatic force at the surface of Mars has yet to be explored comprehensively.

Collisional electical charging of dust particles may also affect the size of the dust objects that are lifted from the surface. Charged dust particles can adhere to one another, clumping together to form dust aggregates up to 1 mm in diameter (*Merrison et al.*, 2004). As larger particles are more easily lifted from a surface than small particles, because smaller particles are more dominated by the restraining interparticle cohesive forces (*Greeley*, 2002), these aggregates are more easily lofted into the atmosphere by near surface winds than the smaller

dust particles from which they form.

An additional effect that may be important to dust lifting on Mars is that of thermophoresis. This lifting mechanism couples the greenhouse effect within the surface dust - in which incident radiation can drive warming in dust particles immediately below the top layer of particles - and the thermophoretic effect - in which momentum is transferred between gas molecules and dust particles along a thermal gradient, from warm to cold (*Wurm and Krauss*, 2006). At the Martian surface, the upwards lift that dust particles experience due to thermophoresis is not enough to directly propel them into the atmosphere, but it may lessen the downwards cohesive forces (*Wurm et al.*, 2008).

While these phenomena should not necessarily be considered insignificant among dust lifting processes on Mars, especially when research into their efficacy is still continuing, they are not yet incorporated into the dust lifting included within Martian global models. This is due to the facts that very large-scale models cannot include every small-scale surface phenomena - for reasons of computing efficiency - and until a dust lifting process is more fully understood there will be limited benefit in parameterising its effect.

2.6 Dust and Spacecraft

Missions to Mars must consider the properties of the atmosphere that the travelling spacecraft will encounter upon arrival. This is true for both orbital and landing missions.

Orbiting spacecraft can particularly be affected by atmospheric conditions upon arrival at Mars. The increased atmospheric loading that occurs during dust storms has an impact on the density of the upper atmosphere (at altitudes of 110-120 km) (e.g. *Keating et al.*, 1998), which can affect the aerobraking operations of spacecraft entering orbit around the planet (*Withers and Pratt*, 2013).

Spacecraft descending to the Martian surface under parachute or using retro thrusters can be affected by local wind fields and wind variability (*Rafkin and Michaels*, 2003; *Tyler et al.*, 2008; *Vasavada et al.*, 2012), by convective turbulence (*Petrosyan et al.*, 2011), and by local variations in atmospheric density

(*Chen et al.*, 2014). Consideration of the predicted meteorology for a region is therefore often incorporated into landing site selection (*Toigo and Richardson*, 2003; *Kass et al.*, 2003; *Forget et al.*, 2011; *Montabone et al.*, 2015a).

The near-surface dust environment is an area of potential concern for landers or rovers that are solar powered, as a build-up of dust on solar panels will reduce the power available to the platform (*Landis and Jenkins*, 2000). Local dust events may actually be beneficial in this regard: the Mars Exploration Rovers (MERs) Spirit and Opportunity both experienced 'dust clearing events' (e.g. *Vaughan et al.*, 2010) that assisted the extension of their nominal missions. These have been attributed to local wind gusts or passing dust devils (*Lorenz and Reiss*, 2015).

Mission planners need to be able to predict a range of Martian atmospheric properties, including the amount of dust in the atmosphere and the likelihood of a spacecraft encountering local (or global) dust events. Computer modelling is one of the best tools currently available for exploring the environmental factors contributing to the timings and occurrence of atmospheric dust events, and their impact on the Martian climate.

Chapter 3

Modelling Dust in the Martian Atmosphere

This chapter describes the Martian atmospheric model used through the majority of this research: a Global Circulation Model (GCM). The GCM used in this work is the UK version of the LMD (Laboratoire de Météorologie Dynamique) Mars Global Circulation Model, as described by *Forget et al.* (1999) with improvements and updates mentioned below as appropriate.

For comparison with the global simulations, experiments were also completed using a Mesoscale Model. The Mesoscale Model used is the LMD Martian Mesoscale Model, described by *Spiga and Forget* (2009); use of this model is detailed within Chapter 6.

3.1 The Mars Global Circulation Model

GCMs are used widely in planetary science to study long-term, global-scale atmospheric circulations and patterns within various planetary atmospheres.

The UK version of the LMD Mars Global Circulation Model (henceforth "the MGCM") is a global, multi-level spectral model of the lower and middle regions of the Martian atmosphere; simulations typically extend up to an altitude of $\sim$100 km.

The MGCM is composed of a spectral dynamic core, which solves equations

of motion on a rotating sphere, and a large number of 'physical subroutines', which implement the parameterisations[1] of physical processes. Many physical processes are available for inclusion in MGCM simulations; this chapter will detail the specific subroutines of the model that are most germane to this research.

3.2 MGCM Dynamics

The MCGM is a spectral model: it uses a truncated series of spherical harmonics to represent horizontal variations in atmospheric fields (*Bourke*, 1972). Field values are stored as coefficients of the spherical harmonic functions.

The model fields evolve with time, their progression realised through a semi-implicit integration method, as described by *Hoskins and Simmons* (1975). Spectral field values are transformed onto a physical-space grid, field tendencies are calculated, and the reverse transformation is undertaken ahead of the next progression in time. (It is computationally more efficient to transform spectral field values onto a physical-space grid, and back again, than it is to attempt calculations involving non-linear terms within spectral-space, *Bourke* 1974.) Two grids are used within the MGCM: one for nonlinear products (which is created by oversampling field values, in order to reduce any aliasing) and one for physical variables.

As time advances, the MGCM dynamic core solves the 'primitive equations' of meteorology to calculate the fluid motion of the atmosphere (e.g. *Kalnay*, 2003; *Wallace and Hobbs*, 2006; *Andrews*, 2010). The derivation of these equations begins with terms for the conservation of mass, momentum and energy.

Conservation of mass, when applied to a fluid system, requires that the increase (or decrease) of mass inside a system is equal to the rate at which mass flows into (or out of) that system:

$$\frac{D\rho}{Dt} + \rho\nabla \cdot \mathbf{u} = 0 \tag{3.1}$$

where ρ is the atmospheric density, and $\mathbf{u}$ is the velocity vector.

[1] *Parameterisation* within climate modelling is the emulation of a complex process (in global modelling, often one which is also small in scale) through the implementation of a simpler process.

585 Conservation of momentum is expressed in this context using the Navier-
586 Stokes equation of fluid flow within a rotating frame of reference:

$$\frac{D\mathbf{u}}{Dt} = \mathbf{g} - 2\mathbf{\Omega} \times \mathbf{u} - \frac{1}{\rho}\nabla p + \mathbf{F} \tag{3.2}$$

587 where $\mathbf{g}$ is the effective gravity experienced within the rotating frame, $\mathbf{\Omega}$ is the
588 planet's angular velocity vector, p is atmospheric pressure, and $\mathbf{F}$ is the frictional
589 force per unit mass.

590 Conservation of energy is expressed with the thermodynamic energy equa-
591 tion:

$$\frac{D\theta}{Dt} = Q \tag{3.3}$$

592 where Q represents diabatic heating and θ is the potential temperature:

$$\theta = T\left(\frac{p_0}{p}\right)^{(R/c_p)} \tag{3.4}$$

593 in which T is temperature, p_0 is a reference pressure (usually taken as 610 Pa
594 for Mars), R is the gas constant per unit mass, and c_p is the specific heat at
595 constant pressure per unit mass.

596 To complete the equations describing a planet's rotating atmosphere, it is
597 necessary to also incorporate the equation of state of an ideal gas:

$$p = \rho RT, \tag{3.5}$$

598 the assumption of hydrostatic equilibrium (a good approximation in a global-
599 scale model, where vertical atmospheric motions are small compared to the
600 height of the atmosphere):

$$\frac{\partial p}{\partial z} = -\rho g \tag{3.6}$$

601 in which z is height and g is acceleration due to gravity; and the assumption
602 that the atmosphere is spherical and thin compared to the radius of the planet.

603 The primitive equations of meteorology can be written in terms of absolute
604 vorticity, divergence, temperature and log-surface pressure (*Hoskins and Sim-*
605 *mons*, 1975), which are represented within the MGCM as spectral field values.

606 These values are then transformed into variables within a three-dimensional

physical-space grid: zonal wind (u), meridional wind (v), temperature (T), and surface pressure (p_s). It is within this grid that physical tendencies are calculated, and the results are then transformed back into spectral field components for the model's next temporal advance.

3.2.1 Vertical Coordinate

The vertical direction within the model is represented by a 'sigma' scheme, such that

$$\sigma = \frac{p}{p_0} \tag{3.7}$$

where p is the atmospheric pressure at a point above the surface and p_0 is the atmospheric pressure at the corresponding point (i.e. of the same latitude, longitude and time) where the atmosphere touches the planet's surface. The vertical layers within this scheme follow the terrain at the surface of Mars, at which $\sigma = 1$.

Use of a terrain-following sigma scheme results in simpler lower boundary conditions than would be possible using other vertical coordinate systems (*Simmons and Burridge*, 1981). Schemes in which atmospheric layers are defined by pressure or geometric height can result in layer boundaries intersecting a planet's surface in regions that include large vertical topographical variations across a relatively small horizontal distance. The Martian surface contains several regions of such topography.

3.3 Physical Subroutines

The gridboxes[2] that comprise the MGCM's physical-space grid are large in scale, spanning dozens or hundreds of horizontal kilometres, depending on latitude and model resolution. A number of physical processes that are important to include within global climate models take place on a much smaller scale, which consequently cannot be modelled explicitly in such a grid. These processes are

[2]Due to the nature of a 3D grid, each intersection $A(x, y, z)$ is most correctly referred to as a grid*point*, and will be termed as such when discussed abstractly. However, when discussing physical-space results, the term grid*box* will be used; this can be visualised as a cube centred on a gridpoint, extending as far as the halfway marks to the adjacent horizontal and vertical gridpoints.

parameterised in subroutines within the MGCM, in order to assess their effect on large-scale behaviours.

The physical subroutines available within the MGCM range from fundamental (the diurnal cycle, the condensation and sublimation of seasonal CO_2 ice caps) to more specific (e.g. water ice cloud microphysics). The inclusion of certain physical subroutines can be selected or deselected when initiating a simulation.

3.3.1 Tracer Transport

An atmospheric 'tracer' is any constituent unit that is carried within the flow of the atmosphere, e.g. dust particles, water molecules, or atoms of various chemical species. If a tracer influences atmospheric circulation it is termed 'active' (or 'radiatively active', due to it having an impact on atmospheric radiative calculations), otherwise it is a passive tracer.

The MGCM's tracer advection scheme is a semi-Lagrangian scheme, in which the amount of a tracer at a model gridpoint P at time t is calculated from the amount of that tracer at a point earlier in the atmospheric flow's trajectory, at time $t-1$ (*Newman*, 2001). Using horizontal and vertical wind velocities, the backwards trajectory of the air parcel at P at time t can be extrapolated, to find its origin point at time $t-1$. The position of this origin is commonly between gridpoints. The tracer mixing ratio at the origin can be calculated by interpolating values from the nearest gridpoints; the mixing ratio can then be propagated through time and space to the desired arrival gridpoint P.

Semi-Lagrangian schemes are not necessarily conservative. In order to conserve mass within the simulation the Priestley method of conservation (*Priestley*, 1993) is incorporated into this tracer advection scheme at the point of calculating final tracer mixing ratios (*Newman et al.*, 2002a).

Tracer sedimentation rates are based upon particle radius and density, using the classic Stokes expression for particle terminal velocity modified following *Rossow* (1978):

$$V = \frac{2}{9}\frac{\rho_{\mathrm{t}} g r_{\mathrm{t}}^2}{\nu}\left(1 + \frac{4}{3}\frac{\lambda}{r_{\mathrm{t}}}\right) \tag{3.8}$$

where ρ_{t} is the density of the tracer particle, r_{t} is the radius is the tracer particle,

662 ν is the atmospheric viscosity and λ is the gas mean free path.

663 It is possible to include a wide range of tracer options within MGCM sim-
664 ulations. These experiments incorporated the dust tracer, but omitted the full
665 available range of trace chemical species. The water cycle and radiatively active
666 water ice particles were also excluded. These decisions were based upon a desire
667 to focus specifically on surface dust lifting, hence eliminating the complicating
668 factor of the full water cycle, and a requirement to limit objective simulation
669 time, hence excluding chemical molecular and atomic tracers that are not rele-
670 vant to these experiments.

671 Specific parameters and behaviours of the dust tracer are described in Section
672 3.4.

673 3.3.2 Atmospheric Turbulence

674 The MGCM includes parameterisations of a number of turbulent atmospheric
675 processes that impact the zonal wind, u, meridional wind, v, potential temper-
676 ature, θ, and the flux of atmospheric tracers. These are:

677 - **Vertical diffusion:** changes in the turbulent kinetic energy within the at-
678 mosphere are calculated using thermal gradients and horizontal wind shear
679 between model layers (*Forget et al.*, 1999). This kinetic energy causes tur-
680 bulent atmospheric motion that drives vertical mixing. Parameterisations
681 related to specific tracer mixing are incorporated into the MGCM calcu-
682 lations of tracer flux, such as processes lifting surface dust (see Section
683 3.5).

684 - **Convective adjustment:** the change in potential temperature between
685 model layers is used to test the stability of the modelled atmosphere. If the
686 potential temperature decreases with height (i.e. $\delta\theta/\delta z < 0$) the convec-
687 tive adjustment parameterisation implements quick mixing of the layers,
688 representing the small-scale convection that would occur in a real atmo-
689 sphere (*Hourdin et al.*, 1993). This adjustment restores a stable vertical
690 profile.

691 - **Gravity wave drag:** atmospheric drag on wind speeds is caused by grav-
692 ity waves arising from topography, both from low-level drag around topo-

graphic features (*Lott and Miller*, 1997), and at the point of a vertically-propagating wave 'breaking', when the wave's momentum is deposited within the immediate surroundings (*Palmer et al.*, 1986).

- **CO_2 condensation and sublimation:** this parameterisation calculates the condensation and sublimation of carbon dioxide both within the atmosphere and on the planet's surface, and the change in near-surface atmospheric pressure due to this change in state (*Forget et al.*, 1998). The sedimentation of CO_2 precipitation through model layers (CO_2 'snow') is included here.

3.3.3 Radiative Flux

Heating processes within the Martian atmosphere are driven by radiative fluxes through the atmosphere and the associated heating (and cooling) rates of the atmospheric components.

Incident radiation is divided into two broad wavelength domains within the MGCM – visible and infrared – and the atmospheric radiative processes are calculated separately for each domain. The heating and cooling rates of atmospheric tracers are calculated from their various absorption, emission and scattering parameters, which are based on particle sizes and particle size distributions (see Section 3.4.1). In the lower and middle Martian atmosphere the most relevant tracers are CO_2 (gas molecules and ice particles), water (vapour and ice particles) and dust (*Haberle et al.*, 2017).

The visible domain is subdivided into two bands: 0.1 - 0.5 μm and 0.5 - 5 μm. The infrared domain is subdivided into three main bands: 5 - 11.6 μm (the "9 μm band"), 11.6 - 20 μm ("15 μm band"), and 20 - 200 μm (the "far-infrared").

The 15 μm band is divided again due to the dominance of CO_2 absorption at these wavelengths. Following the model proposed by *Hourdin* (1992), this section of the spectrum is split into a central region, 14.2 - 15.7 μm, in which CO_2 absorption is very strongly dominant, and the 'CO_2 band wings' either side, within which the absorption is not as strong. MGCM calculations of the atmospheric heating rates associated with the 15 μm band include a simplified model of non-local thermal equilibrium (non-LTE) effects, which are important

724 at higher altitudes (above ∼70 km) (*López-Valverde et al.*, 1998).

725 3.4 Atmospheric Dust

726 3.4.1 The Dust Particles

727 Martian atmospheric dust particles have never been sampled, so their exact
728 size, shape and density are not yet precisely known. The particles are modelled
729 within the MGCM as small spheres. This is a reasonable approximation, as
730 the electromagnetic scattering properties of a particle are considered to be only
731 weakly dependent on the shape of the particle (*Wolff and Clancy*, 2003), and
732 such an approximation allows particle size to be defined simply by radius.

733 The particle size distribution is assumed to be a log-normal distribution,
734 which can be defined by a two-moment scheme, and allows calculation of dis-
735 tribution parameters from knowledge of other parameters (*Heintzenberg*, 1994).
736 Log-normal schemes have previously been used to represent terrestrial aerosol
737 species (*Pollack et al.*, 1995), and it has been shown that a log-normal particle
738 distribution displays scattering parameters that vary little from those observed
739 in both gamma and power law distributions (*Hansen and Travis*, 1974).

740 Within the two-moment scheme, two dust tracers are advected through the
741 atmosphere: the dust mass mixing ratio (mass of dust per unit mass of atmo-
742 sphere), q, and the dust number mixing ratio (number of dust particles per unit
743 mass of atmosphere), N. These values are then used to calculate the effective ra-
744 dius, r_{eff}, and the effective variance, v_{eff}, of the size distribution, quantities that
745 are useful for deriving the scattering properties of a given particle population.

746 The size distribution is initialised with $r_{\text{eff}} = 2.75$ μm and $v_{\text{eff}} = 0.5$. As the
747 dust tracers are advected, the change in the particle population within a gridbox
748 must be recalculated. While v_{eff} is held constant, the new r_{eff} is calculated using
749 the advected values of q and N:

$$r_{\text{eff}} = r_0 \left(\frac{5}{2} \sigma_0^2 \right) \tag{3.9}$$

750 in which σ_0 is the standard deviation of the distribution and r_0 is the geometric

mean radius:

$$r_0 = \left(\frac{3}{4\pi\rho_p} \frac{q}{N} \exp\left[-4.5\sigma_0^2 \right] \right)^{1/3} \tag{3.10}$$

where ρ_p is the density of the dust particles.

The recalculated r_{eff} for each gridbox is used in subsequent radiative transfer calculations. Look-up tables of particle scattering properties have been formulated previously for a range of particle sizes, following *Wolff et al.* (2006), using Waterman's T-matrix method (*Waterman*, 1965; *Mishchenko*, 1991). These values are read from a datafile at simulation initiation.

In experiments that implement a 'prescribed dust scenario' to determine atmospheric dust distribution (see Section 3.4.2) only one set of scattering parameters is used: those that relate to a particle size distribution with $r_{\text{eff}} = 1.5$ μm and $v_{\text{eff}} = 0.3$. These values fall within the ranges identified by a number of Martian dust particle studies (e.g. *Clancy et al.*, 1995; *Pollack et al.*, 1995; *Wolff et al.*, 2009; *Smith et al.*, 2013). The scattering properties of a particle with $r_{\text{eff}} = 1.5$ μm are illustrated in Figure 3.1.

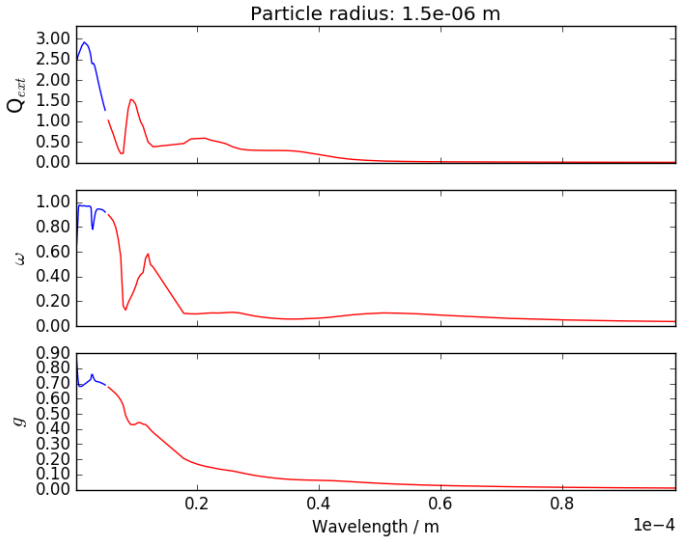

Figure 3.1: Scattering properties by wavelength of the single-size dust particle used in the prescribed atmospheric dust scenario (see Section 3.4.2): the extinction coefficient, Q_{ext}, single scattering albedo, ω, and asymmetry factor, g. The visible domain is drawn in blue and the infrared domain is drawn in red.

The composition of Martian dust particles can be estimated from observa-

tions of the optical properties of the atmosphere; Martian surface and atmospheric dust is believed to be largely basaltic in origin, consisting of related montmorillonite-like and/or palagonite-like materials. To account for this uncertain mix of materials, the density of the particles in the model, ρ_p, is set to 2500 kg m^{-3} in this work. This is an approximate average density for a basaltic rock mix (*Philpotts and Ague*, 2009).

3.4.2 Dust Distribution

When dust is an active tracer, radiative calculations are performed on the atmospheric dust distribution that is formulated as described in the previous section. Dust can also be advected as a passive tracer, in which case the radiative calculations are performed on a prescribed dust distribution that matches a specified 'dust scenario'. The dust scenarios used within the MGCM are taken from *Montabone et al.* (2015b), and are based upon orbital observations of the optical depth of the Martian atmosphere during MY24 to MY32 (*Smith et al.* 2003; *Smith* 2004, 2009; see Chapter 2). The dust scenarios are stored as daily maps of optical depth (i.e. one map per sol) at a resolution of 36 points in latitude and 72 points in longitude.

Modelled dust lifted from the surface is summed vertically to obtain a column density, and then scaled (at gridbox resolution) to match the daily global maps of the optical depth of the Martian atmosphere.

These dust optical depth observations are made from orbit and display the sum of the dust in the atmosphere from the planet's surface to the top of the atmosphere, and cannot provide any information on the vertical distribution of this dust. The vertical profile of atmospheric dust is selected separately in the MGCM. Within the lowest scale height of the atmosphere the dust mixing ratio is constant, representing a well-mixed lower atmospheric layer; above this height a Conrath profile is typically used, in which the density of dust in the atmosphere declines with altitude (*Conrath*, 1975), representing a dust distribution that has undergone a measure of sedimentation. A Conrath profile offers a balance between gravitational sedimentation and vertical mixing: the rate at which the dust density decreases with height is dependent upon the atmospheric scale height and the diffusion and settling times of the dust particles.

The dust scenario for MY24 is used in MGCM simulations as an example of a typical Martian year with average dust loading in the atmosphere. In contrast, MY25 is considered a high dust year; the 2001 global dust storm took place in this year during the northern hemisphere autumn. An example plot of the prescribed atmospheric dust field for MY24 is shown in Figure 3.2.

With dust as a passive atmospheric tracer, any dust particles lifted from the surface of the planet do not impact the atmosphere; i.e. the presence of lifted dust does not affect variables such as local temperature or wind speeds, which would consequently affect the rate of dust lifting. Without this feedback loop, it is possible to explore the effect of specific model parameters on dust lifting processes, without the lifted dust impacting the results. This allows direct comparison of experiments in which these parameters are varied.

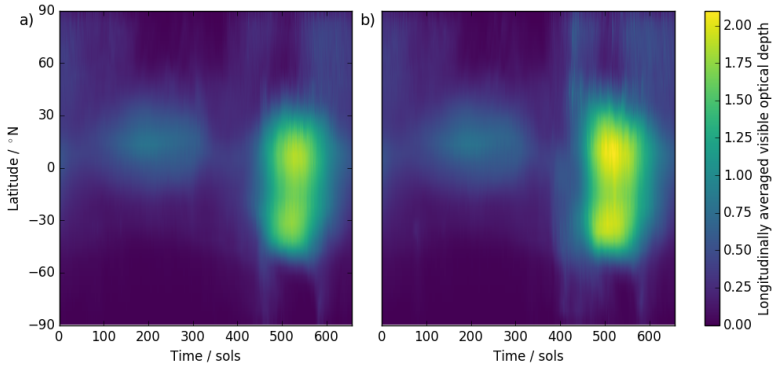

Figure 3.2: Example plots of the longitudinally averaged visible optical depth (0.67 μm) of the prescribed atmospheric dust field for two Martian years: a) MY24, b) MY25; cf. *Montabone et al.* (2015b).

3.5 Dust Lifting

Martian dust enters the bottom of the atmosphere, lifted from the surface. This can be represented within models either as a designated quantity of dust that is arbitrarily 'injected' into the atmosphere (e.g. *Richardson and Wilson*, 2002), or by more explicitly modelling specific dust lifting processes (e.g. *Newman et al.*, 2002a; *Basu et al.*, 2006; *Kahre et al.*, 2006). The dust injection method is suitable for use in simulations that require dust loading in the atmosphere

while other aspects of the climate are being investigated, but it does not allow the identification of locations from which dust is lifted, or the timing of that lifting.

The MGCM incorporates two main processes by which Martian dust is lifted into the atmosphere: lifting by near-surface wind stress and lifting by dust devils.

These processes are distinct subroutines within the model and do not interact at the point of lifting surface dust. If atmospheric dust is radiatively active within a simulation, the dust lifted by both processes will affect the entire atmosphere, which consequently can impact the behaviour of both lifting processes; with dust present only as a passive tracer, the processes remain independent and can be analysed separately.

3.5.1 Near-Surface Wind Stress

Near-surface wind stress (NSWS) is a horizontal force acting upon particles on a surface, which is proportional to the speed of the near-surface wind. Dust particles are lifted by NSWS when the horizontal frictional drag force of the wind is large enough to overcome the forces that hold the particles to the surface.

Lifting by NSWS is considered to be the primary dust lifting process that drives the formation and development of seasonal Martian dust storms (e.g. *Strausberg et al.*, 2005; *Basu et al.*, 2006; *Wilson*, 2011). This process was incorporated into the MGCM by *Newman et al.* (2002a,b) and modified by *Mulholland et al.* (2013).

The amount of dust lifted by NSWS is parameterised within the model, as the real process occurs on a scale that is too small to be modelled explicitly within a global-scale model. Within the parameterisation, surface dust lifting occurs when the friction velocity of the wind, at the boundary where the atmosphere meets the ground, is greater than the threshold friction velocity, i.e. when $u^* > u^*_{\mathrm{t}}$.

The friction velocity, u^*, is found from the local wind speeds and boundary layer drag (*Esau*, 2004):

$$u^* = \frac{\kappa U}{\ln(1 + z/z_0)} \tag{3.11}$$

where U is the magnitude of the near-surface wind speed, calculated from the large-scale zonal and meridional wind components (u and v) within the lowest model layer of the atmosphere, κ is the von Kármán constant, z is the height of that lowest layer, and z_0 is the surface roughness length.

The threshold friction velocity, u_t^*, is also referred to as the 'lifting threshold'. It is derived from a formulation of the fluid threshold by *Shao and Lu* (2000) (implemented within the MGCM by *Mulholland* 2012). The fluid threshold is the minimum speed at which wind shear stress alone is strong enough to lift particles from a surface, implemented in the MGCM dust lifting parameterisation as:

$$u_{\mathrm{ft}} = \sqrt{\frac{0.0246(\gamma\rho_{\mathrm{p}}g)^{0.5}}{\rho_1}} \tag{3.12}$$

where $\gamma = 3 \times 10^{-4}$ kg s^{-2}, ρ_{p} is the material density of the particles, set herein to 2500 kg m^{-3}, g is the acceleration due to gravity, and ρ_1 is the atmospheric density in the lowest model layer of the atmosphere.

Applying this fluid threshold directly to surface models would set an unfeasibly high lifting threshold for dust-sized particles, as it ignores the presence of saltating particles. Saltating particles impacting upon a surface of similar particles result in lower wind speeds being required to lift further particles. This 'impact threshold' is defined as the minimum speed at which wind shear stress is able to lift particles from a surface when impacting saltating particles are present; the impact threshold is always lower than the fluid threshold.

In parallel with the need to modify the fluid threshold to better approximate reality, directly applying the evaluation of u^* from Equation 3.11 to a global-scale model produces an under-estimation of the subsequently lifted dust. The wind magnitude, U, is necessarily computed at the scale of the model gridboxes, which at lower resolutions can be hundreds of kilometres in size. Therefore this calculation of u^* will not capture the effect of stronger, small-scale gusts of wind (*Newman et al.*, 2002a,b).

In order to account for both saltation and small-scale wind gusts, the threshold friction velocity within the MGCM is set to be a proportion of the fluid threshold:

$$u_t^* = Q_t u_{\mathrm{ft}} \tag{3.13}$$

where Q_t is the ratio of the impact threshold to the fluid threshold.

The ratio Q_t for Mars is currently unknown. Estimates for this ratio on Earth range from ≈0.8 (*Bagnold*, 1937) to ≈0.96 (*Almeida et al.*, 2008), but proposed values for Mars are much lower: ∼0.1 by *Kok* (2010), ∼0.3 by *Claudin and Andreotti* (2006), and ∼0.48 by *Almeida et al.* (2008). This is due to the fact that the lower Martian gravity and thinner atmosphere allow particles to saltate in longer and higher trajectories, thus reaching higher velocities and then imparting more energy to surrounding particles when they land.

Modelled dust is lifted from the planet's surface into the lowest layer of the atmosphere when $u^* > u^*_\mathrm{t}$. The vertical dust flux, F_dust, is calculated as a proportion of the horizontal dust flux:

$$F_\mathrm{dust} = \alpha_N F_\mathrm{H} \tag{3.14}$$

where α_N is a tuneable parameter representing the efficiency of dust lifting by NSWS, and F_H is the horizontal dust flux derived by *Mulholland* (2012) following experimental results presented by *Kok and Rennó* (2008):

$$F_\mathrm{H} = 0.25\frac{\rho_1}{g}(u^*)^3\left(1-\left(\frac{u^*_\mathrm{t}}{u^*}\right)^2\right)\left(7+50\left(\frac{u^*_\mathrm{t}}{u^*}\right)^2\right) \tag{3.15}$$

The NSWS dust lifting parameterisations employed currently within the MGCM are similar to the subroutines used within other Martian global atmospheric models (e.g. *Basu et al.*, 2006; *Kahre et al.*, 2006; *Takahashi et al.*, 2011a). The majority of Mars global atmospheric models that implement dust lifting through NSWS include a 'lifting efficiency' parameter analogous to α_N.

3.5.2 Dust Devils

The dust devil parameterisation in operation within the MGCM was implemented by *Newman et al.* (2002a) (and modified subsequently by *Mulholland* (2012) to incorporate the two-moment tracer scheme).

The modelled flux of dust lifted by dust devils at a point on the surface, F_devil, is calculated from the local sensible heat flux, F_s, and the dust devil

thermodynamic efficiency, η:

$$F_{\text{devil}} = \alpha_D \eta F_s \tag{3.16}$$

where α_D is a tuneable parameter representing the 'dust devil lifting efficiency'. This factor must be included in the parameterisation because existing observations of Martian dust devils are not yet able to quantify the actual amount of suface dust lifted by the phenomenon. This parameter is set at a value that best reproduces the annual atmospheric dust cycle, matched against the range of observed dust opacities (*Newman et al.*, 2002a). For the 'climate modelling' resolution (T31, see Section 3.6), $\alpha_D = 1.13333 \times 10^{-8}$ kg J^{-1}. This value is not modified throughout the simulations within this work.

Dust devil thermodynamic efficiency, η, arises from modelling a dust devil as a 'heat engine', following *Rennó et al.* (1998): this quantity is the fraction of the heat input to the dust devil 'system' that is converted into mechanical work.

This thermodynamic efficiency can be approximated as $\eta \approx 1 - b$, where

$$b = \frac{(p_{\text{surf}}^{\chi+1} - p_{\text{top}}^{\chi+1})}{(p_{\text{surf}} - p_{\text{top}})(\chi + 1)p_{\text{surf}}^{\chi}} \tag{3.17}$$

where p_{surf} is the near-surface atmospheric pressure, p_{top} is the pressure at the top of the convective boundary layer, and χ is equal to the specific gas constant divided by the specific heat capacity at constant pressure ($R/c_p = 0.256793$).

The sensible heat flux, F_s, expresses the input heat available to drive the dust devil 'heat engine':

$$F_s = \rho c_p C_D U (T_{\text{surf}} - T_{\text{atm}}) \tag{3.18}$$

in which ρ is the near-surface atmospheric density, C_D is the surface drag coefficient, U is the magnitude of the horizontal wind speed (defined as in Equation 3.11), T_{surf} is the surface temperature, and T_{atm} is the near-surface atmospheric temperature (i.e. the local temperature in the lowest model layer of the atmosphere).

The surface drag coefficient, C_D, is parameterised using the classical expres-

sion for a boundary layer drag coefficient (*Esau*, 2004):

$$C_D = \left(\frac{\kappa}{\ln(1 + z/z_0)} \right)^2 \tag{3.19}$$

where z is the height of the lowest model layer of the atmosphere, and z_0 is the surface roughness length. In the experiments completed for this thesis, neither z or z_0 are varied: $z \sim 5$ m and $z_0 = 0.01$ m. The value of C_D is therefore constant across the planet's surface.

The MGCM dust devil parameterisation has been used as a foundation for similar parameterisations in other Mars atmospheric models. Two such models, the NASA Ames Mars General Circulation Model (GCM) and the Geophysical Fluid Dynamics Laboratory (GFDL) Mars GCM, directly incorporate the *Newman et al.* (2002a) parameterisation (respectively *Kahre et al.* (2006, 2008) and *Basu et al.* (2004)).

3.6 Model Resolution

Horizontal Resolution

The horizontal resolution of a spectral model is defined by the total wavenumber of the spherical harmonic series. Table 3.1 identifies the range of MGCM resolutions used within this research. Figure 3.3 illustrates the relative latitude and longitude sizes of the physical gridboxes used across the different resolutions.

Selecting the horizontal resolution at which an experiment is completed does not require a change to the model's input parameters beyond identifying the wavenumber associated with the spectral model and the consequent number of maximum total rows and columns associated with the horizontal grid used to resolve physical processes. Results from experiments completed at different resolutions can therefore be compared directly: differences observed within the data are a consequence of the changing resolution, not a reflection of the input parameters selected.

Simulation resolution	Number of grid points, latitude and longitude	Approximate physical resolution, ° latitude × ° longitude
T31	36, 72	5.00 × 5.00
T42	48, 96	3.75 × 3.75
T63	72, 144	2.50 × 2.50
T85	96, 198	1.88 × 1.88
T127	144, 288	1.25 × 1.25
T170	192, 384	0.94 × 0.94

Table 3.1: MGCM resolutions used in this research. The wavenumbers used for the series truncation are 'common' spectral model grid resolutions employed originally within terrestrial climate modelling (*National Center for Atmospheric Research Staff (Eds.)*).

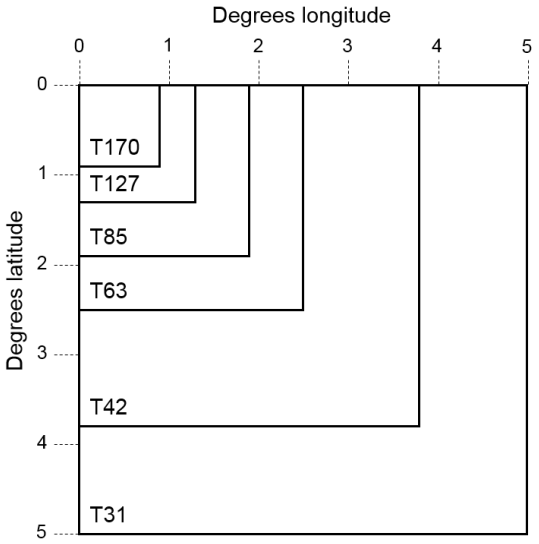

Figure 3.3: Comparison of physical process gridbox sizes across the model resolutions used with this research. 1 degree of latitude on Mars is equal to 59.27 km; for comparison, 1 degree of latitude on Earth is equal to 111.2 km.

Vertical Resolution

The vertical layers in most MGCM simulations are not of a constant depth: layer thickness increases as altitude increases. The lowest layers are shallowest (∼10 to ∼100 metres deep), the layers through the middle of the modelled altitudes are a few kilometres deep, and the uppermost layers are the deepest (> 10 km). This distribution was selected in order to produce the highest vertical resolution near the surface-atmosphere boundary (e.g. *Lewis et al.*, 1999).

Figure 3.4 shows how sigma coordinate and model layer are related, and

the approximate mid-layer altitudes for the resultant model layers (in a typical 25-layer experiment); Figure 3.5 illustrates the difference in model layer depth through the atmosphere.

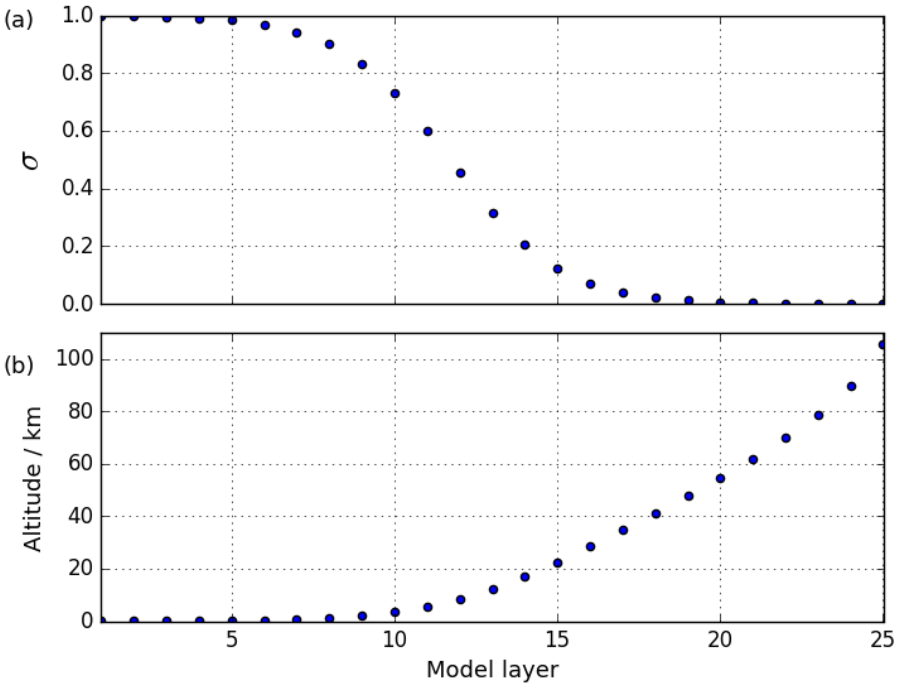

Figure 3.4: Implementation of a vertical 25-layer sigma scheme: (a) σ values by model layer; (b) approximate altitude of model layer mid-points.

Temporal Resolution

At the start of an experiment the rate at which simulation time passes is selected through a parameter specifying the number of model timesteps to be completed per sol. Atmospheric dynamics calculations are completed each timestep, while physical tendency calculations are completed less frequently.

The number of timesteps per sol must be selected with consideration of the horizontal resolution of the simulation. The length of a timestep is limited by the need to satisfy the Courant-Friedrichs-Lewy (CFL) condition for quantities being propagated within a spatial grid: that the timestep, Δt, must be shorter than the time required for information to be transferred over more than one

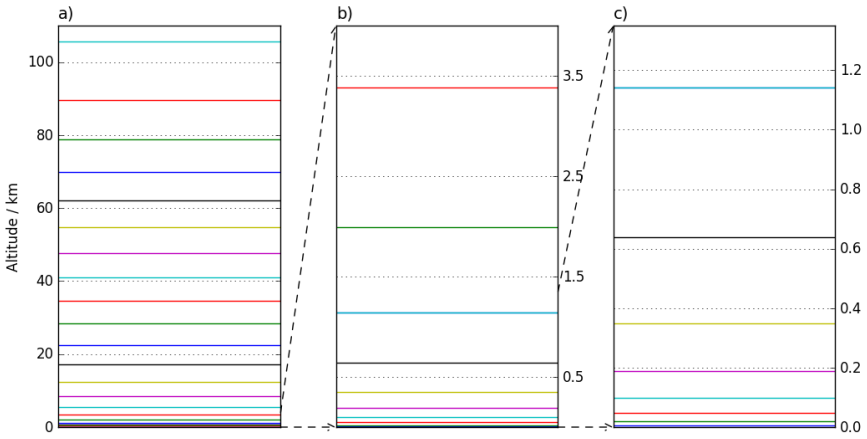

Figure 3.5: Illustration of mid-layer altitudes within an example 25 vertical layer simulation: a) all 25 layers; b) lowest 10 layers; c) layers within the lowest ∼kilometre of the atmosphere.

gridbox:

$$\Delta t \leq \Delta x / u \tag{3.20}$$

where Δx is the grid spacing and u is the speed of propagation (*McGuffie and Henderson-Sellers*, 2005).

Table 3.2 identifies the approximate length of the timesteps used in the different resolution simulations within this research.

Simulation resolution	Timesteps per sol	Dynamics timestep length / minutes	Physics timestep length / minutes
T31	480	3.08	30.82
T42	960	1.54	15.41
T63	1750	0.85	5.92
T85	1750	0.85	5.92
T127	2500	0.59	2.37
T170	5000	0.30	1.18

Table 3.2: Approximate timestep lengths by model resolution. The model completes dynamics calculations each timestep; the Martian sol is 88775.2 seconds long, and the length of this 'dynamics timestep' is approximated here in (Earth) minutes solely to aid comprehension. Physical tendency calculations are completed at a lower rate, the 'physics timestep', defined as a multiple of dynamics timesteps.

3.7 Experimental Procedure

The atmosphere within an MGCM simulation is initialised in a dynamically static state. Atmospheric circulations develop as simulation time progresses and dynamic calculations are completed.

Experiments are run for multiple subjective years before any results are analysed, in order to allow long-period circulations – and consequent atmospheric properties and tracer distributions – to settle into patterns and cycles representative of a full dynamic atmosphere. For most experiments a two year 'spin-up' period is completed, and the third year is analysed to capture the full seasonal cycle (each year starting at solar longitude $L_S = 0°$).

For high resolution simulations the objective time required to complete multi-year simulations becomes prohibitive; for example, a simulation of 60 Martian sols ($\sim 30°$ L_S) at the T170 resolution currently takes around a full real-time calendar month to complete. The two-year spin-up is consequently unfeasible at the highest resolutions.

The solution is to use results from a simulation completed at a lower resolution as a 'stepping-stone', and to interpolate those results up to a larger horizontal grid. MGCM simulations can be started (and restarted) at any point in the Martian year, allowing a high resolution simulation to be started from any chosen sol, provided that a suitable lower resolution simulation exists from which to interpolate data. High resolution simulations can therefore be completed for any selected period throughout the Martian year and the results compared directly with lower resolution simulations.

This interpolation has the potential to introduce artefacts into the data. High resolution simulations started in this manner are therefore always run for a 'settle-down'[3] period before data is analysed for comparison, e.g. a 60-sol settle-down period is completed ahead of the desired 60-sol analysis period. The analysed data will therefore be free of interpolation errors and be an accurate representation of the Martian atmosphere captured at the higher resolution.

[3]The term 'settle-down' is used herein for the pre-analysis period within a simulation that was started from an interpolated moment, while the term 'spin-up' is only used for this period in a simulation started from a static state.

Chapter 4

Wind-Stress Dust Lifting and Model Resolution

4.1 Introduction

Martian dust storms range in size from relatively small, localised events, through 'regional' dust storms, to planet-encircling and global storms. Dust storms are largely seasonal in nature, with the majority of storms being observed during southern hemisphere spring and summer months, $L_S \approx$160-350° (e.g. *Zurek and Martin* 1993; *Cantor et al.* 2001; *Wang and Richardson* 2015, and refer back to Section 2.3).

The formation and development of dust storms on Mars is driven by the interaction of near-surface winds and large scale circulations (e.g. *Leovy et al.*, 1973; *Kahn et al.*, 1992; *Wang et al.*, 2003; *Strausberg et al.*, 2005; *Hinson and Wang*, 2010; *Wilson*, 2011; *Wang and Richardson*, 2015). The near-surface winds lift the dust that populates the storm. This surface dust lifting is a small-scale process; it is consequently incorporated into global models through parameterisation.

It is understood by the modelling community that the resolution at which experiments are completed can have a large impact on the results of those experiments (e.g. *Takahashi et al.*, 2011a; *Toigo et al.*, 2012; *Mulholland et al.*, 2015). For example, changing the horizontal resolution of a simulation will change the

size of the surface features that can be resolved in that experiment, which can impact any parameterisation associated with near-surface phenomena; depending on the settings of the model, a small change at surface level can affect the progression of the entire global simulation.

Few published studies have considered in detail how the results of dust lifting parameterisations are affected by a change in the underlying model resolution (*Takahashi et al.* 2008 identify preliminary investigations but offer no recommendations). The dependence of the results of MGCM dust lifting experiments upon this facet of modelling has not been quantified, and it is not known how robust such results are when compared across changing resolutions.

The work discussed in this chapter uses the MGCM to investigate the representation of dust lifting by near-surface winds across different horizontal and vertical model resolutions. Section 4.2 describes the experimental method used within this work and specifies the different horizontal and vertical resolutions used. Section 4.3.1 presents the impact of changes to the model's horizontal resolution; Section 4.3.2 presents the impact of changes to the model's vertical resolution. Section 4.4 discusses the results, investigating how and why the amount of dust lifted and the spatial distribution of dust lifting are affected by resolution change. The results of multiple experiments are also compared with published observations of dust storms on the surface of Mars. Section 4.5 explores the very high resolution tests completed in this work. Section 4.6 summarises this chapter and details recommendations.

The reader should note the nomenclature used within this chapter: 'dust lifting' is used exclusively to refer to dust lifting by near-surface wind stress (NSWS); 'height', when used to refer to a point in the atmosphere, relates to the height of that point above the local surface (i.e. not with reference to the Mars geoid); Northern Hemisphere and Southern Hemisphere will be abbreviated to NH and SH, respectively.

The longitude-latitude convention used within this work is to define a location using –90° to 90° N in latitude and –180° to 180° E in longitude. The equatorial meridian (0° lat, 0° lon) will always be shown in the centre of globally plotted data.

4.2 Method

Experiments were completed across a range of horizontal and vertical model resolutions. The horizontal resolution of the MGCM is varied by modifying the wavenumber truncation of the model's spectral grid (see Section 3.6); Table 4.1 identifies the horizontal resolutions used within this work. The vertical resolution of the MGCM is varied by modifying the number of modelled vertical layers: an 'L25' simulation uses 25 vertical layers. The vertical layers in a simulation are not equally spaced: the lowest layers are shallowest, in order to provide the greatest vertical resolution in the layers most closely involved in near-surface processes (*Lewis et al.* 1999, and refer back to Figure 3.5). Table 4.2 identifies the vertical resolutions used within this research, and Figure 4.1 shows how the altitude of each model layer varies across simulations with different numbers of vertical layers.

When varying the horizontal resolution, experiments were completed using 25 vertical layers. When varying the vertical resolution, experiments were completed using the T31 horizontal resolution, which produces a physical resolution of $\sim 5^\circ$ lat $\times$ $\sim 5^\circ$ lon. Similar horizontal resolutions are typically used to model the global Martian climate; e.g. by *Newman et al.* (2002a) when implementing a dust transport scheme; by *Basu et al.* (2004) and by *Kahre et al.* (2005) when investigating the seasonal or interannual dust cycles; by *Steele et al.* (2014) when studying the Martian water and cloud cycle. These same studies used a vertical resolution comparable with the resolution achieved by the MGCM's 25 layers.

Resolution ID	Approximate physical resolution / ° latitude × ° longitude	Number of horizontal gridboxes in simulation
T31	5.00 × 5.00	2592
T42	3.75 × 3.75	4608
T63	2.50 × 2.50	10368
T85	1.88 × 1.88	18432
T127[a]	1.25 × 1.25	41472
T170[a]	0.94 × 0.94	73728

Table 4.1: MGCM horizontal resolutions used in this research. [a]This resolution has been used sparingly, see Section 4.5.

Resolution ID	Height of lowest layer / km	Number of layers in lowest 10 km	Height of top layer / km
L25	0.005	12	105.61
L30	0.005	14	106.26
L35	0.005	16	106.71
L50	0.005	22	107.47
L60	0.005	26	107.76
L70	0.005	30	107.96
L100	0.005	41	108.30

Table 4.2: MGCM vertical layer numbers used in this research.

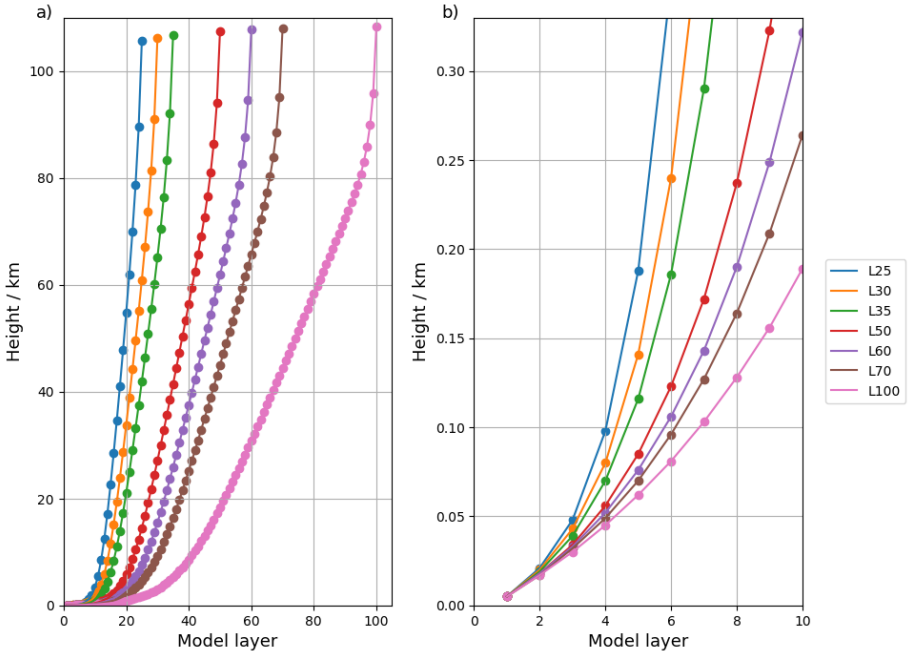

Figure 4.1: The approximate altitudes of layer mid-points across a range of simulations with different numbers of vertical layers. Note that the top of the atmosphere varies little in height across the simulations (a), and that the heights of the lowest layers are similar for the majority of the simulations (b).

The MGCM's parameterisation of dust lifting by near-surface wind stress was implemented by *Newman et al.* (2002a,b); see Section 3.5.1. Similar parameterisations are included in other global Martian atmosphere models (e.g. *Basu et al.*, 2006; *Kahre et al.*, 2006; *Takahashi et al.*, 2011a).

Dust can be lifted from any gridbox at any time if the NSWS is strong enough. The exception to this is if a surface layer of CO_2 ice is present in a gridbox: this is considered a barrier to dust lifting and the recorded lifting rate is zero.

As described in Section 3.5.1, the MGCM NSWS dust lifting parameterisation includes two parameters that can be used to calibrate the amount of dust that is lifted in an experiment: the threshold velocity (the minimum wind speed required to lift dust, u_{t}^{*}) and the lifting efficiency (a tuneable parameter representing how efficient this dust lifting process is, α_N). During the experiments described below these parameters were held constant, in order to solely test the impact the changing resolution had on the results of the experiments. It is anticipated that the information gained from these experiments can be used in future work to set these parameters so as to calibrate the model across resolutions.

Experiments were run for multiple years prior to the period required for data analysis, to allow long-period atmospheric circulations to settle into representative patterns and cycles. This was described in Section 3.7 and is only summarised here: for most experiments a two year 'spin-up' period was completed and only the full third year analysed (starting at $L_S = 0^{\circ}$). For high resolution experiments it was possible to interpolate results from a lower resolution experiment up to a larger horizontal grid, avoiding the prohibitively long spin-up period required at such resolutions. High resolution experiments started in this manner are still run for a short time ($\sim$60 sols) ahead of the required analysis period, in order to eliminate any artefacts introduced by the interpolation.

4.3 Results

4.3.1 Changing the Horizontal Resolution

Global plots of dust lifting through a Martian year are shown in Figures 4.2 to 4.5. Each panel of the plots displays the sum of all dust lifted by NSWS through an $L_S = 30°$-long portion of the year. A coloured gridbox indicates that dust was lifted in this gridbox during the displayed period; white regions indicate a dust lifting rate of zero through this period. The colour-scale is a stretched, pseudo-log scale, used with the sole intent of emphasising the full range of the scale. Note that the total amount of dust lifted varies by two orders of magnitude between resolutions.

These plots show dust lifting across four increasing horizontal resolutions: T31 (Figure 4.2), T42 (Figure 4.3), T63 (Figure 4.4), and T85 (Figure 4.5). T31 is a relatively low resolution, typically used for long-term climate modelling; T85 is a moderately high resolution for Martian global modelling. (All experiments were completed using 25 vertical layers.)

The dust lifting shown in these plots is not constant, but is instead sporadic in nature. An example of this is shown in Figure 4.6: the instants at which dust is lifted through the period 210-240° L_S are shown for each of the horizontal resolutions under discussion, for the location 30° N, –30° E. (This point was selected because it exhibits dust lifting through this period in each of these experiments.)

The data shown in Figures 4.2 to 4.5 are plotted in Figure 4.7, as the amount of lifted dust lifted in each $L_S = 30°$ period through the year (normalised by the number of sols in each period), for each resolution. There is a large difference in the amount of dust lifted in the experiments completed at the T42 and T63 resolutions, compared to the difference between the results for the T63 and T85 resolutions, even though the delta in resolution is similar across each resolution increase. This is discussed in Section 4.4.2.

Figure 4.8 shows the annual, global sum of lifted dust mass against the resolution grid spacing.

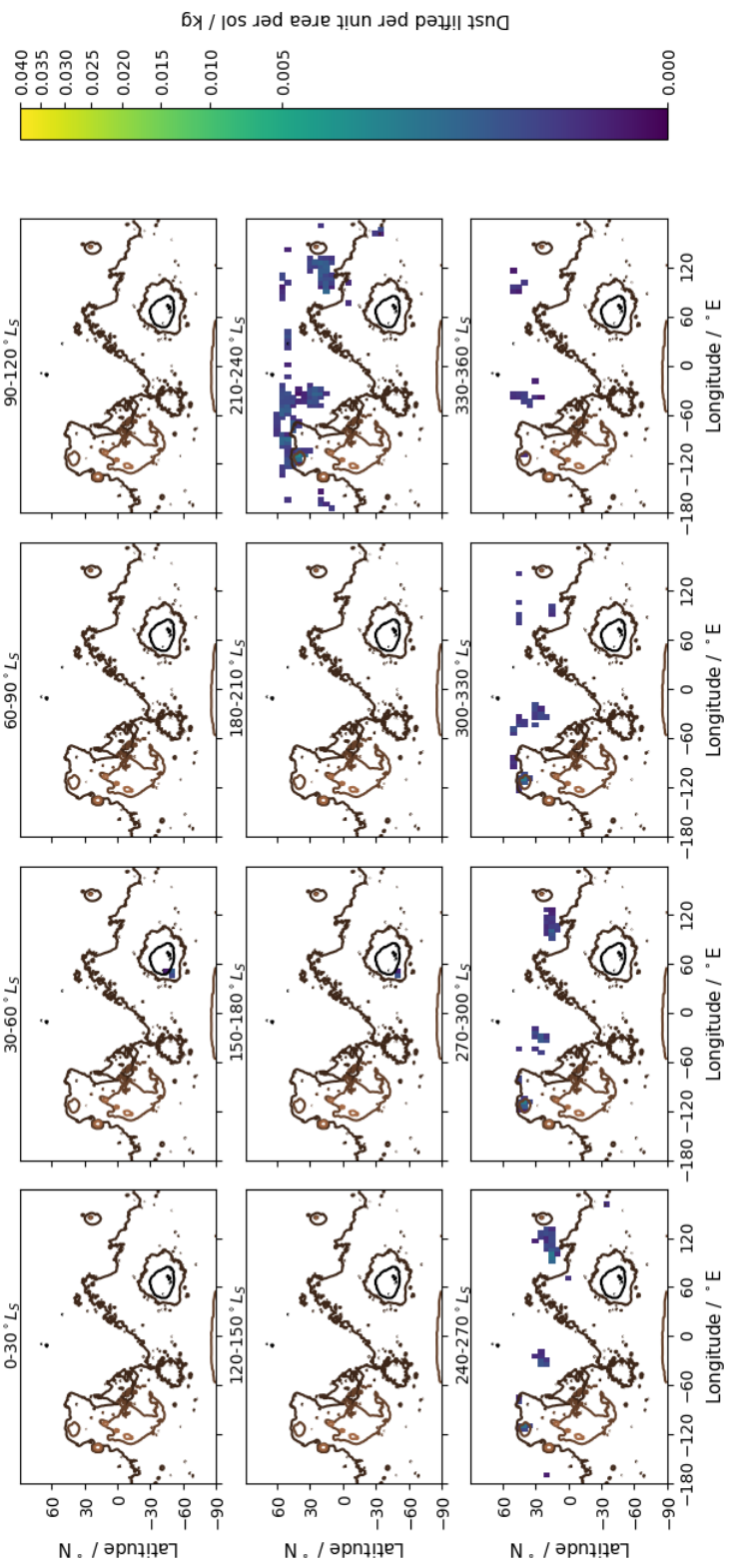

Figure 4.2: Global dust lifting by NSWS within a T31[L25] experiment. Each panel shows lifted dust mass per unit area through a $L_S = 30°$-long period in the Martian year. The colour-scale is a stretched, pseudo-log scale, indicating dust lifting during each $L_S = 30°$ period; white indicates zero lifting. (Topography contours added for reference only, yellow lines indicate higher elevations than dark lines.)

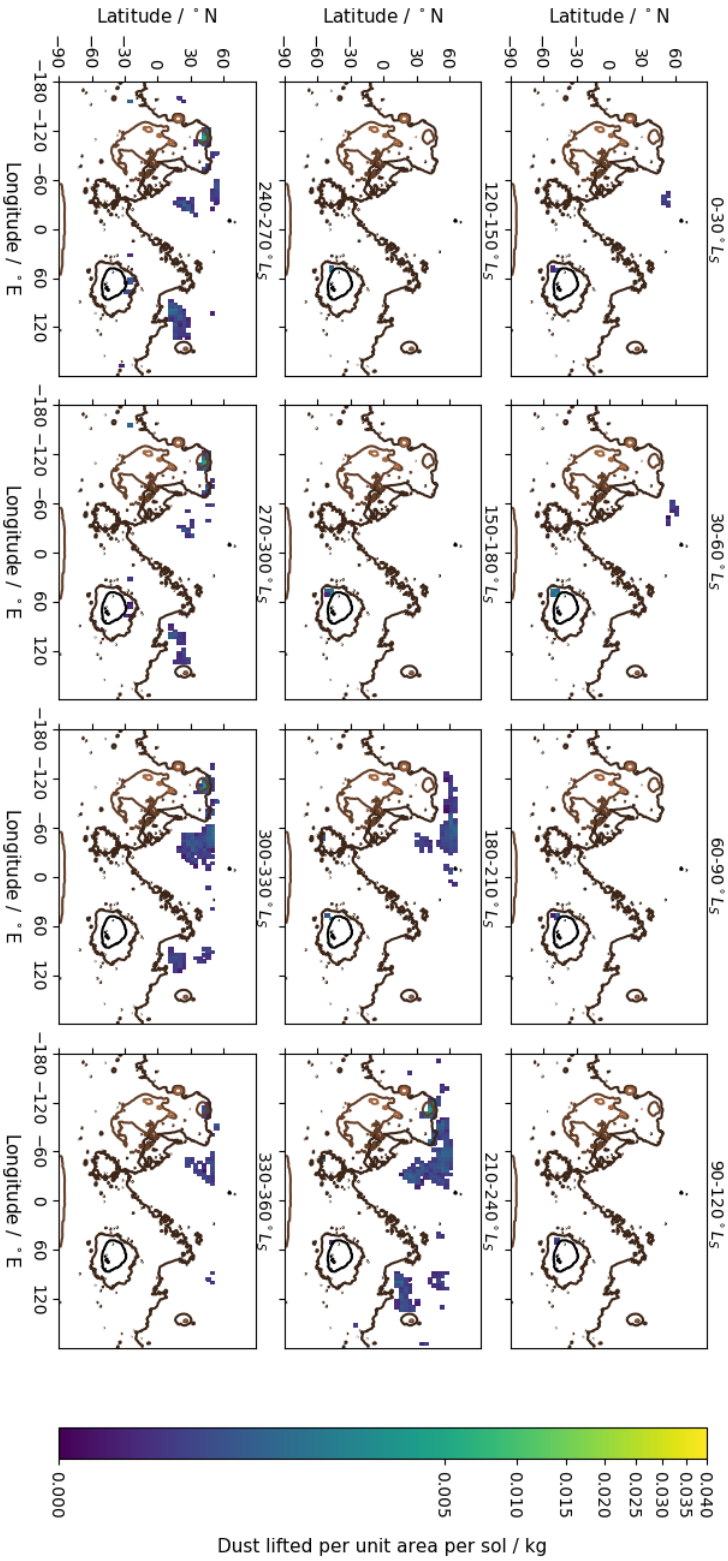

Figure 4.3: As Figure 4.2 for a T42 experiment.

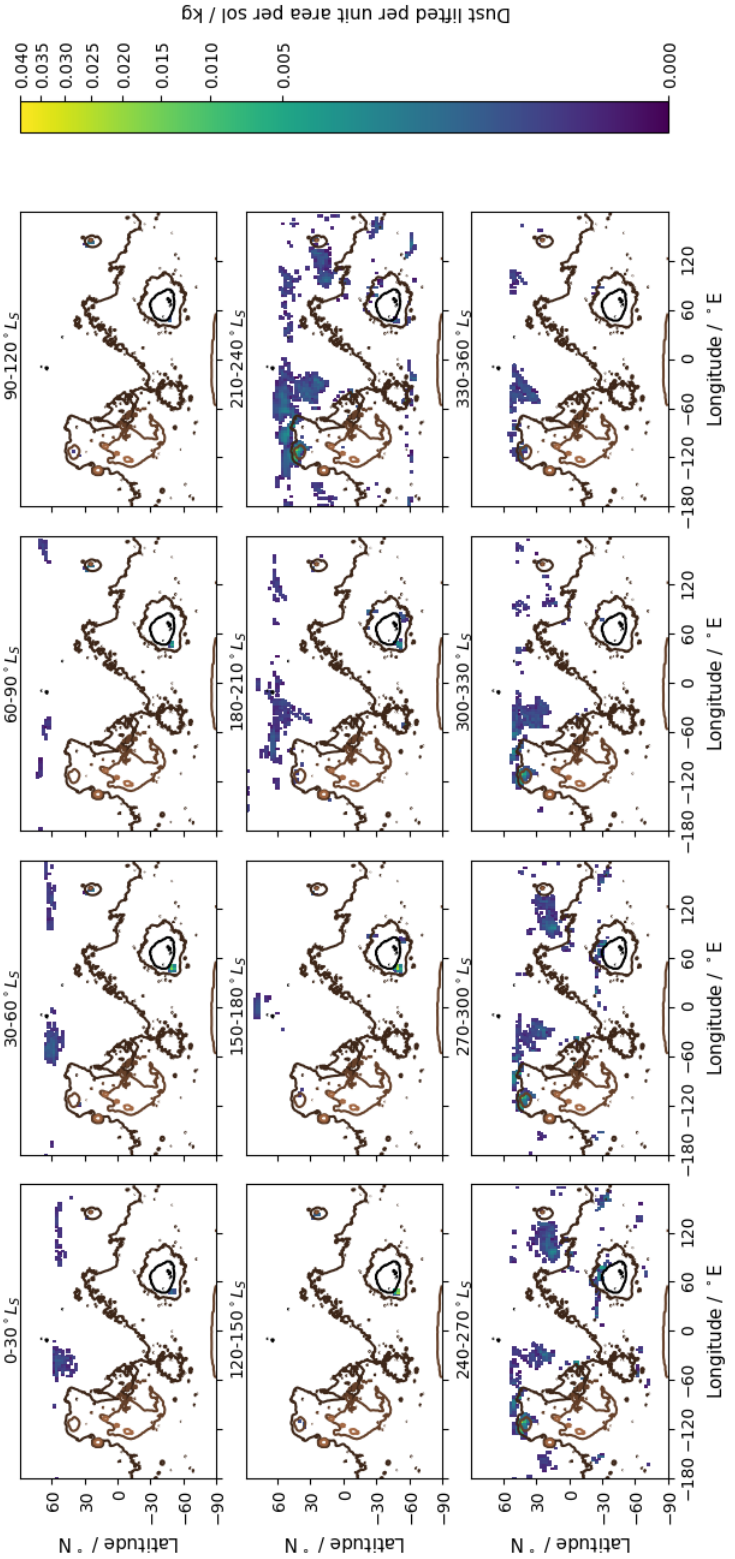

Figure 4.4: As Figure 4.2 for a T63 experiment.

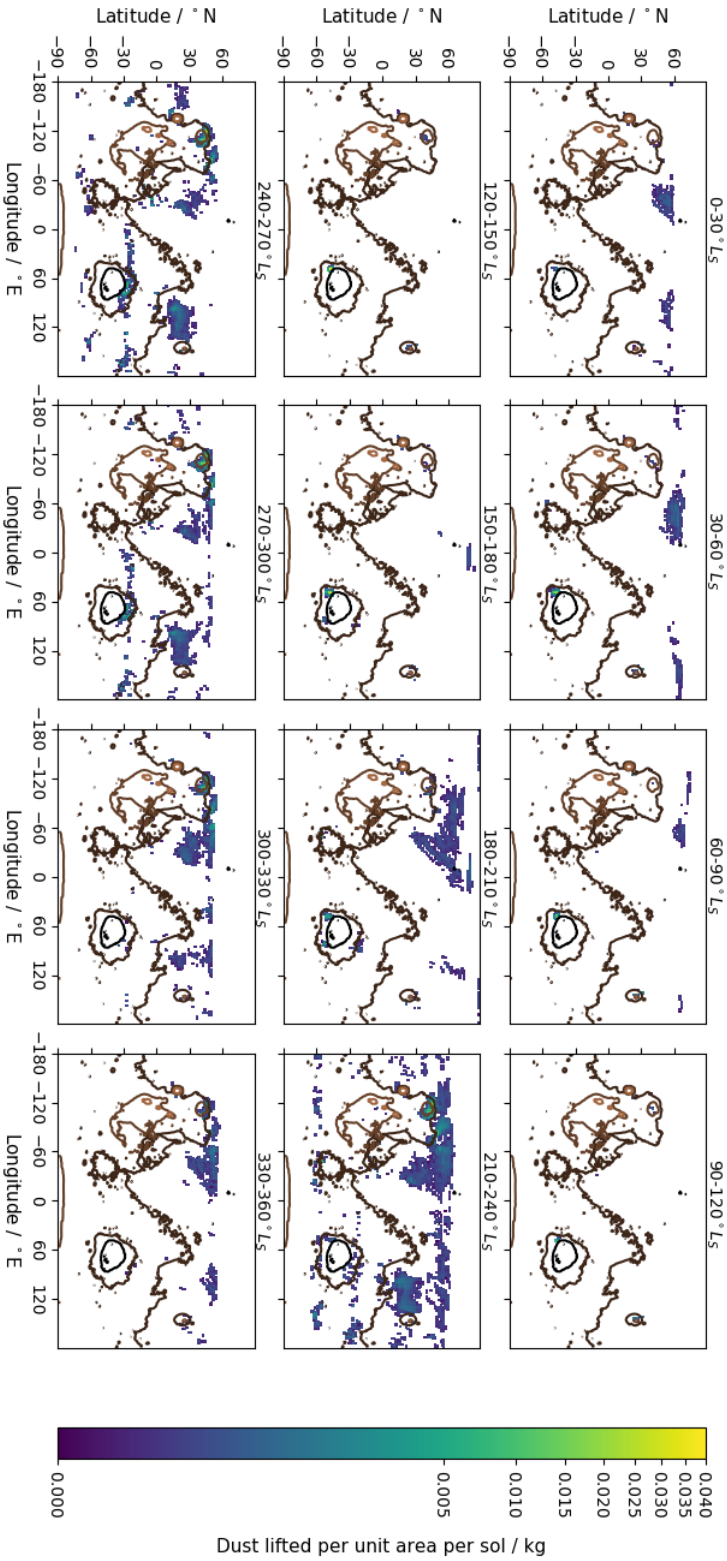

Figure 4.5: As Figure 4.2 for a T85 experiment.

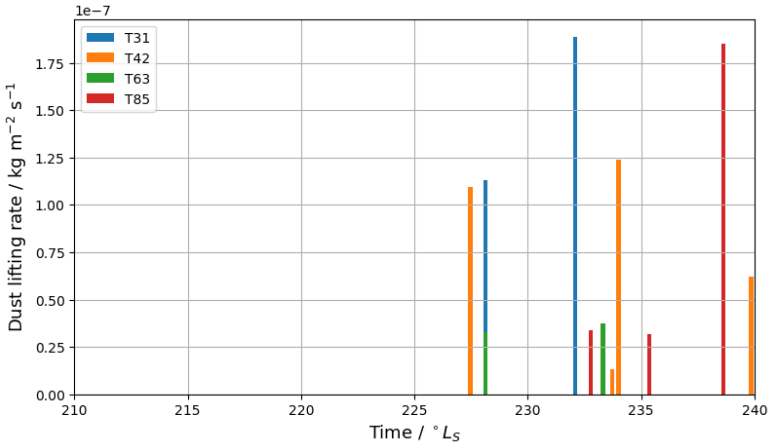

Figure 4.6: The dust lifting rate at an example surface location (30° N, –30° E) in experiments completed across a range of horizontal resolutions, through the period 210-240° L_S.

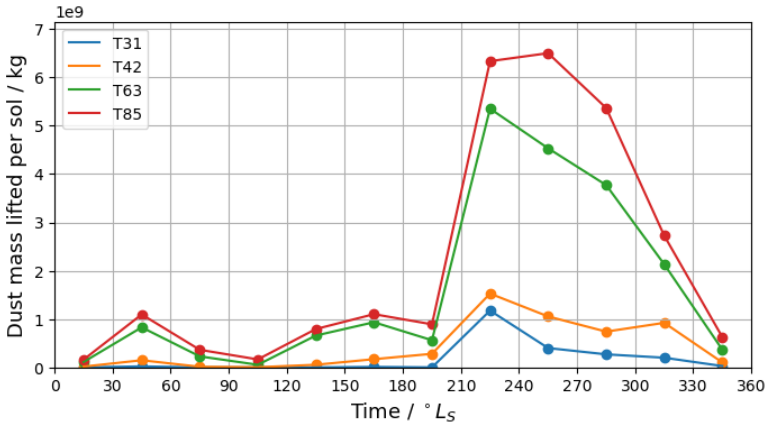

Figure 4.7: The dust mass lifted globally during each $L_S = 30°$-long period of the Martian year, normalised by the number of sols in each period, for each horizontal resolution. Plot lines added only to help the reader to follow each experimental result.

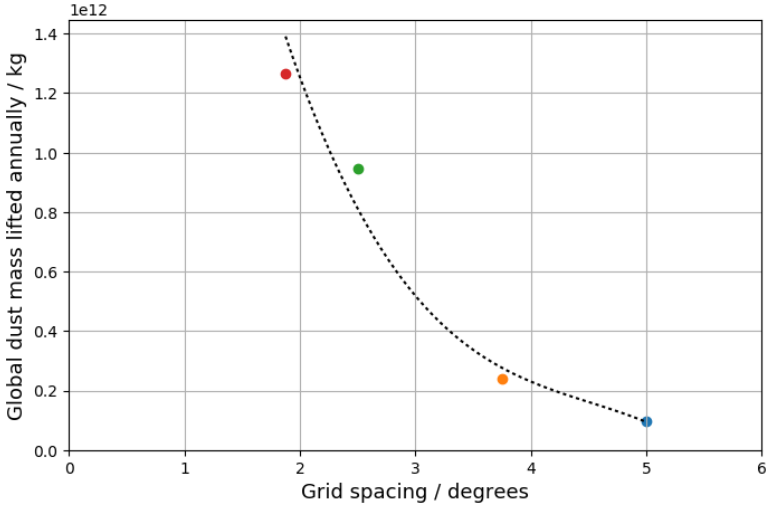

Figure 4.8: Annual, global total lifted dust mass against horizontal physical grid spacing. Resolution increases from right to left: T31 ∼5°, T42 ∼3.75°, T63 ∼2.5°, T85 ∼1.875° (colours correspond to those used in Figure 4.7). Dotted line indicates trendline of $y = 7 \times 10^{12}\,\mathrm{e}^{-0.862x}$.

4.3.2 Changing the Vertical Resolution

Global plots of dust lifting through a Martian year are shown in Figures 4.9 to 4.11, using the same colour indications as in the previous global plots. These plots show dust lifting across increasing vertical resolutions: 35 vertical layers (Figure 4.9), 60 vertical layers (Figure 4.10), and 100 vertical layers (Figure 4.11). Further experiments were completed, as listed in Table 4.2; these plots are included here as examples. (All experiments were completed at the T31 horizontal resolution.)

The data shown in Figures 4.9 to 4.11 are plotted in Figure 4.12 as the amount of lifted dust in each $L_S = 30°$ period through the year (normalised by the number of sols in each period), for each resolution. This plot includes all the vertical resolutions used in this work.

Figure 4.13 shows the annual, global sum of lifted dust mass against increasing resolution.

4.3.3 Summary

Increasing the horizontal resolution of the MGCM increases the amount of dust lifted by NSWS. The geographical distribution of dust lifting changes with increased model resolution: lifting is more widespread in experiments completed at higher resolutions.

Increasing the vertical resolution of the MGCM also tends to increase the amount of dust lifted by NSWS, and to increase the geographical distribution of dust lifting. However, the relationship between resolution and mass lifted/area of lifting is not as straightforward as in the horizontal case, particularly with regard to the results from the experiments completed at the highest resolutions.

In both sets of experiments there is a seasonal trend in dust lifting that is relatively consistent across increasing resolution: more dust is lifted during the SH summer months, i.e. through perihelion.

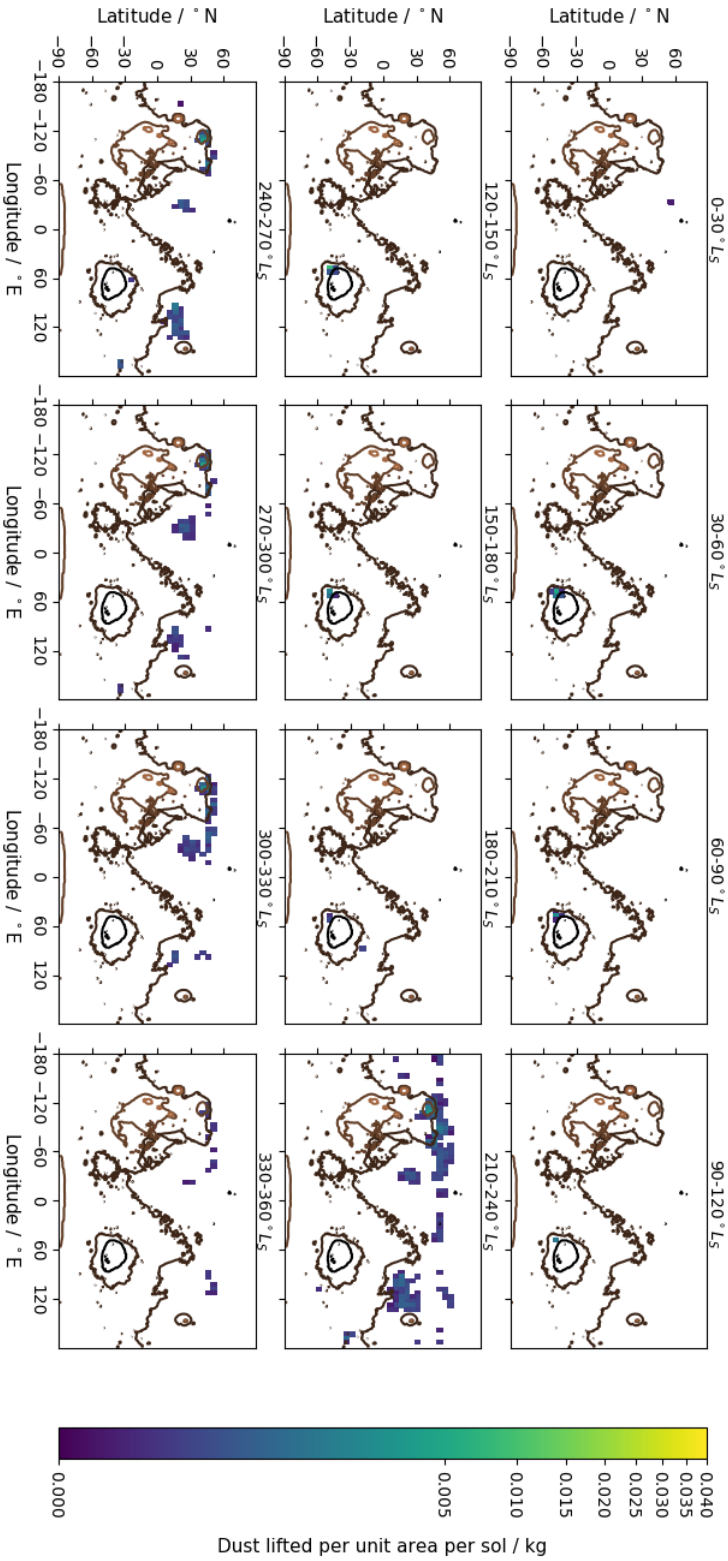

Figure 4.9: Global dust lifting by NSWS in a [T31]L35 experiment. Colour-scheme as for Figure 4.2.

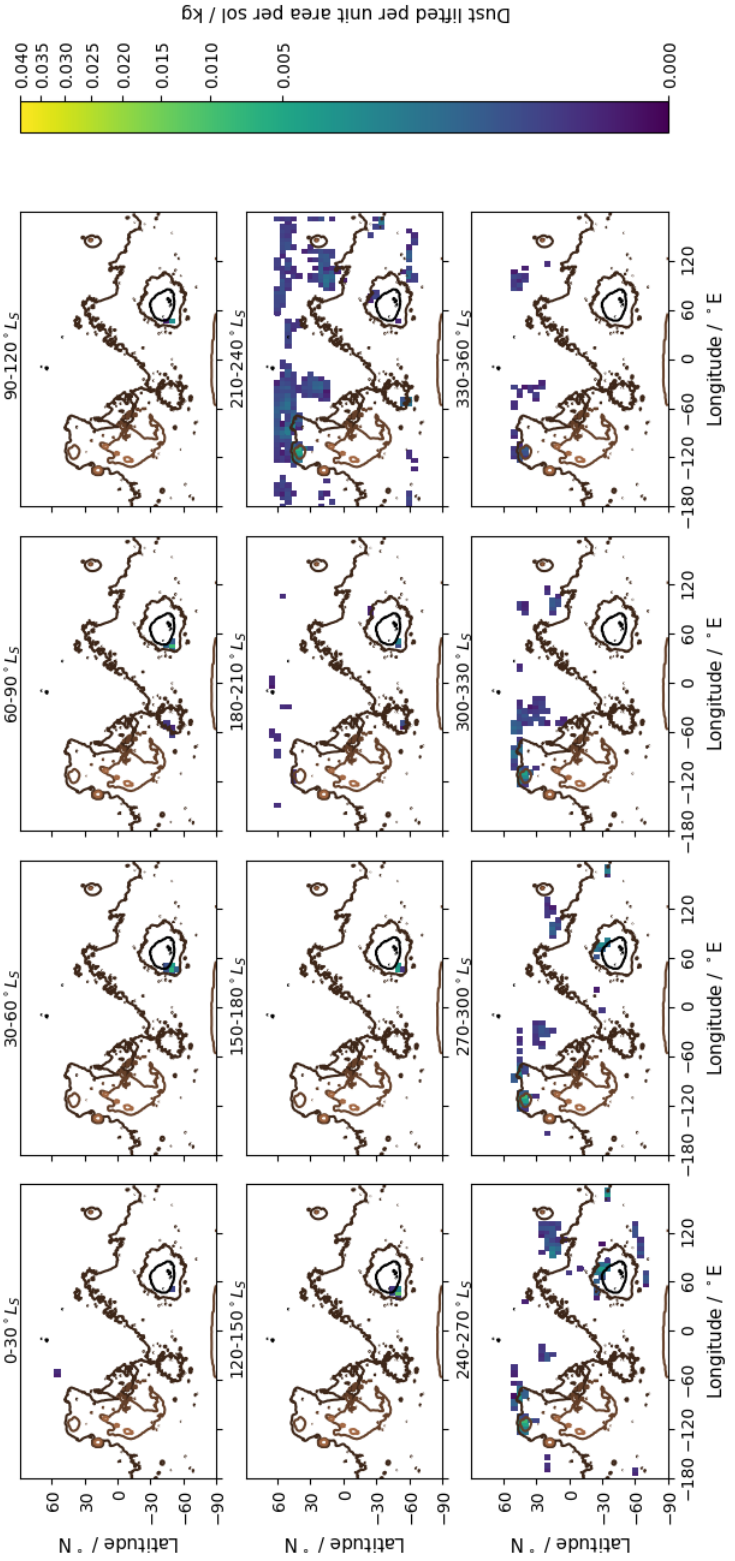

Figure 4.10: As Figure 4.9 for an L60 experiment.

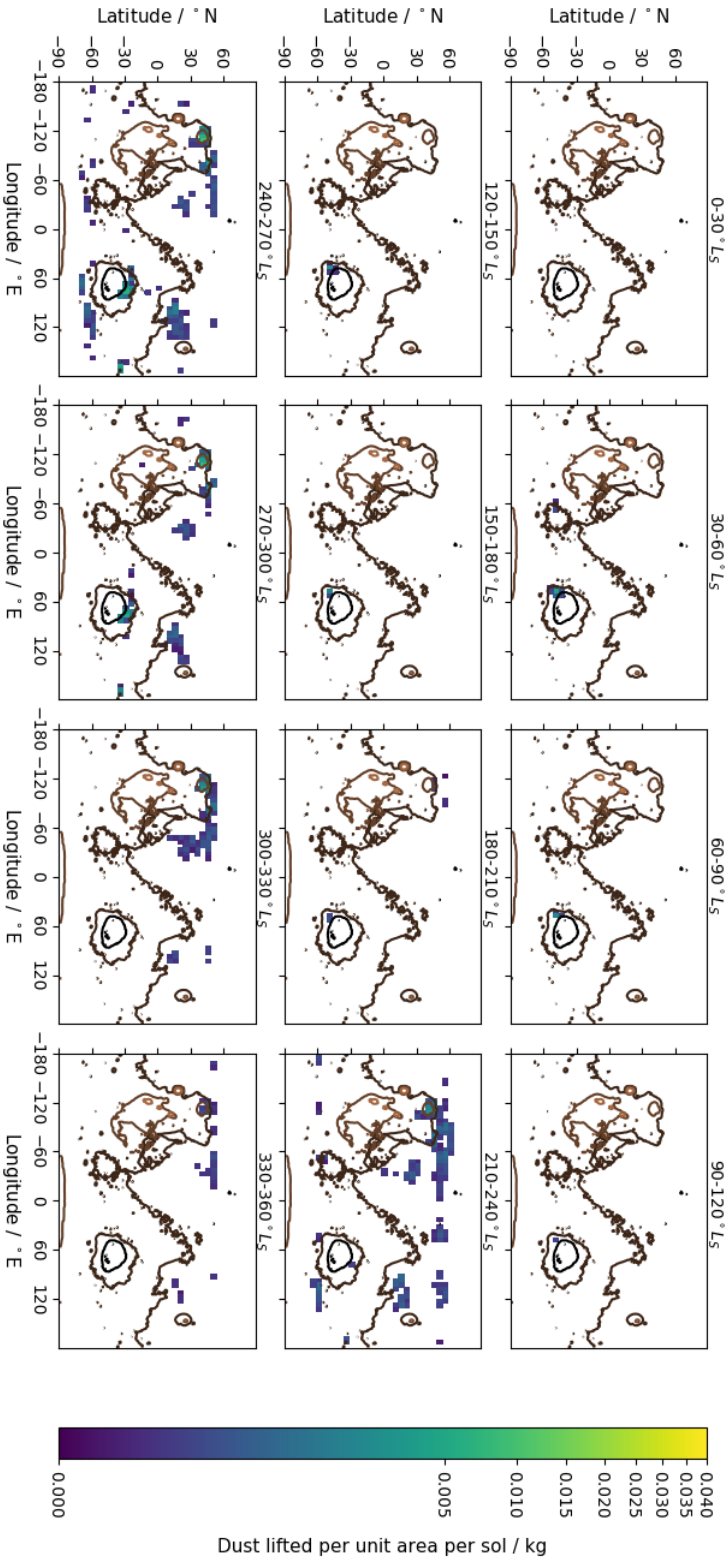

Figure 4.11: As Figure 4.9 for an L100 experiment.

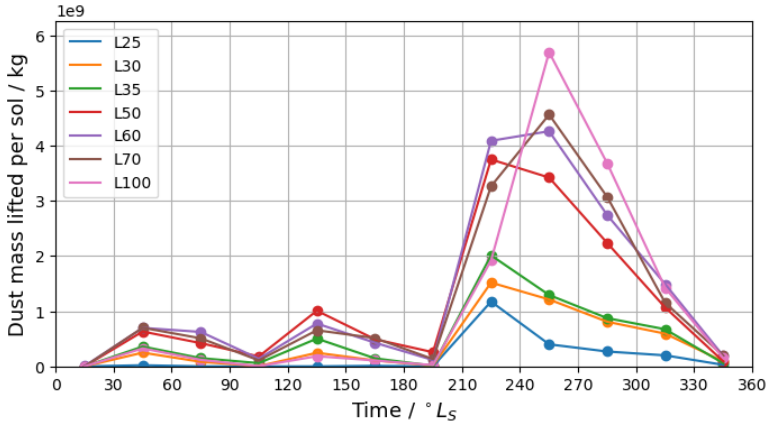

Figure 4.12: The dust mass lifted globally during each $L_S = 30°$-long period of the Martian year, normalised by the number of sols in each period, for each vertical resolution. Plot lines added only to help the reader to follow each experimental result.

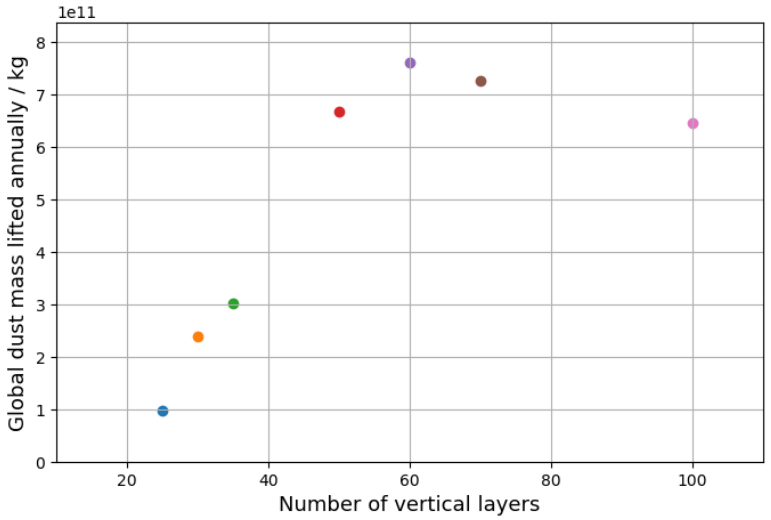

Figure 4.13: Annual, global total lifted dust mass against increasing vertical resolution. (Colours correspond to those used in Figure 4.12).

4.4 Discussion

4.4.1 Comparison with Observations

While this work is concerned with the model's response to changing resolution, it is important to compare the results with observations of Mars. The correlation between surface dust lifting by NSWS and the formation of dust storms can be exploited for this comparison: global maps of observed surface dust lifting cannot be compiled, but maps of dust storm observations can.

A catalogue of 89 dust storm observations was compiled using several published dust storm surveys as sources for storm locations: *Cantor et al.* (2001); *Wang* (2007); *Wang and Fisher* (2009); *Cantor et al.* (2010); *Hinson and Wang* (2010); *Wang and Richardson* (2015). These studies all use observations made from orbit (using MOC on MGS or MARCI on MRO) and the majority of storms identified are 'regional storms' as defined by *Cantor et al.* (2001), i.e. covering an area of at least 1.6 $\times 10^6$ km^2 and lasting at least two sols. These studies cover an observational period from MY24 to MY30.

Figure 4.14 shows maps of T31L25 dust lifting (the horizontal and vertical resolutions in a 'typical' climate model) overlain onto the locations of the catalogued storm observations. The dust lifting colour indications and scale are the same as in the previous global maps (refer back to Figure 4.2).

The first point to consider is the general match between storm observations and modelled dust lifting. There is some correlation between observations and dust lifting across experiments completed at all resolutions. Two examples of this can been seen during a period soon after aphelion and a period approaching perihelion. During the near-aphelion period of L_S = 90-120° there are no observations of dust storms recorded; data across all modelled resolutions display limited or zero dust lifting through this period. In the L_S = 210-240° period approaching perihelion there are a number of widely-spread observations of storms; data from all modelled resolutions display dust lifting during this period of the year in regions that correlate with storms observed in the NH.

The second point to consider is the geographical change in lifting patterns with resolution. Through the perihelion period of L_S = 210-270° storms have been observed in SH locations with latitudes around –60° N. The dust lifting

depicted in the T31L25 experiment (Figure 4.14) does not match these observations, but there is a match with modelled dust lifing produced in experiments completed at both higher horizontal resolutions (T63, T85) and higher vertical resolutions (L60, L100); compare Figures 4.4, 4.5, 4.10, and 4.11.

A similar trend is seen during the period of L_S = 0-60° (NH spring), during which there have been a small number of observed storms with latitudes around 50° N; the lowest horizontal resolution experiment (T31) does not show any dust lifting in this region during this period, but the T42, T63 and T85 experiments show increasing amounts of dust lifting in similar NH locations to the storm observations. In this instance, increasing the vertical resolution of the model did not produce a similar change in dust lifting.

These results suggest strongly that experiments completed at mid- to high-resolution generate more representative surface dust lifting patterns than lower resolution simulations, at least for certain times of year. The improved representation gained by increasing the vertical resolution does not have the same temporal breadth as the improvement gained by increasing the horizontal resolution (i.e. regarding NH spring), for the resolutions tested.

A final point to consider in this comparison is that some parts of the year contain storm observations that do not match with any of the experimental results: the storms observed during the period of L_S = 120-180° (late NH summer/SH winter) do not correlate with strong dust lifting regions exhibited in the results obtained at any resolution. This limitation of the model should be noted for future experiments, but it will not be explored further within this work.

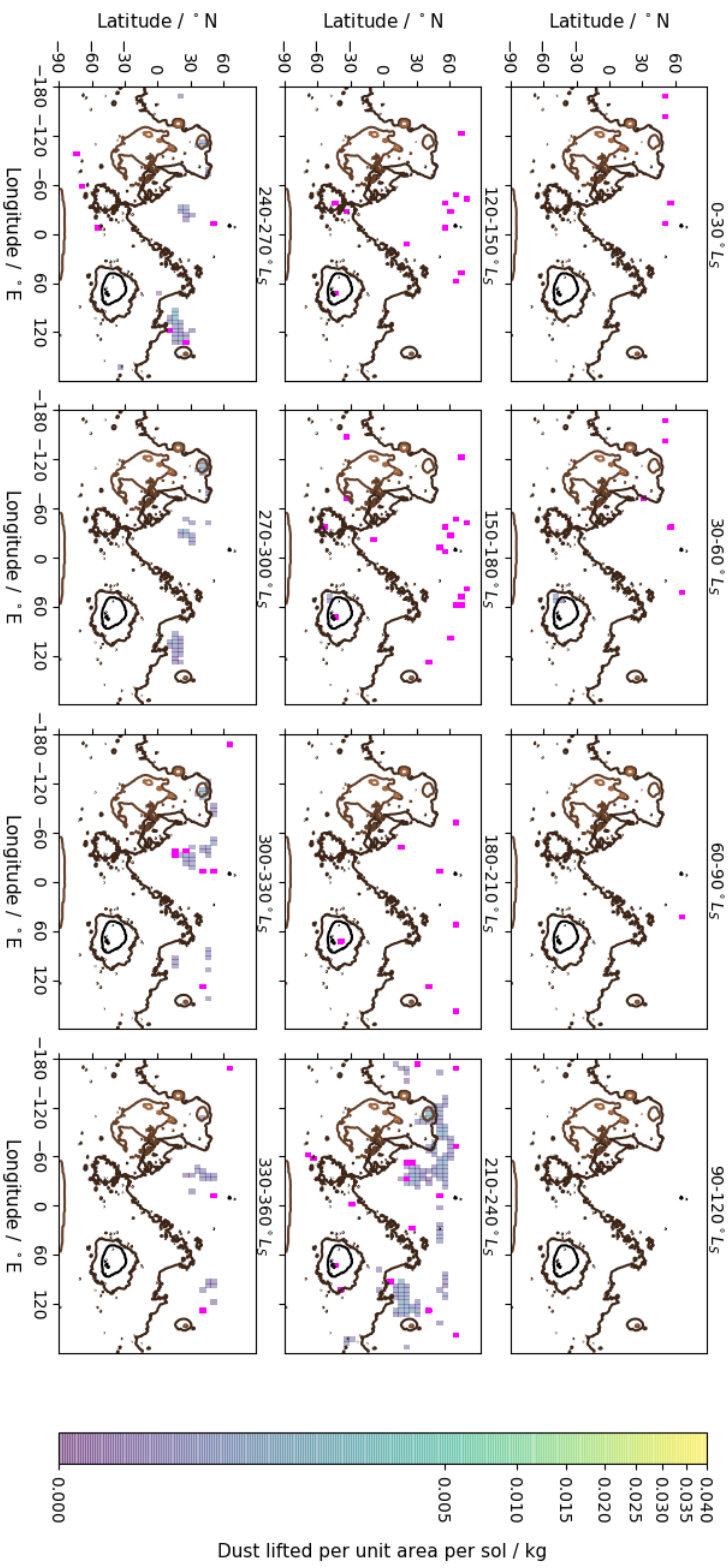

Figure 4.14: The locations of dust storm observations through the period MY24-30, marked in pink. Modelled dust lifting data are that shown in Figure 4.2, colour-faded to enhance visibility of storm observations.

4.4.2 Dust Lifting in Horizontal Resolution Experiments

Increasing the horizontal resolution of the MGCM experiments increases the amount of dust lifted by NSWS: refer back to Figure 4.8, in which the total amount of dust lifted annually is plotted against horizontal grid spacing.

As the horizontal resolution of a simulation is increased, an improved representation of the planet's surface properties can be used. A more detailed representation of surface topography in the experiments improves the depiction of local slopes, and small-scale variations in albedo and thermal inertia. This leads to a better representation of small-scale variability within the near-surface wind, through the improved modelling of local slope winds, such as daytime, upslope anabatic flows and night-time, downslope katabatic flows. This effect is most pronounced in regions where terrain height varies by a large amount across a relatively small distance, such as deep valleys or basins, or at the edge of seasonal CO_2 polar caps. These local winds also interact with larger scale tides, affecting near-surface winds across the planet.

Dust is lifted from a planet's surface when the near-surface wind is strong enough to overcome any forces holding the dust on to the surface. Within the MGCM parameterisation, dust lifting occurrs when the friction velocity of the wind is greater than a threshold velocity ($u^* > u^*_t$; see Section 3.5.1). This friction velocity is calculated from the near-surface wind velocity (Equation 3.11).

Although increasing the horizontal resolution does not affect the calculation of the threshold velocity, the changes in near-surface wind speeds affect the friction velocity acting upon dust on the surface. Figure 4.15 shows example surface plots of the threshold velocity (u^*_t) calculated in T31L25 and T85L25 experiments: the geographical pattern and magnitude of this threshold value is similar between the plots, despite the change in resolution. In contrast, the surface plots of friction velocity (u^*) in Figure 4.16 show how changing the resolution – improving the representation of local slopes and thus local winds – produces velocities of greater geographical complexity and larger magnitude.

The shape of the plot shown in Figure 4.8 allows the calculation of an exponential trendline: $y = 7 \times 10^{12}\, \mathrm{e}^{-0.862x}$. This plot allows future users of the

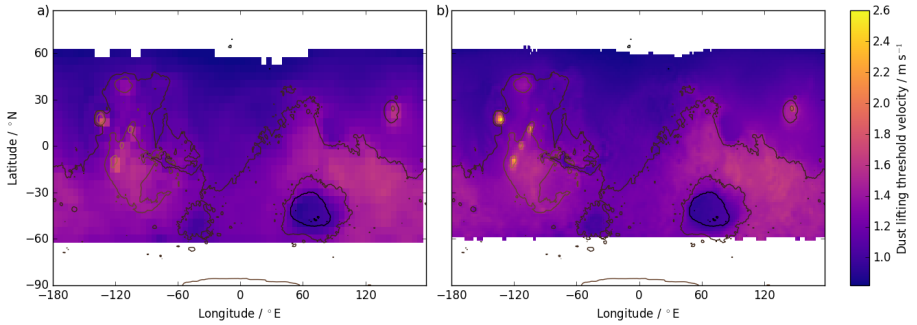

Figure 4.15: Example surface plot of the threshold velocity, u_t^*, in experiments of different resolutions: a) T31L25 and b) T85L25. Data are from $L_S \sim 210°$. (White areas indicate regions for which this value was not calculated: dust lifting was prevented in these areas by overlying CO_2 ice.)

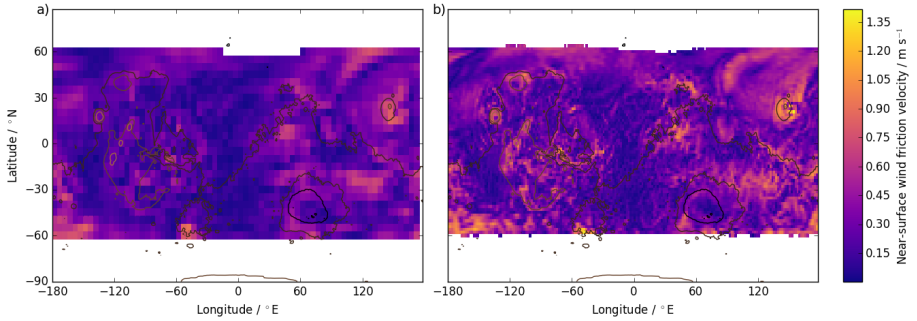

Figure 4.16: As Figure 4.15, but showing the friction velocity, u^*.

model to make an informed decision on the suitability of a particular resolution with regards to surface-level processes, albeit with the caveat that further work is recommended in order to extend the series to even higher resolutions in order to confirm this trend. Such work would not be trivial: see Section 4.5 for a discussion on the very highest horizontal resolution experiments completed within the current investigation.

Seasonal Dust Lifting

The amount of dust lifted in the horizontal resolution experiments is shown in Figure 4.7 for each modelled $L_S = 30°$-long section of the Martian year. A seasonal trend is evident across all resolutions: more dust is lifted during the SH summer months, $L_S = 180$-$360°$. This was expected, assuming that the model is a reasonable representation of the Martian atmosphere: observations

of dust storms increase during this period (the 'dust storm season', see Section 2.3), indicating that more dust lifting should be present from which these storms can form. This plot shows clearly that the seasonal trend in this dust lifting is consistent across resolutions, despite changes in resolution affecting the absolute amount of dust lifted.

Dust Lifting Patterns

As described in Section 4.4.1, the geographical distribution of dust lifting changes with increased model resolution. Two periods of the year have been selected for a deeper study of this behaviour: the early NH spring period of L_S = 30-60°, in which the experiments at all resolutions show limited dust lifting, and the near-perihelion period of L_S = 210-240°, in which all the experiments show large amounts of dust lifting.

Figure 4.17 shows the dust lifting patterns through the period L_S = 30-60° from all the horizontal resolution experiments. The lowest resolution experiment, T31, shows very limited dust lifting during this period, with only one active dust lifting location at the western edge of Hellas Basin; all the higher resolution experiments also display lifting in this location. The higher resolution experiments also display areas of dust lifting in the NH, primarily in the Acidalia (circa 60° N, –60° E) and Utopia (circa 60° N, 140° E) regions, with the area across which dust is lifted tending to increase with increasing resolution.

Figure 4.18 shows peak near-surface wind speeds through this modelled period. The areas of NH dust lifting displayed in Figure 4.17 correlate with locations exhibiting high peak wind speeds at the higher resolutions in Figure 4.18; e.g. within the Acidalia region, peak wind speeds reach ∼21 $\mathrm{m\,s^{-1}}$ in the T85 experiment, compared with ∼13 $\mathrm{m\,s^{-1}}$ in the T31 experiment. This location in particular has been termed a 'storm zone' (*Hollingsworth et al.*, 1996; *Lewis et al.*, 2016) in recognition of the number of storms observed to form here.

Section 4.4.1 identified that storms have been observed at this time of year in the latitude band around 50° N. Through this period of the year, the seasonal CO_2 polar cap retreats from around 50° N to around 70° N. This area of dust lifting is caused by local winds associated with the edge of this polar cap – winds that are not well-represented at the lower model resolutions. This polar edge

cap effect can also be seen in the first three panels in both Figure 4.5 and Figure 4.4: the dust lifting regions shift further north through the successive periods L_S = 0-30°, L_S = 30-60°, and L_S = 60-90°, following the retreat of the cap edge.

Figure 4.19 shows the dust lifting patterns of all the horizontal resolution experiments through the period L_S = 210-240°. Large regions of NH dust lifting are evident across all resolutions, e.g. Acidalia, the northern edge of Ascuris Planum (circa 60° N, –120° E), and east of Cerberus (circa 20° N, 110° E). However, the T63 and T85 experiments again show regions of lifting in both the NH and SH that are not captured at the lower resolutions: along latitudes of around 60° N and –60° N.

Figure 4.20 shows peak near-surface wind speeds through this modelled period: a narrow, longitudinal band of higher peak wind speeds is evident around –60° N in the higher resolution experiments, particularly T85. Within this band, peak wind speeds reach ∼21 $\mathrm{m\,s^{-1}}$ in the T85 experiment, compared with only ∼14 $\mathrm{m\,s^{-1}}$ in the T31 experiment.

Section 4.4.1 identified storm observations through this period of the year in a SH latitude band around –60° N. Mirroring the period earlier in the year, this latitude is associated with the annual retreat of the seasonal southern CO_2 polar cap, suggesting that local winds associated with cap edge topography and albedo variation are driving lifting in this region. There is not such a clear difference in peak wind speeds in the NH to account for the band of lifting around 60° N, but the northern CO_2 polar cap extends to around 65° N at the beginning of this L_S = 30°-long period, correlating with the lifting regions.

Increasing the horizontal resolution of the MGCM improves the geographical distribution of dust lifting, producing a better representation of the range and distribution of the dust lifting regions: compare the lifting patterns in the highest and lowest resolution panels of Figures 4.17 and 4.18 with the storm observation map in Figure 4.14. The rate at which this improvement occurs appears to slow with increasing resolution: the change in dust lifting patterns from T31 to T42 is more distinct than that from T63 to T85.

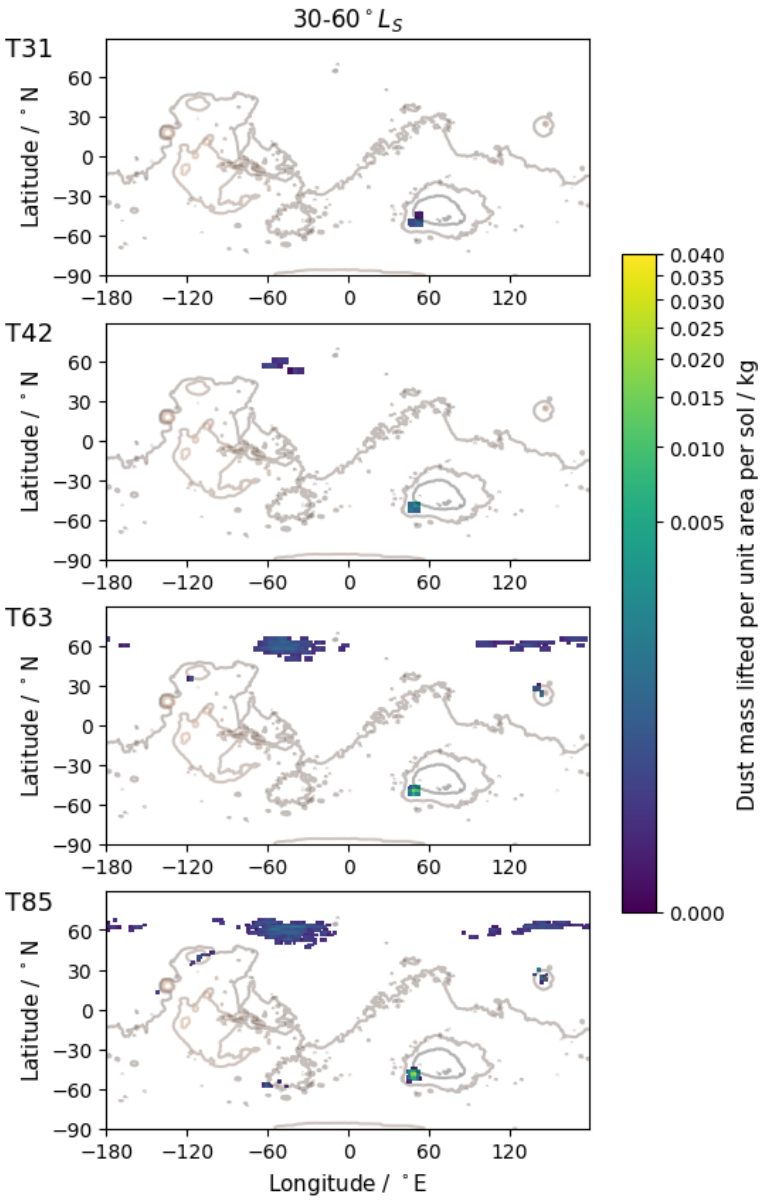

Figure 4.17: Surface dust lifting through the period L_S = 30-60°, for the four horizontal resolution experiments. Colour-scheme as for Figure 4.2.

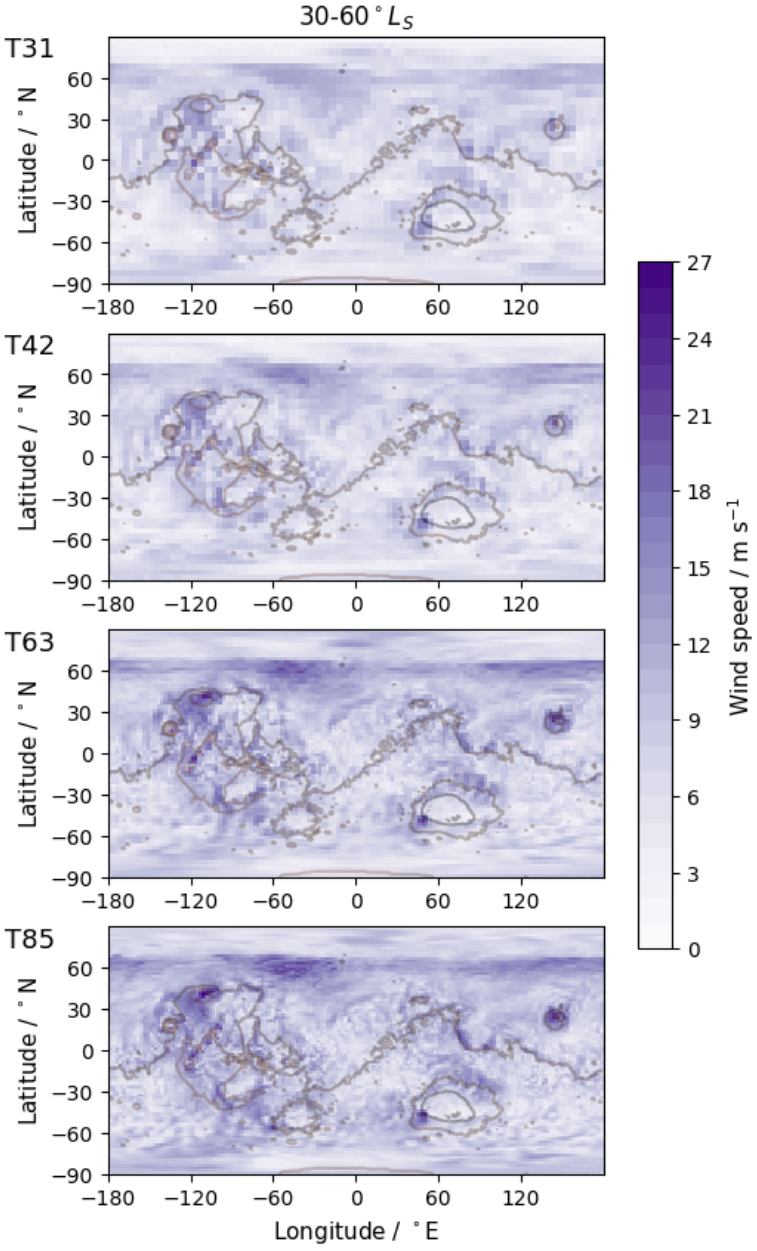

Figure 4.18: Peak near-surface wind speeds through the period L_S = 30-60°, for the four horizontal resolution experiments.

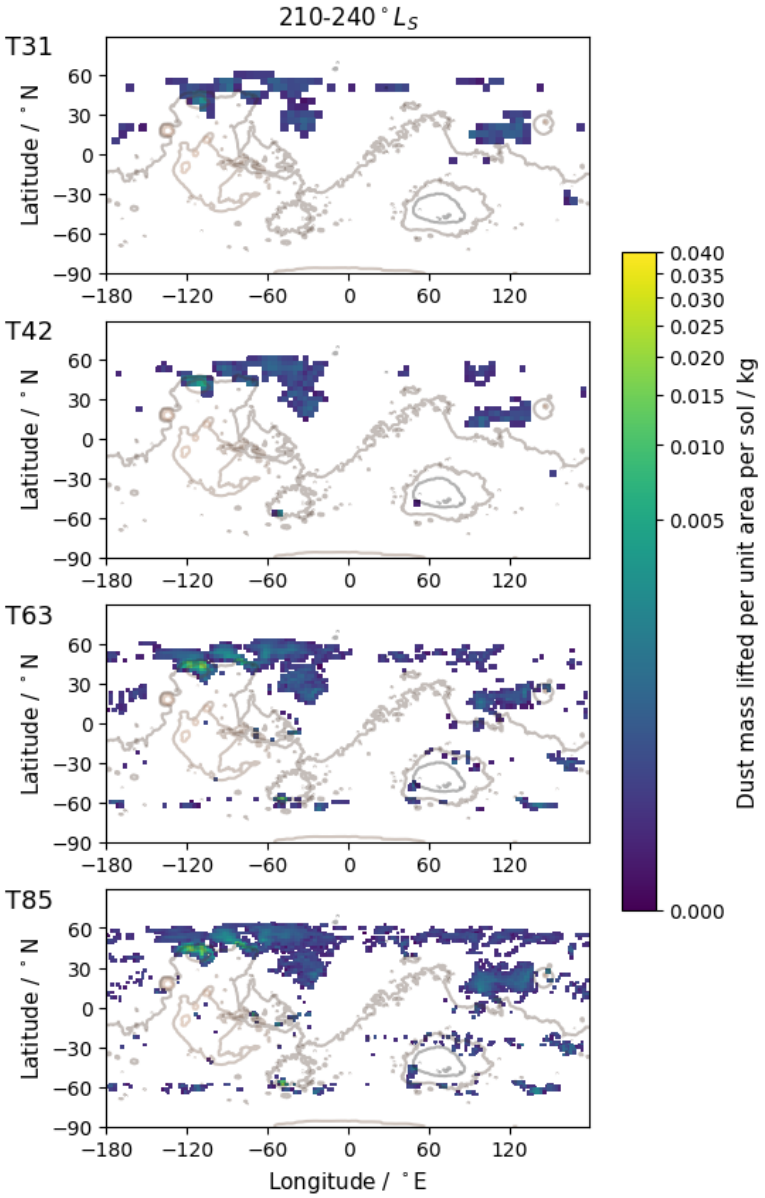

Figure 4.19: As Figure 4.17, for the period L_S = 210-240°.

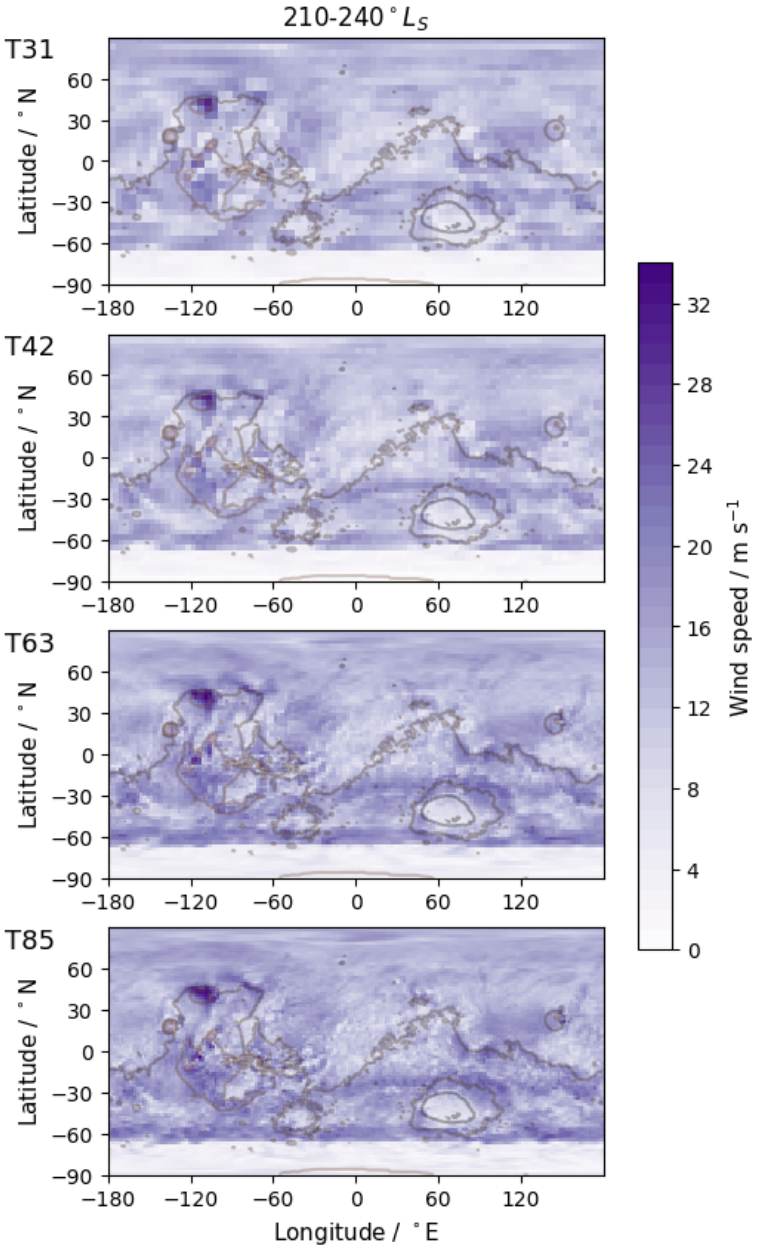

Figure 4.20: As Figure 4.18, for the period L_S = 210-240°.

Peak Wind Speeds

Figure 4.21 shows a box-and-whisker plot of the global peak near-surface wind speeds through the period L_S = 30-60°. As resolution increases, the median value of each peak wind population also increases. Of particular relevance to dust lifting is that the outliers associated with the highest peak wind speeds are more numerous as resolution increases, and reach higher magnitudes. It is these outlier values that achieve the speeds necessary for dust to be lifted.

Figure 4.22 shows the same style of plot for the period L_S = 210-240°. The trend of increasing peak wind speeds with increasing resolution is not as unambiguous in these data. Firstly, the T42 median value is slightly lower than that of the T31 data; however, the T42 data contain more outliers at the higher speeds required for dust lifting. Secondly, the T63 and T85 data are much more similar in their distributions than at the earlier point in the year, although the T85 median is still higher, and the T85 data contain more high speed outliers. The effect of this similarity in wind speed distributions was evident in the plots showing dust lifting through the length of the experimental year (Figure 4.7) and the total dust lifted annually (Figure 4.8): T63 results are more similar to T85 results than to those at the lower resolutions, even though the delta in resolution is similar across each resolution increase.

When the geographical lifting patterns are considered, it is evident that the experiment completed at the T63 resolution is able to resolve dust lifting at polar cap edges in both the NH and SH that the lower resolution experiments could not. The T85 experiment improves on the representation of wind speeds (and therefore dust lifting) in these regions, but it is the inclusion of this lifting where it had previously been absent that makes the largest difference in the aforementioned plots. At these latitudes, a T63 experiment is able to resolve features of lengths below 100 km, while a T42 experiment can resolve features closer to 150 km in length. This suggests that the facility to resolve surface features of the order of 100 km improves the representation of dust lifting within the MGCM. Future work in this area could explore this finding further by correlating these lifting areas with a topographical and geologic survey of these Martian latitudes.

It is also possible there is a degree of uncertainty across the results: an examination of Figure 4.7, with consideration to the posited line of best fit, allows for the possibility that the T42 result discussed here could be a lower-than-average result for such a resolution; the T63 result could be a higher-than-average result. Computing time and data storage constraints did not allow for a comprehensive exploration of the uncertainties involved within the results of long-term simulations at high resolutions. This would also be an interesting topic for future study.

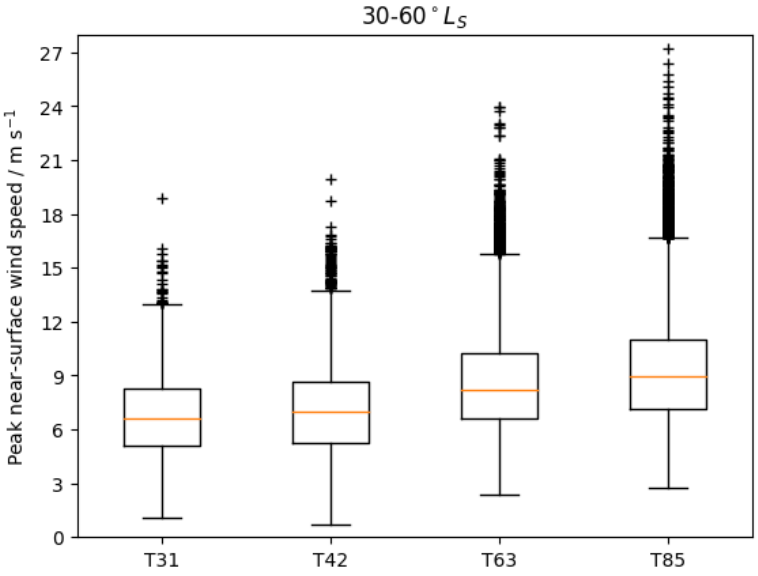

Figure 4.21: Box-and-whisker plot of peak near-surface wind speeds through the period L_S = 30-60°, across horizonal resolution experiments. Orange lines denote the median of each distribution, the box encompasses the Q1 to Q3 interquartile range (IQR); outlier values are those beyond the standard 'Qn ± 1.5 × IQR' whisker length.

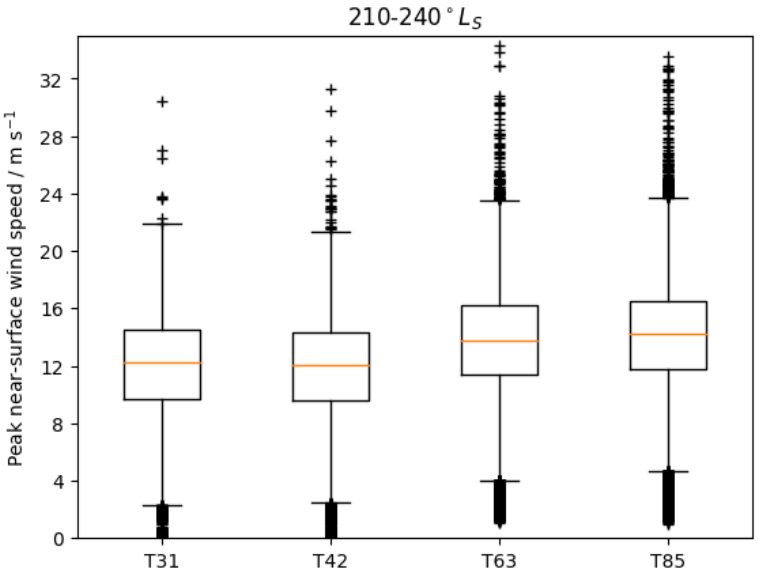

Figure 4.22: As Figure 4.21, for the period L_S = 210-240°.

4.4.3 Dust Lifting in Vertical Resolution Experiments

Increasing the vertical resolution of the MGCM experiments tends to increase the amount of dust lifted by NSWS. In contrast with the direct correlation in the horizontal resolution experiments, in the vertical resolution experiments this trend only continues up to a certain number of vertical layers, see Figure 4.13; past this point, experiments lift a reduced amount of dust.

The seasonal trend for dust lifting identified previously can be seen again in Figure 4.12: more dust is lifted during the SH summer months, L_S = 180-360°, across all vertical resolution experiments. However, this trend is not as simple as in the case of the horizontal resolution experiments: the L70 experiment lifts less dust in the period L_S = 210-240° than the L60 experiment; the L100 experiment lifts less dust again through this period.

Dust Lifting Patterns

While changing the horizontal resolution of the model resulted in a large change in the geographical distribution of dust lifting, changing the vertical resolution does not result in as widespread an effect. Figures 4.23 and 4.24 show dust lifting through the periods L_S = 210-240° and L_S = 240-270° across four example vertical resolution experiments, from the 'standard' L25, through a medium resolution L35, a high resolution L60 and the very high resolution L100. (For clarity and conciseness only these four vertical resolutions will be included in the following discussion.)

The general trend across these figures is that as resolution is increased, more dust lifting regions are evident. During the later period, L_S = 240-270°, this trend is simple, with the L100 experiment showing the most widespread dust lifting. However, during the earlier period, L_S = 210-240°, the spread of dust lifting in the L100 experiment is *less* than in the L60 experiment. This complements the findings that the total amount of dust lifted during this period is greatest in the L60 experiment: the L_S = 210-240° period is often the portion of the Martian year during which the majority of dust lifting occurs within these experiments.

Increasing the vertical resolution of the MGCM does improve the geograph-

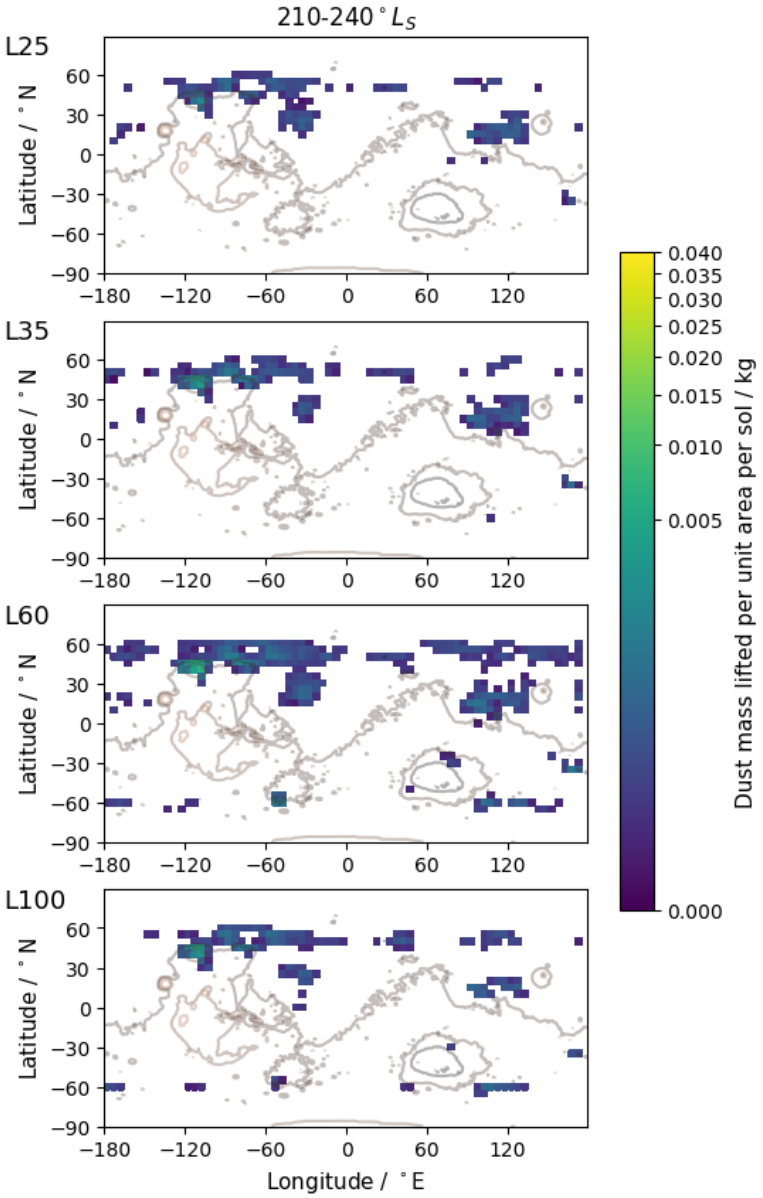

Figure 4.23: Surface dust lifting through the period L_S = 210-240°, for four vertical resolution experiments. Colour-scheme as for Figure 4.2.

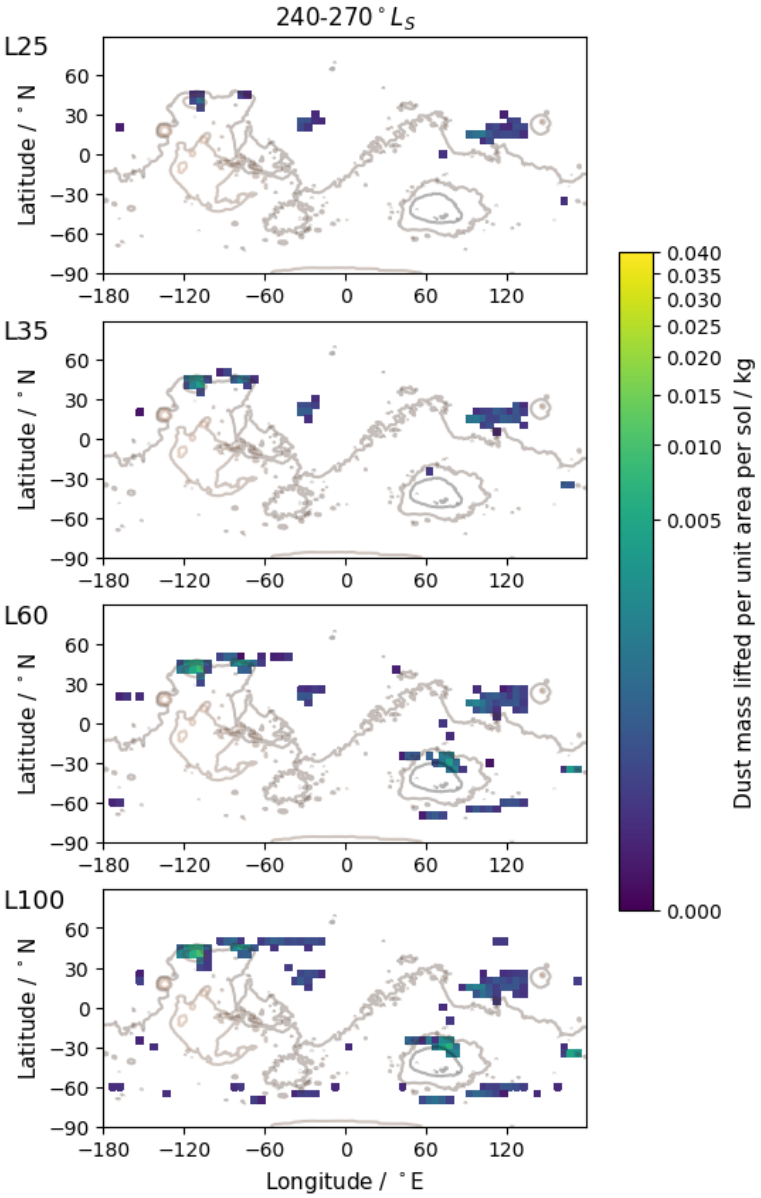

Figure 4.24: As Figure 4.23, for the period L_S = 240-270°.

ical distribution of dust lifting, producing a better representation of the range and distribution of the dust lifting regions: compare the lifting patterns in the highest and lowest resolution panels of Figures 4.23 and 4.24 with the storm observation map in Figure 4.14.

Peak Wind Speeds

Figures 4.25 and 4.26 show differences in the peak horizontal near-surface wind speeds across the modelled surface during the periods L_S = 210-240° and L_S = 240-270°; the difference in speed is taken from the results of the standard L25 experiment. Faster wind speeds can be identified clearly in some regions associated with higher dust lifting at the higher vertical resolutions. For example, peak wind speeds are ∼15 $\mathrm{m\,s^{-1}}$ faster around –60 ° N, 110 ° E in the L60 results than in the L25 results, across both periods displayed here. As in the horizontal resolution experiments, the areas in which these higher wind speeds occur tend to correlate with seasonal polar cap edges.

To investigate how changing the vertical resolution affects wind speeds in the lower region of the atmosphere, vertical profiles of peak wind speed have been constructed. Peak wind speeds are considered rather than average wind speeds, as dust lifting only occurs in the presence of local peak wind speeds: the average wind speed does not produce a friction velocity that can overcome the lifting threshold.

Three vertical profiles of peak wind speeds during the period L_S = 240-270° are analysed below. The locations of these profiles were selected by considering the changing geographical patterns of dust lifting across resolution, as seen in Figure 4.24: a point at the southern CO_2 polar cap edge, associated with increased lifting with increased resolution (Profile A), a lowland NH point associated with lifting across all resolutions (Profile B), and an equatorial point in a region of mid-level terrain (Profile C). These locations are specified in Table 4.3 and mapped in Figure 4.27.

Figure 4.28 shows the vertical profiles at the identified locations, extracted from the experiments completed using 25, 35, 60 and 100 vertical layers; panels a), b) and c) show full height profiles, and panels d), e) and f) show the lowest ∼5 km of the atmosphere. In general, the profiles are similar in shape for most

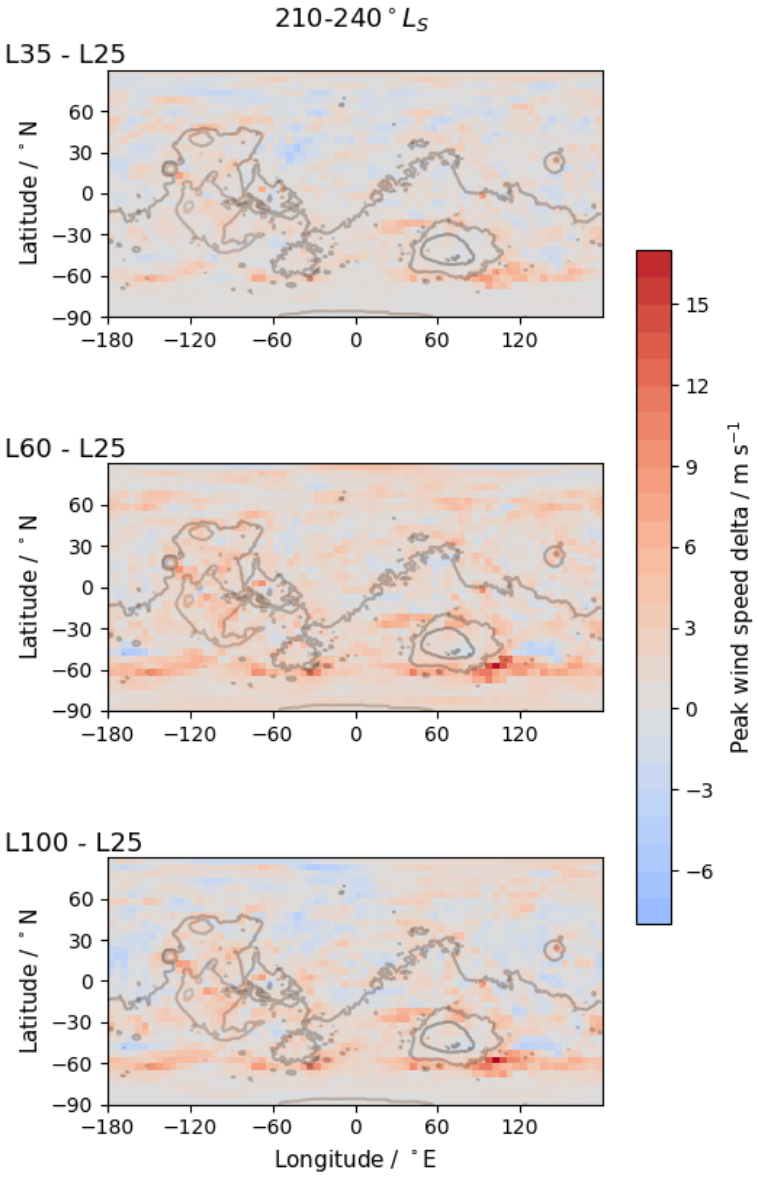

Figure 4.25: Difference in peak near-surface wind speeds across the Martian surface through the period L_S = 210-240°. The difference is taken from the 'standard' L25 results.

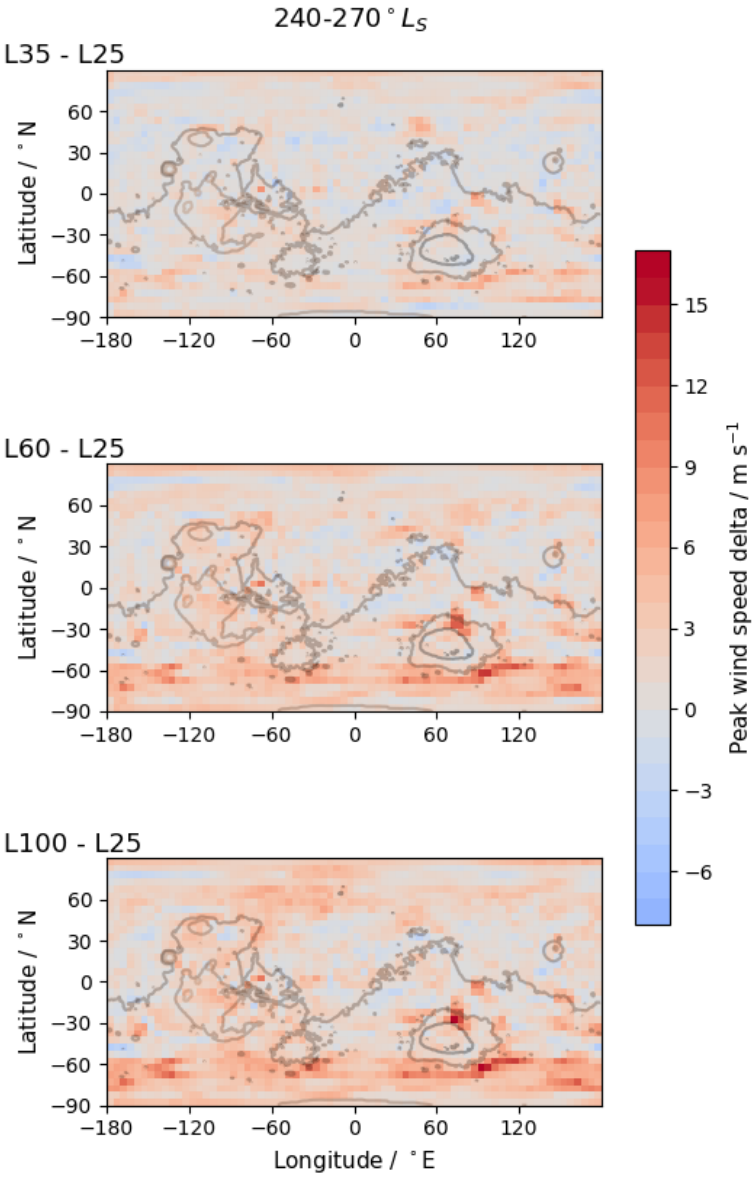

Figure 4.26: As Figure 4.25, for the period L_S = 240-270°.

Profile label	Location (lat ° N, lon ° E)	Comment
A	–62.5, 115	Cap edge
B	22.5, –30	Lowlands region
C	0, 0	Equatorial location

Table 4.3: The locations of the studied vertical profiles.

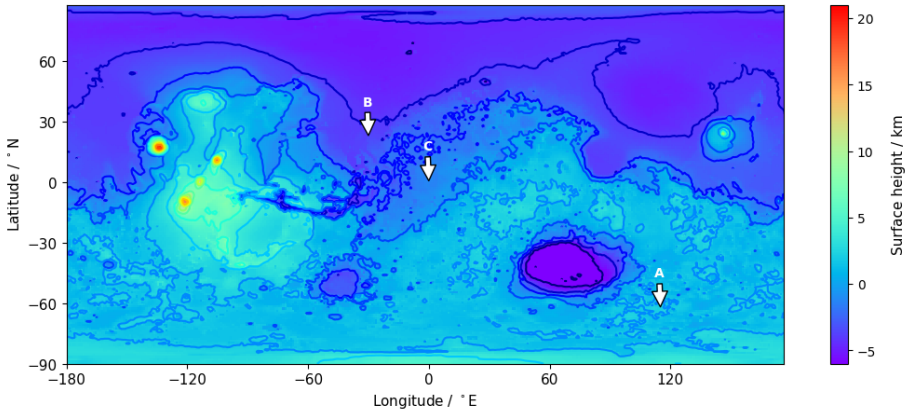

Figure 4.27: Global topography plot labelled with the locations of the studied vertical profiles listed in Table 4.3.

of their height, with discrepancies becoming evident at heights above ∼80 km (Fig. 4.28 panels a, b and c). The behaviour of the upper atmosphere within the MGCM is less constrained than at lower levels; these discrepancies should be noted for any future work involving the MGCM that focuses on high-level atmospheric processes, but further discussion of this aspect of the data is beyond the scope of this investigation. Figure 4.28 panels d), e) and f) display data in which patterns of peak wind speed with height are similar across the changing vertical resolutions, although the lower region of Profile A (panel d) does show a distinct increase in absolute peak wind speeds as resolution is increased.

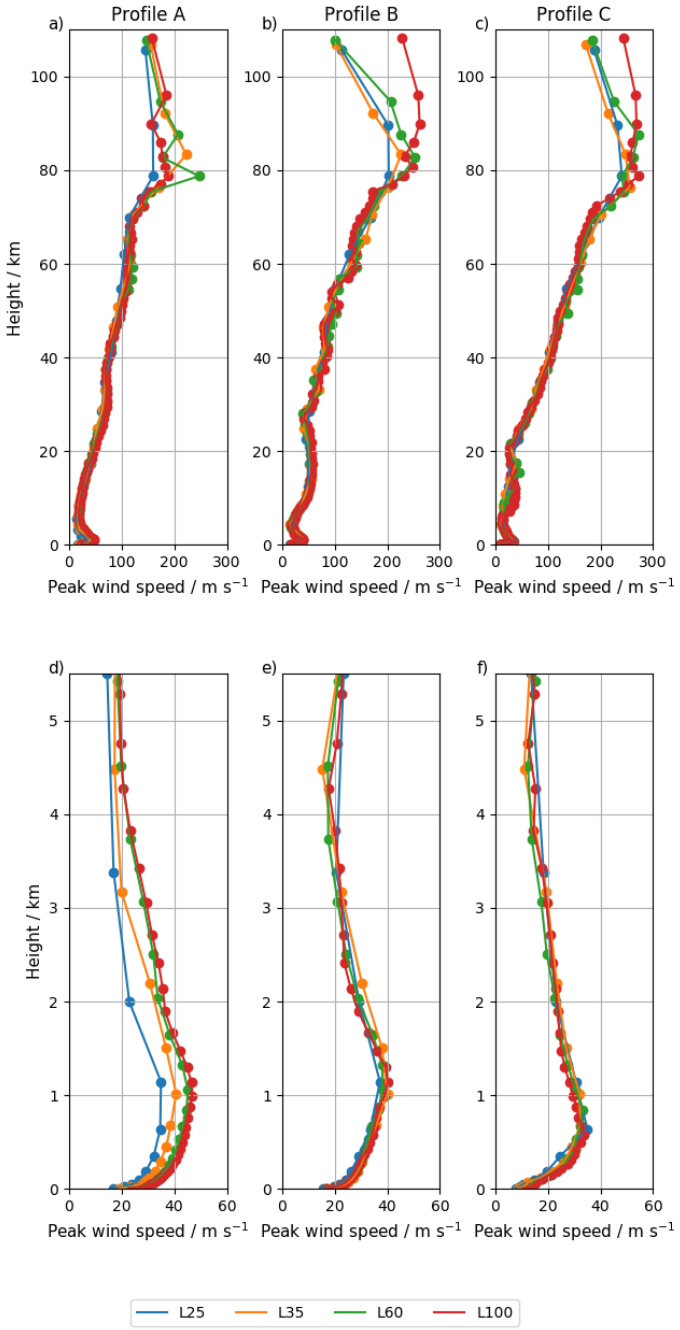

Figure 4.28: Vertical profiles of peak wind speed through the period L_S = 240-270° at the locations identified in Table 4.3, for four vertical resolution experiments. Full height profiles are shown in panels a), b) and c); the lowest ∼5 km of the atmosphere are shown in panels d), e) and f).

Figure 4.29 shows the peak wind speed at the base of the identified vertical profiles (i.e. peak wind speed in the lowest model layer at each location), across the vertical resolution experiments. In general, near-surface peak wind speeds are higher at increased vertical resolutions, but there is not a linear correlation between peak wind speed and number of vertical layers. This is displayed clearly in the data relating to Profile A: the change in near-surface peak wind speeds between the L25 and L35 experiments is much larger than the change in near-surface peak wind speeds between the L60 and L100 experiments, despite the larger jump in resolution between the latter. A similar distribution is also seen in the Profile C data shown here. The Profile B data do not show such a distinct pattern (in fact, the highest near-surface peak wind speed at this point is in the L35 data).

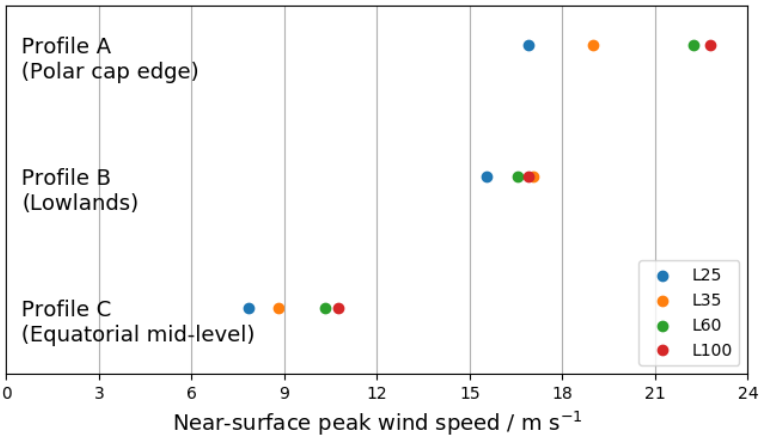

Figure 4.29: Diagram illustrating the near-surface peak wind speed at the base of the analysed vertical profiles, across four vertical resolutions.

Higher resolution simulations tend to produce the more geographically representative dust lifting patterns, as identified in Section 4.4.3, due to these higher near-surface peak wind speeds. The pattern identified in Figure 4.29 suggests that near-surface peak wind speeds will not increase indefinitely with increasing resolution: the rate at which the peak wind speeds increase appears to slow down at higher resolutions. In such a circumstance, increasing the vertical resolution of an experiment will provide a real improvement in the geographical representation of dust lifting only up to a point – after that point, any improve-

ments are likely to be incremental and may not outweigh the increased time required to complete higher resolution simulations.

Considering altitudes above the immediate near-surface, a number of peak wind speed vertical profiles exhibit features at higher resolutions that are not evident in lower resolution experiments. Figure 4.30 shows portions of three peak wind speed vertical profiles, each depicting a different range of altitudes in order to highlight the notable features. Panel a) shows Profile C, as seen in Figure 4.28; b) shows Profile D, taken from the same polar cap edge region as Profile A but through the earlier period of L_S = 210-240°; c) shows Profile E, from the highland region of Syria Planum (–17.5 ° N, -105 ° E), also through L_S = 210-240°. For clarity, only data from the lowest and highest resolutions (L25 and L100) are shown here; note that these profiles are not shown against the same vertical scale.

The reader's attention is drawn to the distinct discrepancies between the L25 data and the L100 data; the descriptions here will concentrate on how the higher resolution data deviate from the results of the 'standard' L25 experiment. The deviation in Profile C (Fig. 4.30a) is a 'bulge' of higher peak wind speeds between heights of ∼6.5 km and ∼15 km. The deviation in Profile D has consistently higher peak wind speeds from the surface up to a height of ∼4.5 km, and a distinct 'hump' in the speeds at heights between ∼0.8 km and ∼1.8 km. The deviation in Profile E is a relatively sharp spike in speeds at heights between ∼0.25 km and ∼1.2 km.

It should be noted that such perturbations in peak wind speeds are not apparent in every vertical profile: see Profiles A and B in Figure 4.28, within which the plotted curve of the higher resolution data is much more similar in shape to that of the lowest resolution data.

The precision at which these features can be resolved will impact how – or if – they affect lower altitude and near-surface wind speeds: a surge in wind speed at a height of a kilometre will effect a different change in wind speeds at lower heights when it is resolved across ∼10 model layers (e.g. an L100 experiment) compared to when it is resolved across ∼5 model layers (e.g. an L60 experiment). This may begin to explain why a decrease in global dust mass lifting is seen in Figure 4.13 past the point of the L60 experiment.

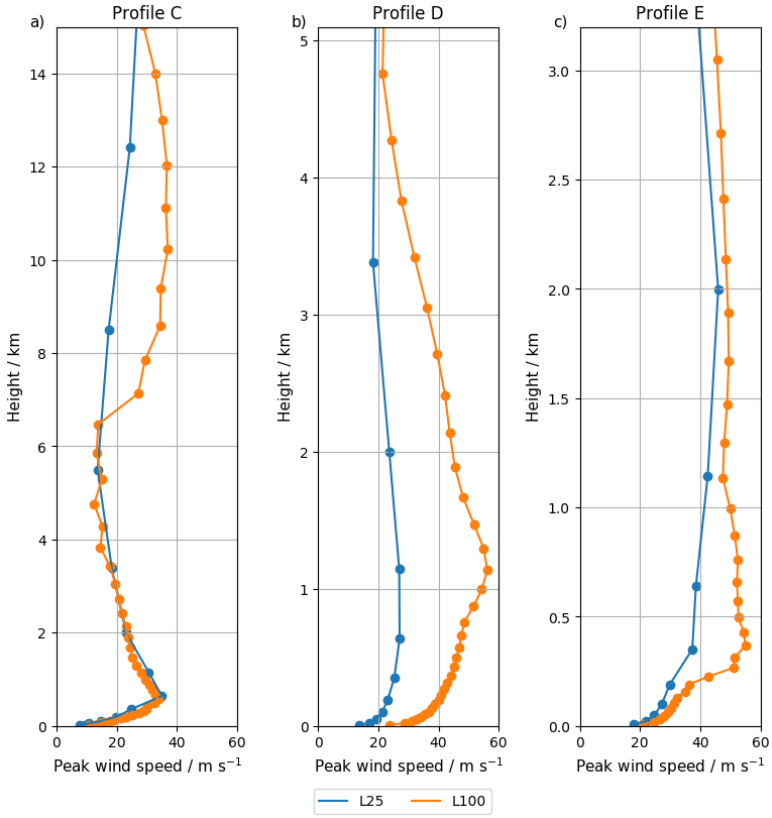

Figure 4.30: Partial-height peak wind speed vertical profiles from experiments completed at low and high vertical resolutions, L25 and L100: a) Profile C, to a height of ∼15 km above the surface; b) Profile D, to a height of ∼5 km; c) Profile E, to a height of ∼4 km.

An example profile supporting this interpretation is shown in Figure 4.31, in which Profile E is plotted using results from the L60 experiment as well as the L25 and L100 data plotted previously. The change in the perturbation feature with increased vertical resolution is evident (panel a), and it is the L60 profile that exhibits the highest near-surface peak wind speed (panel b).

It is conceivable that such perturbations in peak wind speeds are an artefact of the model. However, a number of facts argue against this interpretation: that these features are not present in all profiles; that the same point sampled at different times of year shows differences in perturbation (Profiles A and D); and that these perturbations vary both in magnitude and in the height at which they occur. These perturbations appear to occur across relatively shallow vertical

distances (less than ∼8 km in depth), meaning that low vertical resolution experiments are not able to resolve such features, leaving their effect on the atmosphere unrepresented.

It should be noted that not all profiles display such a clear trend with increasing resolution as that in Figure 4.31. However, it is reasonable to assert that increasing the vertical resolution of the MGCM provides a better representation of the potentially-complex structure within the Martian atmosphere.

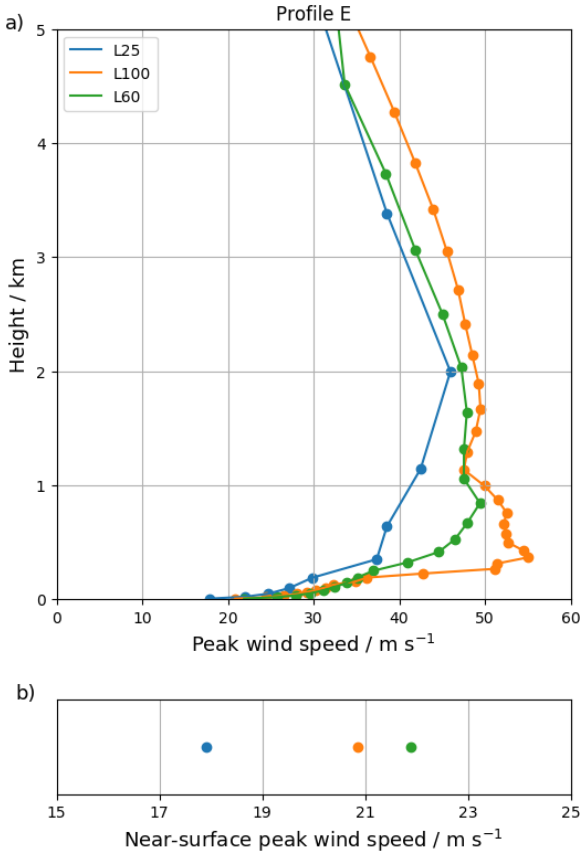

Figure 4.31: a) Partial-height peak wind speed vertical Profile E, showing data from experiments completed at three vertical resolutions: L25, L60 and L100. b) Detail of the near-surface peak wind speeds (i.e. in the lowest layer of the profile) at each resolution.

4.5 Highest Horizontal Resolutions

The highest horizontal resolutions used within this research are those designated T127 and T170 (Table 4.4). In the current build of the MGCM, compilation attempts of very high horizontal resolution models fail when using even standard numbers of vertical layers. Solving this issue would form a substantive core of future study. Compilation of stable models at resolutions of T127 and T170 was possible using 15 vertical layers (L15).

Tests on simulations using such a low number of layers have confirmed that L15 experiments lift a limited amount of dust (in total mass and with regards to the geographical spread of dust lifting), and do not provide a good representation of Martian dust lifting. The experiments discussed in this section cannot be compared directly with any experiments mentioned previously. Nevertheless, these experiments can be compared with each other, and an initial view of the model response at very high resolutions can be gained.

Resolution ID	Approximate physical resolution, ° latitude × ° longitude	Horizontal gridboxes
T127L15	1.25 × 1.25	41472
T170L15	0.94 × 0.94	73728

Table 4.4: The very high horizontal MGCM resolutions used in this research. For experiments at both of these resolutions the lowest layer is at a height of 0.005 km above the surface and the highest layer is at a height of 95.88 km.

T127

In order to compare the full range of horizontal resolutions, a new set of experiments was completed for all lower horizontal resolutions, using only 15 vertical layers. Figure 4.32 shows the amount of dust lifted in each $L_S = 30°$-long period through the year across these experiments. The anticipated seasonal pattern in lifted mass is still present, and the previously identified trend of increasing dust lifting with increasing resolution is true across these experiments. Figure 4.33 shows the annual, global sum of lifted dust mass against increasing resolution, in which the trend is very similar to that in Figure 4.8.

For completeness, Figure 4.34 shows the global plots of normalised dust lifting through each $L_S = 30°$-long portion of the Martian year for the experiment

completed at a horizontal resolution of T127.

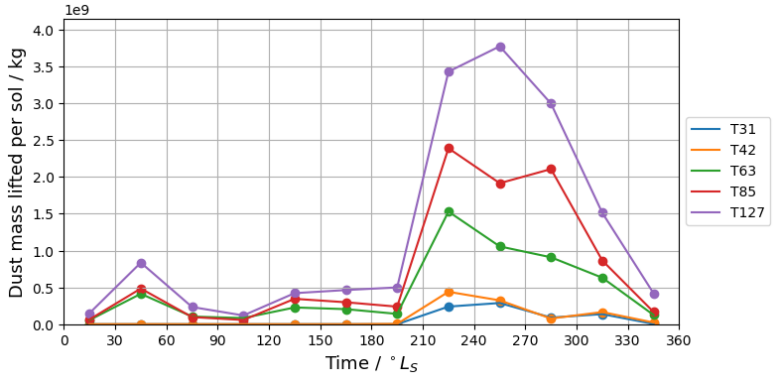

Figure 4.32: The dust mass lifted globally during each $L_S = 30°$-long period of the Martian year, normalised by the number of sols in each period, for the experiments discussed in Section 4.5. Plot lines added only to help the reader to follow each experimental result.

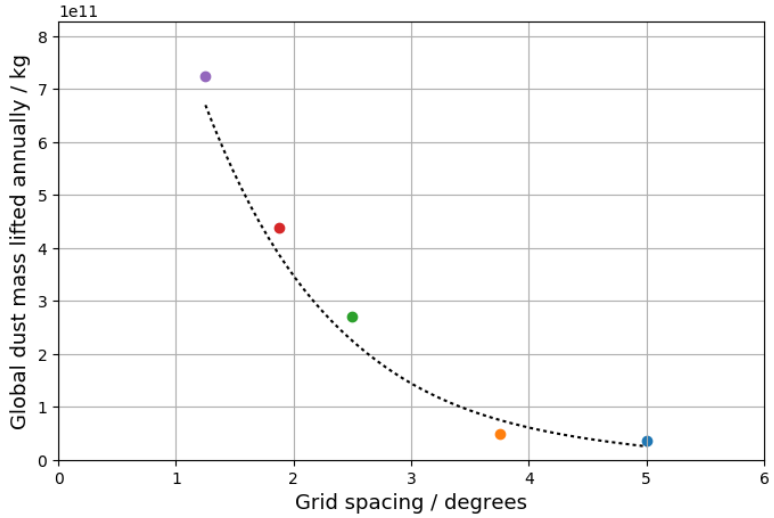

Figure 4.33: Annual, global total lifted dust mass against horizontal physical grid spacing, in experiments completed using 15 vertical layers. Resolution increases from right to left, colours correspond to those used in Figure 4.32. Dotted line indicates trendline of $y = 2 \times 10^{12}\,\mathrm{e}^{-0.875x}$.

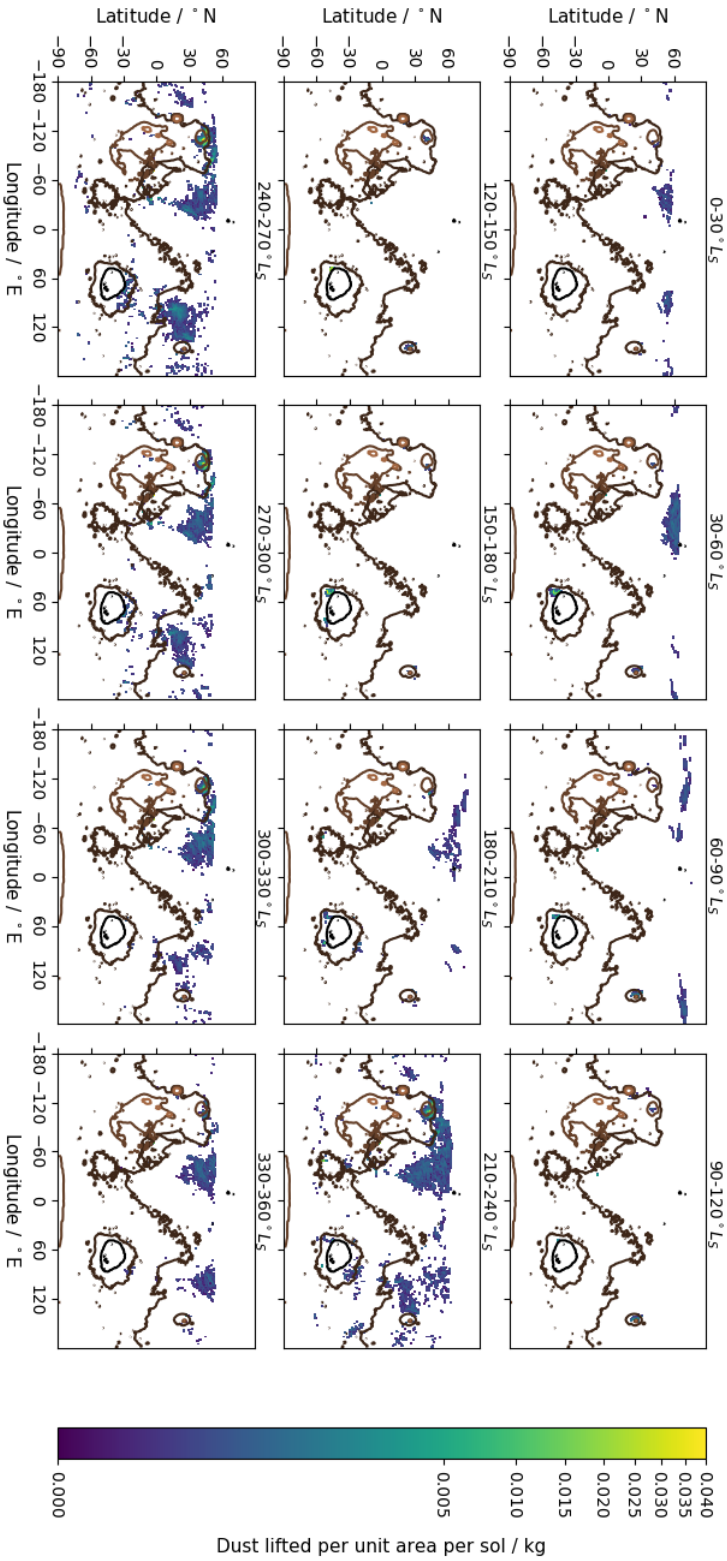

Figure 4.34: Global dust lifting by NSWS in a T127L15 experiment. Colour-scheme as for Figure 4.2.

T170

The simulation time required to complete experiments with a horizontal resolution of T170 is prohibitive. As mentioned in Section 3.7, interpolation of data from lower resolution results allows some of this simulation time to be 'leap-frogged', but the experiments are still time-consuming. In order to gain results in a reasonable time-frame, the experiments discussed in this section were only completed using one data output per sol. This output rate is not optimal when considering surface-level processes, as every timeslice of the results file contains global data only relating to one single point of time in the sol; it is therefore not possible to gain a good temporal representation of the processes at the surface-atmosphere boundary, and the results presented here have been obtained using a large amount of extrapolation. Experimental data obtained at a rate of one output per sol cannot be compared directly with data obtained at a higher output rate.

Consequently, for the following comparisons a new set of experiments was completed for all horizontal resolutions, using a data output rate of one output per sol. The experiments discussed in this section can only be compared with each other and cannot be compared directly with any experiments mentioned previously. For the T170 resolution only one full $L_S = 30°$-long period has been completed[1]. The period $L_S = 30\text{-}60°$ was chosen in an attempt to select a section of the year in which the trend of the 'dust mass lifted with increasing resolution' in the L15 one-output-per-sol experiments was as similar as possible to the trend of this quantity in the standard L25 five-outputs-per-sol, to best allow possible comparisons between the datasets.

Figure 4.35 shows the dust mass lifted in experiments completed at various horizontal resolutions through the period $L_S = 30\text{-}60°$. The data suggest a trend of increasing dust mass lifting with increasing resolution. This trend is not unambiguous: more dust was lifted in the T63 experiment than in than the T85 experiment, making the T63 result a divergence from the potential trend. (This divergence is believed by the author to be an artefact of the sub-optimal data output rate, although further work would be required to confirm this.)

Figure 4.36 shows the maps of dust lifting through the period $L_S = 30\text{-}60°$ for

[1] This experiment took 16 weeks to complete.

the four highest horizontal resolution experiments. The regions of dust lifting are similar in location across the resolutions, with slightly more widespread lifting in regions correlating with topographical features (mountains and the NH seasonal polar cap) at the higher resolutions. However, any improvement gained in the geographical representation of dust lifting regions at these higher horizontal resolutions must be weighed against the prohibitive simulation time required to complete such experiments.

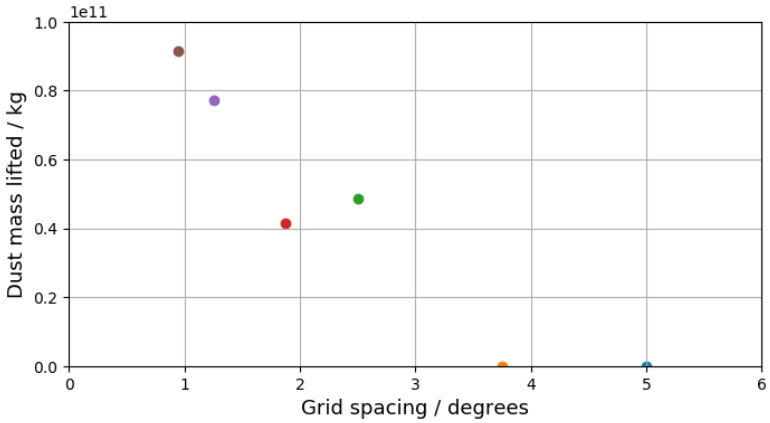

Figure 4.35: Global dust mass lifted during the period L_S = 30-60°, across multiple horizontal resolution experiments. Resolution increases from right to left, colours correspond to those used in Figure 4.32: T31 ∼5°, T42 ∼3.75°, T63 ∼2.5°, T85 ∼1.875°, T127 ∼1.25°, T170 ∼0.94°.

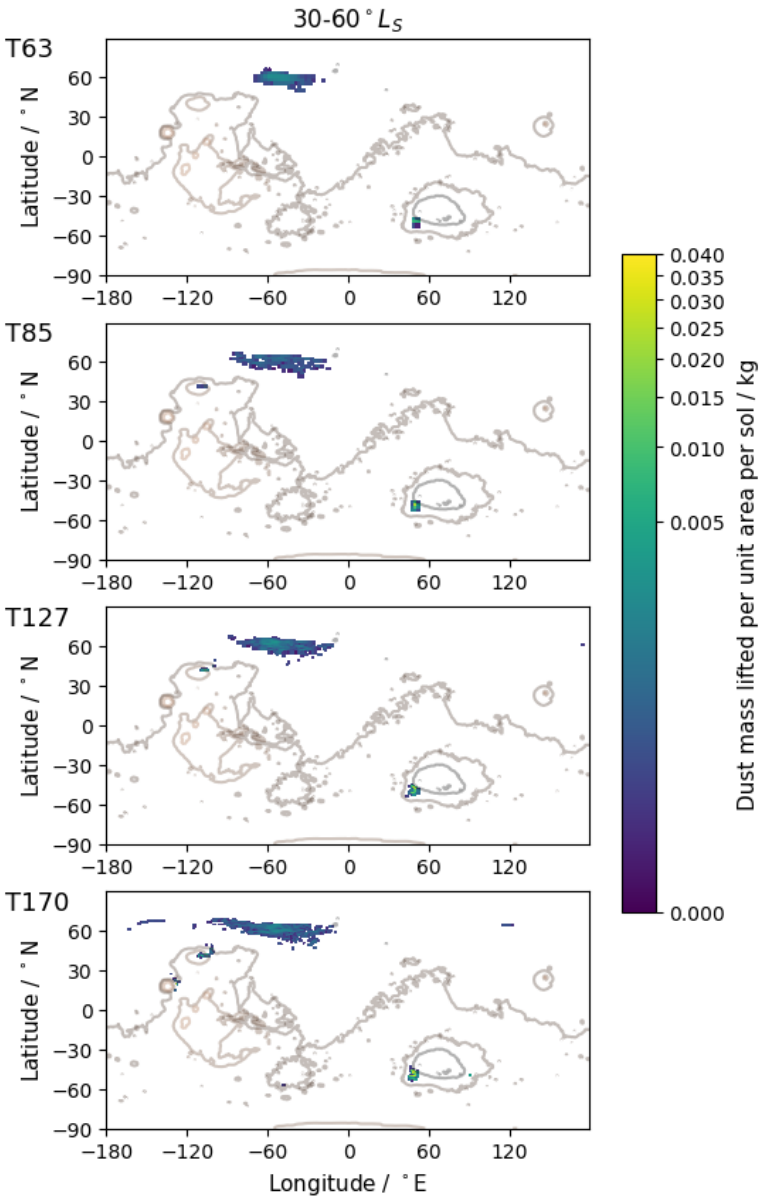

Figure 4.36: Surface dust lifting through the period L_S = 210-240°, for the highest horizontal resolution experiments. Colour-scheme as for Figure 4.2.

4.6 Summary and Recommendations

Increasing the resolution of an MGCM experiment, either horizontally or vertically, results in more geographically widespread lifting of dust by NSWS. Comparisons with observations of storm locations suggest that the geographical pattern of dust lifting at the lowest horizontal or vertical resolutions is not a good representation of surface dust lifting regions on Mars.

Horizontal Resolutions

Higher horizontal resolution experiments give a better representation of geographical dust lifting patterns, as well as lifting more dust in total. This is the case through both near-aphelion and near-perihelion periods, although the seasonal trend of more dust lifting during the SH summer is evident across all resolutions. Near-surface peak wind speeds are generally larger in the higher resolution experiments, particularly in regions of topographical variation.

Particular areas of improved representation appear to be associated with receding edges of seasonal CO_2 polar caps, especially during SH summer approaching perihelion, when important storm-forming regions in the NH are represented by dust lifting in the higher resolution experiments that is limited or absent in the lower resolution experimentals. The higher resolution experiments also show dust lifting during this period in regions along the edge of the SH polar cap, correlating with further storm observations.

The total amount of dust lifted globally by these experiments increases with increasing resolution, but the data obtained so far suggest that this trend is asymptotic. This is reflected in the differences between the areas across which dust is lifted: the geographical distribution of dust lifting changes most noticeably between lower resolution experiments (T31 to T42) than between higher resolutions (T63 to T85). The results from the very highest resolution tests (T127 and T170) seem to support these identified trends, but due to the limitations of those tests, they should only be considered a 'first pass look' at very high resolution simulations.

Vertical Resolutions

Higher vertical resolution experiments give a better representation of geographical dust lifting patterns, as well as generally lifting more total dust than lower resolution experiments. The areas of improved representation are again generally associated with seasonal polar cap edges, although increasing the vertical resolution does not give rise to as many 'new' dust lifting regions as were seen through increasing the horizontal resolution. The change in the total annual lifted dust mass with vertical resolution is also not as great as in the horizontal case.

Across much of the planet, near-surface peak wind speeds are larger in the higher resolution experiments than in the lower resolution experiments. One possible cause of this is the vertically-shallow features identified in some – but not all – of the analysed peak wind speed vertical profiles: high peak wind speeds that are evident in high vertical resolution experiments and absent in those at low resolution. These features may be atmospheric perturbations that occur across relatively shallow vertical distances, which cannot be resolved at the lowest vertical resolutions, and therefore are not represented in those results.

Recommendations

Increasing the horizontal resolution of the MGCM provides a better representation of underlying topographical features, affecting local wind circulations and driving a better geographical representation of surface dust lifting. Increasing the vertical resolution of the MGCM also provides a better representation of the geographical patterns of surface dust lifting, potentially due to a better resolution of the vertical structure of the lower atmosphere.

Based on the findings detailed above, this author recommends that the low horizontal and vertical MGCM resolutions typically used for long-term climate modelling should no longer be regularly used in experiments exploring the annual or seasonal change in surface dust lifting by NSWS. It is a relatively small step further to recommend that they are not used for any experiments that are designed to investigate a variety of surface-level processes, or to study the impact that any products of such processes have on the wider atmosphere, as it

is likely that these processes (and their production of any tracers, etc.) will not be well represented at these low resolutions.

Specific recommendations on MGCM resolutions must balance any improvement in the representation of dust lifting against the increased time required to complete experiments at higher resolutions. Horizontally, this author recommends that a resolution of at least T63 is used when possible, in order to achieve a reasonable geographical representation of dust lifting. A precise vertical resolution is more difficult to recommend. The representation of the vertical structure of the atmosphere improves with increasing resolution, but a direct relationship between the identified high speed wind features and the higher near-surface wind speeds is as yet unproven. This author therefore recommends a vertical resolution of at least 50 layers is used when possible, in an attempt to achieve a more representative pattern of dust lifting while minimising the increase in simulation time required. It is strongly recommended that any experiments designed specifically to study the behaviour of the Martian atmosphere's Convective Boundary Layer are completed at a high vertical resolution, using at least 100 vertical layers, in order to fully explore this potentially-complex region.

Combining any of these recommended resolutions may result in prohibitively long simulation times. A final recommendation is that careful consideration of the aims of any MGCM experiment is undertaken before high resolution simulations are attempted. It may be possible to use mid-level resolution experiments (e.g. T42L40) for a portion of any investigation, and then to interpolate the results to higher resolutions for a more detailed analysis of specific, shorter time periods.

Section 7.3 identifies a number of potential avenues of further work on this topic.

Chapter 5

Diurnal Variation in Martian Dust Devil Activity

Work from this chapter was published in *Icarus* in January 2017: R. M. Chapman et al., **Diurnal Variation in Martian Dust Devil Activity**. *Icarus* 292 (2017) p154-167, DOI 10.1016/j.icarus.2017.01.003. This chapter expands upon the published content. Sections 5.3 and 5.4 are based upon experiments and analysis completed solely by the author.

5.1 Introduction

Dust devils are small-scale atmospheric vortices that entrain surface dust particles into a vertical, upwardly spiralling column; see Section 2.4 for a full description of this phenomena. They have been observed directly in images of Mars captured both from orbit (e.g. *Thomas and Gierasch*, 1985; *Fisher et al.*, 2005; *Stanzel et al.*, 2006) and from the surface (e.g. *Ferri et al.*, 2003; *Greeley et al.*, 2006), and the tracks they leave behind on the surface have also been imaged from orbit (e.g. *Cantor et al.*, 2006).

Dust is ubiquitous in the Martian atmosphere. Outside the annual dust

storm season, dust devils are considered to be the lifting process that is responsible for the constant atmospheric haze. Understanding their temporal behaviour – on seasonal and shorter scales – is therefore a crucial aspect of understanding the annual, planetary dust cycle.

Due to the lack of direct measurements of most Martian dust devil characteristics (almost anything beyond the population's size distribution), analogies are often drawn between dust devils on Mars and on Earth. Diurnal variation in activity is one of the characteristics for which such a parallel has been proposed.

Observations of terrestrial dust devils suggest that they are generally most active in the afternoon: *Sinclair* (1969) described dust devil observations that spanned the period between 10:00 to 16:30, with activity reaching a maximum between 13:00 and 14:00 (Arizona, USA); *Snow and McClelland* (1990) observed dust devils starting around 11:00, peaking in number between 12:30 and 13:00, and ending by 16:00 (New Mexico, USA); *Oke et al.* (2007) reported dust devil observations occurring between 11:20 and 17:40, with activity at a peak between 14:00 and 15:40 (New South Wales, Australia); and *Lorenz and Lanagan* (2014) used pressure data to identify dust devil events starting around 09:00, peaking twice during the afternoon, around 14:00 and then 16:00, and lasting until 20:00 (Nevada, USA). This chapter explores the diurnal variation in Martian dust devil activity: the results presented here suggest that the generally accepted description of dust devil behaviour on Mars is incomplete.

Section 5.2 outlines the methods used in this work; Section 5.3 shows the results and Section 5.4 details the comparison of the results with observational data. Section 5.5 contains the discussion and summary of this work.

5.2 Method

The rate at which surface dust is lifted by dust devils ("dust devil lifting") is used herein as a proxy for assessing the level of dust devil activity at any specific location and time. Dust devils are too small in scale to be modelled explicitly within a global model: dust devil activity levels represent the larger scale effect of multiple instances of this small phenomenon within a model gridbox. It is not possible to extrapolate any information about the number or size of the dust devils represented by any given level of activity. The MGCM parameterisation of dust devil lifting is described in Section 3.5.2.

The MGCM allows frequent sampling of atmospheric variations through a long period of simulated time. Experiments were completed at a data rate of 12 outputs per day, spaced evenly throughout the sol. Each data output produces a global 'snapshot' of the Martian atmosphere at a single time: a rate of 12 outputs per day allows sampling of any result variable at any specific location every two hours.

The rate at which dust devils lift dust can be extracted for each surface gridbox, over the whole course of a simulation. In order to investigate temporal trends in the lifting rate, the data for each 2-hourly output were averaged across 30° L_S-long sections of the Martian year. The resulting dataset allows dust devil activity rates to be tracked through the sol: the time-of-sol at which dust devils were commonly most active within each gridbox, during each portion of the year, can be identified.

For clarity, extremely low levels of dust devil lifting were eliminated from subsequent calculations. Dust lifting rates of less than 1×10^{-11} kg m^{-2} s^{-1} are treated as zero lifting; this 'threshold' value was chosen by considering dust lifting rates at specific sites across the surface, see Section 5.4.

5.3 Peak Dust Devil Lifting Time

Figure 5.1 shows an example global map of the 'peak dust devil lifting time': the time-of-sol at which dust devils were most active within each gridbox, throughout the displayed period. This dataset is from an experiment completed at the

T31 resolution (a physical gridbox size of approximately 5° latitude × 5° longitude, see Section 3.6), utilising a relatively low atmospheric dust loading that represents a Martian year similar to MY24 (see Section 3.4.2).

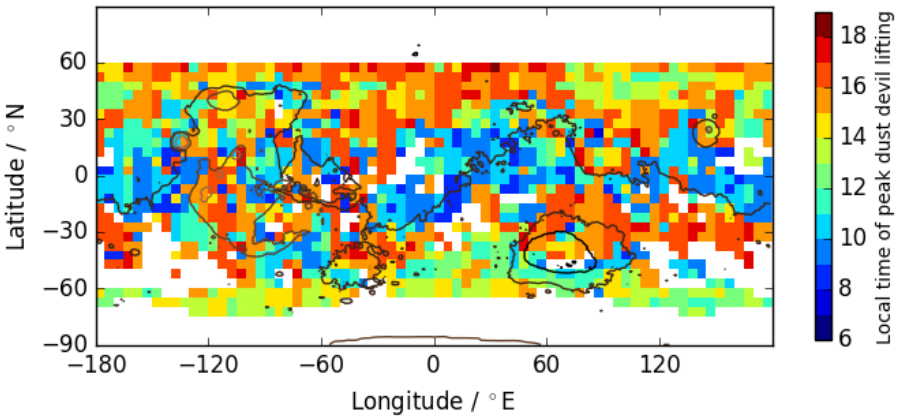

Figure 5.1: Global map in which the colour scale identifies the diurnal timing of peak dust devil lifting. The data displayed here show dust devil lifting averaged across L_S = 0-30°, corresponding to early Northern Hemisphere spring. Gridboxes coloured yellow, orange or red denote peaks in dust devil lifting during the afternoon; blue gridboxes denote peaks in dust devil lifting during the morning. White gridboxes indicate no lifting or below threshold lifting. (Topographic contour lines included for illustration only.)

The diurnal pattern within this data is best displayed using histograms of the peak dust devil lifting time across all surface gridboxes. Figures 5.2 and 5.3 show histograms for each 30° L_S section of the year, using the same colour scheme as in Figure 5.1.

The histograms depicting the aphelion Martian season spanning L_S = 330-210°, relating to late winter through to summer in the Northern Hemisphere (Fig. 5.2a-f; Fig. 5.3a and Fig. 5.3f), show a clear bimodal distribution of peak dust devil lifting times: a large maximum during the afternoon, between 15:00 and 17:00, and a secondary maximum during the morning, generally between 09:00 and 11:00. There is a seasonal shift in the diurnal distributions of this peak dust devil lifting time: the histograms depicting the perihelion season, L_S = 210-330°, relating to Southern Hemisphere summer (Fig. 5.3b-e), show a unimodal distribution with a single maximum in peak dust devil lifting times during the afternoon, between 14:00 and 17:00.

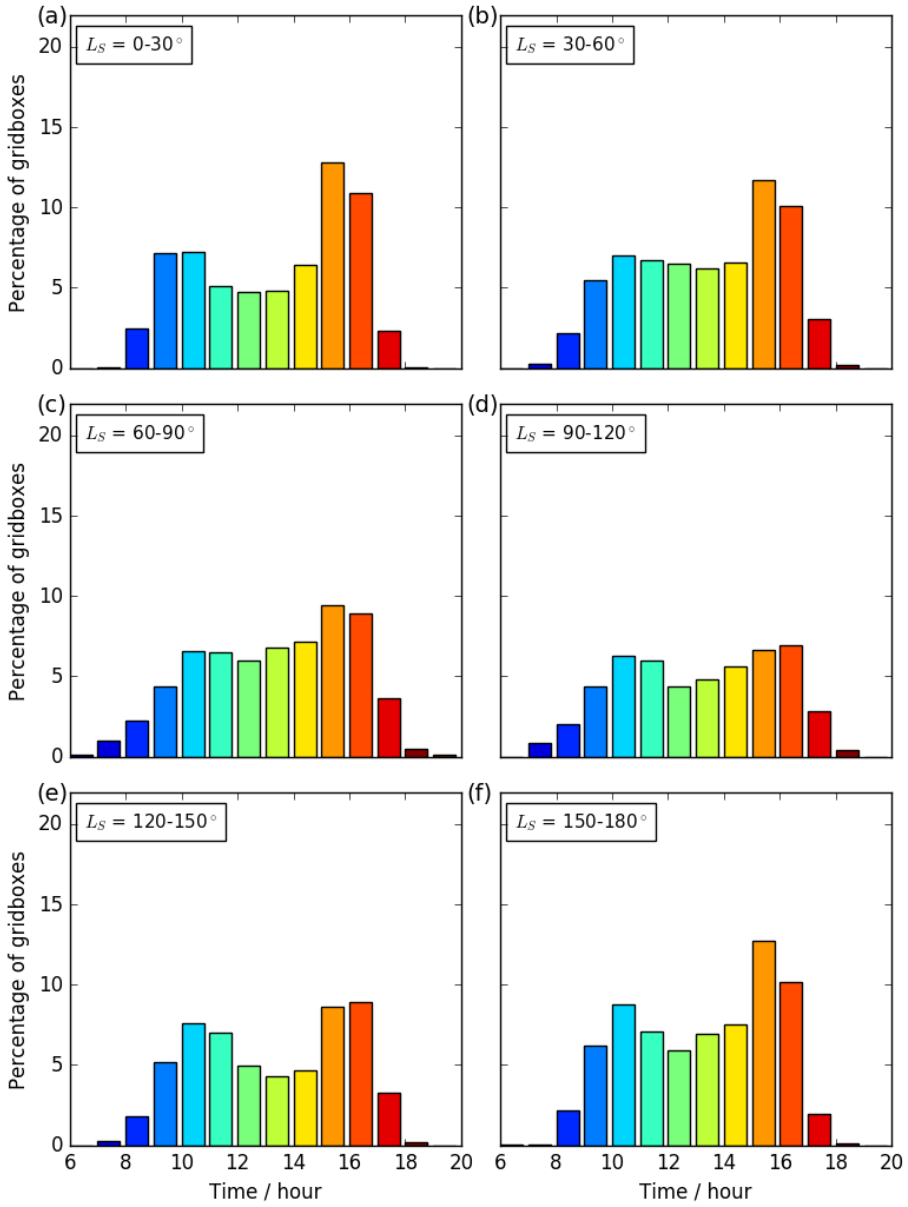

Figure 5.2: Histograms showing the diurnal timing of peak dust devil lifting as a percentage of all surface gridboxes, through L_S = 0-180°, split into 30° L_S sections. The colour scheme replicates that of Figure 5.1; the top left panel here shows the same data as in that global plot.

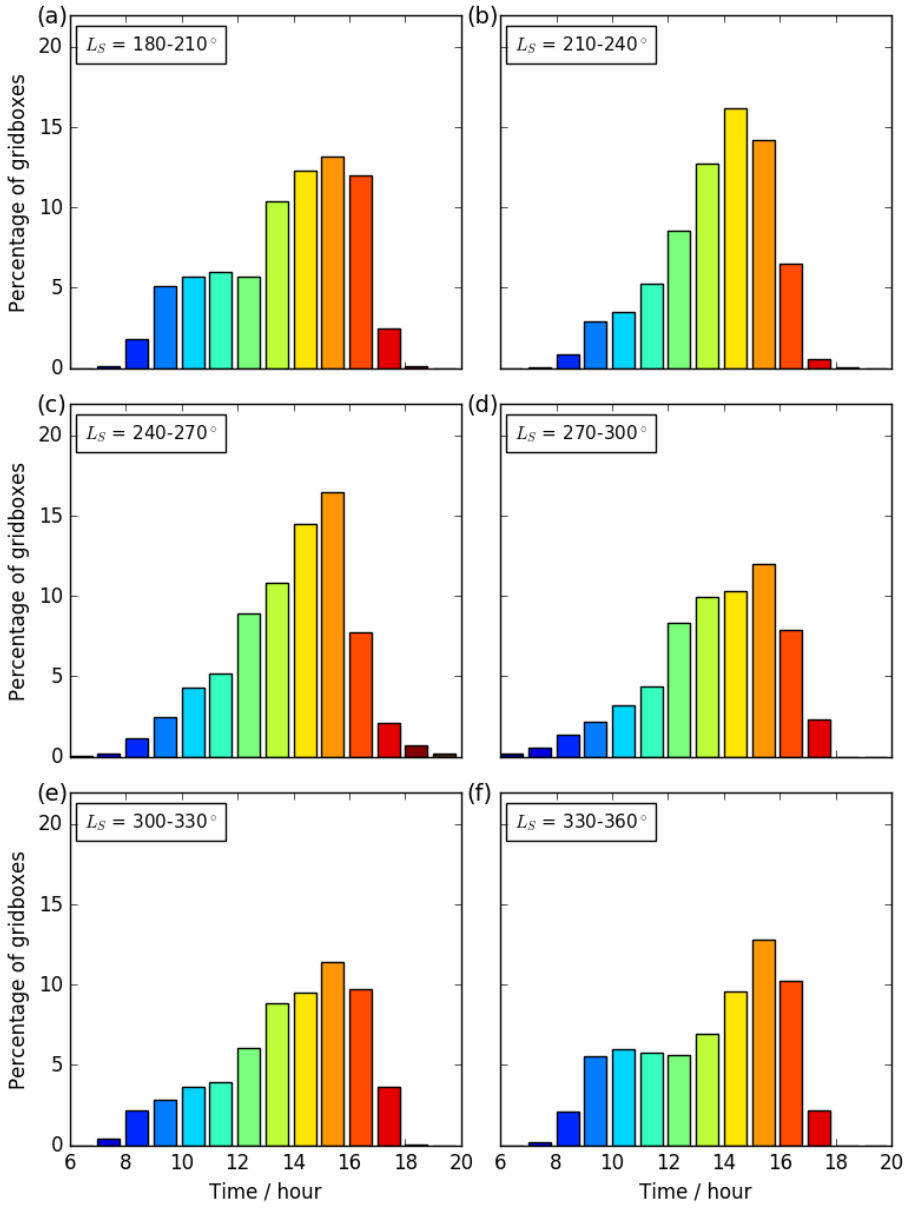

Figure 5.3: As Figure 5.2, for L_S = 180-360°.

The experiment that produced the data shown in Figures 5.1 to 5.3 was completed utilising an atmospheric dust loading that represented the dust loading observed in the Martian atmosphere during MY24, a year that did not experience a global dust storm (refer to Section 3.4.2 for more detail). This experiment was repeated utilising a relatively high atmospheric dust loading, representing a Martian year similar to MY25, in which a global dust storm was observed. This higher atmospheric dust loading does not greatly affect the resultant histogrammed data: the bimodal distribution of peak dust devil lifting times is still evident through aphelion (Figure 5.4), and the unimodal distribution is present through perihelion (Figure 5.5). The seasonal shift between the two distributions occurs earlier in the experiment using a higher dust loading, with the period L_S = 180-210° (Fig. 5.5a) now displaying the unimodal rather than bimodal distribution. The maxima of the distributions through L_S = 210-270° (Fig. 5.5b-c) are shifted slightly earlier in the afternoon than seen in the previous experiment, but the timing remains similar. The other panels in this figure show little difference to those seen previously.

To test the robustness of these results, the initial experiment was replicated at a higher horizontal resolution: the T42 resolution, which corresponds to an approximate physical gridbox size of 3.75° latitude × 3.75° longitude. Again, the results are similar to those of the first experiment. Figure 5.6 shows that through L_S = 0-180° a bimodal distribution is still generally present, although the data in the section spanning L_S = 90-120° (Fig. 5.6d) displays a flatter distribution at this resolution. Figure 5.7 shows the shift to a unimodal distribution extending through the majority of the perihelion season, although the beginning (L_S = 180-210°) and the end of the period (L_S = 330-360°) still show indications of bimodality (Fig. 5.7a and 5.7f; compare with the unimodal shape shown in panels Fig. 5.7b-e).

One assumption made so far is that the surface roughness length, z_0, is constant across the whole of Mars: this parameter was set to a 'standard' value of 1 cm for all the experiments above. To test how this assumption affected these results, a further experiment was completed that employed a surface roughness map derived from rock abundance data (described in *Hébrard et al.* 2012), across which z_0 varies from around 0 to ∼2 cm.

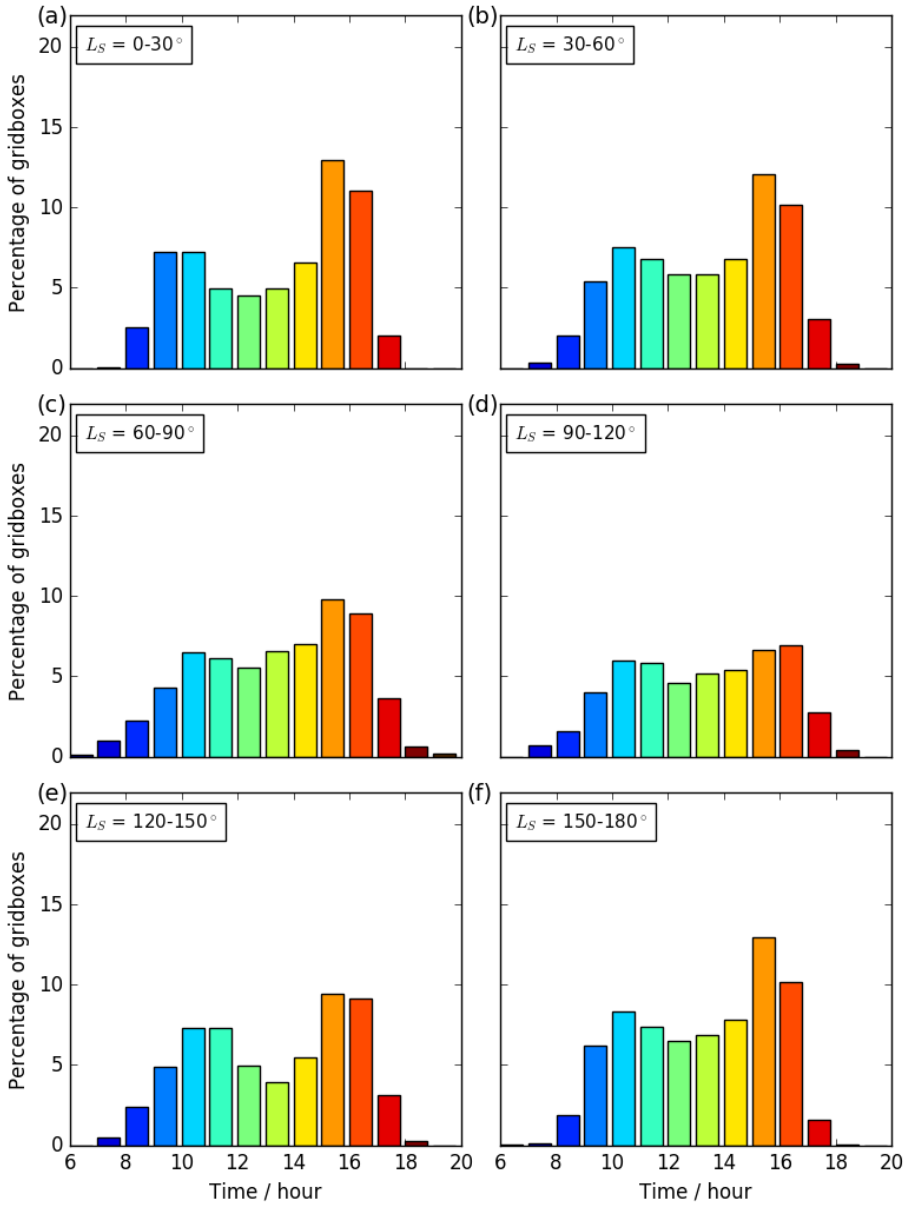

Figure 5.4: As Figure 5.2, displaying histogram data from an experiment utilising a high atmospheric dust loading.

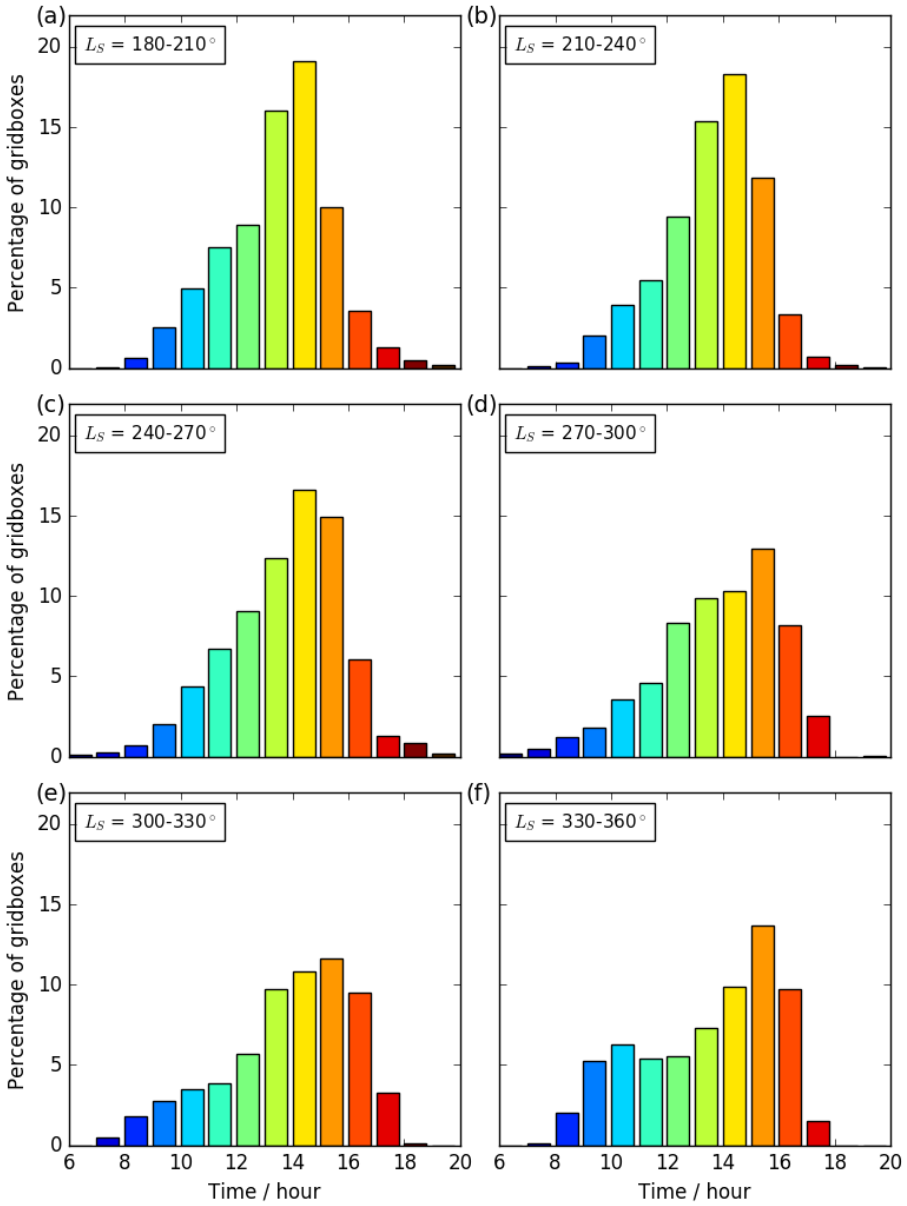

Figure 5.5: As Figure 5.3, displaying histogram data from an experiment utilising a high atmospheric dust loading.

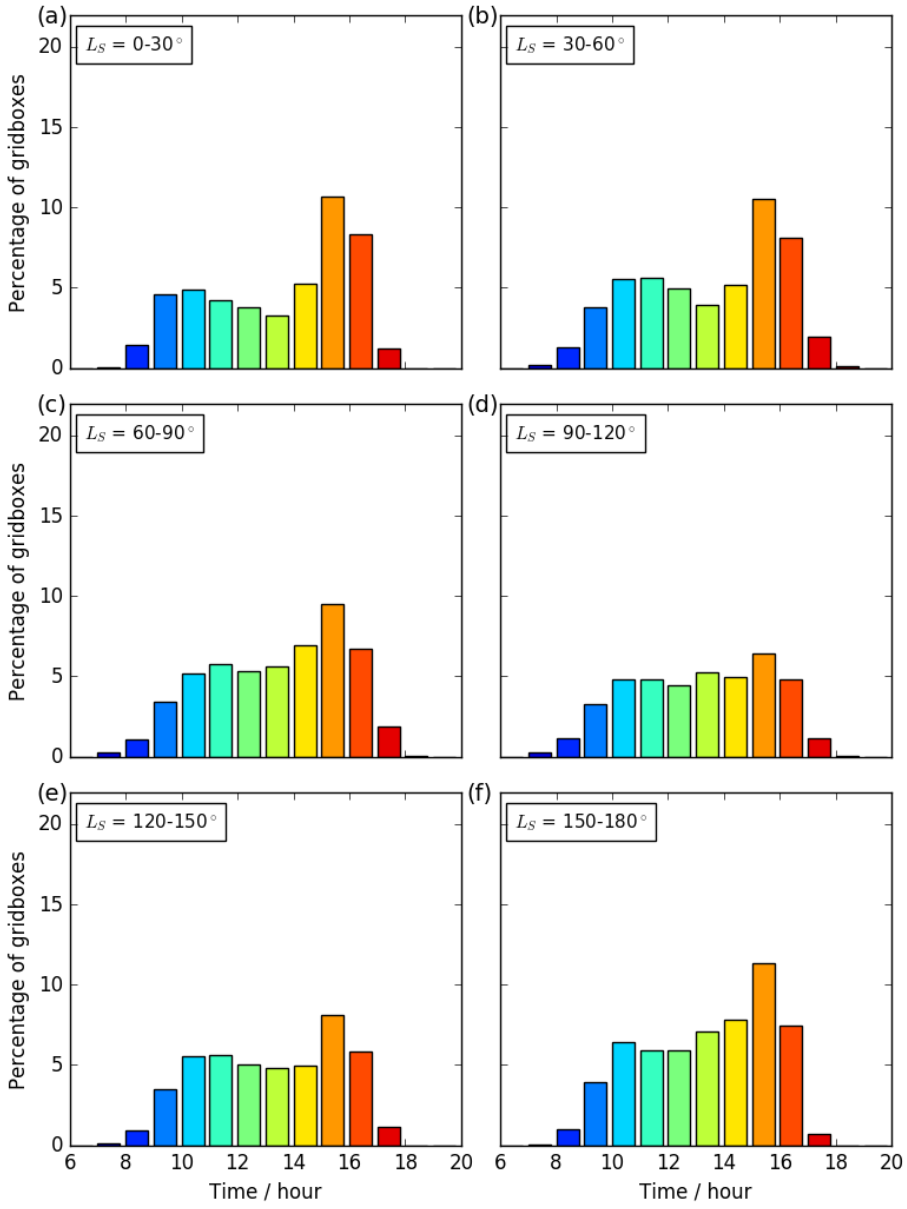

Figure 5.6: As Figure 5.2, displaying histogram data from an experiment completed at the T42 resolution.

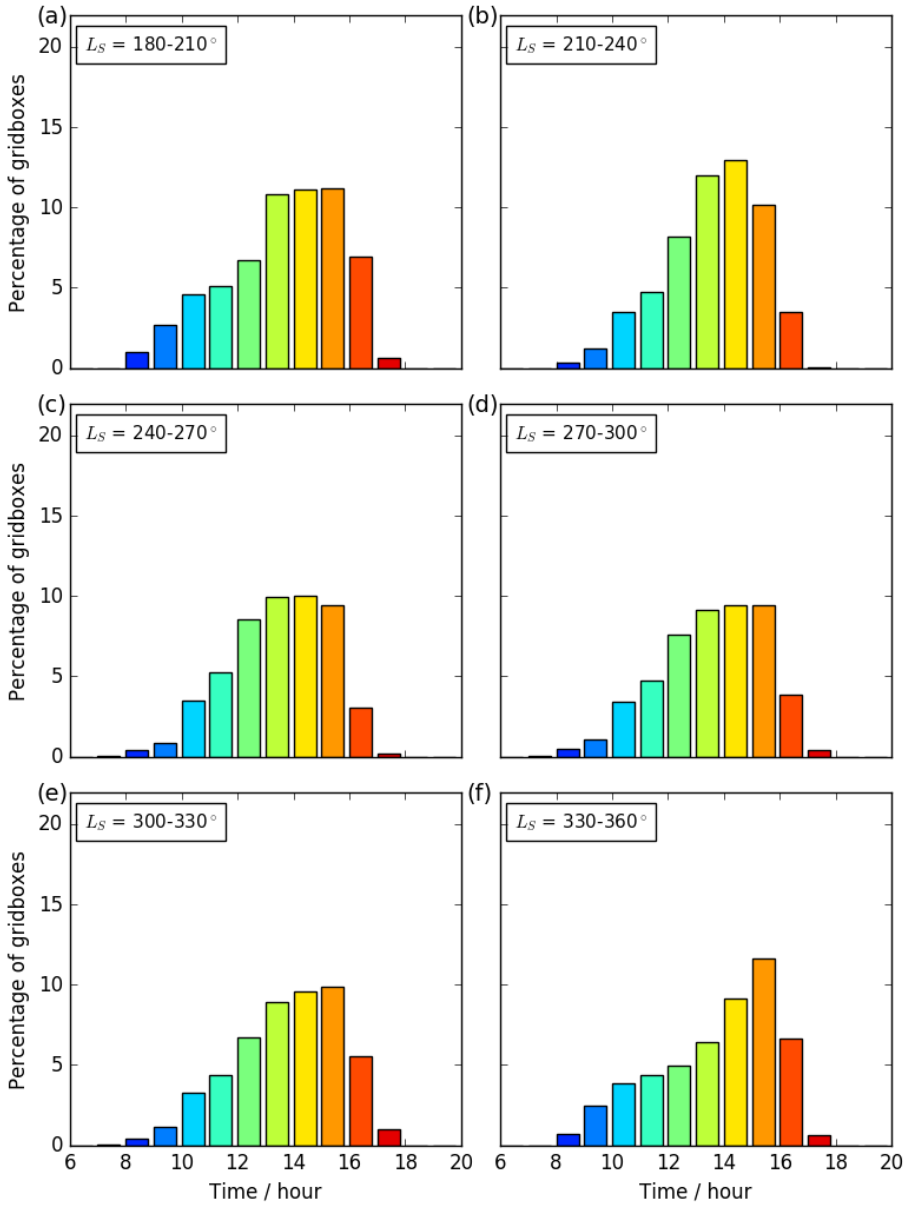

Figure 5.7: As Figure 5.3, displaying histogram data from an experiment completed at the T42 resolution.

Surface roughness is incorporated into the dust devil parameterisation within the calculation for surface drag (Equation 3.19): increasing the surface roughness length increases the surface drag coefficient. This produces higher overall levels of dust devil activity, as increased surface friction contributes to the forcing of warm air into the base of a forming dust devil (*Rennó et al.*, 1998). Employing the varying surface roughness map results in more total dust being lifted by dust devils through the length of the modelled period, but the timing of the dust devil activity (both seasonally and diurnally) was not affected greatly.

The previous bimodal distribution is still evident through the majority of the aphelion season: $L_S = 330\text{-}210^\circ$ (i.e. beginning before the Northern Hemisphere spring solstice, $L_S = 0^\circ$, and lasting from the start of the year until the Northern Hemisphere autumn). There is a flattening of this curve in the data through the immediately-post-aphelion period, $L_S = 90\text{-}120^\circ$ (Fig. 5.8d). The bimodality of the data on either side of this period ($L_S = 60\text{-}90^\circ$ and $L_S = 120\text{-}150^\circ$, Fig. 5.8c and Fig. 5.8e) is also less pronounced than in the experiment using a constant $z_0 = 0.01$ m. The unimodality through the perihelion season, $L_S = 210\text{-}330^\circ$ (Fig. 5.9b-e), is very similar to that seen previously.

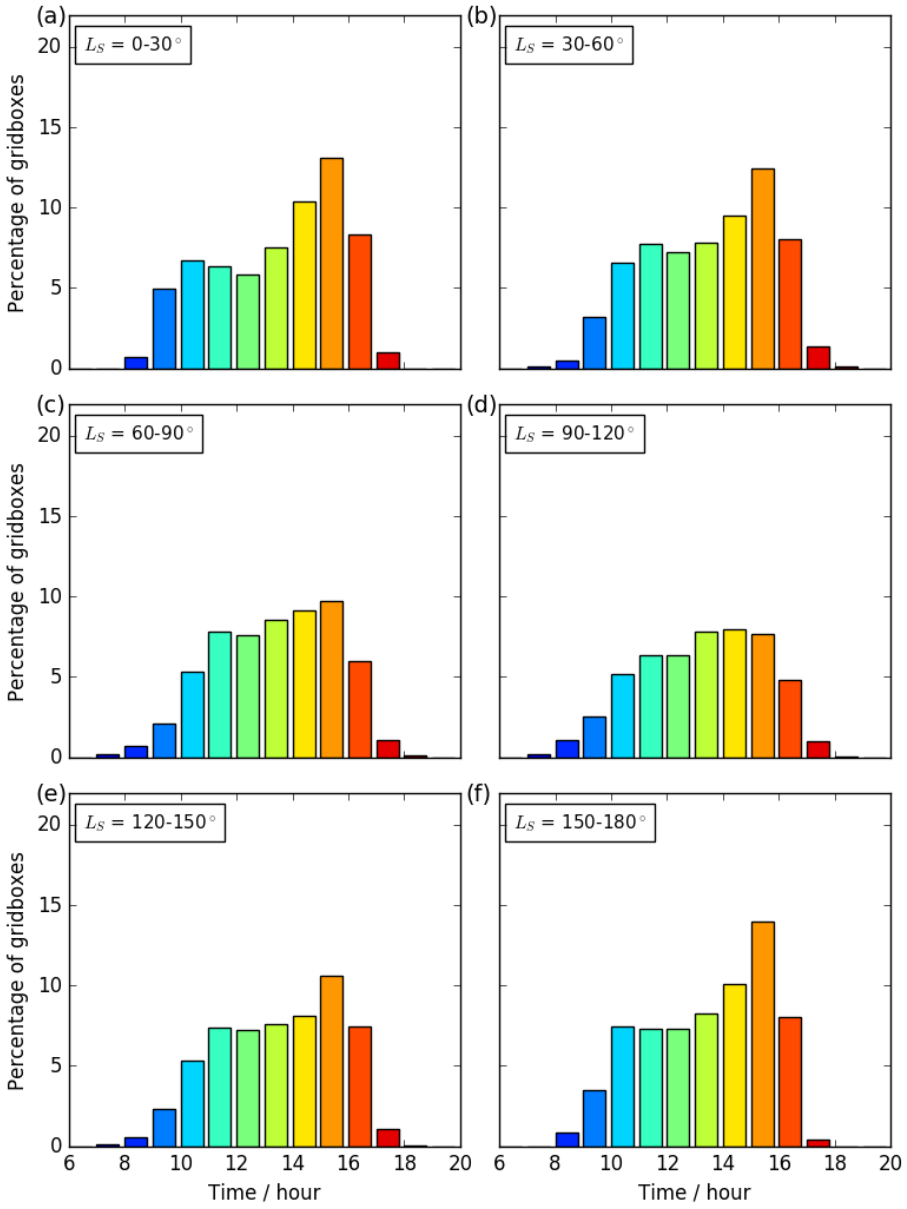

Figure 5.8: As Figure 5.2, displaying histogram data from an experiment completed using a map of varying surface roughness rather than assuming that z_0 is a constant value.

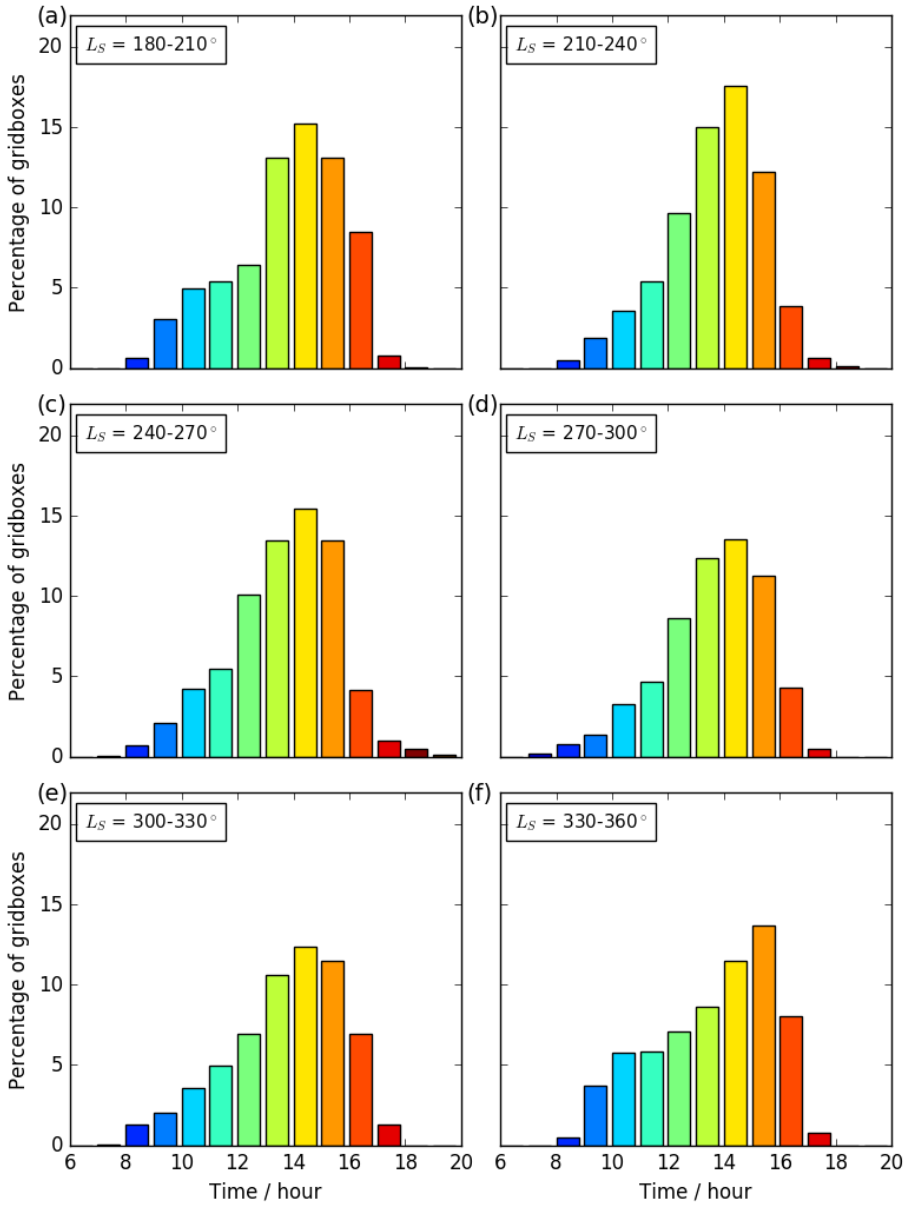

Figure 5.9: As Figure 5.3, displaying histogram data from an experiment completed using a map of varying surface roughness.

5.3.1 Variability of Individual Gridboxes

While Figure 5.1 shows the global view of diurnal peaks in dust devil lifting, there can be considerable variation in the timings displayed for any one gridbox. Figure 5.10 illustrates that some individual gridboxes display dust devil lifting only in the morning, some display lifting only in the afternoon, and others display lifting distributed more widely throughout the sol, even showing a bimodal lifting pattern within a single gridbox.

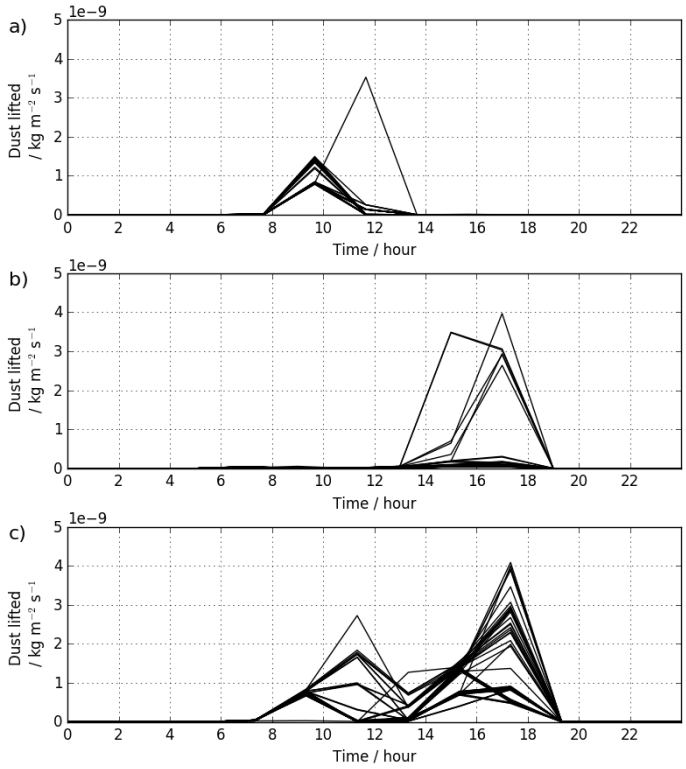

Figure 5.10: Dust devil lifting within individual gridboxes through L_S = 120-150° (time of year chosen as an example period). Each plotted line corresponds to the dust devil lifting through one sol, with the period covering 60 sols in total. The plots show varying diurnal timings of dust devil lifting: a) morning-only dust devil lifting (gridbox centred on -12.5° N, 175° E), b) afternoon-only dust devil lifting (37.5° N, 75° E), and c) through-sol dust devil lifting, displaying a nominal bimodal distribution (27.5° N, -10° E).

5.3.2 Variability Resulting from the Parameterisation

The origin of the identified temporal variability in modelled peak dust devil lifting can be found by examining the component variables within Equations 3.16 and 3.18, reproduced here for convenience as one equation:

$$F_{\text{devil}} = \alpha_D \eta \rho c_p C_D U (T_{\text{surf}} - T_{\text{atm}}) \tag{5.1}$$

These experiments held constant the values used for the dust devil lifting efficiency α_D, the specific heat capacity at constant pressure c_p, and the surface drag coefficient C_D (apart from the single surface roughness test mentioned above), so these variables cannot cause the diurnal variation displayed in the dust devil lifting. The variables that show a consistent diurnal variation are the thermodynamic efficiency, η, the near-surface atmospheric density, ρ, and the surface-to-atmosphere temperature gradient, $(T_{\text{surf}} - T_{\text{atm}})$.

Thermodynamic Efficiency

The variation of the thermodynamic efficiency, η, follows the diurnal variation of the depth of the Convective Boundary Layer (CBL). The depth of the CBL, represented by $p_{\text{surf}} - p_{\text{top}}$ in the calculation of dust devil thermodynamic efficiency (Equation 3.17), is directly forced by insolation-driven heating of both the surface and the near-surface atmosphere (*Spiga et al.*, 2010), and the consequent increase in heat in the lower portion of the atmosphere. Temporal variation of the depth of the CBL therefore follows the diurnal pattern of heating in the lowest levels of the atmosphere: CBL depth increases steadily during the morning, reaches a peak in the late afternoon, and decreases in the evening (at a faster rate than the morning increase). This is illustrated in Figure 5.11, which shows example η curves calculated for the gridbox centred on -2.5° N, -5° E (covering the region of the landing site of NASA's Opportunity rover in Meridiani Planum) at $L_S \approx 245°$, in a year experiencing a low atmospheric dust loading (MY24).

While the local depth of the CBL varies considerably over the planet depending on local surface elevation (*Hinson et al.*, 2008), the diurnal pattern of CBL depth variation is consistent across the planet due to its dependence on

insolation. The value of η will therefore consistently reach a maximum in the late afternoon; its local value will be determined by the local depth of the CBL: a CBL depth of ∼5 km results in η ∼0.06 and a CBL depth of ∼8 km results in η ∼0.08. (From Equation 5.1 it can be seen that η must be greater than zero for any dust devil lifting to occur.)

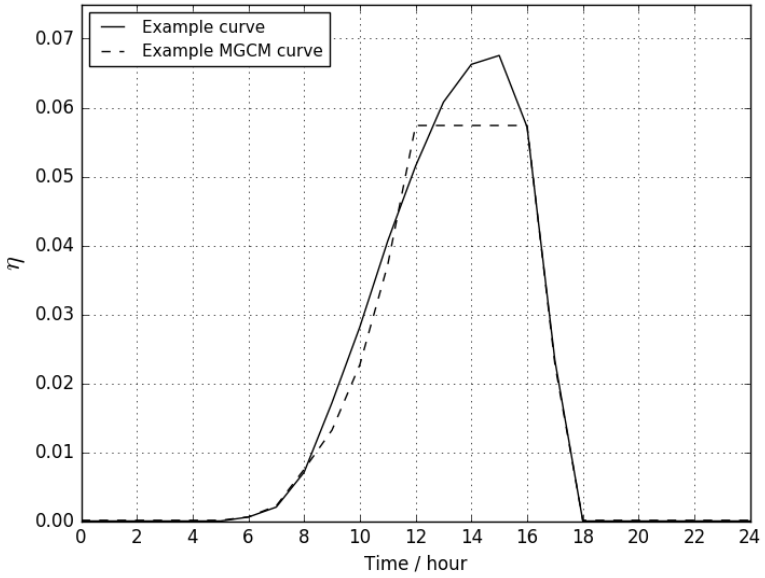

Figure 5.11: The example η curve (solid line) was calculated using a representative diurnal CBL depth curve extracted from the Mars Climate Database (*Lewis et al.*, 1999). The example MGCM η curve (dashed line) illustrates how the calculation of η within the model is affected by the discretisation of atmospheric layers. This truncation/quantisation effect is due to the depth of the model's vertical layers, which are shallow close to the surface (i.e. tens of metres deep in the lowest layers) but increase in depth as altitude increases (e.g. ∼2000 m deep at an altitude of 5 km). In both curves η increases during the morning, reaches a maximum shortly after peak insolation, and then decays more quickly in the evening.

Near-surface Atmospheric Density

Near-surface atmospheric density, ρ, varies widely by location, driven by local variations in the near-surface atmospheric pressure. Despite this difference in absolute value, the diurnal variation of this quantity is broadly consistent across the planet's surface. Figure 5.12 illustrates this with ρ curves from surface locations at extremes of altitude.

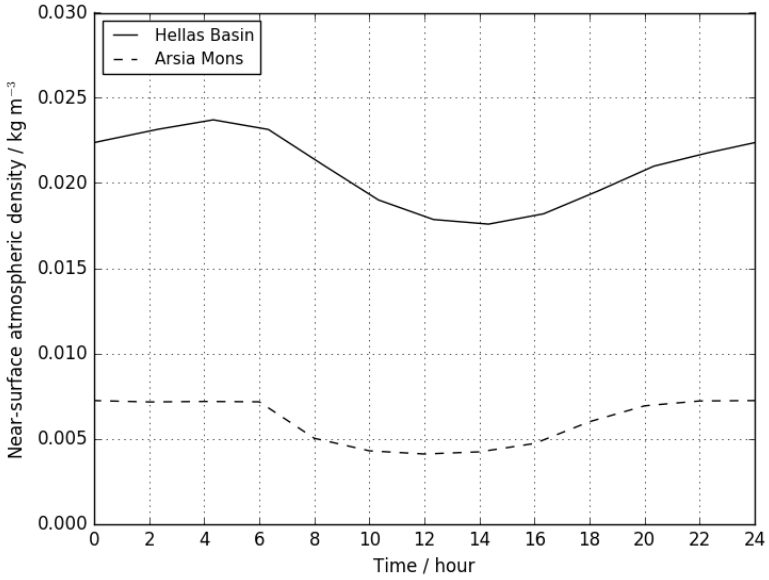

Figure 5.12: Near-surface atmospheric density at two locations: within Hellas basin (at an altitude ∼6.7 km below Mars datum) and in the vicinity of Arsia Mons (at an altitude ∼15.5 km above Mars datum). These values were averaged over the period L_S = 240-270°. The shape of the diurnal curve is similar for both sites through the length of a sol.

Near-surface Temperature Gradient

The temperature gradient between the surface and the near-surface atmosphere, $(T_{\mathrm{surf}} - T_{\mathrm{atm}})$, has a predictable diurnal cycle, with a magnitude dependent on latitude and time of year. Surface temperature reaches a peak at the point of maximum insolation, around 13:00 local time, while near-surface atmospheric temperature peaks later in the sol, between 16:00 and 17:00. This lag between the temperature curves produces a maximum in $(T_{\mathrm{surf}} - T_{\mathrm{atm}})$ that occurs slightly ahead of the peak in surface temperature (illustrated in Figure 5.13).

Although surface and near-surface temperatures vary by a large amount across latitudes and altitudes, the timings of the peaks in the temperature curves remain relatively consistent. The difference ($T_{\mathrm{surf}} - T_{\mathrm{atm}}$) must be greater than zero for any dust devil lifting to occur, see Equation 5.1.

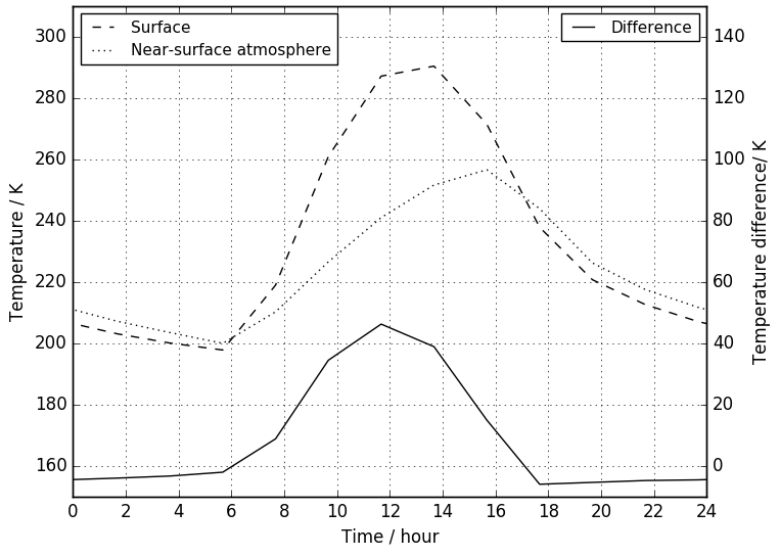

Figure 5.13: Surface temperature and near-surface atmospheric temperature curves are plotted against the left axis and temperature difference ($T_{\mathrm{surf}} - T_{\mathrm{atm}}$) is plotted against the right axis. Values were averaged over L_S=240-270°; this gridbox is centred on -2.5° N, -5° E. The peak in temperature difference occurs around 12:00, leading the timing of the peak in surface temperature.

Near-surface Wind Speed

The final component in Equation 5.1 is the near-surface wind speed, U. This is calculated from the large-scale winds within the lowest model layer of the atmosphere (held at a height of ∼5 m above the surface), and can be highly variable throughout the course of one sol. Figure 5.14 shows an example of the variability present in near-surface wind speed within a selected gridbox. The associated dust devil lifting is also shown: in this particular gridbox the timing of the dust devil lifting is distributed broadly throughout daylight hours. (Figure 5.15 shows the near-surface wind speeds associated with the examples of morning-only and afternoon-only dust devil lifting plotted in Figure 5.10.)

Figures 5.16 and 5.17 show histograms of the diurnal timing of peak near-

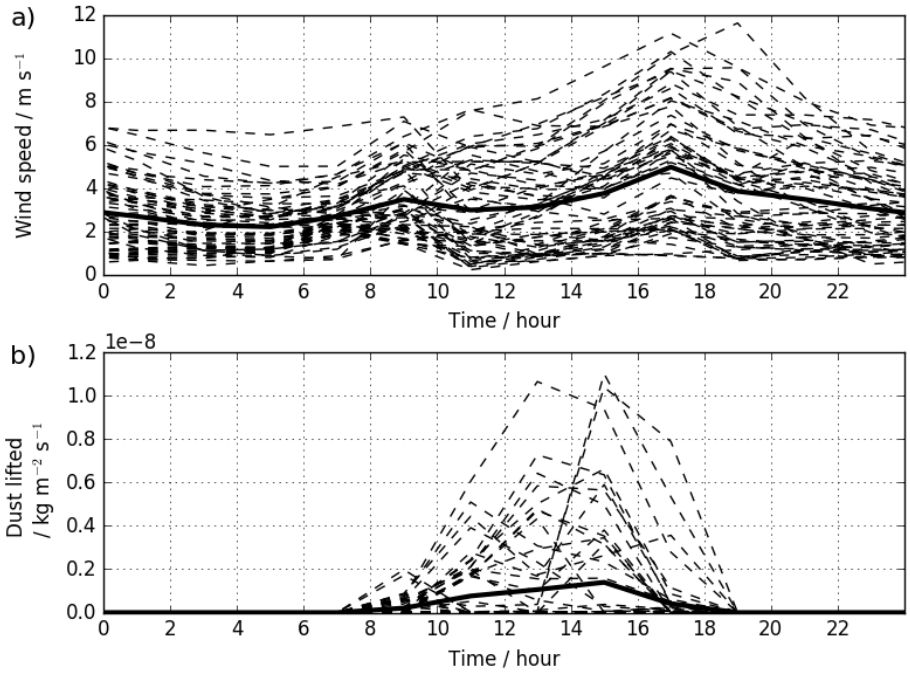

Figure 5.14: Near-surface wind speeds and dust devil lifting within an individual gridbox (47.5° N, 135° E) through the period L_S = 0-30°. Each dashed line corresponds to values through one sol (60 sols in total), and the heavy solid line shows the average of this period. These panels show the variability of the plotted values: a) wide variation in the amplitude of wind speeds, b) variation in the timing and amplitude of dust devil lifting.

surface wind speeds through the course of a year. A bimodal distribution of timings is evident during the period of Northern Hemisphere spring and summer, and a unimodal distribution is evident through Northern Hemisphere autumn and winter. This pattern closely matches the distributions identified in the diurnal timings of peak dust devil lifting (compare with Figures 5.2 and 5.3), including the seasonal shift between distributions.

The near-surface wind speed is the only component in Equation 5.1 that does not follow a regular pattern through each sol: the diurnal variations in η, ρ, and $(T_{\mathrm{surf}} - T_{\mathrm{atm}})$ follow smooth, predictable curves, while the variation in wind speed from sol to sol is more stochastic in nature. It is therefore reasonable to conclude that, while insolation is the root driver of Martian dust devil formation, the identified variability in the timing of modelled dust devil lifting depends primarily on the speed of the near-surface wind.

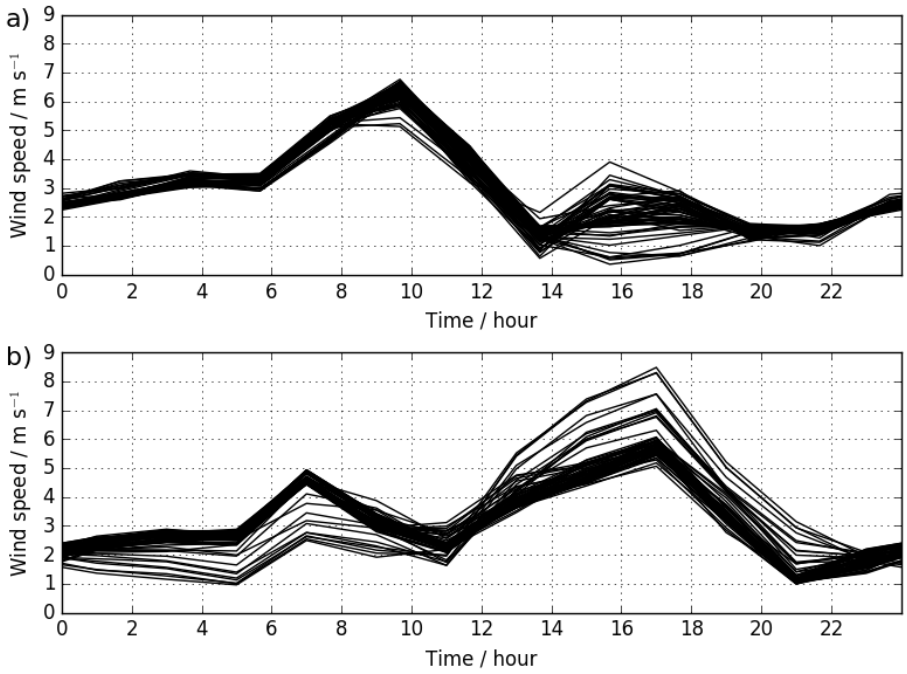

Figure 5.15: Near-surface wind speeds within individual gridboxes through the period L_S = 120-150°. Each plotted line corresponds to the varying wind speed through one sol (60 sols in total). a) gridbox centred on -12.5° N, 175° E, b) gridbox centred on 37.5° N, 75° E. Compare with panels a) and b) in Figure 5.10.

As described by this dust devil parameterisation scheme: the period of the sol during which there is a positive value of sensible heat at the planet's surface provides an envelope of time during which dust devils *can* form, but precisely *when* dust devils form within that timing envelope is governed by the instantaneous near-surface wind speed. Figure 5.18 shows how the wind speed and temperature difference terms of the parameterisation can vary globally, and highlights examples of the correlation between these terms and the resultant level of dust devil lifting.

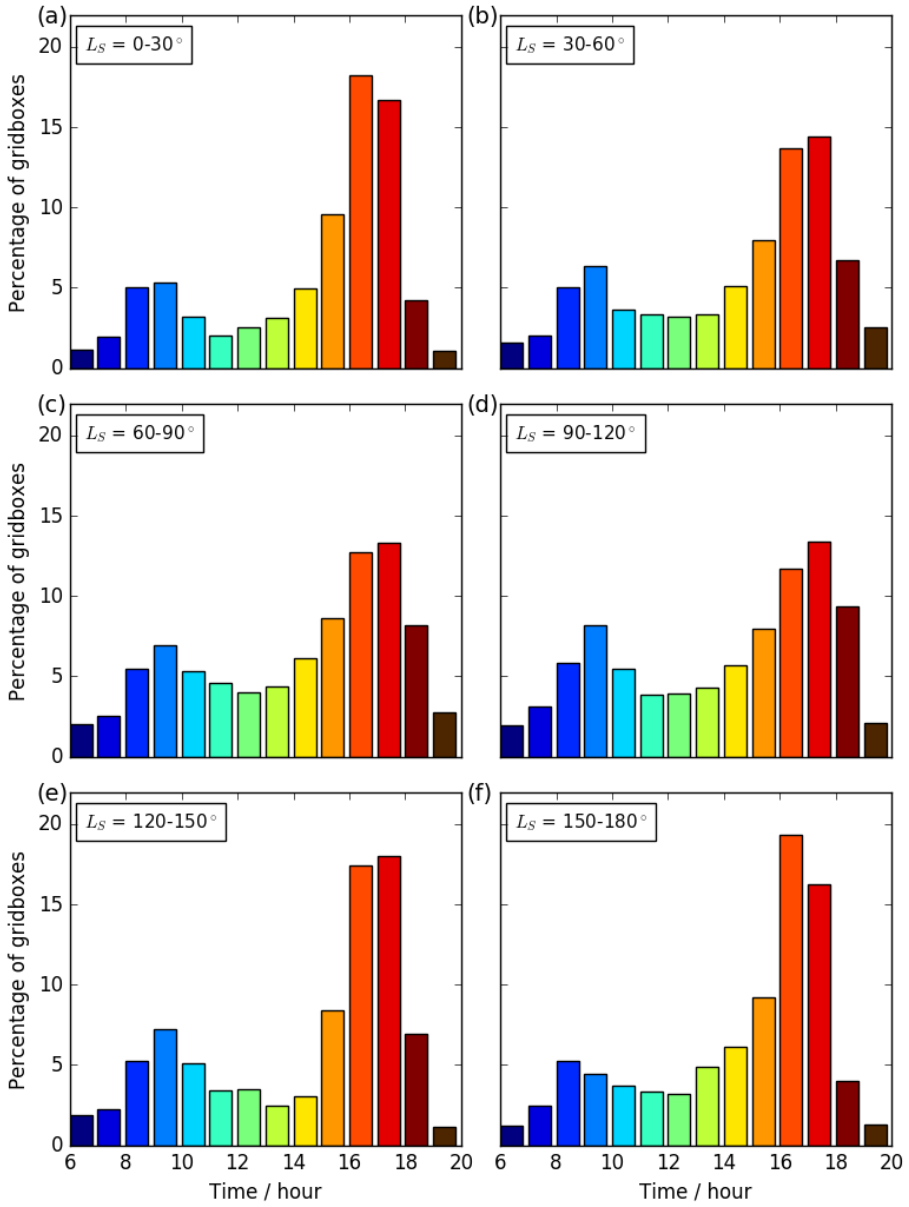

Figure 5.16: Histograms showing the diurnal timing of peak near-surface wind speeds as a percentage of all surface gridboxes, through L_S = 0-180°, split into 30° L_S sections. The colour scheme replicates the one used in Figure 5.1. A clear bimodal distribution in timings is evident in all panels.

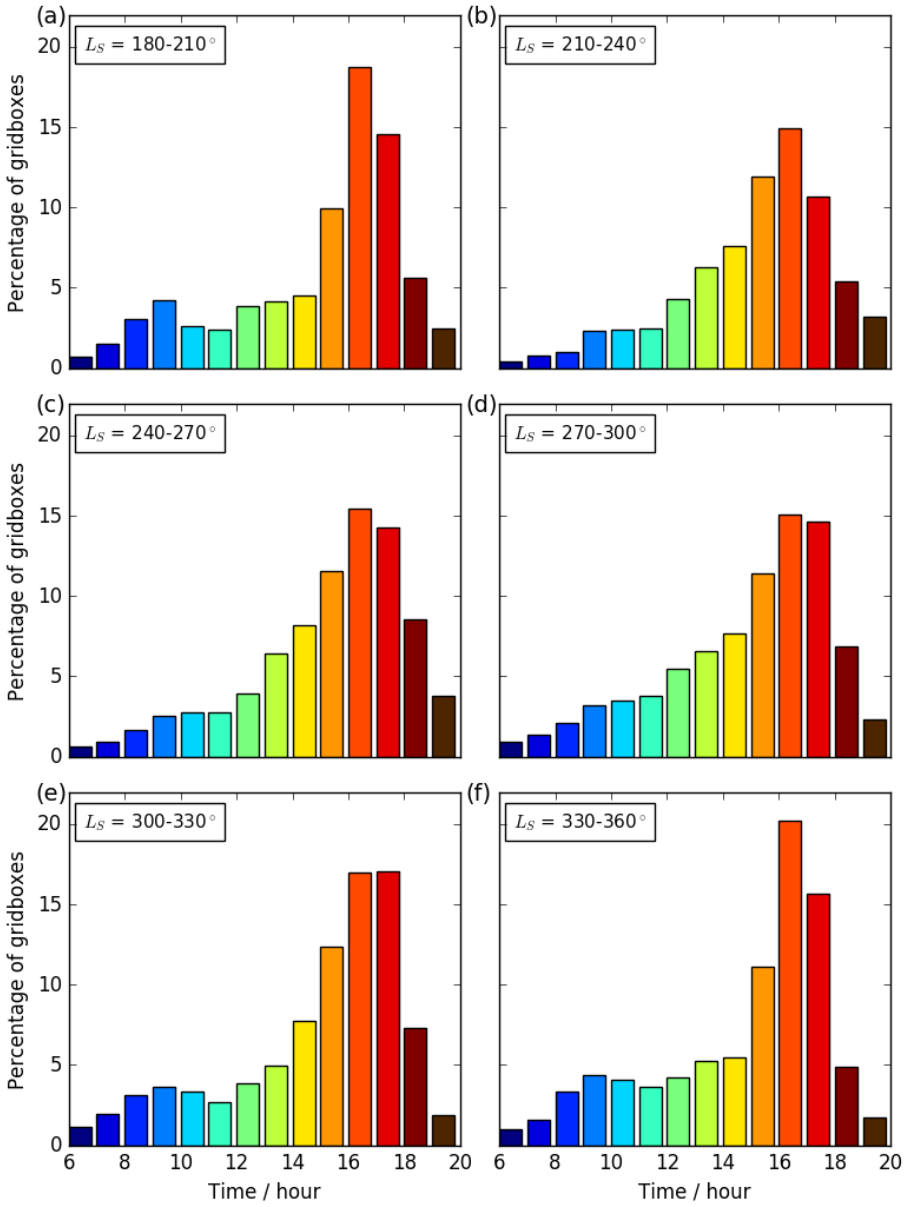

Figure 5.17: As Figure 5.16, for L_S = 180-360°. The periods spanning L_S = 210-300° tend towards a unimodal distribution, while a bimodal distribution is apparent in the other panels.

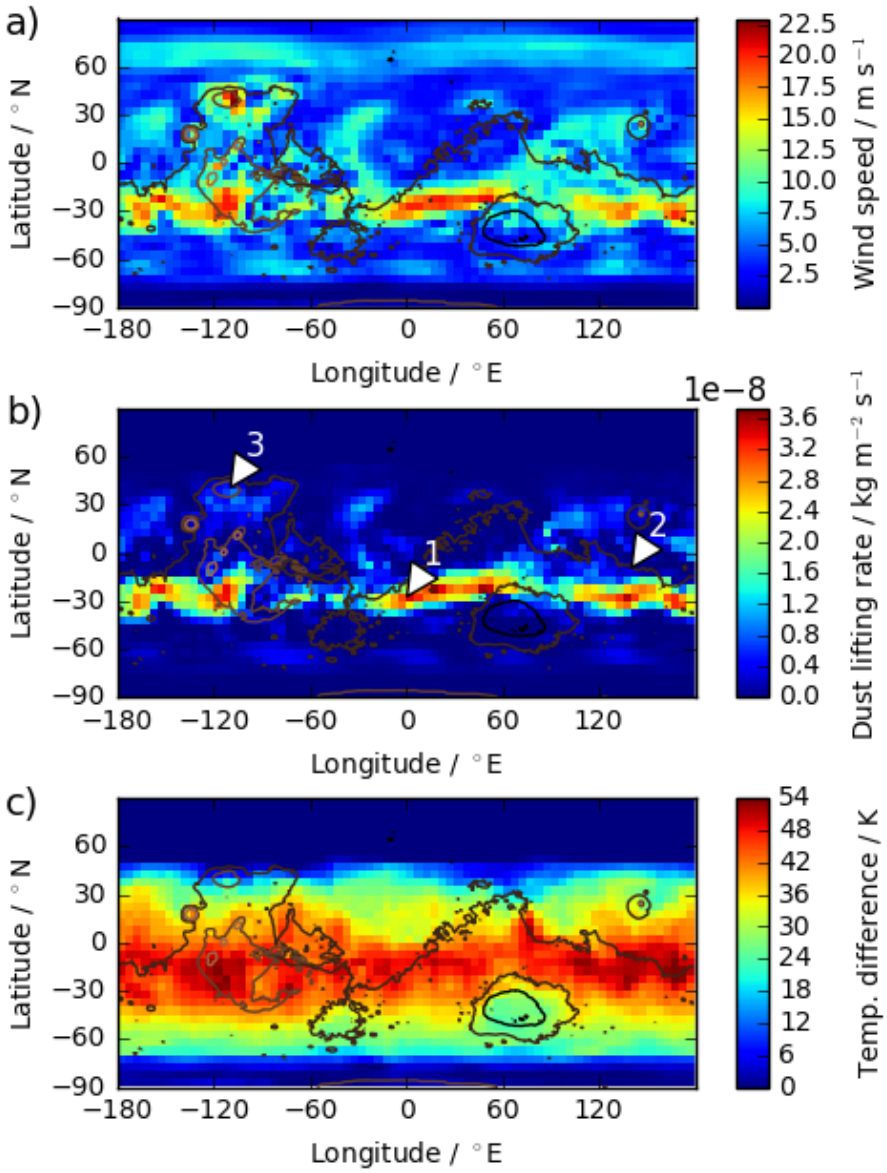

Figure 5.18: Global map of a) near-surface wind speeds, b) dust devil lifting and c) surface-atmosphere temperature difference, ($T_{\mathrm{surf}} - T_{\mathrm{atm}}$). All gridboxes are displayed at a local time of 13:00, providing a global picture of activity at one specific time of sol. Values have been averaged over L_S = 240-270°. Dust devil lifting is possible within the 'permitted' sensible heat envelope represented by ($T_{\mathrm{surf}} - T_{\mathrm{atm}}$) > 0, but only occurs at specific locations, as governed by wind speeds. Compare the locations labelled in panel b): 1. -28° N, 0° E (high temperature difference, high winds, high lifting), 2. -10° N, 140° E (high temperature difference, low winds, low lifting), 3. 40° N, -110° E (low temperature difference, high winds, low lifting).

5.4 Comparison With Observations

Validation for the model results was attempted through comparison with observations of Martian dust devils obtained from orbit and from the surface. Global plots and histograms were compared with orbital observations; more localised results were compared with surface observations.

5.4.1 Orbital Observations

There have been limited surveys of global dust devil diurnal variation using orbital observations. Some dust devil surveys are temporally constrained by the viewing angle provided by the platform: for example, surveys using Mars Global Surveyor (MGS) Mars Orbital Camera (MOC) images are restricted to a local time of 13:00-15:00 (*Cantor et al.*, 2006), limiting their use for investigations into the diurnal variability of any surface phenomena.

Stanzel et al. (2008) used Mars Express (MEx) High Resolution Stereo Camera (HRSC) images to complete a survey of dust devils and their characteristics. HRSC images span 06:00 to 20:00; all seasons of the year were included in the image survey, and the regions selected for scrutiny had been identified in earlier studies as 'active dust devil areas'. The study observed dust devils in images captured after 11:00, recorded a strong peak in dust devil numbers between 14:00 and 15:00, with a smaller peak between 12:00 and 13:00; it did not observe the morning peak in dust devil activity that is evident in the model results. However, it should be noted that the number of dust devils observed in orbital images is necessarily limited by the resolution of those images: Mars landers and rovers have observed many small dust devils that could not currently be seen from space (*Stanzel et al.*, 2006).

5.4.2 Surface Observations

Surface observations provide more information on the diurnal variation in dust devil lifting than can be gained from orbital observations. Direct investigations of Martian dust devils are still limited, but there are a number of studies which discuss pressure detections of atmospheric vortices. The two data types are not completely equivalent: although all dust devils are vortices, not all vortices en-

train dust. In analysing the model results, it was assumed that all Martian dust devils are similar in their dust lifting efficiency; i.e. the presence of more dust devils results in more dust being lifted, allowing a direct comparison between the number of vortices detected and the amount of lifted dust.

The dust devil activity reported in published studies using surface data can be compared with model results for specific locations on the Martian surface. The surface locations of the landers and rovers discussed in these studies are identified in Table 5.1 and Figure 5.19. For the shorter duration missions (Pathfinder and Phoenix), the studies reported on the full length of the mission; for the multi-year missions (Viking Lander 2 and Mars Exploration Rover Spirit), the studies covered only a portion of the whole mission. Of these comparison studies, only one reported on direct images of dust devils, while four used atmospheric vortice detections.

Lander	Lander location (latitude, ° N × longitude, ° E)
Viking Lander 2 (VL2)	47.97, 134.25
Pathfinder	19.33, -33.55
Phoenix	68.22, -125.70
MER Spirit	-14.61, 175.47
MSL Curiosity	-4.59, 137.44

Table 5.1: Locations of NASA landers, Mars Exploration Rover (MER) Spirit and Mars Science Laboratory (MSL) Curiosity.

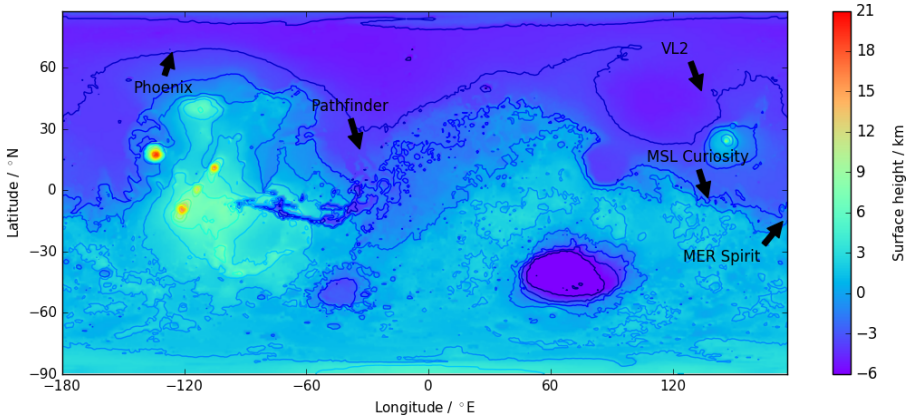

Figure 5.19: Map identifying approximate locations of landers listed in Table 5.1. Surface topography contours mark every 2 km of height.

Based upon the location of a lander or rover, an identification can be made of the gridbox that best correlates with that location. For each location, the diurnal cycle of modelled dust devil lifting is then compared with the published observations, taking into account the time of year at which the observations were captured, as well as the associated local atmospheric dust environment.

Dust devil lifting is affected by the amount of dust present in the local atmosphere primarily through its impact on surface and near-surface temperatures. Atmospheric dust absorbs incident solar radiation, resulting in a heating of the atmosphere and a reduction of surface insolation (*Zurek*, 1978). A high level of atmospheric dust, such as that observed during dust storms, will cause an increase in near-surface atmospheric temperatures and a decrease in (insolation-driven) surface temperatures. This reduces the surface-to-atmosphere temperature difference ($(T_{\mathrm{surf}} - T_{\mathrm{atm}})$ in Equation 5.1), which results in a reduced amount of surface-level heat available to drive dust devil formation.

The local atmospheric dust environment during a lander's observations can be approximated using the prescribed dust scenarios available within the MGCM (Section 3.4.2). If a dust map has been constructed for the year in which a mission took place (for example, the Phoenix mission landed in MY29), a simulation utilising that year's atmospheric dust loading scenario was used for the comparison analysis. For missions that took place before the earliest constructed dust map (MY24, beginning in July 1998), the modelled optical depth that would be reported at a point on the surface in the vicinity of a lander's position can be compared to the optical depth recorded by that lander during its observations. Experiments were completed utilising multiple dust loading scenarios; results from the closest matching simulation were then used for the analysis.

Figures 5.20 and 5.21 show the diurnal variation in dust devil lifting for each lander or rover location. The envelope encompassing all of the model results obtained through the analysed time period is shown in grey, the average is identified by a solid line. (The reader should note that the amounts of dust lifted across the different lander sites vary by two orders of magnitude).

Figure 5.20a shows modelled dust devil lifting in the vicinity of the VL2 landing site plotted against the left axis; data from the comparison study by *Ringrose et al.* (2003) are plotted against the right axis. The Viking mission

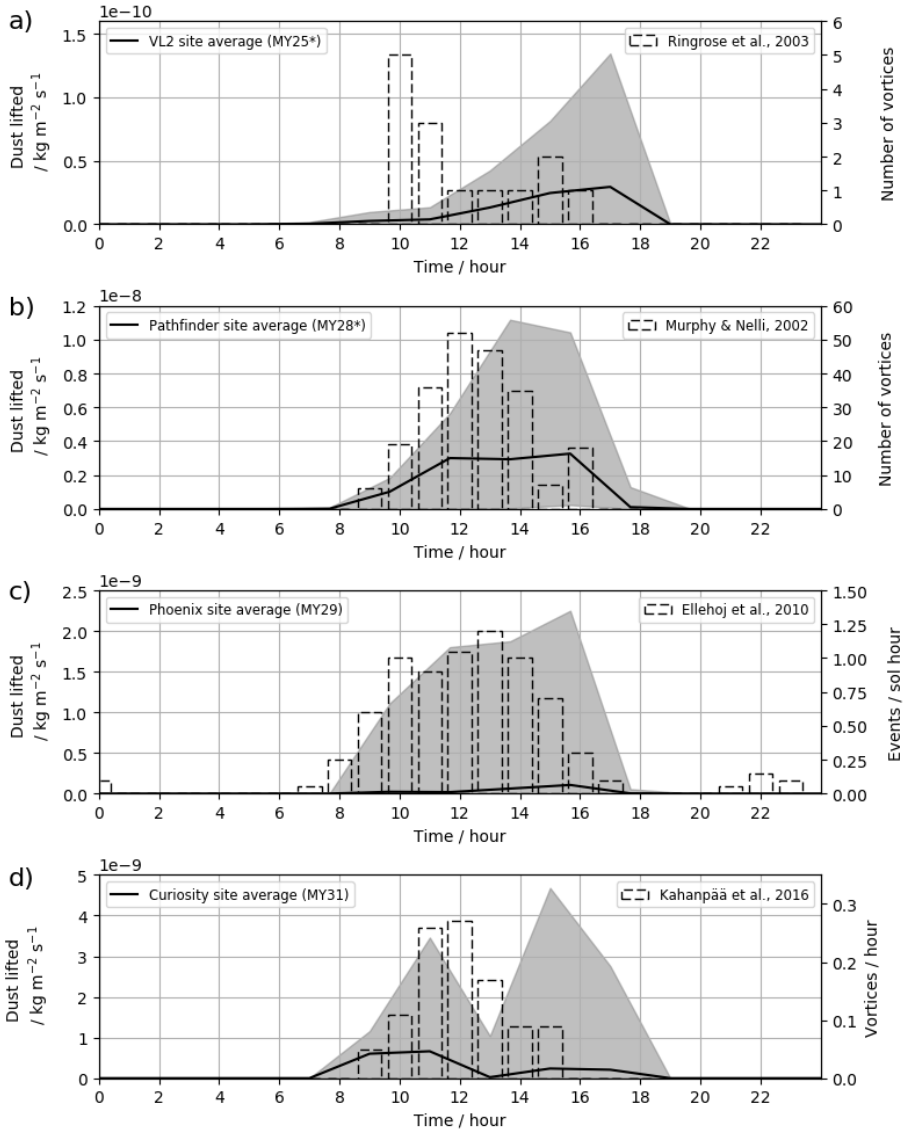

Figure 5.20: Hourly dust devil lifting in the vicinity of four lander/rover sites, plotted against the left vertical axes. For each site, the average is displayed as a black solid line, and the grey shading is the envelope of all model results from the relevant time period. Plot legend includes relevant atmospheric dust loading used in experiment; analogue years indicated with an asterisk, see main text for details. Plotted against the right vertical axes are data from the comparison studies: a) VL2 landing site results and data from *Ringrose et al.* (2003) (L_S = 117-148°); b) Pathfinder landing site results and data from *Murphy and Nelli* (2002) (L_S = 140-190°); c) Phoenix landing site results and data from *Ellehoj et al.* (2010) (L_S = 77-148°); d) MSL Curiosity site results and data from *Kahanpää et al.* (2016) (L_S = 157° MY31 to L_S =157° MY32). The landers' published dust devil rate is normalised to the availability of meteorological data.

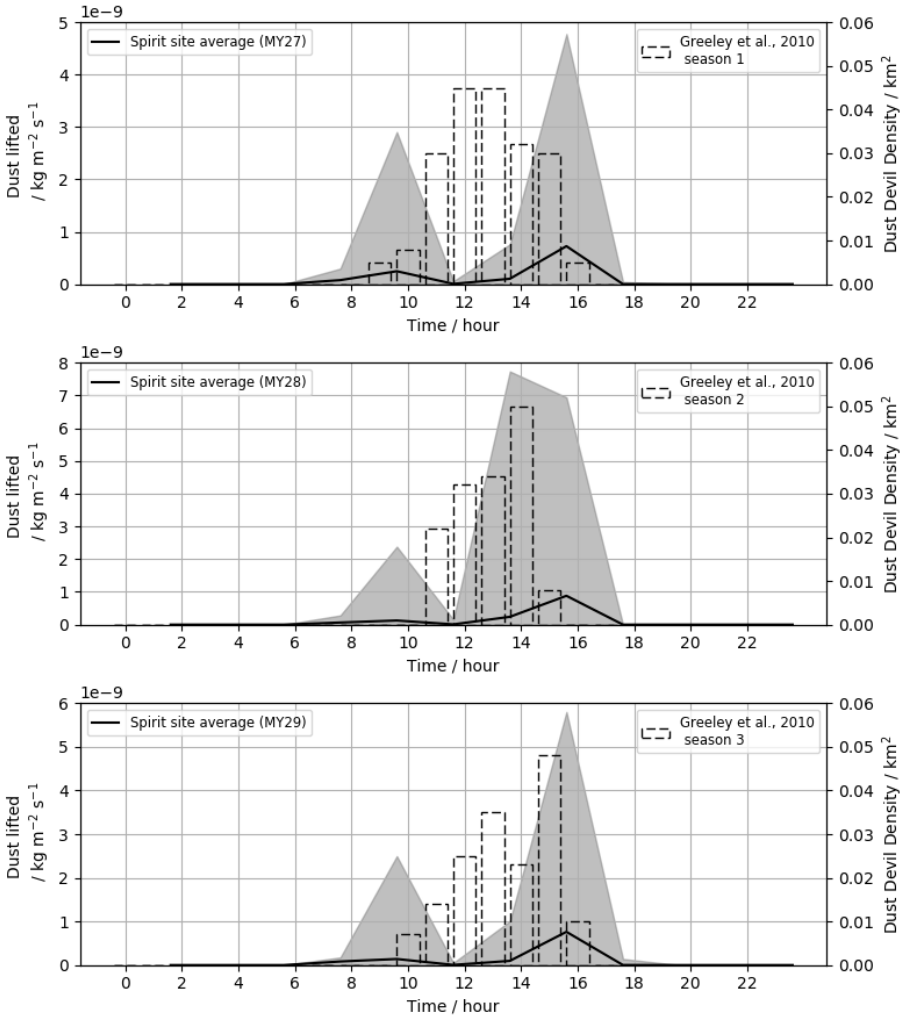

Figure 5.21: Hourly dust devil lifting in the vicinity of the MER Spirit site across the three Mars years considered, plotted against the left vertical axes. Each average (black solid line) is displayed, and the grey shading encompasses all results produced during the time periods (each L_S = 170-359°). Plotted against the right vertical axes are data from the comparison study by *Greeley et al.* (2010).

reached Mars during MY12, a year that experienced large dust storms and a subsequent high atmospheric dust loading. The visible optical depth observed at the VL2 landing site during the earliest portion of the mission (L_S = 117-148°) is reported as ∼0.3-0.4 (*Pollack et al.*, 1977; *Colburn et al.*, 1989). This is best matched by the visible optical depth simulated in this region at this

time of year in the MGCM simulation using the MY25 dust map; MY25 also experienced a large dust storm.

Figure 5.20b shows modelled dust devil lifting in the vicinity of the Pathfinder landing site plotted against the left axis; data from the comparison study by *Murphy and Nelli* (2002) are plotted against the right axis. The Pathfinder mission took place during MY23, L_S = 140-190°. The visible optical depth observed by the lander varied from ∼0.4 shortly after landing to ∼0.6 towards the end of the mission (*Smith and Lemmon*, 1999). The MGCM simulation using the MY28 dust field produces a visible optical depth of ∼0.5 in this region throughout the length of the mission.

Figure 5.20c shows modelled dust devil lifting in the vicinity of the Pathfinder landing site plotted against the left axis; data from the comparison study by *Ellehoj et al.* (2010) are plotted against the right axis. The Phoenix mission landed in MY29, operating through the period L_S = 77-148°.

Figure 5.20d shows modelled dust devil lifting in the vicinity of the Curiosity site through the first full year (668 sols) of the rover's operation plotted against the left axis; data from the comparison study by *Kahanpää et al.* (2016) are plotted against the right axis. MSL Curiosity landed in MY31, beginning its mission on L_S = 150°. This mission is still ongoing.

Figure 5.21 shows modelled dust devil lifting in the vicinity of the Spirit operational site plotted against the left axes; data from the comparison study by *Greeley et al.* (2010) are plotted against the right axes. The long duration of the MER Spirit mission enabled extended surface observations of dust devils, encompassing multiple years. The annual dust devil 'season' observed by the rover spanned the second half of the Martian year, $L_S \sim$ 175-355°. This study covers observations from three full dust devil seasons, spanning MY27-MY29.

The comparisons between modelled results and the observations reported in the aforementioned studies are detailed here and then summarised in Table 5.2.

Mission: Viking Lander 2, **Study:** *Ringrose et al.* (2003).

This study identifies 38 vortices in pressure data recorded during the first 60 sols of the VL2 mission. An afternoon peak in vortex numbers is observed, although it is seen in the early afternoon (13:00-13:30) rather than the anticipated mid-afternoon timing. A higher peak in vortex numbers is seen in the

morning (10:00-10:30). The study's authors comment on the morning peak, suggesting that it is not a peak in 'naturally generated' atmospheric phenomena; instead, at least some of these vortexes are likely to be a result of the local wind interacting with the body of the lander itself.

The averaged model results for this location show a diurnal dust devil distribution that more closely aligns with that expected by *Ringrose et al.* (2003): a peak during the late afternoon, around 17:00 (Figure 5.20a). Within the model results there is limited dust devil lifting during the morning, although some lifting is still evident before the afternoon peak. The match between the observations and model results is described as a 'partial match' in Table 5.2, following the suggestion by the study authors that up to four of the nine morning observations could be false positives.

Mission: Pathfinder, **Study:** *Murphy and Nelli* (2002).

This study used pressure data to identify 79 vortices passing over or near the lander. The pressure data was recorded through the full length of the Pathfinder mission: $L_S = 142\text{-}183°$. A peak in vortex numbers is identified around midday, between 12:00 and 13:00.

The averaged model results for this location show a relatively flat 'plateau' of afternoon dust devil lifting between 12:00 and 16:00 (Figure 5.20b). However, the envelope displaying all the results for this location shows a diurnal distribution that is similar in shape to the distribution identified by *Murphy and Nelli* (2002), with the peak of the curve shifted approximately one hour later in the sol. This comparison is considered a good match.

Mission: Phoenix, **Study:** *Ellehoj et al.* (2010).

This study identifies 502 "probable" vortices from drops in pressure data that was recorded through the length of the Phoenix mission. The analysis by *Ellehoj et al.* (2010) of these vortices is split into those that occurred during the period $L_S = 77\text{-}111°$, and those that occurred during the period $L_S = 111\text{-}148°$; this split arises from the authors' observation that the 'dust devil season' at the lander location began around $L_S = 111°$. In the period outside the dust devil season (prior to $L_S = 111°$), vortex observations peak around 12:00. During dust devil season ($L_S = 111°$ onwards) the observed dust devil distribution appears to show two peaks: one in the morning, around 11:00, and one in the

afternoon, around 13:00. *Ellehoj et al.* (2010) suggest that the true peak in the distribution is around 12:00, and that the apparent bimodality in the data is due to an operational, rather than meteorological, effect: there is a repeated gap in observations every sol during the mission (∼30 minutes around mid-sol) when the lander paused operations to complete data transfer.

The averaged model results for this location show a peak in dust devil lifting around 16:00 (Figure 5.20c). The averaged values are extremely low, caused by an extended section of the 'outside dust devil season' period containing zero modelled dust devil lifting. The observed increase in dust devil activity that is used by *Ellehoj et al.* (2010) to identify the start of the dust devil season is not evident in the model results until $L_S \approx 144°$; the majority of the model results shown in Figure 5.20c occurred through the period L_S = 144-148°. While these results therefore cover a limited period of time, the diurnal distribution is very similar in shape and timing to the observed distribution, albeit including a small spike around 16:00 that is absent from the observed data, and is considered a good match.

Mission: MSL Curiosity, **Study:** *Kahanpää et al.* (2016).

This study identifies 252 vortices in pressure data recorded during the first full year of the Curiosity rover's mission: 668 sols from $L_S = 157°$ MY31 to $L_S = 157°$ MY32. A peak in vortex numbers is observed between 11:00 and 13:00.

The averaged model results for this location show a bimodal distribution of dust devil lifting, with activity peaking in both the morning and the afternoon (Figure 5.20d). The modelled morning peak, around 11:00, is an hour ahead of the peak in the observed data, but is similar in shape. Afternoon observations identify some vortices, but the modelled peak in the afternoon does not occur in the observations. This comparison is considered a partial match.

In order to complete a thorough survey, the MSL Curiosity study by *Steakley and Murphy* (2016) on vortex activity at Gale crater was also considered for comparison with the model results. *Steakley and Murphy* (2016) identify 245 vortices in pressure data captured through the first 707 sols of the mission; as the reported diurnal variation within these observations is a close match to that reported by *Kahanpää et al.* (2016), only the latter study is used in this

comparison.

Mission: MER Spirit, **Study:** *Greeley et al.* (2010).

This study identifies dust devils within images captured by the Spirit rover. Three local dust devil seasons were imaged, each of which began around $L_S = 181°$. Imaging during the latter two seasons was more limited than during the first season due to power considerations; later observations were inhibited by the rover's locations being less favourable for viewing dust devils, and were also truncated by the arrival of a local dust storm (in the second season). The diurnal distributions of dust devil observations in this multi-year survey are varied: season 1 (502 observed dust devils) shows a broad peak in 'dust devil density' between 12:00 and 14:00, season 2 (101 observed dust devils) shows a narrower peak between 14:00 and 15:00, and season 3 (127 observed dust devils) shows a small early-afternoon peak, between 13:00 and 14:00, and a larger peak later in the afternoon, between 15:00 and 16:00.

The averaged model results for this location do not show the same variation: the distributions are similar across the three modelled years that match the observed seasons, and all three display a bimodal distribution in dust devil lifting. In all three years the results envelopes show a small peak in the morning, consistently between 09:00 and 10:00, and a larger peak in the afternoon, with a maximum between 13:00 and 16:00. Year 1 results are not considered a good match with the study's season 1: although *Greeley et al.* (2010) do identify dust devils during both the morning and afternoon periods encompassed by the results envelope, the modelled results do not reproduce the mid-sol peak of the observations. Year 2 results are a closer match to the study's season 2, showing a broader afternoon peak spanning 13:00 to 16:00, while observations peak between 14:00 and 15:00. Year 3 results are a partial match with season 3: again, the results do not reproduce the observed mid-sol activity, but results and observations match closely on the timing of the afternoon peak.

Lander/rover site	MGCM results	Observation results	Comment on match
VL2	Strong afternoon peak (17:00)	Strong peak 10:00-11:00, second peak 15:00-16:00	Partial match: morning lifting present but limited, afternoon lifting late
Pathfinder	Strong afternoon peak (14:00)	Strong peak 12:00-13:00	Good match in shape of distribution, timing similar
Phoenix	Broad span, sharp peak around 16:00	Broad span, peaking 13:00-14:00	Good match to timing of distribution
MER Spirit	Morning and afternoon peaks	Peak spanning mid-sol	Minimal match: mid-sol peak not seen
		Mid-afternoon peak 14:00-15:00	Good match: afternoon lifting encompasses most observations
		Mid-sol lifting, afternoon peak 15:00-16:00	Partial match: mid-sol peak not seen but afternoon peak matches observations
MSL Curiosity	Late morning (11:00) and mid-afternoon (15:00) peaks	Strong peak 11:00-12:00	Partial match: morning peak early, afternoon lifting greater than observed

Table 5.2: Summary of MGCM dust devil lifting results and dust devil observations from the comparison studies, with comment on the match of results to observations. Reproduced from *Chapman et al.* 2017.

The model results are not always a good match with the relevant lander/rover study, but there are at least four caveats to consider:

1. The resolution at which the simulation was completed results in gridboxes that cover several hundred square kilometres in area. The data produced in such a simulation relate to quantities present in these large-scale gridboxes, not at specific local points upon the surface. The locations used in the above comparisons provide the closest possible correlation to the lander/rover sites. (MSL Curiosity, in particular, is in the deep Gale Crater; atmospheric circulations within a crater can vary considerably from large-scale circulations outside the crater, e.g. *Tyler and Barnes* 2015.)

2. Studies that use pressure data can only detect vortices, and not all vortices will necessarily entrain dust. Therefore any survey that draws a direct parallel between the number of vortices and the number of dust devils may over-estimate the dust devil population.

3. The study using image data was sometimes impacted by a restricted field of view (rover camera pointing and the local topography) and by the mission's reduced data capture abilities (rover power considerations).

4. The model provides a value for the rate of dust lifting by dust devils, but this lifting rate contains no information on either the number or the size of the dust devils that would be required to lift such an amount of dust.

5.5 Discussion and Summary

The results of this investigation show that, within MGCM simulations, dust devil activity displays a wider than anticipated diurnal range. More dust is lifted by dust devils during morning hours than was anticipated previously (i.e. following terrestrial observations, see Section 5.1), and many locations actually experience a peak in dust devil activity before mid-sol, rather than activity consistently peaking in the afternoon. There are two possible explanations for these results:

- the dust devil parameterisation developed for use in MGCMs does not provide a good representation of diurnal Martian dust devil behaviour;

- the accepted description of dust devil behaviour on Mars is not complete.

The model results presented herein suggest that the MGCM dust devil parameterisation *does* provide a good representation of Martian dust devil activity throughout the sol. As described in Section 5.4.2 and summarised in Table 5.2, the model results are a reasonably good match to published studies of Martian dust devil observations. All of the comparison studies report observations of dust devils (or the proxy measure: pressure vortices) during morning hours. The observed maximum in dust devil activity is usually after mid-sol, but there is a range in the timing of that peak in the studies. Across the seven comparisons made with the published studies (counting each of the three seasons in *Greeley et al.* (2010) separately), three show a good match between modelled results and observations, three show a partial match, and one shows a minimal match. These studies comprise the majority of investigations into Martian dust devils using surface observations, from which diurnal timing information can be extracted.

Studies that use orbital observations to survey Martian dust devils have not identified a high level of dust devil activity during morning hours. These studies are few in number, and it should be noted that the reported diurnal distribution of dust devils as observed from orbit is not a good match to the majority of surface observations. Images used for such surveys are often temporally constrained by spacecraft positioning (*Fisher et al.*, 2005; *Cantor et al.*, 2006), rendering them of limited use for a study into the diurnal variation of surface or atmospheric phenomena. Images captured from orbit also enforce a bias towards the observation of large dust devils, and so the surveys may not accurately capture the full dust devil population (*Stanzel et al.*, 2008).

If the parameterisation is a good representation of dust devils, then it is proposed that the generally accepted description of dust devil behaviour on Mars is incomplete. Assumptions of Martian dust devil behaviour are based upon observations of terrestrial dust devils, and the dust devil parameterisation within the MGCM was designed to reproduce the terrestrially observed diurnal pattern. However, Martian dust devil activity does not necessarily peak in the early afternoon, and local wind speeds may act as a strong governor of the timings of dust devils.

The dust devil parameterisation in operation within the MGCM has been used as the basis for similar parameterisations in the NASA Ames Mars GCM and the GFDL Mars GCM. Parameterised dust devil activity depends upon the sensible heat available to the dust devil and its thermodynamic efficiency. This thermodynamic efficiency (i.e. how readily it converts the available heat into work) is driven by the depth of the local CBL, which in turn is driven by atmospheric heating due to insolation and thus follows a predictable diurnal pattern. Most of the parameters used to calculate the sensible heat flux available to the dust devil also follow predictable diurnal patterns; the only exception is the near-surface wind speed. It is the variability within the near-surface wind speed that introduces variability into the diurnal timings of dust devils.

The near-surface wind on Mars arises from a complex interaction of local and large-scale influences, affecting both the magnitude and direction of the resulting flow. Global-scale diurnal thermal tides are driven by solar heating; local variations in surface properties affect the smaller-scale flow of such tides (*Wilson and Hamilton*, 1996). Surface thermal properties (e.g. variations in albedo and thermal inertia) have a changing effect on the flow of local-scale winds throughout the diurnal heating cycle (*Read and Lewis*, 2004), and variations in topography give rise to slope winds (upslope during daylight hours and downslope during the night). Interactions between these locally-forced winds and other large-scale, regional circulations (e.g. lower-level Hadley circulation) add to the complexity (*Toigo and Richardson*, 2003).

Observations of the wider meteorological context within which terrestrial dust devil arise suggest that mild ambient winds must be present for the initiation of dust devils, but that high winds may inhibit their formation. (*Sinclair* (1969) observed dust devil numbers decreasing as wind speeds increased; *Oke et al.* (2007) reported the presence of dust devils only when ambient wind speeds were between 1.5 and 7.5 $\mathrm{m\,s^{-1}}$; *Kurgansky et al.* (2010) observed more dust devils when wind speeds were between 2 and 8 $\mathrm{m\,s^{-1}}$ than otherwise.) One proposal is that any convective vortices beginning to form in high wind conditions will suffer a destructive shearing of the upper portion of the vortex from the lower portion due to the wind speeds present (*Oke et al.*, 2007); models of terrestrial dust devil populations have found that the level of dust devil activity

can be curbed using increasing wind speeds (*Lyons et al.*, 2008; *Jemmett-Smith et al.*, 2015).

In comparison, observations have been made of Martian dust devils travelling at speeds considerably faster than those achieved by terrestrial dust devils. Martian dust devils have been observed travelling in the direction of the ambient wind (*Stanzel et al.*, 2008; *Reiss et al.*, 2014b) at horizontal speeds of around 27 $\mathrm{m\,s^{-1}}$ calculated using surface observations (*Greeley et al.*, 2010), and up to 59 $\mathrm{m\,s^{-1}}$ calculated using images captured from orbit (*Stanzel et al.*, 2008). High resolution numerical simulations of Martian dust devils (*Toigo et al.*, 2003) were able to form dust devils either in 'no wind' or 'high wind' scenarios, but did not produce dust devils in low or medium wind scenarios. Such observations and modelling may indicate that ambient wind speeds are another aspect of terrestrial dust devil theory that cannot be transposed directly to the Martian environment: limited *in situ* data are currently available from which to assess Martian near-surface wind speeds (*Balme et al.*, 2012), but if there is a systematic inhibition of dust devil formation on Mars due to high ambient wind speeds, it must occur at much higher speeds than those curbing terrestrial dust devils.

Theories of dust devil formation should be further developed, or perhaps need to be tailored specifically, to be applicable to an environment in which vortices form in a thin, cold atmosphere over a desert covering the entire surface of a planet. *Ringrose et al.* (2003) remark that Martian dust devils could form earlier in the diurnal cycle than the terrestrial counterpart due a combination of the lower dry adiabatic lapse rate within the Martian atmosphere and a higher thermal efficiency of convective plumes on Mars, somewhat complementing an analysis of terrestrial dust devils in which a modelled lower lapse rate widened the diurnal range of potential dust lifting activity (*Jemmett-Smith et al.*, 2015). It has also been suggested that dust devils may be "systematically more common" within low pressure environments (*Lorenz and Radebaugh*, 2016).

Recent parameterisations of terrestrial dust lifting have had some success, such as the Convective Turbulent Dust Emission (CDTE) parameterisation of *Klose and Shao* (2013), which uses statistical distributions of wind stress in

Large Eddy Simulations (LES) to describe the stochastic nature of convective dust lifting phenomena. The CDTE parameterisation has been tested against observations of dust lifting in China and Australia, and has been successful in predicting the diurnal periods of dust lifting in the tested regions, as well as the amount of dust lifted. Dust lifting by large eddies may also be an important phenomena on Mars (e.g. *Spiga et al.*, 2010); however, terrestrially-based parameterisations such as CDTE include consideration of soil moisture and vegetation, and are tailored to a particle size distribution that is representative of Earth soils (*Klose et al.*, 2014). Such a parameterisations would have to be modified carefully for application within the Martian environment.

While an improvement of dust devil theory is necessary, it is also possible that the parameterisation needs improvement. For example, consider the input heat source driving the dust devil 'heat engine' model. On Earth the sensible heat flux is a large factor in the total surface energy budget (*Larsen et al.*, 2002), and so within models of terrestrial dust devils this flux is the dominant heat source driving their formation (e.g. *Koch and Rennó*, 2005). In contrast, the lower density of the Martian atmosphere means that the surface energy budget calculation on Mars is dominated by radiative fluxes (*Petrosyan et al.*, 2011). It follows that a truly accurate Martian dust devil parameterisation may need to incorporate a more complex representation of the amount of heat available at the Martian surface-atmosphere boundary for dust devil formation.

Chapter 6

Case Study: ExoMars EDM Landing Site

6.1 Introduction

The European Space Agency (ESA) ExoMars 2016 mission to Mars included the ExoMars Entry Demonstrator Module (EDM) Schiaparelli. This module descended through the Martian atmosphere on 19th October 2016. Unfortunately the landing was not successful and Schiaparelli did not return any data from the surface. The module did, however, transmit data during its descent: data captured by engineering sensors and telemetry data from the module's guidance, navigation and control system. By combining data on the module's reported speed and attitude with dynamic modelling of its motion through the atmosphere, the ExoMars AMELIA (Atmospheric Mars Entry and Landing Investigations and Analysis) team (*Ferri et al.*, 2012) have been able to reconstruct the EDM's trajectory during most of the entry and descent phase of the mission (*Aboudan et al.*, submitted).

Following this reconstruction, the AMELIA team have retrieved profiles of atmospheric density, temperature and wind speed (*Ferri et al.*, 2012, 2017; *Aboudan et al.*, submitted). These profiles extend from ∼104 km to ∼2.8 km above the average MOLA radius (as the landing site is 1.44 km below this average radius, the profiles cover ∼105 km to ∼4.2 km above the Martian surface)

and span a time period of approximately 3 minutes, ending at around 13:00 local time. The descent took place during the Southern Hemisphere summer, at 244.4° L_S.

This chapter investigates the EDM's descent trajectory as a case study assessing how results from MGCM experiments compare with spacecraft data; of particular interest are the behaviours of low-level wind speeds.

Results from mesoscale model experiments are included for further comparison. Previous comparisons of global-scale and mesoscale modelling have focused largely on areas containing small-scale topographical variations that are not present in the global scale models (e.g. *Rafkin et al.*, 2001; *Kass et al.*, 2003; *Toigo and Richardson*, 2003; *Michaels et al.*, 2006). This work considers the relatively flat topography of the Schiaparelli site – a location that is more representative of the majority of historical Martian landing sites than areas that contain severe, small-scale topographical variation.

Section 6.2 outlines the spacecraft data and identifies the models used in this research. In Section 6.3 the results of modelling experiments are presented and compared with spacecraft data: atmospheric temperature and density vertical profiles (Section 6.3.1), wind speed vertical profiles (Section 6.3.2) and surface-level dust lifting processes (Section 6.3.3). In Section 6.3.4 the discrepancies in the results obtained from the different-scale models are discussed. Section 6.4 summarises this work and details recommendations.

6.2 Data Sources and Method

6.2.1 Spacecraft Data

The EDM crashed near the edge of its planned landing ellipse in Meridiani Planum: –2.05° N, –6.2° E. Figure 6.1 shows this location on a global map; Figure 6.2 shows a closer view of the landing ellipse (*Pacifici et al.*, 2014) and illustrates the terrain of the local environment.

Figure 6.3 shows the spacecraft's reconstructed trajectory from an altitude of ∼100 km down to the surface. Data are missing for the central portion of this trajectory due to the transmission blackout caused by the plasma sheath that

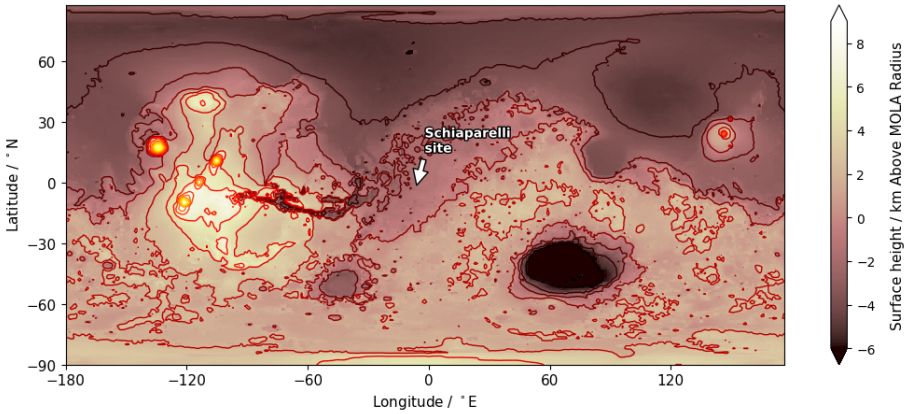

Figure 6.1: EDM Schiaparelli planned landing site.

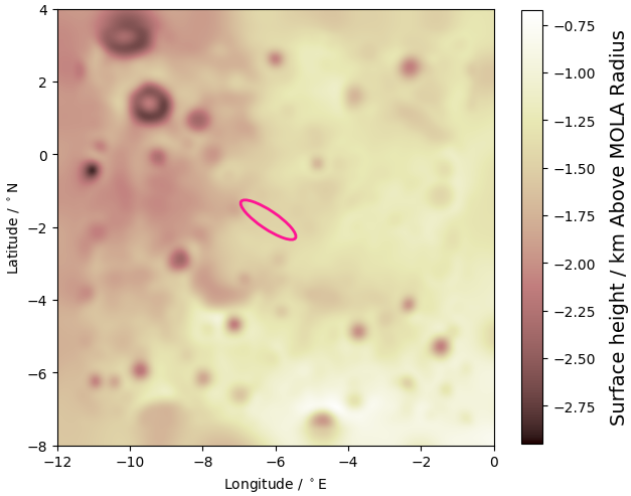

Figure 6.2: EDM Schiaparelli planned landing ellipse in Meridiani Planum.

develops around spacecraft during descent into an atmosphere. This portion of the descent, and the final few kilometres, have therefore been interpolated. The trajectory shown here was used to identify the model gridboxes from which to extract the vertical profiles for data comparison.

The calculated profiles for atmospheric density and temperature were provided by members of the AMELIA team; these profiles include raw data for the regions outside the plasma blackout and interpolated data through the missing portion of the trajectory. The raw data covers descent altitudes of 104-68 km

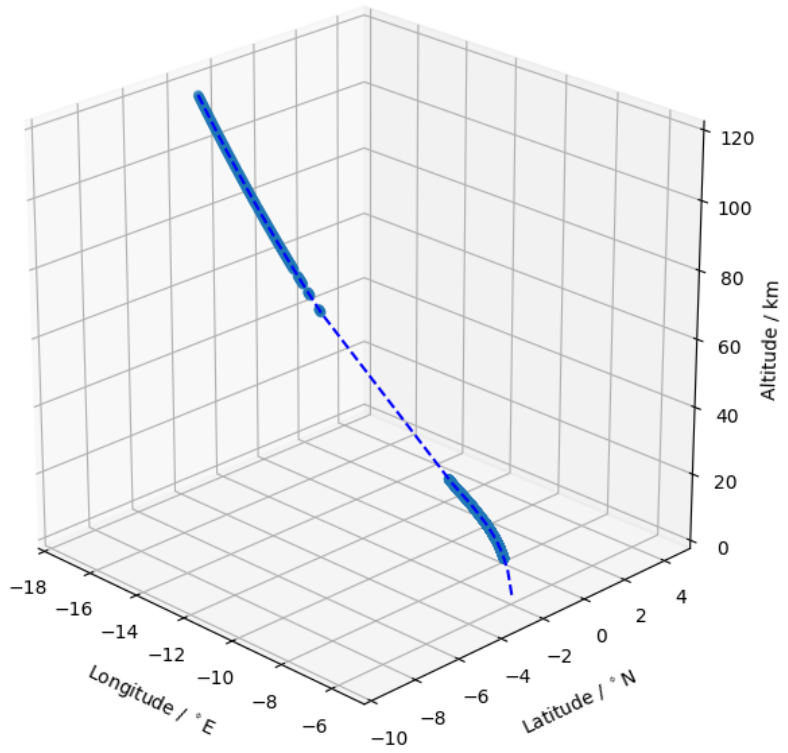

Figure 6.3: Reconstructed descent trajectory of the EDM, from an altitude of 100 km down to the surface. Markers indicate points in the descent for which data has been retrieved; dotted lines indicate portions of the trajectory that have been extrapolated.

Above MOLA Radius (AMR)[1] above the blackout (although this data coverage is patchy between ∼79-68 km AMR) and 30-2.8 km AMR below the blackout. The AMELIA team also produced smoothed profiles (see later figures) by iteratively interpolating the raw data (*Aboudan et al.*, submitted).

Data on wind speed and direction were reconstructed by the AMELIA team using the motion of the EDM during parachute descent (*Ferri et al.*, 2017; *Aboudan et al.*, submitted). These profiles only encompass altitudes 8.4-2.8 km AMR.

[1] Altitudes within this chapter will be given as a height Above MOLA Radius (AMR) for ease of comparison with the spacecraft data source documents.

6.2.2 Models

The MGCM used in this work is that described previously (see Chapter 3). The mesoscale model used is the LMD Martian Mesoscale Model (MMM), as described by *Spiga and Forget* (2009). The subroutines governing physical processes within the MMM are the same as those used within the MGCM; the dynamical core is based on the National Center for Atmospheric Research (NCAR) Advanced Research Weather Research and Forecasting (AR-WRF) model (*Skamarock and Klemp*, 2008). For the experiments discussed herein, initial and boundary conditions for the MMM simulations were constructed from an MGCM results file (see Section 6.3.1 for comments on the selected MGCM file).

MMM simulations can be completed using a single resolution domain or a configuration of nested domains, in which each domain has a higher spatial resolution than the one outside it. The size of the area to be modelled within an experiment is set through selection of the horizontal resolution and the number of gridpoints. The MMM experiment used in this work contained three nested domains operating with one-way feedback, meaning that outer domains affect inner domains but the reverse is not true. While two-way nesting has been shown to produce more accurate results in areas that include complex features (*Urrego-Blanco et al.*, 2016), this is dependent on the specific nesting technique implemented (*Soriano et al.*, 2002), and one-way nesting is considered sufficient for short-term simulations in less complex areas (*Qi et al.*, 2018). As simulations involving two-way feedback are also more computationally expensive the decision was taken not to use the method in this work.

While the MGCM parameterisations of the dust cycle were ported into the MMM during its development, the representation within the model of the processes involved in this cycle, including surface dust lifting, has not been explored before now (*Spiga and Forget*, 2009; *Spiga and Lewis*, 2010). The MMM experiment analysed in this chapter includes surface dust lifting through both near-surface wind stress (NSWS) and dust devils, and compares these results with those of MGCM experiments.

In order to place the EDM data in a wider climatological context, the space-

craft data are also compared against data extracted from the Mars Climate Database (MCD). The MCD is a freely available database of Martian meteorological fields and statistics constructed from the results of multiple, long-term climate simulations completed using GCMs (both the LMD and UK versions) and validated against observations (*Lewis et al.*, 1999; *Millour et al.*, 2015; *Forget et al.*, 2015).

Model Resolutions

Figure 6.4 shows vertical profiles of atmospheric temperature data extracted from MGCM experiments that were completed at different horizontal and vertical resolutions; refer back to Section 4.2 for more detail on specific MGCM resolutions.

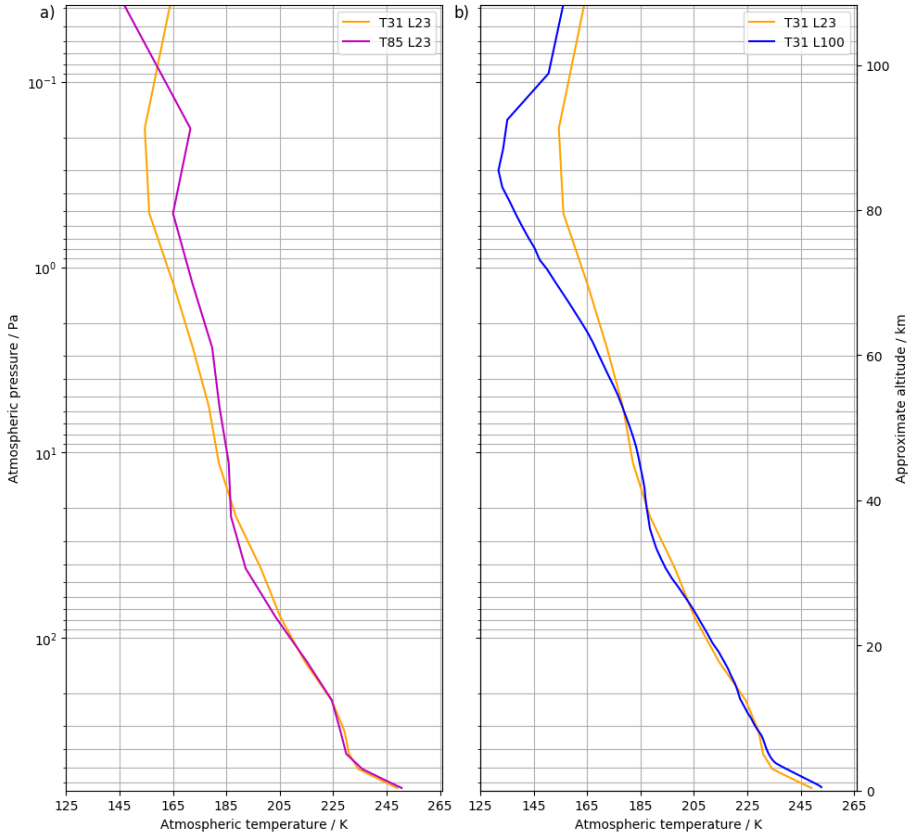

Figure 6.4: Vertical profiles of atmospheric temperature from MGCM experiments completed at different resolutions: a) varying horizontal resolution, b) varying vertical resolution.

As noted in Chapter 4, analysing the high-altitude variations between model resolutions is beyond the scope of this research (although these variations should be noted for future work involving high-level atmospheric processes). This study shall focus primarily on atmospheric behaviour at lower altitudes; practically speaking, this restricts direct comparisons with EDM data to altitudes below ∼30 km, i.e. below the plasma blackout region.

Figure 6.4a shows the vertical profiles taken from MGCM experiments completed at two horizontal resolutions: T31 and T85 (both using 23 vertical layers). While Chapter 4 concluded that the typical 'climate modelling' resolution of T31 was not sufficient when studying surface-level processes, it appears that for a vertical profile of atmospheric temperature taken along the EDM's trajectory at this point in the Martian year, there is little variation in results obtained using different horizontal resolutions. The Root Mean Square Deviation (RMSD) between the T31 results and the T85 results is 5.52 K; in the region below 30 km altitude this decreases to 2.51 K. This similarity across resolutions was expected to a certain extent, as the area chosen for the EDM's landing zone is relatively flat and level at the scales of these model resolutions.

Figure 6.4b shows the differences in the vertical profiles taken from T31 experiments completed at multiple vertical resolutions: 23 vertical layers (L23) and 100 vertical layers (L100). The RMSD between the L23 results and the L100 results is 11.69 K, which decreases to 4.50 K when only the region below 30 km altitude is considered.

Given the similar shapes and small RMSD values of these atmospheric temperature profiles, and the fact that the spacecraft data are reported at a high vertical resolution, results from a T31L100 experiment are used for comparison with the EDM atmospheric profile data in the following work. The data selected for analysis are six vertical profiles, each relating to a different sol within 4° L_S (around 6 sols) of the descent date of the EDM. The precise timings of these profiles range from 12:25 to 13:40, while the EDM descended at a local time of 13:00. This spread of profile timings was initially selected on the basis of the available data outputs and then examined for any identifiable progression with time. It was found that the variability in the data across the hour-long timeslot was comparable to the variability between sols, and these profiles are thus used

confidently as a representative set of vertical profiles at the time of the EDM's descent. The profiles extend from the surface up to an altitude of ∼100 km. With regards to surface-level processes, a higher horizontal resolution MGCM experiment was considered: a T85L25 experiment. The rationale for this choice is explained in Section 6.3.3.

The MMM experiment used in this work involved three nested domains of increasing resolution. The data used in the following analysis are from five vertical profiles taken from five consecutive days within 4° L_S of the descent date of the EDM; the profiles all relate to a local time of 1336 (the MMM outputs data every hour, timed from midnight at the meridian). The profiles extend from the surface up to an altitude of ∼50 km.

Table 6.1 summarises the model resolutions used in this work.

Model		Vertical layers, extent in altitude	Gridbox resolution at –2° N / km
MGCM			
	T31L100	100, ∼100 km	296 × 296
	T85L25	25, ∼100 km	111 × 111
Mesoscale		60, ∼50 km	
	Domain 1		63 × 63
	Domain 2		21 × 21
	Domain 3		7 × 7

Table 6.1: Model resolutions used in this research.

6.3 Results and Discussion

6.3.1 Atmospheric Temperature and Density Profiles

An initial atmospheric temperature comparison is shown in Figure 6.5, in which profiles from a number of climate scenarios and atmospheric dust loadings available within the MCD are shown against the EDM raw and smoothed data. For clarity, the multiple profiles extracted from the MCD have been split across two panels: broadly, profiles that are a good match to the EDM data have been plotted on the left (Fig. 6.5a) and profiles that are not a good match to the EDM data have been plotted on the right (Fig. 6.5b). The profiles that are not such a good match to the spacecraft data include those drawn from scenarios that utilise a high atmospheric dust loading – such as the dust storm scenario, the MY25 scenario (a year that experienced a global dust storm), and a dusty non-storm atmosphere (the 'Warm' scenario), which all exhibit high optical depths of $\tau \gtrsim 2$ in this region during southern summer months – as well as the 'Cold' scenario, which relates to an atmosphere that is mostly clear of dust (i.e. a low optical depth of $\tau = 0.35$ in the summer). The profiles that are a good match to the EDM data include those drawn from scenarios using relatively low dust loadings (summer $\tau = 0.8$-1.1): scenarios corresponding to dust loadings observed across multiple Martian years that did not experience global dust storms (MY24, MY26-32) and the 'Climate' scenario, which uses a 'representative standard' dust distribution constructed by averaging optical depth observations through those years. Given the match between the temperature profiles from the low dust MCD scenarios and the EDM data, it is reasonable to assert that the module descended through an atmosphere containing relatively low amounts of atmospheric dust.

A preliminary comparison was also made against MGCM data, in which only the regions outside the plasma blackout were compared, i.e. model profile deviation from spacecraft interpolated data was not considered. In the previous chapters the MY24 scenario has been used as a standard 'low dust' scenario in all experiments (refer back to Section 3.4.2 for more detail on the atmospheric dust fields implemented in the MGCM); the MY25 scenario provides a 'high dust' comparison. Figure 6.6 shows the EDM temperature profile plotted against tem-

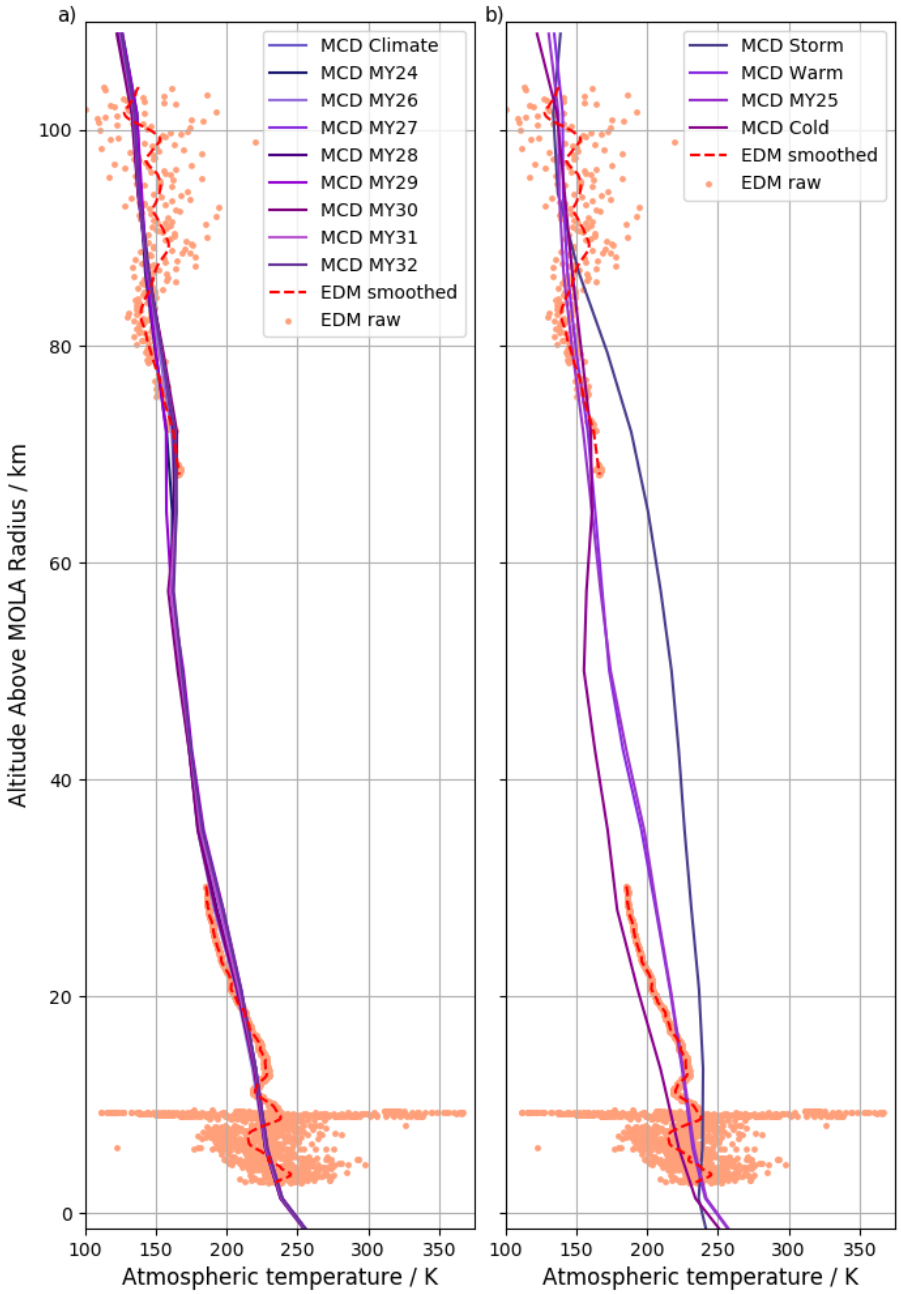

Figure 6.5: Comparison of EDM raw and smoothed data with atmospheric temperature profiles extracted from the Mars Climate Database, shown across two panels solely for clarity. a) Multiple profiles that display a good match with the spacecraft data. b) Profiles extracted from the MCD that display a poorer match with the spacecraft data.

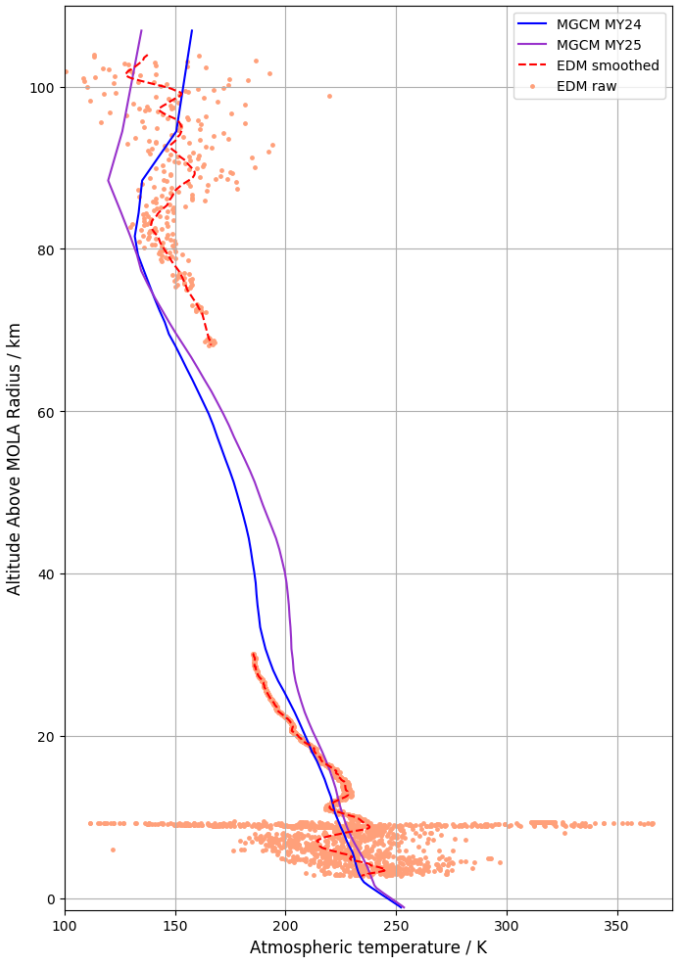

Figure 6.6: Atmospheric temperature profiles from MGCM experiments using 'low' (MY24) and 'high' (MY25) atmospheric dust loadings, alongside raw and smoothed EDM data. MGCM data are averaged over six individual profiles.

perature profiles from MGCM experiments completed using MY24 and MY25 dust scenarios. The RMSDs between modelled data and the smoothed EDM data were calculated: the MY24 profile has an RMSD of 9.79 K through the full height of the profile, decreasing to 7.26 K for data below an altitude of 30 km; the MY25 profile has an RMSD of 15.35 K through the full height of the profile, decreasing to 9.37 K below 30 km. The MY24 profile is a better match to the data than the MY25 profile; therefore, the decision was taken to use MGCM experiments completed using the low dust MY24 scenario for further comparison with EDM data.

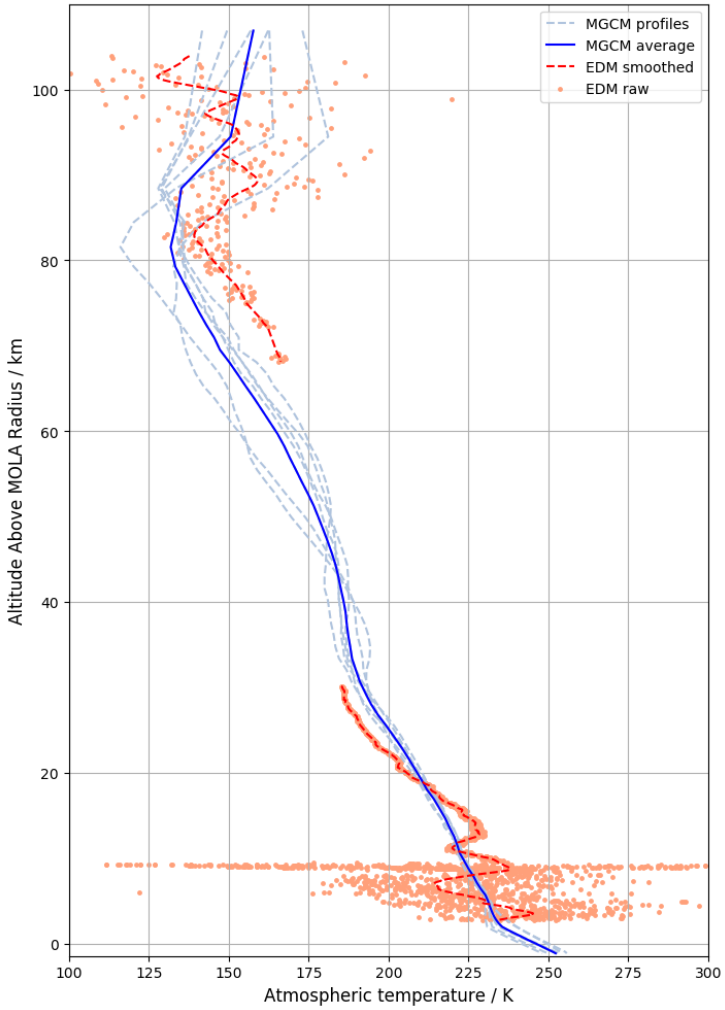

Figure 6.7: Comparison of model and EDM atmospheric temperature vertical profiles. Model data in dashed lines show data from individual profiles, solid line indicates the average.

Figure 6.7 shows the MGCM T31L100 individual and average atmospheric temperature profiles alongside the raw and smoothed EDM data. Figure 6.8 shows atmospheric temperature profiles from MMM experiments. The three profiles in this figure are averages across the five vertical profiles extracted from each nested resolution domain: 63 km, 21 km, 7 km. As expected, the trend across the three resolutions is very similar, with only a deviation of a few degrees at low altitudes (below 2 km AMR).

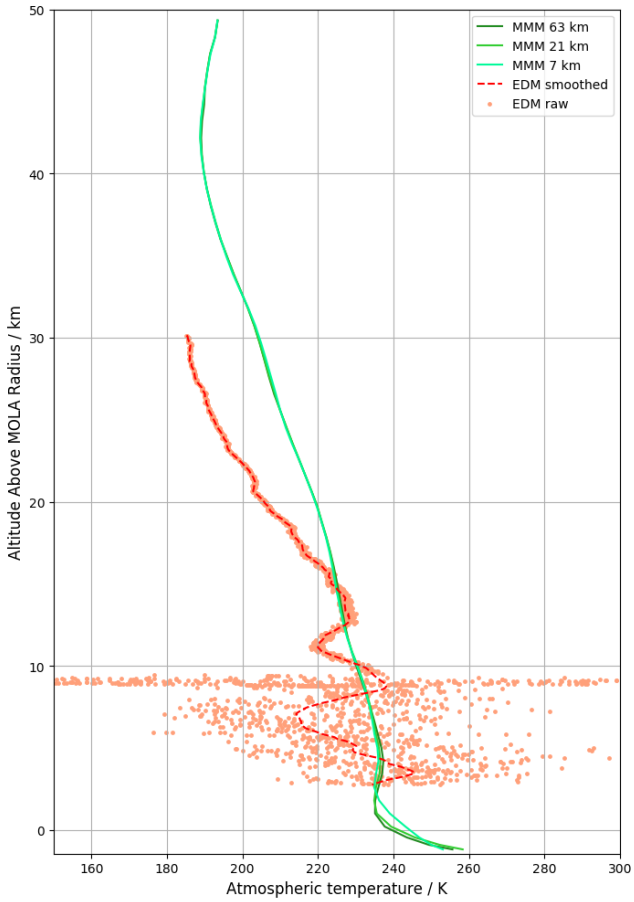

Figure 6.8: Comparison of model and EDM atmospheric temperature vertical profiles. Model lines indicate the average across five profiles, for each modelled resolution domain. The three domains exhibit very similar behaviour for the majority of this vertical profile, and consequently overlay each other for most of the height depicted here.

Figure 6.9 shows MGCM and MMM atmospheric density profiles against EDM data. At altitudes above the plasma blackout the MGCM density profile is not a good match to the EDM data, with some model values diverging from the spacecraft data by an order of magnitude. This discrepancy is not unexpected; as noted previously, the MGCM used within these experiments is accepted as less representative of the Martian atmosphere at the top of the range of modelled altitudes due to multiple factors (e.g. atmospheric sponge layers, limited atmospheric chemistry, no interaction with a thermosphere model). More focus is therefore given here to comparing the profiles within the lower portion of the atmosphere.

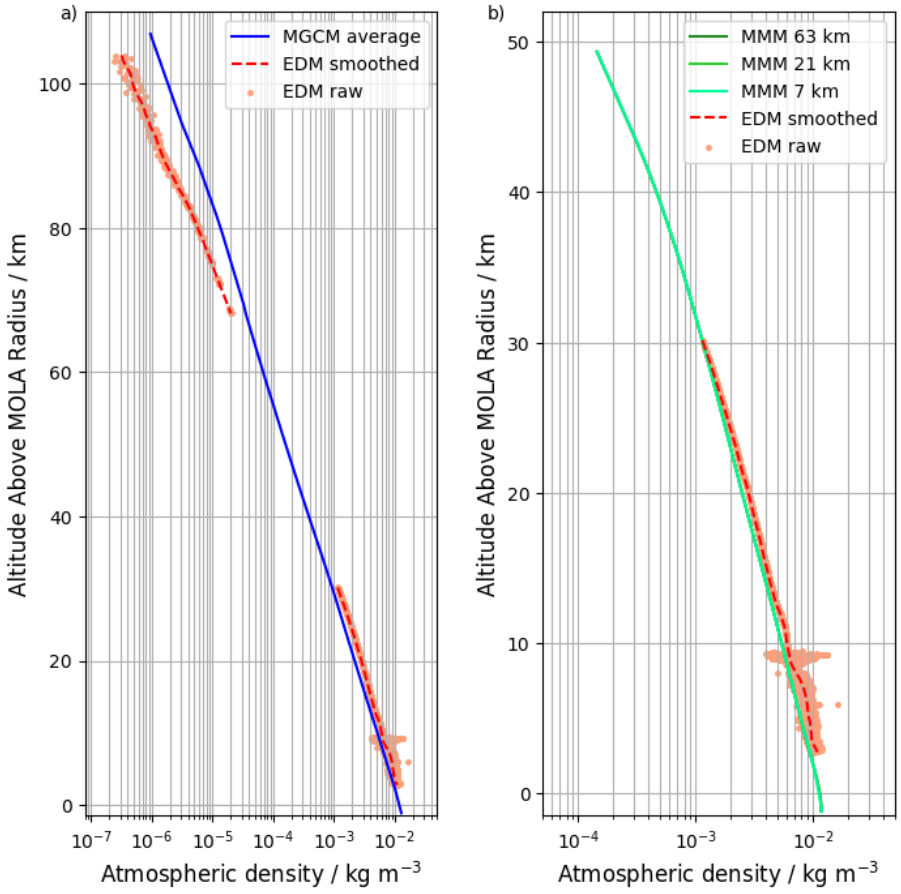

Figure 6.9: Comparison of model and EDM atmospheric density vertical profiles. a) MGCM data are averaged across six profiles. b) MMM data are averaged across five profiles within each resolution (which display very similar behaviour and consequently overlay each other).

The portion of the atmosphere below the plasma blackout is shown in Figure 6.10. The density values in the MMM profile are a closer match to the EDM data than those in the MGCM profile, exhibiting an average deviation of around 10% from the EDM data, while the MGCM data exhibits an average deviation of more than 17% from the EDM data, see Figure 6.11. However, this figure also shows that it is the MGCM data that has a trend more similar to that of the EDM data: as the profiles descend from 30 to ∼9 km AMR the deviation of the MMM data from the EDM data tends to grow, while the deviation of the MGCM data tends to reduce. The values of the MMM data are close to the EDM profile at a height of 30 km AMR but shift away with decreasing altitude, while the MGCM profile is more consistent in its relationship to the EDM profile.

The raw EDM density data below ∼9.5 km AMR are spread very widely. It is not a coincidence that the reported height at which the spacecraft's parachute was released is 9.4 km AMR, and the AMELIA team completed additional processing on the spacecraft data below this point in order to derive the vertical profile. Although *Aboudan et al.* (submitted) then corrected some elements in this 'noisy' data in an attempt to eliminate the most spurious data points, the resulting line still shows considerable variation, which may or may not relate to real atmospheric features.

A feature in the EDM data that *is* believed to be a true atmospheric feature is a small, positive 'bump' in density followed by an inversion, between 12 and 10 km AMR, just prior to parachute release; this atmospheric variation was corroborated by independent pressure sensors located on the front shield of the spacecraft (*Aboudan et al.*, submitted). One possible explanation for this feature is the presence of clouds: ice clouds have been observed in equatorial and tropical regions throughout the year (e.g. *Pearl et al.*, 2001; *Smith et al.*, 2003) and modelling experiments indicate that water ice clouds can have a large effect on properties of the Martian atmosphere (e.g. *Madeleine et al.*, 2012; *Steele*, 2014). However, ice clouds at these latitudes would likely dissipate during morning hours at this time of year (approaching perihelion), and the EDM descended shortly after midsol. An alternative explanation is a detached dust cloud/layer, such as has been observed during daylight hours by NASA's

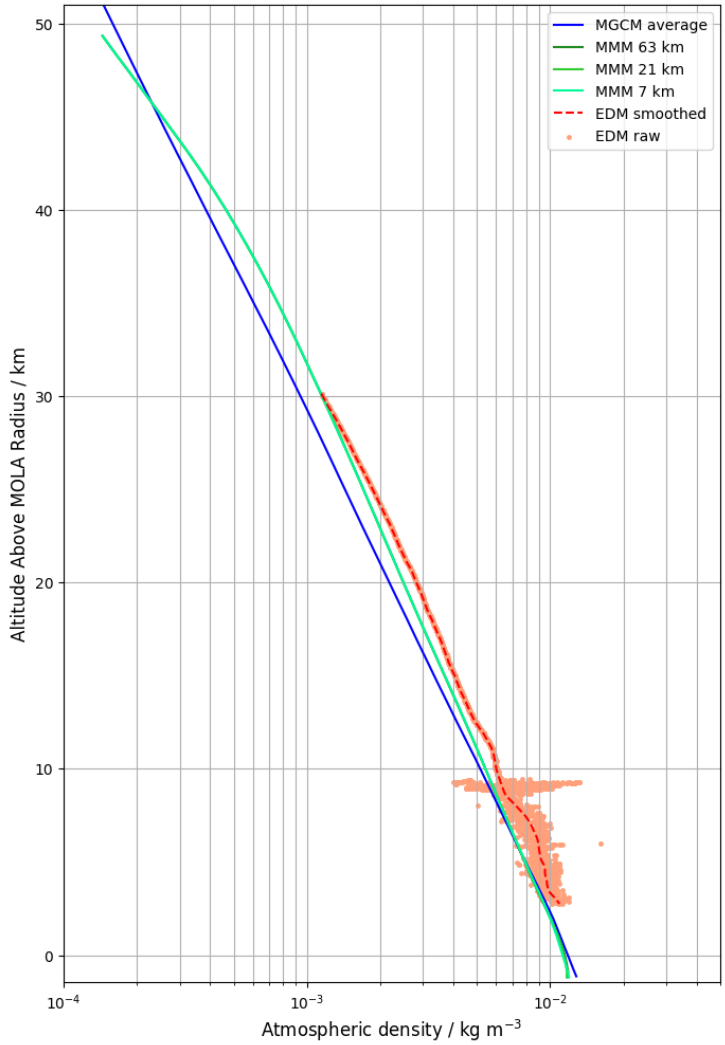

Figure 6.10: Comparison of MGCM, MMM and EDM atmospheric density vertical profiles, through the lower ∼50 km of the atmosphere.

Phoenix lander (*Komguem et al.*, 2013; *Daerden et al.*, 2015), the Thermal Emission Spectrometer (TES) aboard the Mars Global Surveyor (MGS), and Mars Climate Sounder (MCS) aboard the Mars Reconnaisance Orbiter (MRO) (*Guzewich et al.*, 2013a; *Heavens et al.*, 2014). Neither of these conditions would be captured in the current experiments, which do not incorporate ice cloud-forming parameterisations nor routines to simulate detached dust layers. In particular, simultaneously operating both dust lifting and cloud microphysics

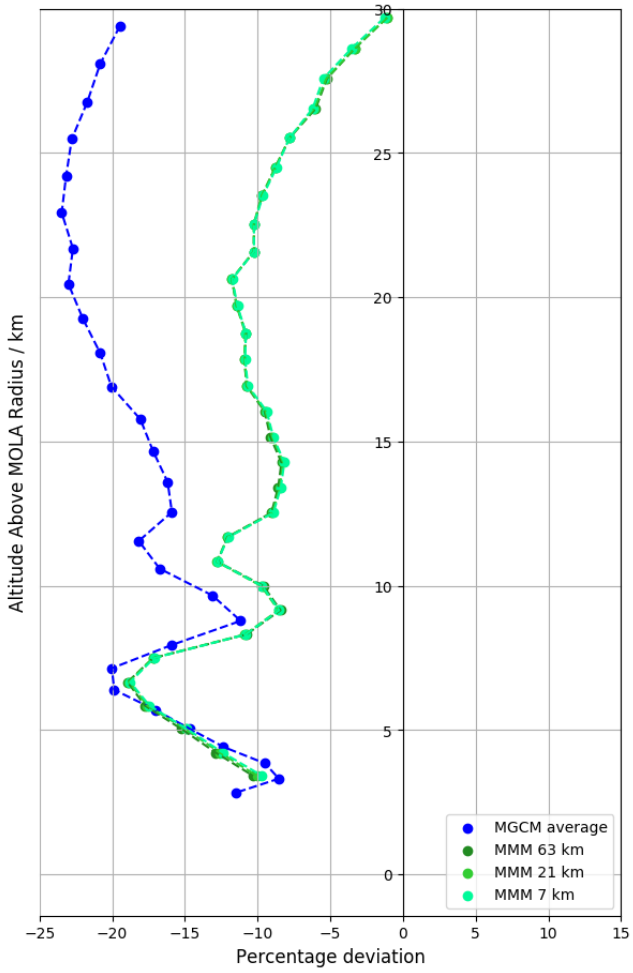

Figure 6.11: Percentage deviation between atmospheric density profiles of modelled data and EDM data, for the lower portion of the atmosphere

submodels in the MGCM and MMM has been largely unsuccessful to date.

Interestingly, NASA's MER Opportunity experienced an atmospheric temperature inversion at a similar height, ∼10 km AMR, during its descent (*Withers and Smith*, 2006); Opportunity landed in the same geographical region as the EDM, albeit at a later point in the year (339.1° L_S). The sister mission, MER Spirit, did not experience such an inversion. There is no definitive explanation for these observations, although *Withers and Smith* (2006) suggest a local dust storm may have had an impact on atmospheric conditions.

In an attempt to gain additional 'ground truth' data, temperature observations from the MCS instrument (*McCleese et al.*, 2007) are shown in Figure 6.12, alongside EDM and MGCM profiles. The comparison between the profiles must include a caveat: the most appropriate MCS observations have been used to create this figure (observations taken ∼30 minutes from the EDM's descent time), but the data are not directly aligned geographically with the EDM's descent trajectory. The MCS profile relates to a latitude of around –5° N but covers a spread of longitudes, varying between –1.9° E (at 85 km AMR) and –4.7° E (at 24 km AMR). The MCS temperature data span an altitude of 24-85 km AMR; through most of this height the EDM experienced plasma blackout, leaving limited overlap between the spacecraft profiles. Indeed, an inversion occurs in the MCS profile at an altitude of 45-55 km AMR that unfortunately falls within the EDM plasma blackout (and which does not occur in the MGCM data). At high altitudes (68-85 km AMR) the MCS and EDM values vary by up to 15 K, but through the overlap in the lower portion of the profile (30-25 km AMR) the MCS and EDM data vary by less than 1.5 K. This correlation gives a measure of validation to the values through at least some of the reconstructed EDM profile. No other spacecraft have released contemporaneous data suitable for additional comparisons.

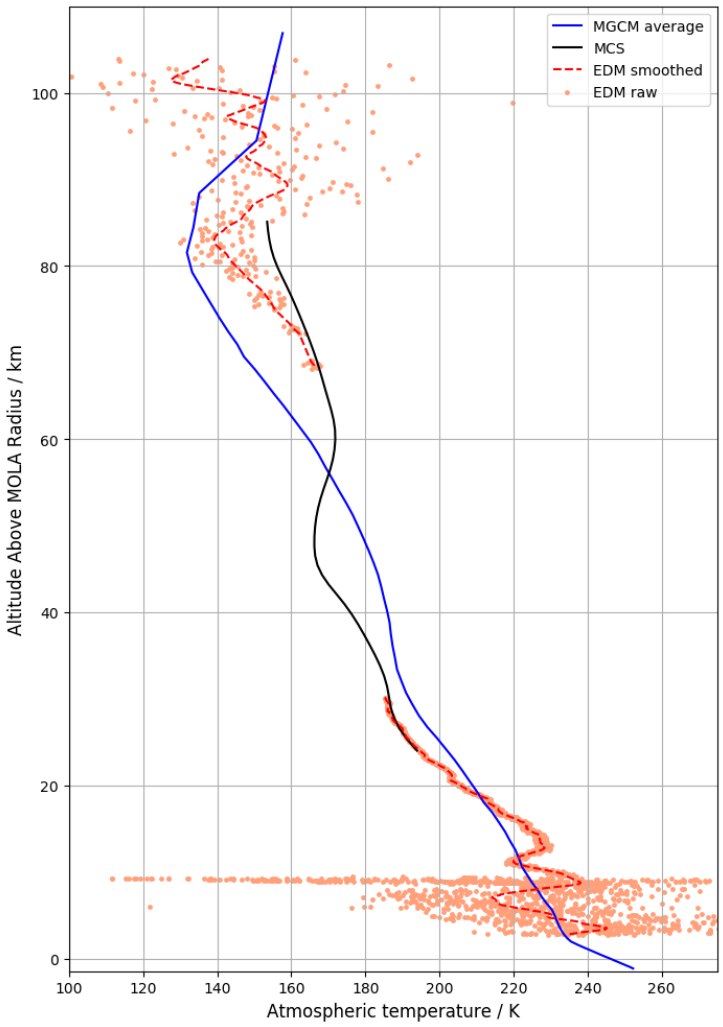

Figure 6.12: Comparison of MGCM and EDM atmospheric temperature vertical profiles, alongside MCS observations obtained from orbit. The MCS data used to create this profile are the closest possible match in time and location to the descent trajectory of the EDM.

It is impossible to verify the raw (or smoothed) EDM atmospheric density data through the final portion of the profile (i.e. below ∼25 km AMR), and *Aboudan et al.* (submitted) admit that some oscillations in the EDM data are due to "unmodelled dynamics of the parachute-probe system". Crucially, the AMELIA team used the density profile to calculate both the pressure and temperature profiles: variations in the atmospheric density profile will affect these further calculations. To assess how the inclusion of potentially inaccurate data in these calculations may impact the temperature profile, a 'proposed mean' density profile has been derived by fitting a line of regression through the EDM smoothed data spanning 30-12 km AMR and extending this trend down to a height approximately that of the final point in the profile. This new profile is shown in Figure 6.13. When the MGCM and MMM density profiles are compared with this proposed mean profile, the trends identified above are reinforced: with decreasing altitude the deviations of MMM data from EDM data grow and the deviations of MGCM data reduce.

The proposed mean density (ρ) profile is used to recalculate pressure (p) and temperature (T), following *Aboudan et al.* (submitted), by using the hydrostatic equilibrium equation:

$$\frac{\partial p}{\partial z} = -\rho g \tag{6.1}$$

where g is acceleration due to gravity, and the ideal gas equation:

$$T = \frac{pM}{\rho k_B N_A} \tag{6.2}$$

where z is height, M is the mean molar gas of the Martian atmosphere (43.41×10^{-3} kg mol^{-1}), k_B is the Boltzmann constant and N_A is the Avogadro constant. The consequent 'proposed mean' temperature profile through this portion of the atmosphere is shown in Figure 6.14.

Figure 6.15 shows the percentage deviation of the MGCM and MMM profiles from the EDM smoothed and proposed mean temperature profiles. The MGCM data are a better match to the EDM smoothed profile and to the proposed mean profile.

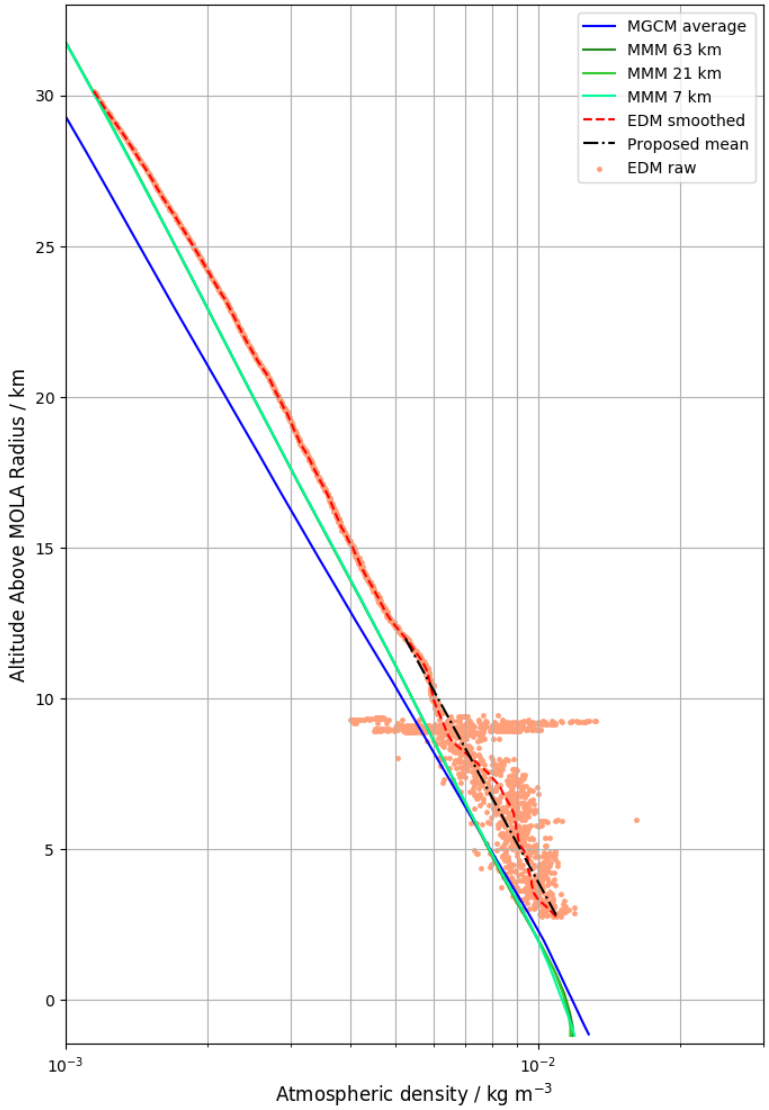

Figure 6.13: As Figure 6.10, for altitudes below ∼30 km AMR, with the addition of a 'proposed mean' line for the EDM data.

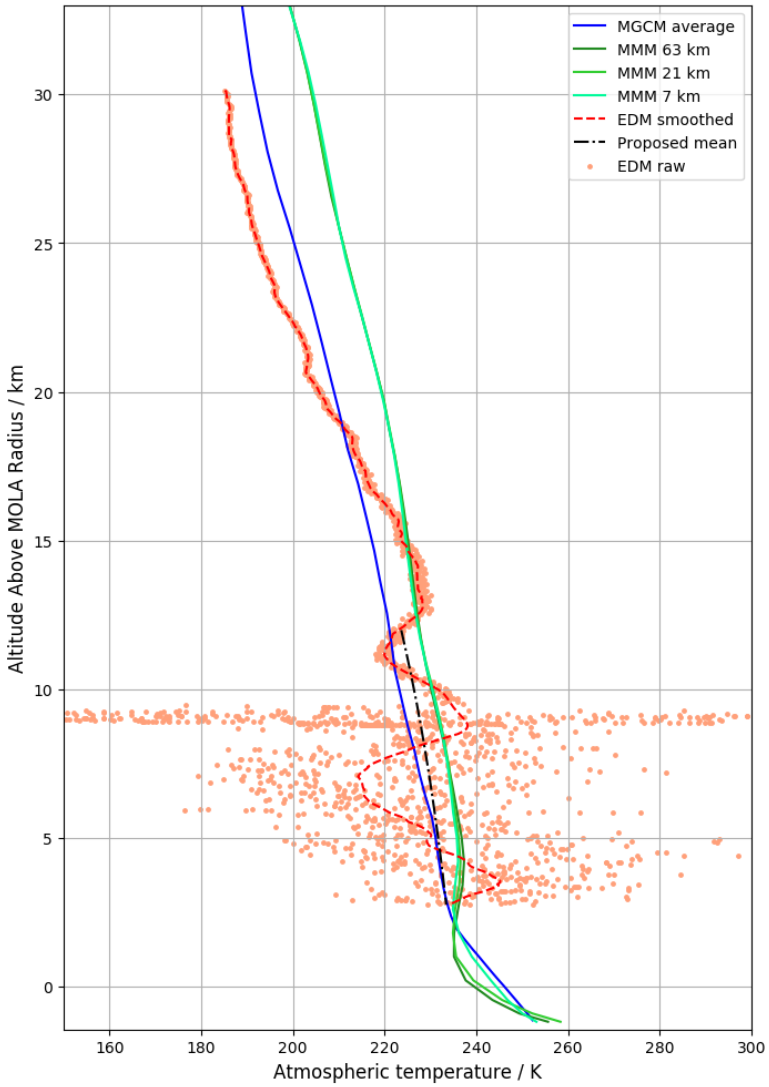

Figure 6.14: Comparison of model and EDM atmospheric temperatures through the lowest ∼30 km of the profiles, with the addition of a 'proposed mean' temperature profile calculated from the proposed mean EDM density profile. (As identified earlier, the three MMM domains overlay each other for most of the height depicted here.)

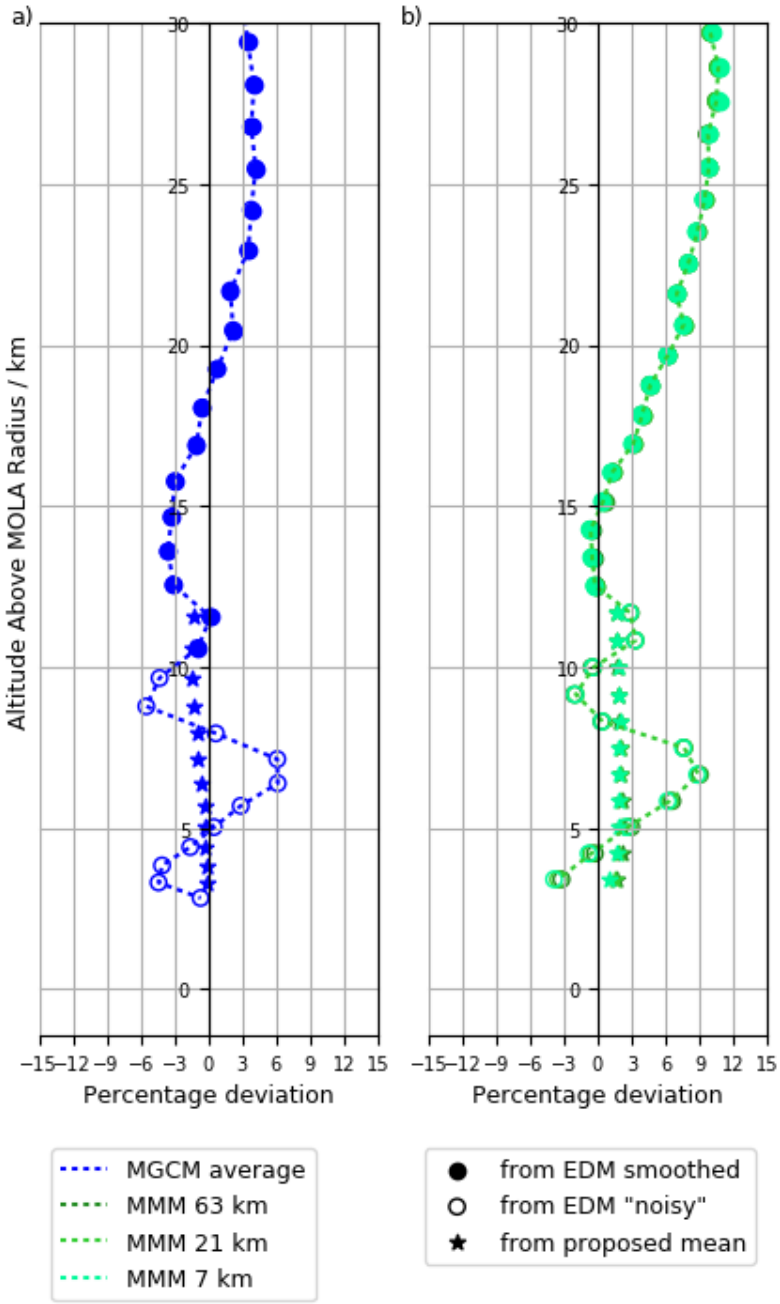

Figure 6.15: Percentage deviation of model data from EDM smoothed and mean/extrapolated temperature profiles: a) MGCM data, b) MMM data. Filled markers relate to model data deviation from EDM smoothed data above parachute release, open markers relate to model data deviation from EDM smoothed data after parachute release; stars relate to model data deviation from proposed mean temperature profile.

Two scenarios are envisaged here:

- That the modelling of the EDM's motion under parachute, performed by *Aboudan et al.* (submitted), is incomplete, and that the implementation of a complete, corrected model would reduce the apparent variations in density to a smoother profile, potentially closer to that of the 'proposed mean' profile. It is anticipated that the MGCM results would display a similar gradient to that of the corrected profile, although would not match the absolute values. The divergence of the MMM results from the EDM smoothed results at lower altitudes suggests that the MMM values would continue to be a poor match to any such corrected profile.

- That the variations in the density profile are indicative of atmospheric features that have not been captured by either of the models.

Both of these scenarios may apply, to varying extents. Any future data releases received from the AMELIA team could be used to assess the veracity of the first scenario; for the second scenario, potential features can be identified. Candidate atmospheric phenomena include local dust features such as a dust cloud, a small dust storm or a dust devil. The presence of a dust cloud or small storm would affect the local atmospheric density and temperature – and could also induce local variations in wind speeds that were not accounted for in the parachute-motion model.

It would seem unlikely that the EDM happened to encounter a dust devil upon its descent into this region (see Section 6.3.3 for discussion of the local dust devil environment), but dust devils with heights of more than 8 km have been observed (*Fisher et al.*, 2005), therefore it is not an impossibility that a dust devil – or a dust-free convective vortex – could have been present at this point in space and time. Measurements of the wind speeds within Martian dust devils are currently very limited, although *Choi and Dundas* (2011) were able to complete a study using images from HiRISE and report dust devil tangential wind speeds of 20-30 $\mathrm{m\,s^{-1}}$, and large eddy models of Martian convective vortices produce tangential wind speeds of up to 10 $\mathrm{m\,s^{-1}}$ (*Toigo et al.*, 2003; *Nishizawa et al.*, 2016). (For comparison, peak wind speeds of ∼10-20 $\mathrm{m\,s^{-1}}$ have been recorded within dust devils on Earth, e.g. *Ryan and Carroll* 1970; *Fitzjarrald*

1973; *Schwiesow and Cupp* 1976; *Balme et al.* 2003a.) It is feasible that such wind speeds could impact the motion of a descending spacecraft, but more detailed modelling of the specific module and its parachute would be required for any conclusions to be drawn.

A small dust cloud or storm could be too small for the MGCM to resolve, and small-scale convective plumes and dust devils are not discretely modelled by either scale model. MRO Mars Color Imager (MARCI) images of the sols immediately preceding the EDM's descent show no storms active in the region (*Malin et al.*, 2016); the instrument has a resolution of a few kilometres per pixel (*Malin et al.*, 2001). The low likelihood of local dust lifting (see Section 6.3.3) argues against a dust storm forming in this location, but even small storms can travel some distance; if this were the case, the limited area of the MMM model potentially precludes such a phenomenon being captured within the higher resolution experiment.

6.3.2 Wind Speed and Direction

The EDM wind profiles include zonal and meridional wind speeds and the calculated magnitude of the resultant wind. These profiles span most of the distance through which the EDM was descending by parachute, from 8.4 km AMR down to 2.8 km AMR. Figure 6.16 shows the EDM wind speed and magnitude data against MGCM and MMM data. The variation between modelled sols can be seen in both the MGCM and MMM data. The raw EDM zonal wind data is highly variable above ∼7 km, which is then reflected in the calculated magnitude.

For clarity, Figure 6.17 shows the smoothed EDM winds data alongside the average vertical profiles (across multiple sols) for both models. The most obvious discrepancy between the modelled and EDM profiles is that the model data do not display the ∼1 km-wavelength oscillation in both zonal and meridional winds that is apparent in the EDM profiles.

Comparing the EDM profiles with the MGCM profiles, there is some similarity: zonal winds are generally in the westward direction, averaging around 8.5 $\mathrm{m\,s^{-1}}$ through the ∼6 km of altitude available for comparison (8.7 $\mathrm{m\,s^{-1}}$ in the EDM data, 8.2 $\mathrm{m\,s^{-1}}$ in the model data); meridional winds are generally southward and weaker in nature, averaging 2.4 $\mathrm{m\,s^{-1}}$ in the EDM data and 1.6 $\mathrm{m\,s^{-1}}$ in the model data. The RMSD between MGCM data and EDM data is 5.5 $\mathrm{m\,s^{-1}}$ for the zonal wind speed profiles and 4.6 $\mathrm{m\,s^{-1}}$ for the meridional wind speed profiles.

The EDM comparison with the MMM data reveals a poorer match between the profiles. The MMM zonal wind profiles are generally westward in nature, but peak around 5 $\mathrm{m\,s^{-1}}$ and only average ∼3.5 $\mathrm{m\,s^{-1}}$. The MMM meridional wind profiles have an average speed of ∼3.9 $\mathrm{m\,s^{-1}}$, higher than that of the EDM profile, and appear to display a directional shift that is the opposite of the shift in the EDM data. The RMSD between MMM data and EDM data for the zonal wind speed profiles, averaged across the three domain resolutions, is 7.2 $\mathrm{m\,s^{-1}}$; for the meridional wind speed profiles, averaged across domains, it is 7.9 $\mathrm{m\,s^{-1}}$.

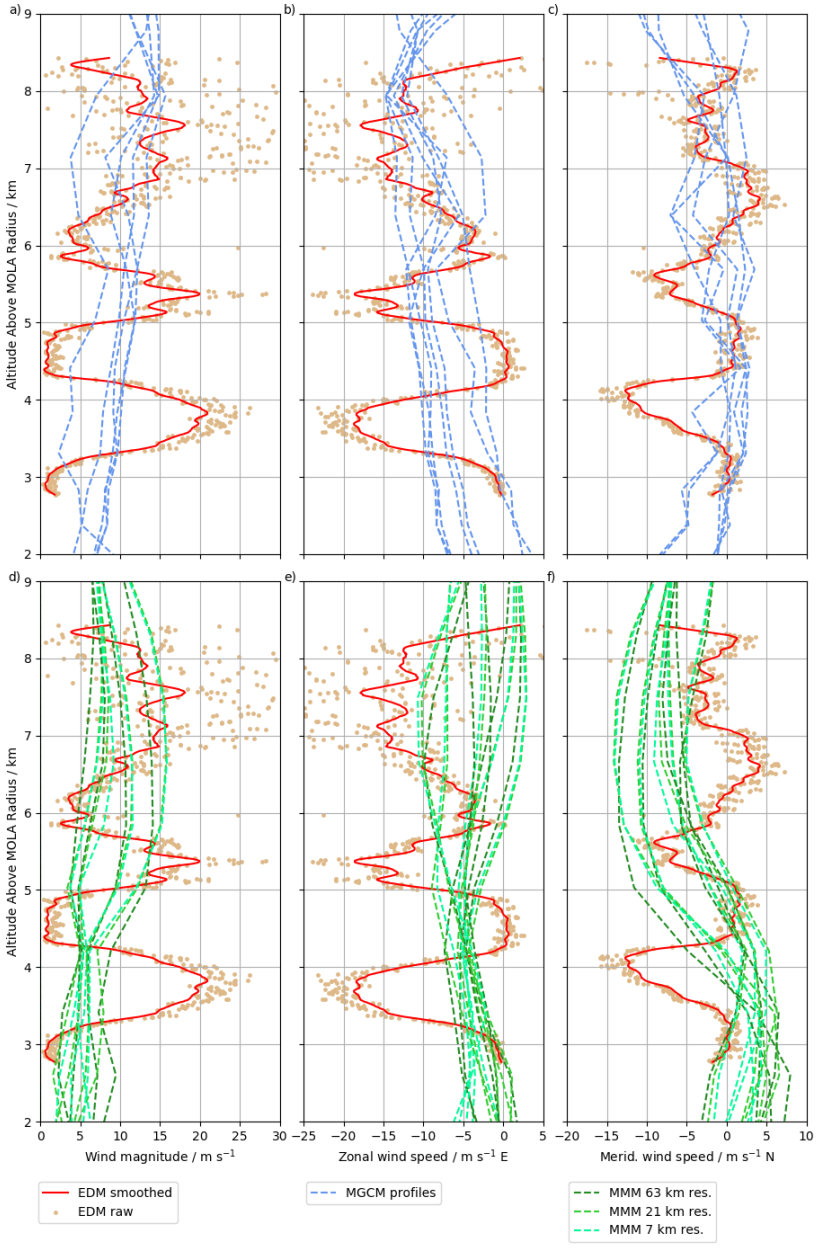

Figure 6.16: Comparison of the EDM raw and smoothed wind data with MGCM profiles (a, b, c) and MMM profiles (d, e, f): the calculated magnitude of the wind (a, d), the zonal wind speed (b, e), and the meridional wind speed (c, f). The dashed lines indicate data from individual model profiles. (Profiles from the three MMM resolution domains all display similar variation through this period.)

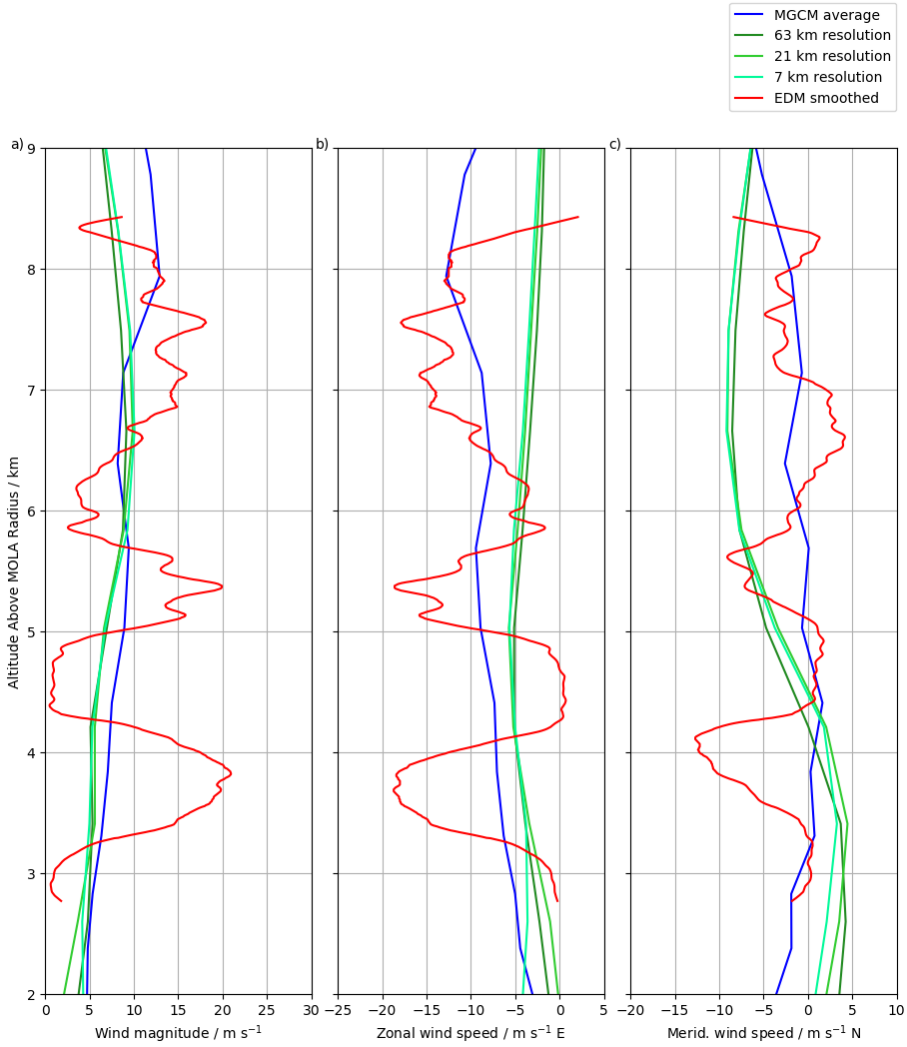

Figure 6.17: MGCM (blue), MMM (green) and EDM (red) vertical profiles of winds: a) wind magnitude, b) zonal wind speed and c) meridional wind speed. (Results from the three MMM resolutions are all plotted, but there is no significant difference between the profiles.)

Figure 6.18 presents wind vector data in a format inspired by the style of a Hovmöller diagram. This plot shows the changing direction of the wind vectors in the EDM, MGCM and MMM data: each arrow is a 'bird's-eye view' of the wind data in a profile at each step in height; the direction of each arrow correlates with the compass points illustrated in the diagram. The top of the diagram relates to data points near the top bound of this portion of the atmosphere (∼9 km AMR), the bottom relates to the lower bound (∼3 km AMR). The MGCM displays a continuous west-southwestward wind through this ∼6 km of altitude, while the MMM profiles describe a clockwise shift in direction from south-southwestward at the top of this vertical range to northwestward at the bottom of the range. This plot displays clearly the changeability of the EDM wind profile; although the southwestward direction is dominant, the wind vectors vary such that the resultant magnitude is a downward, clockwise spiral – an impression of this can be gained from the views shown in Figure 6.19.

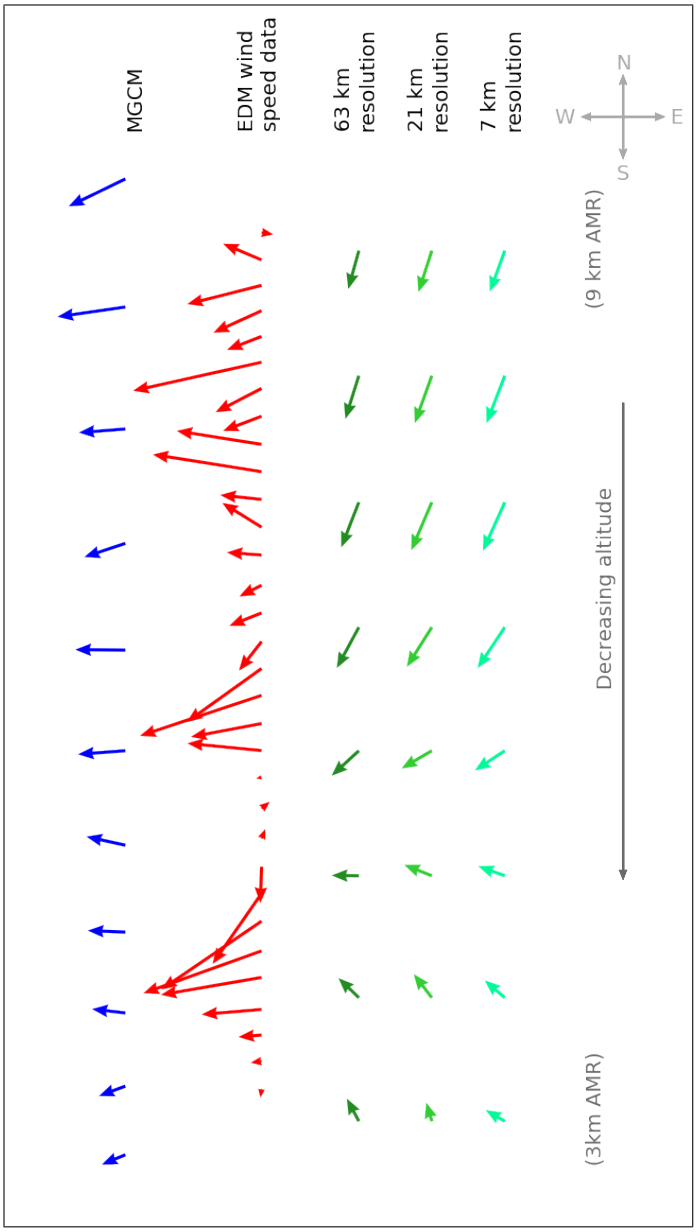

Figure 6.18: Vector plot of the wind profiles discussed herein: MGCM average, EDM data, MMM averages for each resolution. From the top to the bottom of this diagram, altitude decreases. Each arrow is a top-down view of the wind vector at a given height, with the resultant wind direction at that point in the profile correlating with those marked in the compass. For diagrammatic clarity, the EDM data has been sampled every ∼250 m of altitude rather than attempt to display every value.

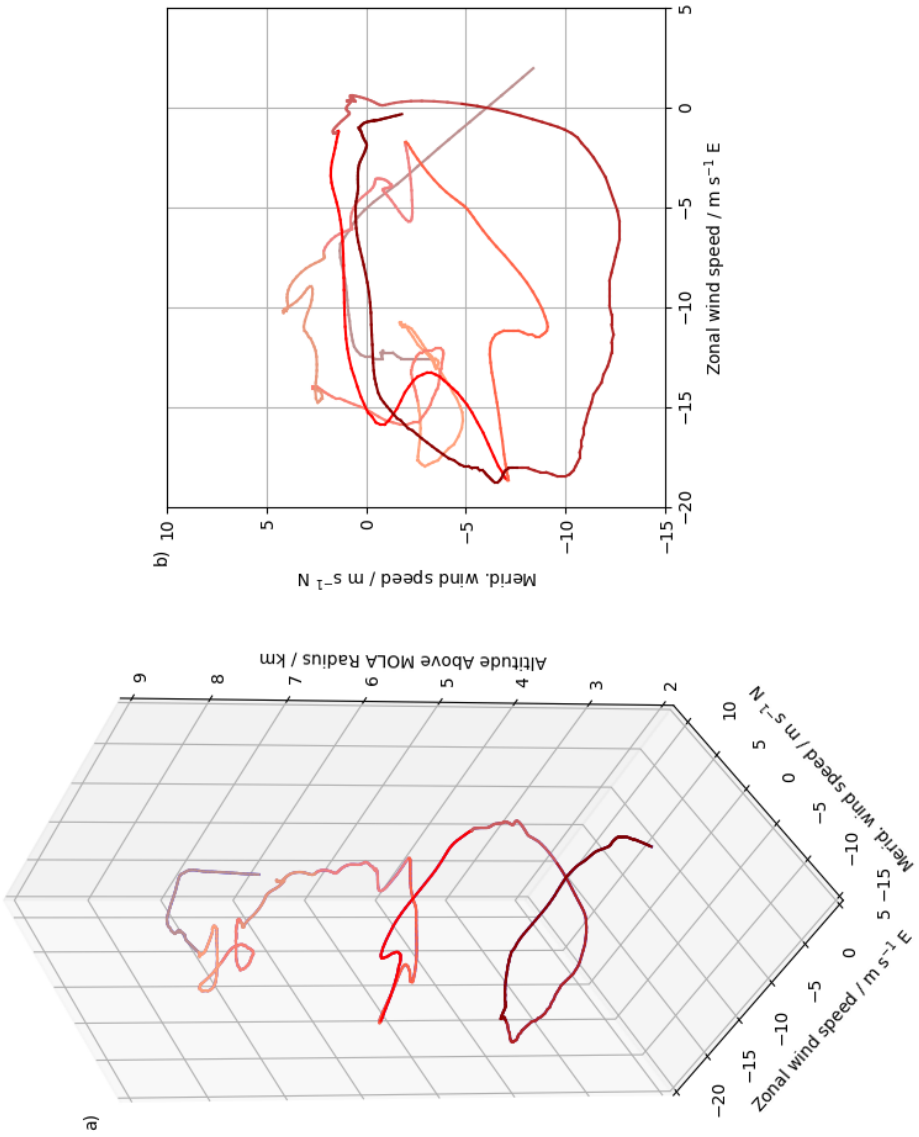

Figure 6.19: EDM smoothed wind magnitude profile data displayed in two views: a) three dimensions, b) from above. The colour variation along the plotted line is added solely to assist in comparison between the views.

To further investigate the directional trends within the EDM data, a rolling mean profile[2] was calculated for each of the zonal, meridional and magnitude profiles. Figure 6.20 compares the modelled profiles against this mean profile.

The EDM mean zonal wind profile is westward in nature, varying between –13.3 $\mathrm{m\,s^{-1}}$ east and –6.6 $\mathrm{m\,s^{-1}}$ east. The MGCM zonal wind profile is a good match to the direction and speed of this mean wind, with a zonal RMSD of 2.6 $\mathrm{m\,s^{-1}}$ and a meridional RMSD of 3.4 $\mathrm{m\,s^{-1}}$; the MMM zonal wind profile is a poorer match, with an averaged zonal RMSD of 5.7 $\mathrm{m\,s^{-1}}$ and a meridional RMSD of 6.4 $\mathrm{m\,s^{-1}}$. The EDM mean meridional wind profile shows minimal wind around 7 km AMR and then displays a small southward directional shift with descending altitude. The MGCM meridional wind profile is a reasonable match at this minimum point, but shows lower speeds than the mean for most of the profile height, only shifting southwards in direction below 3 km AMR. The MMM meridional profile shows a directionality which is the opposite of the trend in the EDM mean profile, showing instead a northward directional shift around 6 km AMR, although there is a return to a southward direction below 3 km AMR.

Figure 6.21 shows the EDM smoothed and rolling mean profiles alongside the 'residual' profile (calculated by subtracting the smoothed profile from the mean values). The assumption herein is that the EDM experienced a large-scale wind described by the mean profiles (a predominantly southwestward wind) and a smaller-scale oscillation that is depicted by this residual profile. This small-scale oscillation may be a feature of the EDM's motion under parachute that was not captured by the AMELIA team's dynamic modelling, or it may be related to small-scale atmospheric features that have not been captured by either the MGCM or the MMM.

[2] A 201-point rolling mean was chosen, based on the approximate number of data points through one 'wavelength' of the apparent oscillation; 201 data points span approximately 1-1.5 km in height.

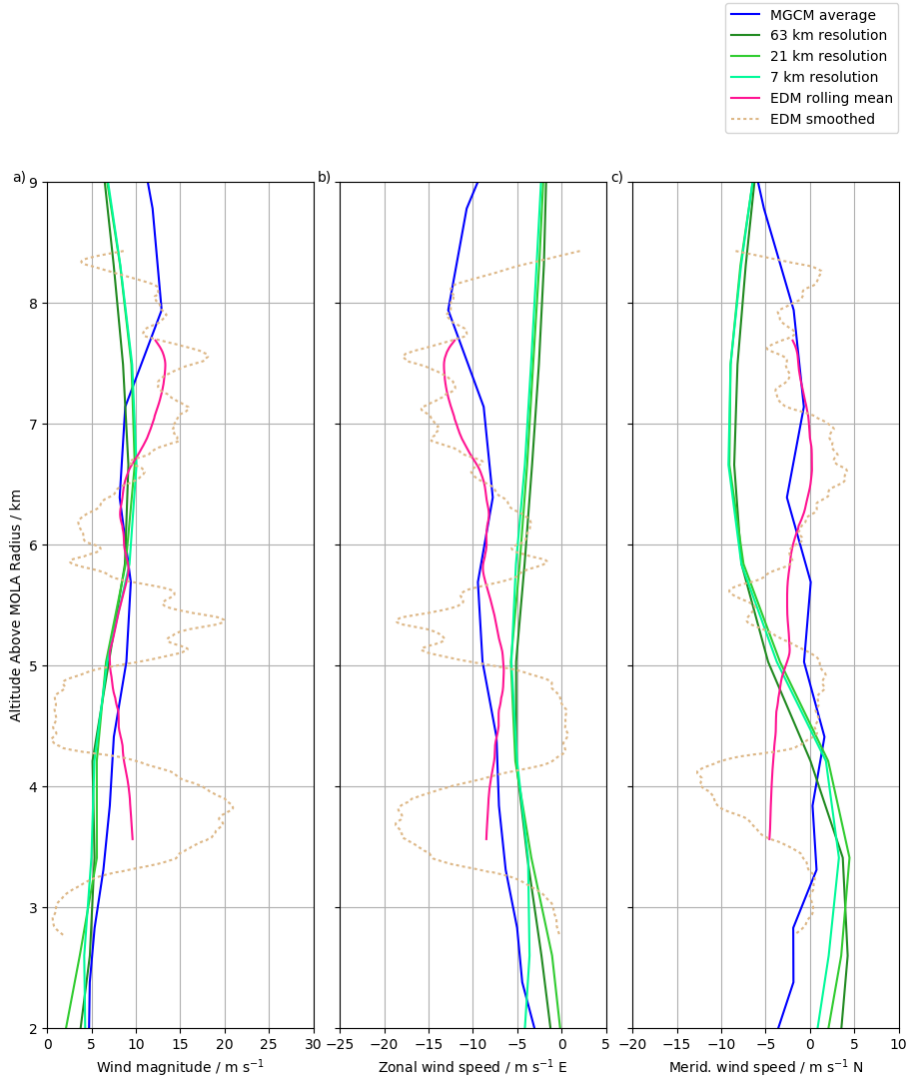

Figure 6.20: As Figure 6.17, with the inclusion of the calculated rolling mean profile.

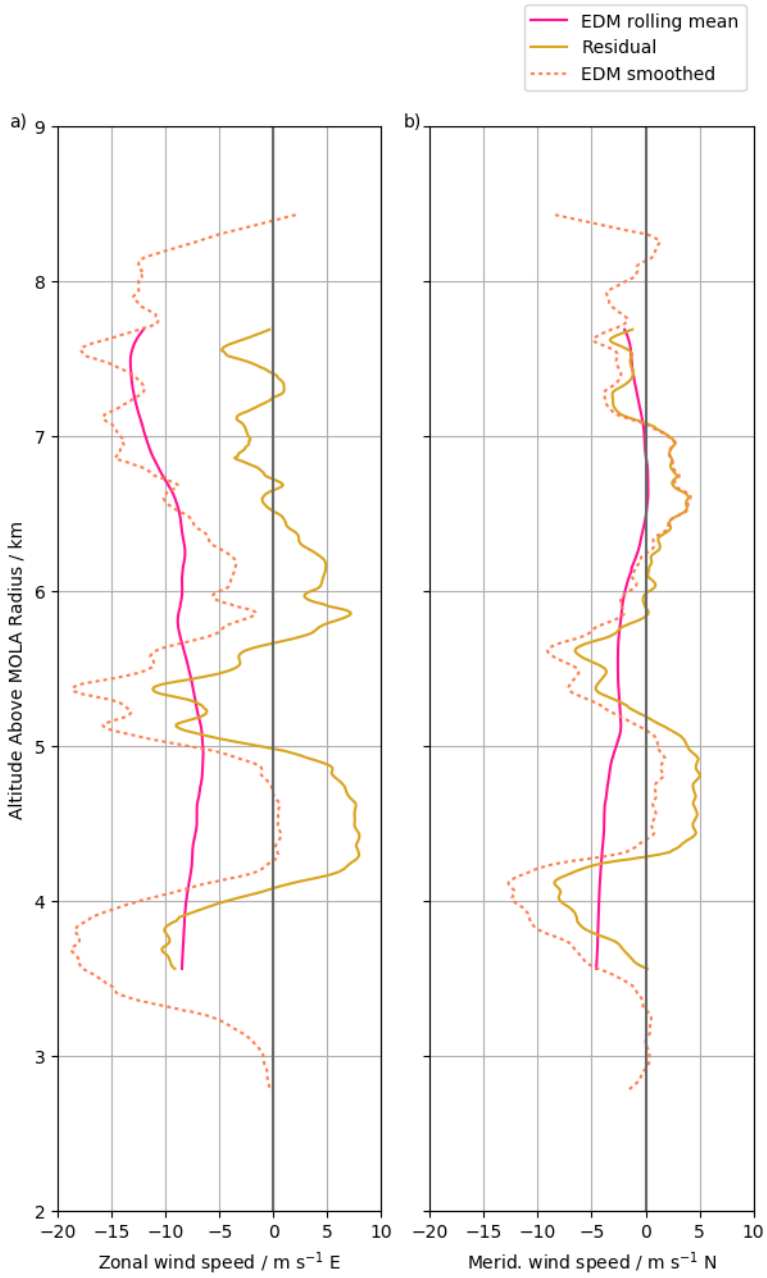

Figure 6.21: EDM smoothed and mean profiles, alongside the calculated residual values: a) zonal wind speeds, b) meridional wind speeds.

A mission suitable for comparison with the ExoMars EDM is that of the twin NASA MER spacecraft, which also descended under parachute in equatorial locations. Modelling analysis of the MER descents – completed prior to the mission – identified that in that case the module-parachute system was sensitive to oscillations of wavelengths of ∼1.5 km or greater (*Kass et al.*, 2003). This is a similar wavelength to the apparent oscillation seen in the EDM wind speed profiles, and may reveal a sensitivity in this system not incorporated into the AMELIA team's dynamic models. *Aboudan et al.* (submitted) admit that the model of the 'parachute-probe system' may not be complete, and identify small, short-period (1.2 seconds) wind speed oscillations in both zonal and meridional data that are caused by parachute dynamics rather than atmospheric features.

If the ∼1-km wavelength oscillation does relate to a real feature, one possible explanation is a thermal wind – i.e. a horizontal thermal gradient that is affecting local wind speeds. While traditional calculations of thermal gradients require the area under study to be in geostrophic balance (*Andrews*, 2010), which cannot be assumed for this equatorial location, preliminary calculations can be made using a generalised thermal wind equation for zonal flow (*White and Staniforth*, 2008). The results of these calculations suggest that a (meridional) temperature gradient capable of driving the sharp changes in zonal wind speed described by the apparent spiral seen in Figure 6.19 would have to be of the order of 1 $\mathrm{K\,m^{-1}}$. This is unfeasibly high: MGCM results for this region display temperature gradients $\sim 1\times10^{-5}$ $\mathrm{K\,m^{-1}}$, while MMM result display temperature gradients up to $\sim 1\times10^{-4}$ $\mathrm{K\,m^{-1}}$; temperature gradients of this order are also observed on Earth (*Wallace and Hobbs*, 2006). Therefore, if these oscillations in wind speed are true features of the environment the EDM encountered, the cause must be a local atmospheric phenomenon (potentially associated with a dust lifting event) rather than a large-scale wind driven by thermal gradients.

6.3.3 Surface Dust Processes

To explore the likelihood of the EDM encountering a dust event (either a dust storm or dust devil) during its descent, surface dust lifting in the region of the landing site was investigated through modelling and comparison with historical observations. The EDM Schiaparelli carried a meteorological station as part of its science payload; the DREAMS (Dust characterization, Risk assessment and Environment Analyzer on the Martian Surface) experiment would have returned temperature, pressure and wind speed data from the planet's surface, and it was intended that sand saltation rates and velocities of wind-blown particles would also be investigated (*Esposito et al.*, 2014). Unfortunately, these experiments were not possible, and the comparison here is primarily between MGCM and MMM data, with a brief discussion of surface observations from the Opportunity mission.

As discussed in Chapter 4, MGCM experiments completed at the T31 resolution (5° latitude × 5° longitude) do not provide a good representation of surface-level processes. The MGCM experiment with the highest combination of horizontal and vertical resolutions is the T85L25 experiment, which provides a horizontal resolution of ∼1.875° latitude × ∼1.875° longitude and uses 25 vertical layers[3]. Data from this experiment were used as a comparison with the MMM results for the following analysis.

Near-Surface Wind Stress Dust Lifting

When considering surface dust lifting by NSWS, it is the magnitude of the near-surface wind that is important, rather than the direction of that wind. Figure 6.22 shows the magnitude of the near-surface wind at the endpoint of the EDM's trajectory, for the modelled and EDM data (i.e. the winds in the lowest layer of the model experiments, at ∼5 m height). For completeness, the full diurnal period has been considered: the MGCM values represent the wind magnitude at this point in every model output ±4° L_S from the EDM's descent date (12 sols in total); the MMM values represent the wind magnitude at this point in

[3]While T127 and T170 simulations offer higher horizontal resolutions, such simulations must currently be operated with limited vertical resolution, adversely impacting their representation of surface-level processes.

every hour during the modelled five sols. The 'Potential EDM' value represents a downward extrapolation of the wind magnitude calculated from the proposed mean zonal and meridional winds.

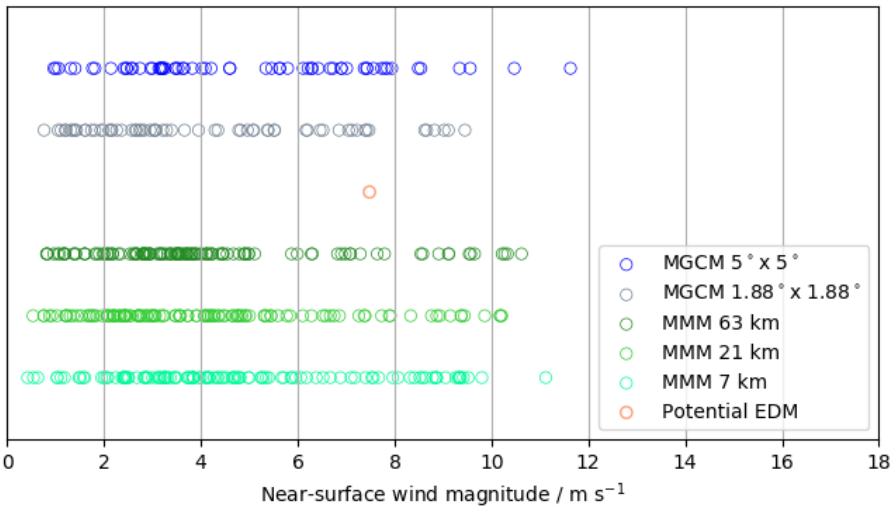

Figure 6.22: Near-surface wind magnitudes at the EDM site through the modelled period. MGCM and MMM markers indicate values for every modelled output. Potential EDM marker indicates a value calculated from extrapolation of the mean EDM winds.

The range of magnitudes shown in Figure 6.22 are similar across MGCM and MMM data: minima of 0.76-0.96 m s^{-1} (MGCM) and 0.42-0.81 m s^{-1} (MMM), maxima of 9.45-11.63 m s^{-1} (MGCM) and 10.21-11.12 m s^{-1} (MMM). The Potential EDM extrapolated value is within the range of the modelled values, at 7.48 m s^{-1}; this estimate cannot, unfortunately, be verified by ground truth.

The key point to observe for all these near-surface winds is that they are not forceful enough to lift any dust. In Chapter 4 dust lifting was observed in regions with near-surface wind speeds approaching ∼20 m s^{-1}. The wind speed required to lift dust will vary slightly geographically, depending on the near-surface atmospheric density, but dust lifting was not predicted to occur in regions experiencing near-surface wind magnitudes of the values shown in Figure 6.22.

The results from the MGCM experiments consequently do not show any NSWS dust lifting at the Schiaparelli landing location at any point during the

year, in either the T31 or the T85 resolution. Within the results from the MMM experiments there are small amounts of dust lifting in the surrounding region, although none at the selected landing site. Figure 6.23 shows an example of the patterns of dust lifting seen in the results for the MMM 21 km and 7 km resolution experiments; no NSWS dust lifting occurs in the 63 km resolution experiment. Both panels show data from the same sol and time, $L_S \sim 247°$, around 21:40. All of the modelled NSWS dust lifting in this region occurs during the night, primarily between 19:00 and 01:00, although the 21 km resolution displays some very minor patches of early-morning lifting until 05:00. The local terrain height is also depicted in this figure, showing clearly that the patches of dust lifting are associated with topographical features, e.g. the edge of a small crater (Fig. 6.23b). The module's estimated landing ellipse is drawn in both panels.

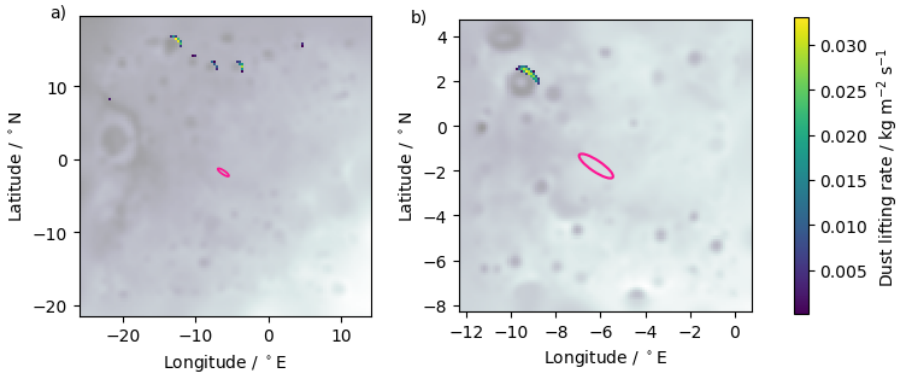

Figure 6.23: NSWS dust lifting in the region surrounding the EDM site as modelled in two MMM resolution domains: a) 21 km, b) 7 km. These results relate to the same point in time: $L_S \sim 247°$, around 21:40. The estimated landing ellipse is drawn in both panels for reference. The underlying terrain height is displayed in monochrome: dark areas are low, bright areas are high (cf. Figure 6.2).

As the EDM did not successfully return any data from the planet's surface, no comparison can be made between observations and model results for near-surface wind magnitudes or dust lifting estimates at this precise location. However, NASA's Opportunity rover is also located in Meridiani Planum: with a landing location of –1.95° N, –5.53° E, it is approximately 50 km from the EDM site. Opportunity does not carry a wind speed sensor, but studies have

investigated surface particle mobility using images returned by the rover. *Sullivan et al.* (2007) identify some movement of surface dust local to Opportunity, but only through the peak of the dust storm season, and then only on patches of ground where surface dust cohesion had already been disturbed by the rover's wheels. *Kinch et al.* (2012) propose a slow, annual deposition-removal dust cycle in Meridiani Planum, suggesting generally limited dust movement in the region. Such observations agree with the near-zero levels of modelled NSWS dust lifting in the vicinity of the EDM site.

Dust Devils

Figure 6.24 shows the rate at which dust is lifted by dust devils at the EDM site, for a period of $\sim 4^\circ$ L_S either side of the module's landing date, across two MGCM resolutions. Figures 6.25 and 6.26 show the maximum dust devil lifting rate modelled in every surface gridbox through the same period. These figures illustrate the relatively low level of MGCM dust devil activity at this location and in the immediate area. The higher resolution experiment shows higher levels of dust devil activity, but the data are within an order of magnitude across the experiments and the absolute values are low relative to other locations across the planet's surface, see Figures 6.25 and 6.26.

Similar dust devil activity is apparent in the MMM results. Figure 6.27 shows examples of the dust devil activity patterns across the different MMM resolutions; all panels in this figure show the same sol and time. In the 63 km resolution experiment there is dust devil activity in the wider region through most daylight hours, but dust devils only occur in the locale of the landing ellipse around 10:40 (shown here). In the 21 km resolution experiment there is dust devil activity in the vicinity of the landing ellipse between 09:40 and 10:40. In the 7 km resolution experiment the highest density of dust devil lifting is also through 09:40-10:40, although more scattered activity occurs in the surrounding region until 14:40. The patterns of dust lifting are not an exact match across MMM and MGCM results, but the geographical distributions and timings are similar: compare panels Fig. 6.25b, Fig. 6.26b, and Fig. 6.27a. The MMM dust devil lifting rate in the vicinity of the EDM ellipse is similar to that seen in the MGCM data: of the order of 1 $\mu g\,m^{-2}\,s^{-1}$.

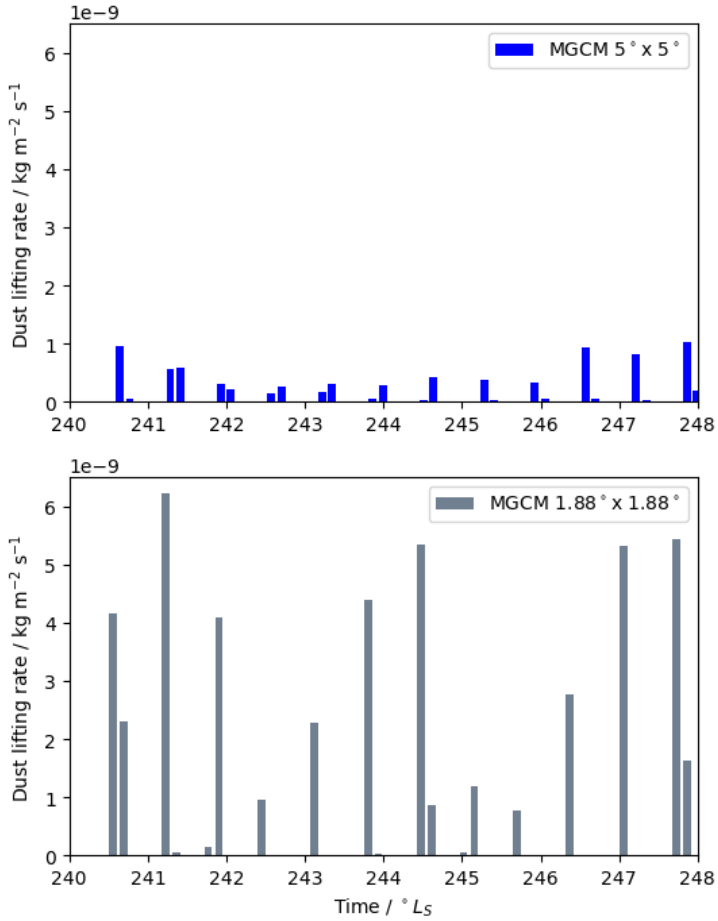

Figure 6.24: Dust devil dust lifting rates at the EDM landing site, as modelled in the MGCM, for ∼4° L_S either side of the module's landing date, for a) a T31 resolution experiment, and b) a T85 resolution experiment.

Opportunity rover data can again be used as an analogy to assess the accuracy of these model results. While other Mars landers and rovers have directly imaged multiple dust devils (e.g. *Ferri et al.*, 2003; *Greeley et al.*, 2006, 2010), Opportunity has rarely captured images containing dust devils (*JPL*). In addition, studies that have included Meridiani Planum as a target for dust devil surveys (e.g. *Cantor et al.*, 2006) have identified the region as exhibiting a low number of dust devils. Observations therefore suggest that this region does not exhibit a high level of dust devil activity, but that the phenomenon is not entirely absent; the model results are consistent with such observations.

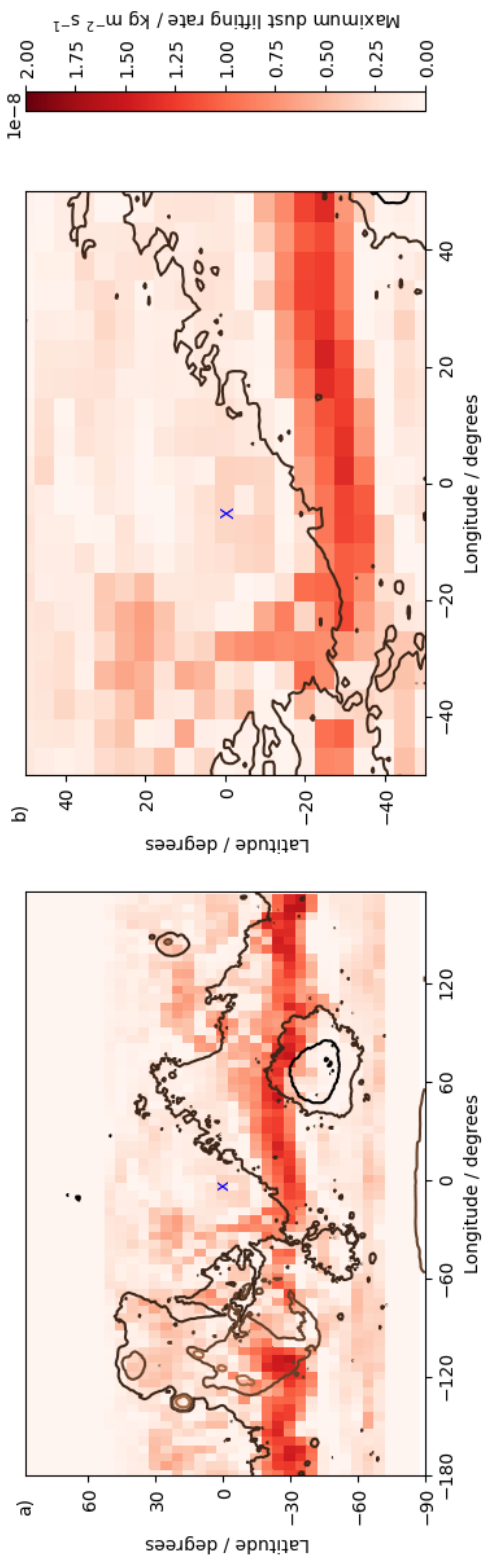

Figure 6.25: Maximum dust devil lifting rates through the period $\sim 4°$ L_S either side of the module's landing date, at the T31 ($5° \times 5°$) resolution: a) every MGCM surface gridbox, b) a magnification of the Meridiani Planum region. The location of the Schiaparelli landing site is indicated with a cross.

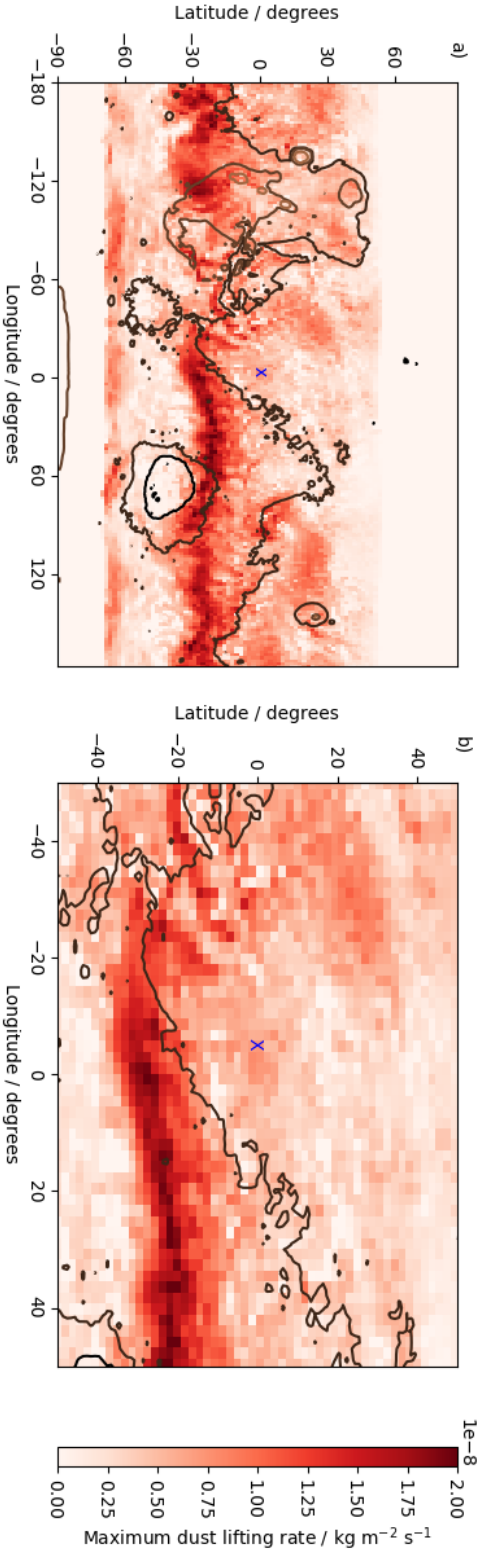

Figure 6.26: As Figure 6.25 for the MGCM experiment modelled at the T85 (1.875° × 1.875°) resolution.

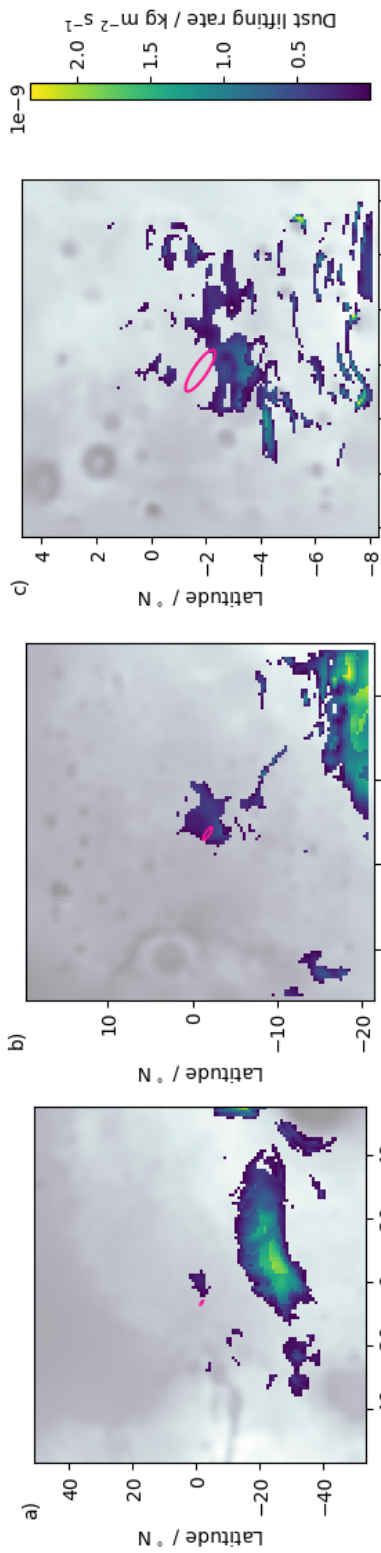

Figure 6.27: As Figure 6.23 for dust lifting by dust devils, in three MMM resolution domains: a) 63 km, b) 21 km, c) 7 km. These results relate to the same point in time: $L_S \sim 247°$, around 10:40. The estimated landing ellipse is drawn in all panels.

6.3.4 Models Comparison

The discrepancies between the atmospheric results achieved from the MGCM and the MMM are interesting, as the physics subroutines within the models are in general very similar, indeed sometimes identical, and the boundary conditions for the MMM experiments were constructed from MGCM results. Despite this, the results differ in several instances. The MMM atmospheric density profile exhibits values higher than the MGCM profile for much of their comparable height. The MMM temperature profile values are also higher than those in the MGCM profile, and the MMM data display a minor temperature inversion (∼1-2 K) below 4 km AMR that is not present in the MGCM profile. Interestingly, the MMM 7 km resolution temperature profile deviates from the other MMM profiles below ∼2.5 km AMR, but is a good match for the MGCM profile at this near-surface altitude.

The prime explanation for such discrepancies between models is the difference in simulation resolution. As discussed in Chapter 4, with reference to changing MGCM resolutions, increasing the horizontal resolution of a simulation allows an improved representation of a planet's surface properties, such as topography, albedo and thermal inertia. The properties of the Martian surface have a strong influence on low-altitude atmospheric heating and cooling, and on associated local winds (*Peterfreund*, 1981; *Forget et al.*, 2011). It is important to model accurate and appropriate surface data in order to facilitate the development of properly representative atmospheric dynamics within the modelled region (*Tyler and Barnes*, 2014). Local winds also interact with larger scale tides, and thus local variability can propagate to larger scales. Atmospheric circulations of a length that can only be resolved in the mesoscale will be missed in global simulations (*Tyler and Barnes*, 2014), and so their larger-scale impact will not be incorporated in global-scale results.

The MMM experiments use maps of Martian surface properties derived from observations made by instruments aboard the MGS spacecraft: MOLA topography and TES albedo and thermal inertia data. At the equatorial landing site, the resolutions of these data are: ∼1.4 km for topography (*Smith et al.*, 2001), ∼7.4 km for albedo and ∼3.0 km for thermal inertia (*Christensen et al.*, 2001).

The surface properties used within MGCM simulations are also based on MOLA and TES data, but are calculated from a dataset with a resolution of 1 pixel per degree (a maximum length of 59.3 km), which is then scaled to match the selected horizontal resolution of the experiment; this results in a grid spacing of ∼296 km at the landing site – a much poorer resolution than the surface in the MMM experiments (at 63 km, 21 km and 7 km).

While this discussion intimates that the higher resolution of a mesoscale model will always produce results that improve on the results obtained with a global-scale model, it is more accurate to state that simulations performed at the mesoscale are always expected to diverge slightly from those performed at a global scale. That divergence is often observed to be improvement, particularly when the modelled region involves highly varying topography such as chasms (*Spiga and Forget*, 2009), craters (*Rafkin et al.*, 2016) and mountains (*Spiga et al.*, 2011). However, *Tyler and Barnes* (2014) highlight the fact that, for certain locations, some Martian mesoscale models require an element of tuning to best represent the climate and weather patterns of a particular time of year.

Another possible explanation for the divergence between models is that they operate different dynamical cores. The MMM implements the LMD MGCM physics subroutines alongside an adaptation of the dynamical core of the NCAR AR-WRF (*Skamarock and Klemp*, 2008; *Spiga and Forget*, 2009), while the MGCM operates the same physics subroutines alongside the spectral core of the UK AOPP (Atmospheric, Oceanic and Planetary Physics department, Oxford) (*Hoskins and Simmons*, 1975; *Forget et al.*, 1999). *Tyler et al.* (2002) compared the performance of Martian global and mesoscale models and identified the different dynamical cores between the models as a potential cause of differences in the results; *Held and Suarez* (1994) even found some discrepancies in results achieved using two global models with different dynamical cores. Detailed investigations would be required to explore this topic, forming the core of a substantial future research project.

In contrast to the between-model variations seen in the atmospheric profiles, the comparison of MGCM and MMM surface dust lifting processes shows reasonable agreement between the models. Experimental results from both models display near-surface wind speeds at the EDM site that are within a similar range,

with maxima around 11 $\mathrm{m\,s^{-1}}$, and are below the speeds that could be expected to lift dust. Modelled dust devil activity is low through this period in both models. It should be noted that these near-surface MGCM results were obtained at a higher resolution than the atmospheric MGCM results, $\sim$1.88°, resulting in a gridsize of $\sim$111 km at the landing site, suggesting that the closer agreement between the models in these near-surface tests is related to the improvement in MGCM resolution.

All the experiments performed herein were completed under the assumption of hydrostatic equilibrium. While this is applicable at MGCM resolutions of hundreds of kilometres, it is possible for very high resolution mesoscale simulations to reach scales at which the hydrostatic assumption is no longer valid (*Spiga*, 2014). However, this will not greatly impact results until the modelled horizontal scale approaches that of the vertical length of any small-scale dynamic motions (*Tyler et al.*, 2002). As the smallest horizontal scale in the MMM experiments completed herein is 7 km, it is expected that an assumption of hydrostatic equilibrium will not adversely impact the performance of the simulation. In addition, for the version of the MMM that was available for these experiments it was recommended that the model be operated in hydrostatic mode to maintain stability – this is particularly the case for nested simulations – and the non-hydrostatic mode has not been tested with the incorporation of the dust lifting routines used herein. The author has not yet achieved successful nested, non-hydrostatic MMM experiments involving dust lifting, but this aspect of the MMM's performance would be an interesting subject for future work.

6.4 Summary

This case study of the EDM Schiaparelli landing site has focused on the lower portion of the atmosphere, comparing MGCM and MMM experimental results with the EDM profiles of atmospheric density, temperature and wind speeds through the available altitudes. The density and temperature profiles were compared through the portion of the atmosphere below the plasma blackout until the final data point: 30 to 2.76 km AMR. The wind speed profiles were compared only below 8.4 km AMR.

While MMM atmospheric density values are a closer match to the EDM data than MGCM values, for the portion of the descent from 30 to ∼9 km AMR, the percentage deviation in the comparison of MMM and EDM data increases with descent. In contrast, the percentage deviation in the comparison of MGCM and EDM data reduces with descent.

The variation in the EDM atmospheric density data below the height at which the parachute was opened (9.4 km AMR) could be the result of incomplete dynamic modelling through this portion of the descent. To assess how the potential inclusion of inaccurate data may have impacted forward calculations of atmospheric pressure and temperature, a proposed mean density profile was derived and then used to recalculate those quantities. The MGCM atmospheric temperature profile is a better match than the MMM results to both the EDM smoothed profile and to the proposed mean profile.

The EDM zonal and meridional wind speed profiles span most of the EDM's parachute descent, 8.4 to 2.8 km AMR. The EDM data exhibit an oscillation that is not present in the results from either model, and calculation of the resultant wind magnitude shows that the EDM wind vector describes a descending spiral. To explore this aspect of the data, mean wind speed profiles were calculated for both the zonal and meridional data. Comparing the modelled data against both the EDM smoothed and proposed mean profiles, the MGCM is a better match than the MMM to the direction and speeds in the EDM profiles.

The divergence between the results obtained from the global- and mesocale models is primarily due to the difference in experiment resolution. Higher resolution simulations allow a better representation of the small-scale variation in

surface properties such as topography, albedo and thermal inertia, which in turn affects small and larger scale fluctuations in temperature, density and wind. A higher resolution experiment will also capture smaller-scale atmospheric circulations that are missed in global-scale models. Thus, although the physical subroutines used across both scales of model are similar, the weather and climate patterns within the models can diverge. In previous Martian mesoscale studies this divergence has tended to result in an improvement over global-scale results, but the experiments completed within this case study suggest that this is not necessarily the result for every region.

The variation in the EDM atmospheric density and wind speed profiles may be evidence of true atmospheric features – for example, the density/temperature inversion in the EDM data at a height of ∼10 km AMR is believed to be a true feature – or may be artefacts of an incomplete parachute-motion model. This feature, and the variation in the final few kilometres of the descent, could be related to local atmospheric phenomena such as a small dust storm or dust cloud, or a convective vortex. Such phenomena could affect the local atmospheric temperature and density, and may provoke changes in small-scale wind patterns and speeds. These phenomena could be of a scale that is too small to be resolved by the MGCM or the MMM.

To explore the likelihood of the descending spacecraft encountering a dust event, modelled dust lifting within the region was investigated. A comparison of MGCM and MMM surface dust lifting processes shows reasonable agreement between the models through a period spanning the time of the EDM's descent. Results at the EDM site from both models show near-surface wind speeds that are of a similar range, and none of the experiments exhibited wind speeds high enough to lift dust at this location. Minor amounts of NSWS dust lifting occur in the region within the MMM model, at points associated with topographical variation. Modelled dust devil activity in the vicinity of the EDM site is low through this period in both of the models. The low levels of NSWS and dust devil lifting within the region encompassing the EDM site agree with observations of the area made by NASA's Opportunity rover.

The predicted low level of NSWS dust lifting at this site does not, in itself, preclude the existence of a small dust storm or cloud in the vicinity during the

EDM's descent, as the phenomena could have formed elsewhere and travelled through the region at the right time. The same is true of dust devils and convective vortices.

6.4.1 Recommendations

Through the lower portion of the EDM trajectory, the MGCM is able to provide a good (± 5% deviation) prediction of the proposed mean atmospheric temperature profile encountered by the spacecraft, and to generally match the direction and speed of the proposed mean wind field (RMSD of less than 3.5 $\mathrm{m\,s^{-1}}$ both zonally and meridionally) through the lowest ∼9 km of the descent. The MGCM should be used with confidence when predicting the large-scale atmospheric properties and circulations associated with future landing sites that are similar in topography and latitude to that of the ExoMars EDM.

The MMM as a model is not as mature as the MGCM. This investigation suggests that, in certain circumstances, MGCM simulations of mission entry and descent profiles are able to provide information that is of equal or greater accuracy than that produced by higher resolution MMM simulations. Since it is the case that a baseline MGCM simulation must be completed in order to generate the initial and boundary conditions for any MMM simulation, anyone planning future work on this topic should consider this finding when planning global and mesoscale modelling. It may be the case that spending a large portion of the planned modelling time completing a comprehensive set of high resolution global experiments, and then only modelling very local, short-term situations in the mesoscale, is a better use of time than a quick adoption of a mesoscale modelling regime.

That is not to assert that mesoscale experiments do not have their place, and such complex, high resolution simulations are indeed required when investigating certain aspects of the Martian atmosphere, such as detached dust layers (*Spiga et al.*, 2013), polar jets (*Toigo et al.*, 2012), crater circulations (*Tyler and Barnes*, 2015; *Rafkin et al.*, 2016; *Steele et al.*, 2017, 2018), polar water-ice cap edge sublimation (*Tyler and Barnes*, 2014), and water-ice clouds (*Michaels et al.*, 2006). It is also true that the more detailed representation of surface-level dust lifting processes that is possible within mesoscale results

is important in this particular avenue of study. However, for wide, relatively flat, equatorial landing locations – such as those often chosen historically for Mars surface missions – global scale modelling can provide atmospheric vertical profile information that is at least as accurate as mesoscale modelling.

With regard to surface dust lifting processes, it is difficult to fully assess the accuracy of the model results without ground truth data. However, MGCM and MMM results are consistent in their estimations of near-surface winds – and consequent NSWS dust lifting rates – and with respect to dust devil lifting rates, and these results are consistent with the limited ground-based and orbital observational data on this topic. As this work is unique in comparing the results of MMM surface dust lifting experiments against MGCM experiments for terrain of this type, this consistency across the different scale models is a positive outcome, indicating that the MMM dust cycle parameterisation is suitable for use in future research.

Chapter 7

Summary and Conclusions

This thesis set out to answer three research questions:

1. Does the model exhibit an accurate geographical representation of dust lifting, and is this representation robust?

2. Can the temporal variability of Martian dust lifting be deduced by comparison with terrestrial processes?

3. Is the model's prediction of the atmospheric and near-surface environment at a selected landing site accurate enough to aid mission planning?

This chapter summarises the work completed within this research and answers the questions with recommendations for the implementation of dust lifting processes within atmospheric models. This thesis concludes with suggestions for future work.

7.1 Overview of Research

To investigate the research questions three research themes were developed:

- Geographical representation of dust lifting
- Temporal representation of dust lifting
- Landing site case study

7.1.1 Geographical Representation of Dust Lifting

This work found that increasing the resolution of a Mars Global Circulation Model (MGCM) experiment, either horizontally or vertically, resulted in more geographically widespread lifting of dust by near-surface wind stress (NSWS). Few prior studies had considered how dust lifting parameterisations are affected by changes in model resolution. The increase in dust lifting with increased horizontal resolution was anticipated; the increased lifting with increased vertical resolution was not anticipated, and is believed to be an area not yet given proper consideration by the atmospheric modelling community.

Higher horizontal resolution experiments resulted in more geographically widespread dust lifting, as well as more dust lifting in total. The association between NSWS dust lifting and dust storm formation (e.g. *Kahn et al.*, 1992; *Strausberg et al.*, 2005; *Wang and Richardson*, 2015) allowed comparison of the results of these experiments with observations of storm forming regions, as dust must be lifted in order for storms to form. The higher resolution simulations produced a better geographical representation of the observed dust lifting regions, such as important storm-forming regions in the northern hemisphere during the approach to perihelion, and in regions along the edge of the southern hemisphere polar cap.

The total amount of dust lifted globally by the horizontal-resolution experiments increased with increasing resolution, displaying an asymptotic trend: the geographical distribution of dust lifting altered more noticeably between lower resolution experiments (T31 to T42) than between higher resolutions (T63 to T85). Very high resolution experiments were completed (T127 and T170), the results of which are tentatively used to support the identified trend, but these experiments are only considered preliminary tests due to model limitations at such high horizontal resolutions.

Increasing the model's vertical resolution also resulted in an improved geographical representation of dust lifting. As with the increasing horizontal resolution experiments, the areas within which more dust is lifted are generally associated with seasonal polar cap edges, although there are not as many 'new' dust lifting regions as were seen with horizontal change. These results were

not anticipated prior to these experiments. Within the field of Martian global atmospheric modelling, consideration has been given to how many vertical layers are required to best represent thermal tides (*Wilson and Hamilton*, 1996) and Hadley circulation (*Wilson*, 1997), but there is no published literature on the impact that changing model vertical resolution may have on surface-level processes.

This investigation found that near-surface peak wind speeds are larger in the higher vertical resolution experiments than at lower resolutions, consequently increasing NSWS dust lifting. A possible cause of this is the vertically-narrow features identified in some peak wind speed vertical profiles. These high peak wind speed features may be atmospheric perturbations that occur across relatively narrow vertical distances: they cannot be resolved at the lowest vertical resolutions, and therefore are not represented in those results.

7.1.2 Temporal Representation of Dust Lifting

This investigation found that dust devil activity within MGCM simulations displays a wider diurnal range than was anticipated, and that many regions actually display a peak in dust devil activity before mid-sol. Prior to this work there had been no published studies exploring this aspect of Martian dust devil behaviour: it was generally assumed that Martian dust devils would be most active during afternoon hours, as is the case on Earth (e.g. *Sinclair*, 1969; *Snow and McClelland*, 1990; *Lorenz and Lanagan*, 2014). Two possible explanations for this Martian dust devil behaviour are proposed:

- the dust devil parameterisation in use within MGCMs does not provide a good representation of the diurnal behaviour of Martian dust devils;
- the accepted description of dust devils on Mars is not complete.

The comparison of model results with published studies of observations of Martian dust devils suggests that the MGCM dust devil parameterisation *does* provide a good representation of Martian dust devil activity throughout the sol. Across the seven comparisons made with the published studies, three show a good match between modelled results and observations, three show a partial match, and one shows a minimal match. All of the comparison studies report

observations of dust devils (or pressure vortices) during morning hours. The observed maximum in dust devil activity is usually after mid-sol, but the timing of that peak varies across the studies.

Given that this parameterisation is a good representation of dust devils, it is therefore proposed that the generally accepted description of dust devil behaviour on Mars is incomplete. Martian dust devil activity does not necessarily peak in the early afternoon across all regions, and local wind speeds may act as a strong governor of the timings of dust devils. Parameterised dust devil activity depends upon the sensible heat available to the dust devil and its thermodynamic efficiency. Most of the parameters involved in calculating both of these quantities follow predictable diurnal patterns that peak in mid-afternoon (including surface temperature), with the exception being the near-surface wind speed. It is the variability within the near-surface wind speed that introduces variability into the diurnal timings of dust devils.

7.1.3 Landing Site Case Study

This case study found that, for certain landing locations on Mars, the global-scale MGCM performs as well as the higher resolution Mars Mesoscale Model (MMM), with regard to predictions of atmospheric conditions the lander will encounter. Prior to these experiments it was expected that the mesoscale results would depict more accurately a lander's descent environment. Previous comparisons of results from different scale models have often focused on areas featuring large variations in local terrain (e.g. *Rafkin et al.*, 2001; *Spiga and Forget*, 2009), rather than the relatively flat location selected for the landing site of the ESA ExoMars Entry Demonstrator Module (EDM).

This study focused on the lower portion of the EDM's trajectory towards the selected landing site. (The very top of the MGCM's range of modelled altitude is less representative of the Martian atmosphere, due to factors such as atmospheric sponge layers and limited atmospheric chemistry, and the EDM entered a plasma blackout between 68 km Above MOLA Radius (AMR) and 30 km AMR.) Model and spacecraft data for atmospheric density and temperature profiles were compared through altitudes of 30 to 2.76 km AMR, while wind speed profiles were compared only below 8.4 km AMR. Neither MGCM nor

MMM data predicted precisely the values in the data returned by the spacecraft for atmospheric densities or temperatures, but the MGCM results generally display a better match to the EDM data. When comparing the EDM mean wind speed profiles, the MGCM is the model that best predicts the wind direction and speeds.

The discrepancy between model results and spacecraft data may be evidence of a more complex dust environment in the mid-altitude Martian atmosphere than that currently used in the MGCM or the MMM. The typical vertical dust profile used in the MGCM and MMM is a Conrath profile (*Conrath*, 1975), in which the density of dust in the atmosphere is greatest in the near-surface boundary region and decreases with height. Recent Mars Climate Sounder (MCS) data (*Heavens et al.*, 2011a) and data from the Mars Global Surveyor (MGS) Thermal Emission Spectrometer (TES) (*Heavens et al.*, 2011b) have identified discrete dust layers around altitudes of 60 km, higher than the top of the well-mixed dust region in the lower atmosphere. *Guzewich et al.* (2013b) were able to improve the match between MarsWRF (Weather Research and Forecasting) GCM results and TES data by implementing a dust climatology that included these high altitude dust layers; similar improvement may be possible within the MGCM and MMM.

EDM reported data below the point of parachute deployment show rapid variation, and the reported wind speed profiles exhibit a $\sim$1 km-wavelength oscillation that is not present in the results from either model. The variation in the profiles below this altitude (9.4 km AMR) may be a result of true atmospheric features, or a product of incomplete dynamic modelling through this portion of the descent.

True atmospheric features that could have affected the EDM during descent include local atmospheric phenomena such as a small dust storm or dust cloud, or a convective vortex (which might be a dust devil). Modelled dust lifting within the region was explored, to investigate the likelihood of the descending spacecraft encountering a dust event. The MGCM and MMM dust lifting data show agreement on low levels of NSWS dust lifting and dust devil activity within the region surrounding the landing site, through the sols immediately before and after the landing time. This is corroborated by surface and orbital observations

of the area. No published studies have compared directly surface dust lifting across global-scale and mesoscale models, and parameterisations of NSWS dust lifting have rarely been used in prior MMM experiments.

7.2 Conclusions and Recommendations

7.2.1 Question 1: Does the model exhibit an accurate, robust geographical representation of dust lifting?

Climate models can be considered robust if they produce results that show agreement with observations (*Knutti and Sedláček*, 2013). Robustness within computer modelling in general is "the degree to which a system or component can function correctly in the presence of invalid inputs" (*IEEE*, 1990). With regard to these MGCM experiments, the 'invalid input' could be considered to be the limitations inherent in global-scale resolutions, and the geographical spread of dust lifting is one assessment of the accuracy of the results.

Increasing model horizontal resolution provides a better representation of underlying topographical features, affecting local wind circulations and driving a better geographical representation of surface dust lifting. This study found that the trend of improved representation with increased resolution is not linear: T63 results are more similar to T85 results than to those at the lower resolutions (across wind speed distributions, geographical spread of dust lifting, and total dust lifted annually), despite each step in resolution increase being approximately equal.

This investigation found that the experiment completed at the T63 resolution resolves dust lifting in regions that the lower resolution experiments could not. The T85 experiment improves on the representation of wind speeds and dust lifting in these regions, but it is the inclusion of this lifting (compared to its previous absence) that drives the difference in the results between the lowest and highest resolutions. These dust lifting regions, at polar cap edges in both hemispheres, correlate with observed storm-forming regions. At such latitudes, a T63 experiment is able to resolve surface features of lengths below 100 km. These results suggest that the ability to resolve surface features of the order of

100 km improves the representation of dust lifting within the MGCM.

This work shows that increasing the vertical resolution of the MGCM also provides a better representation of the geographical patterns of surface dust lifting, potentially due to a better resolution of the vertical structure of the lower atmosphere. The correlation between improved representation and increased resolution is more ambiguous than in the horizontal case, with the highest vertical resolutions investigated herein (L100) displaying a reduced geographical spread of dust lifting (and total dust lifted annually) compared to mid-range resolutions (e.g. L60).

Prior to these experiments consideration had been given, within the field of Martian global atmospheric modelling, to how many vertical layers are required to best represent large-scale phenomena such as thermal tides (*Wilson and Hamilton*, 1996) and Hadley circulation (*Wilson*, 1997), but there is no published literature on the impact that changing model vertical resolution may have on surface-level processes.

Recommendations

This work showed that, within MGCM experiments, the geographical pattern of dust lifting produced at the typical 'climate modelling' horizontal and vertical resolutions is not a good representation of surface dust lifting regions on Mars. This author recommends that the model's geographical representation of dust lifting should only be considered robust when operated using a horizontal resolution of T63 ($\sim$2.5° latitude $\times$ $\sim$2.5° longitude) or higher, and with a vertical resolution of at least 50 layers.

It is recommended that the low horizontal and vertical MGCM resolutions typically used for long-term climate modelling (e.g. *Basu et al.*, 2004; *Kahre et al.*, 2005; *Newman et al.*, 2005; *Toigo et al.*, 2012; *Steele et al.*, 2014) are no longer used in any experiments designed to investigate surface-level processes (such as studies of ground sources of methane), or to study the impact on the wider atmosphere of the products of such processes. It is likely that these processes, their seasonal and annual variation, and any atmospheric tracers they produce, will not be well represented at these low resolutions. These findings are crucially important for future users of this particular MGCM, but will also

be useful for anyone using global atmospheric models – Martian and otherwise – to explore surface-level processes.

Combining these recommended resolutions within global-scale model simulations may result in prohibitively long simulation times. Hence a final recommendation is that the goal of any MGCM experiment is considered carefully prior to the initiation of any high resolution simulations. Completing a long-term simulation at a mid-level resolution (e.g. T42L40), interpolating the results, and then completing a shorter-term experiment at a higher resolution, may provide one route for optimising simulation time. The success of this approach will necessarily depend on the precise nature of the experiments in question.

7.2.2 Question 2: Can the temporal variability of Martian dust lifting be deduced from terrestrial processes?

Modelled Martian dust devils display a higher level of dust devil activity during morning hours than was anticipated. This activity is also spread more widely throughout the length of the sol than expected.

This investigation has shown that diurnal variation in dust devil activity within the MGCM is governed by near-surface wind speeds. Within the range of daylight hours, higher wind speeds tend to produce higher levels of dust devil activity, rather than the activity being simply governed by the availability of heat at the planet's surface, which peaks in early afternoon.

These findings were corroborated by comparing modelled results with published surface mission *in situ* observations of Martian dust devils. There are caveats in the corroboration to be considered, such as the fact that some of the studies used pressure data to detect atmospheric vortices, and not all vortices entrain dust, so drawing a direct parallel between vortice numbers and dust devils number may over-estimate the dust devil population. In addition, the model reports the rate of dust lifting by dust devils, but cannot specify the number or the size of the dust devils required to lift a given amount of dust. Finally, the simulations were completed at a resolution resulting in gridboxes with areas of several hundred square kilometres, so the data relate to quantities present in these large-scale gridboxes rather than at more local points upon the

surface. However, even allowing these caveats, the model results provide at least a partial match with dust devil observations in the majority of the published studies.

The generally accepted model of Martian dust devil behaviour follows that of terrestrial dust devils, with activity peaking during afternoon hours. This thesis proposes that the generally accepted description of dust devil behaviour on Mars is incomplete, and that theories of dust devil formation may need to be modified specifically for the Martian environment. The results of these experiments are useful both to atmospheric modellers and to researchers studying Martian dust devils through surface and orbital observations.

Recommendations

Theories of Martian dust devil formation may need to be re-assessed, and should at least be better tested with further observations. The model for terrestial dust devil formation may need to be tailored specifically in order to be more appropriate within a thin, cold, dry atmosphere that spans the surface of a planet, to allow for higher rates of dust devil formation during morning hours.

The differences between the terrestrial and Martian atmospheres should also be considered carefully during the parameterisation of surface-atmosphere processes. The current MGCM parameterisation of dust devils is not necessarily incorrect, but it may be incomplete. One example of this is the input heat source driving the dust devil 'heat engine' model. In models of terrestrial dust devils the sensible heat flux is a key factor in the total surface energy budget, and so it is used as the dominant heat source driving dust devil formation. In contrast, in the lower density Martian atmosphere the surface energy budget calculation is dominated by radiative fluxes. A more accurate Martian dust devil parameterisation would incorporate a more complex representation of the input heat available for dust devil formation.

Further surveys of dust devil observations are required to support modification of theory and improvement in model parameterisation. Such studies must extend throughout the full diurnal period, and should encompass surface and orbital observations. Ideally, any observations should be placed within a wider meteorological context, including measurements of local temperatures and wind

speeds. This would allow further investigation into connections between the behaviour of dust devils and the local meteorological environment, and also facilitate comparisons with studies of terrestrial dust devils.

7.2.3 Question 3: Is the model's prediction of the environment at a selected landing site accurate enough to aid mission planning?

This case study showed that through the lower portion of the EDM's trajectory, the MGCM is able to provide a reasonable prediction of the trends in atmospheric properties encountered by the spacecraft (e.g. model temperature predictions deviate only ± 5% from the proposed mean atmospheric temperature profile encountered by the spacecraft). The MGCM results also show winds that generally match the direction and speed of the mean wind fields reported through the final few kilometres of the module's descent, with a model-to-observations Root Mean Square Deviation of less than 3.5 $\mathrm{m\,s^{-1}}$ both zonally and meridionally. The MMM results provide a comparable prediction of atmospheric density but are a poorer match for temperatures and wind fields.

These findings suggest that, at least in certain circumstances, MGCM simulations of mission entry and descent profiles can provide results that are of equal or greater accuracy than those produced by higher resolution MMM simulations. The MGCM can therefore be used with confidence when predicting large-scale atmospheric properties and circulations associated with future landing sites – if those sites are relatively flat and uninterrupted by areas of steep topographic gradient.

With regard to surface dust lifting processes, the MGCM and MMM results are consistent in their estimations of dust lifting rates (and are also consistent with the limited observational data). This work is unique in comparing the results of MMM surface dust lifting experiments against MGCM experiments for terrain of this type, and so this consistency across the different scale models is a positive outcome, indicating that the MMM dust cycle parameterisation is suitable for use in future research.

Recommendations

Mesoscale experiments are still crucial for detailed investigations into complex aspects of the Martian atmosphere, and further exploration of mesoscale representations of surface-level dust lifting processes will be an important avenue of study.

However, this thesis proposes that future planning of global and mesoscale modelling campaigns should consider carefully the near-surface environment being modelled: it is possible that spending a large portion of the modelling schedule completing a comprehensive set of high resolution global experiments, and only then modelling local, short-term situations in the mesoscale, will be a better use of time than an early adoption of the mesoscale modelling regime.

7.3 Further work

Model Resolution Studies

This work has quantified the effect of model resolution on one Martian surface dust lifting process, and made specific recommendations with regard to the operation of the MGCM. However, a large number of future avenues of research still exist within this theme, including further work to test the robustness of this aspect of the model:

- **Very high horizontal resolution simulations**
  - Correct the MGCM code to facilitate the compilation and completion of experiments at very high horizontal resolutions, such as T127 and T170, with an improved vertical resolution to that currently possible.
  - Run T170 experiments at a higher data output-rate-per-sol, to enable direct comparison with the set of lower resolution simulations completed within this work.
- **Increased vertical resolution simulations**
  - Investigate the impact of increasing the vertical resolution to L60 and above in experiments using mid-to-high horizontal resolutions

(i.e T63 and upwards). Note: such experiments will take a long time to complete with the current build of the MGCM.

- **Atmospheric features in vertical profiles**
  - Explore apparent features identified in wind speed vertical profiles. Investigate frequency, diurnal and seasonal timings, potential trends in altitude, association with terrain height or surface properties.
  - Test the likelihood of such features affecting near-surface wind speeds.
- **Storm observation comparisons**
  - Investigate the lack of modelled dust lifting through L_S = 120-180°. A number of storms have been observed during this period, widely spread across the Northern Hemisphere, but the associated dust lifting is not exhibited in the model results at any resolution so far tested.
  - Expand the storm observation survey to include smaller, local storms, and attempt a more temporally discrete comparison between observations and model results.
- **Extending tests of model robustness**
  - Explore the interaction of the lifting efficiency parameter, α_N, and the lifting threshold velocity, u_t^*, as horizontal and vertical model resolution are increased.
  - Run repeated identical simulations at multiple horizontal and vertical resolutions to assess and quantify the variability within long-term experiments, and whether this is affected by resolution change. This could assist future improvements in long-term simulations using different climate states, e.g. experiments modelling the past or future Mars climate, which may vary parameters such as obliquity.

Temporal Variability of Dust Lifting

The subject of the diurnal variability of Martian dust lifting processes allows several opportunities for further investigation:

- **Dust devil lifting**
  - Test the current Martian dust devil parameterisation by incorporating it into an Earth GCM. GCMs used in Earth climate modelling usually do not include detailed parameterisations of dust devil behaviour (*Engelstaedter and Washington*, 2007), primarily because the contribution to the global aerosol budget of dust lifted by dust devils is minimal (*Jemmett-Smith et al.*, 2015), although Large Eddy Simulations have been developed that consider convective lifting phenomena (*Klose and Shao*, 2013).
  - Improve the representation of the input heat available for dust devil formation within the parameterisation, i.e. use radiative fluxes, rather than sensible heat flux, to calculate the surface energy budget.
  - Consider the specific differences between the Martian and terrestrial atmospheric environments and develop a more tailored theory of Martian dust devil formation.
- **Near-surface wind stress lifting**
  - Explore the diurnal variability of NSWS dust lifting, and how this may vary through the course of the year.
- **Comparison with observations**
  - Compare the diurnal timings of future observations of dust devils with the findings of this investigation, both orbital (e.g. CaSSIS) and surface (e.g. Curiosity, InSight) missions, with a goal of assessing the wider meteorological context surrounding Martian dust devil formation and development.
  - Compare the modelled Martian dust devil activity with future terrestrial studies of the diurnal timings of dust devil, such as *Klose et al.* (2014) and the Europlanet Moroccan desert study completed in June

2018 (led by J. Raack), which test the assumption that terrestrial dust devils are always more common during afternoon hours.

Landing Site Predictions

Although the data returned by the EDM are limited in nature, the results of this case study still open up further lines of research:

- **Model improvements**
  - Explore the discrepancies between MGCM temperature profile data and the EDM and Mars Climate Sounder data, with regard to potential temperature inversions at mid-altitudes; this should include comparisons with descent profiles obtained from other spacecraft.
- **Increased complexity in simulations**
  - Test the impact of increasing the vertical resolution of MMM simulations.
  - Run MMM simulations including the dust lifting parameterisations for different locations across the surface of the planet, including regions that have more varied topography than the EDM landing site.
  - Test the operation of the dust lifting parameterisations within non-hydrostatic MMM simulations.
  - Complete longer-term MMM experiments.
  - Explore two-way nesting within MMM simulations.
  - When possible, explore the results of very high horizontal and vertical resolution MGCM simulations at the EDM landing site location.
- **Model comparisons**
  - Investigate whether MGCM results still out-perform MMM results at this location through different seasons, and at different times during the sol.
  - Explore similar historical and potential landing sites (i.e. equatorial latitudes with relatively flat topography) and compare MGCM and MMM results.

  - Quantify the differences between the Martian surface used in both models (e.g. details in topography, albedo and thermal inertia) and assess how any divergence in the representation of surface properties may impact the dust lifting parameterisations.

- **Further comparison with observations**

  - Comparison of MGCM and MMM results with observations of the (relatively) local environment recorded by Opportunity, and any images taken by the rover during the sol of the EDM's descent, could provide additional information on the low-altitude dust environment that the EDM encountered. These data have not yet been released at the time of writing.

7.4 Final Words

Atmospheric dust is a key component in the Martian climate. Improving our understanding of the dust cycle (lifting, transportation and deposition) improves our insight into Martian long-term weather and climate patterns, and facilitates better predictions of the future climate of the planet. This work has explored in detail one aspect of the Martian dust cycle, focusing on the representation of surface dust lifting processes within a global atmospheric model, and considering the impact of dust lifting on the near-surface environment.

The recommendations made with regard to changes in model resolution are crucially important for future users of this particular MGCM, and are expected to be relevant to researchers currently using other Mars GCMs. The findings in this thesis may also be of use to scientists operating global atmospheric models for other terrestrial bodies.

The dust devil parameterisation in operation within the MGCM has been used as the basis for similar parameterisations in the NASA Ames Mars GCM and the GFDL Mars GCM. The findings of this investigation are therefore relevant and important to the wider Martian atmospheric modelling community. The results are also of interest to scientists planning dust devil observation campaigns for Martian surface missions.

The landing site case study found that, for certain landing locations on Mars, the global-scale MGCM performs as well as the mesoscale MMM. This is an important finding that should be considered when planning atmospheric modelling campaigns for Mars landing missions.

The MGCM is a robust global atmospheric model. It is a crucial experimental ground for further exploration of the temporal and geographical variation in Martian surface dust lifting processes.

Bibliography

Aboudan, A., G. Colombatti, C. Bettanini, F. Ferri, S. R. Lewis, B. Van Hove, O. Karatekin, and S. Debei, Schiaparelli Module Trajectory and Atmospheric Profiles Reconstruction, submitted, space Science Reviews.

Almeida, M. P., E. J. R. Parteli, J. S. Andrade, and H. J. Herrmann, Giant saltation on Mars, *Proceedings of the National Academy of Sciences*, *105*, 6222–6226, 2008.

Anderson, E., and C. Leovy, Mariner 9 Television Limb Observations of Dust and Ice Hazes on Mars, *Journal of the Atmospheric Sciences*, *35*, 723–734, 1978.

Andrews, D. G., *An Introduction to Atmospheric Physics*, second ed., Cambridge University Press, 2010.

Bagnold, R. A., The Transport of Sand by Wind, *The Geographical Journal*, *89*, 409–438, 1937.

Balme, M. R., and R. Greeley, Dust devils on Earth and Mars, *Reviews of Geophysics*, *44*, RG3003, 2006.

Balme, M. R., S. M. Metzger, M. C. Towner, T. J. Ringrose, R. Greeley, and J. Iversen, Friction wind speeds in dust devils: A field study, *Geophysical Research Letters*, *30*, 2003a.

Balme, M. R., P. L. Whelley, and R. Greeley, Mars: Dust devil track survey in Argyre Planitia and Hellas Basin, *Journal of Geophysical Research: Planets*, *108*, 5086, 2003b.

3483 Balme, M. R., et al., Field measurements of horizontal forward motion velocities
3484 of terrestrial dust devils: Towards a proxy for ambient winds on Mars and
3485 Earth, *Icarus*, *221*, 632–645, 2012.

3486 Basu, S., M. I. Richardson, and R. J. Wilson, Simulation of the Martian dust
3487 cycle with the GFDL Mars GCM, *Journal of Geophysical Research*, *109*,
3488 E11,006, 2004.

3489 Basu, S., J. Wilson, M. I. Richardson, and A. Ingersoll, Simulation of sponta-
3490 neous and variable global dust storms with the GFDL Mars GCM, *Journal*
3491 *of Geophysical Research*, *111*, E09,004, 2006.

3492 Bourke, W., An efficient, one-level, primitive-equation spectral model, *Monthly*
3493 *Weather Review*, *100*, 683–691, 1972.

3494 Bourke, W., A Multi-Level Spectral Model. I. Formulation and Hemispheric
3495 Integrations, *Monthly Weather Review*, pp. 687–701, 1974.

3496 Cantor, B. A., MOC observations of the 2001 Mars planet-encircling dust storm,
3497 *Icarus*, *186*, 60–96, 2007.

3498 Cantor, B. A., P. B. James, M. Caplinger, and M. J. Wolff, Martian dust storms:
3499 1999 Mars Orbiter Camera observations, *Journal of Geophysical Research*,
3500 *106*, 23,653, 2001.

3501 Cantor, B. A., K. M. Kanak, and K. S. Edgett, Mars Orbiter Camera obser-
3502 vations of Martian dust devils and their tracks (September 1997 to January
3503 2006) and evaluation of theoretical vortex models, *Journal of Geophysical*
3504 *Research*, *111*, E12,002, 2006.

3505 Cantor, B. A., P. B. James, and W. M. Calvin, MARCI and MOC observations
3506 of the atmosphere and surface cap in the north polar region of Mars, *Icarus*,
3507 *208*, 61–81, 2010.

3508 Chapman, R. M., S. R. Lewis, M. Balme, and L. J. Steele, Diurnal Variation in
3509 Martian Dust Devil Activity, *Icarus*, *292*, 154–167, 2017.

3510 Chen, A., A. Cianciolo, A. R. Vasavada, C. Karlgaard, J. Barnes, B. A. Cantor,
3511 D. M. Kass, S. C. R. Rafkin, and D. Tyler, Reconstruction of Atmospheric

Properties from Mars Science Laboratory Entry, Descent, and Landing, *Journal of Spacecraft and Rockets*, *51*, 1062–1075, 2014.

Choi, D. S., and C. M. Dundas, Measurements of Martian dust devil winds with HiRISE, *Geophysical Research Letters*, *38*, n/a–n/a, 2011.

Christensen, P. R., et al., Mars Global Surveyor Thermal Emission Spectrometer experiment: Investigation description and surface science results, *Journal of Geophysical Research: Planets*, *106*, 23,823–23,871, 2001.

Clancy, R. T., S. W. Lee, G. R. Gladstone, W. W. McMillan, and T. Rousch, A new model for Mars atmospheric dust based upon analysis of ultraviolet through infrared observations from Mariner 9, Viking, and Phobos, *Journal of Geophysical Research*, *100*, 5251, 1995.

Clancy, R. T., B. J. Sandor, M. J. Wolff, P. R. Christensen, M. D. Smith, J. C. Pearl, B. J. Conrath, and R. J. Wilson, An intercomparison of ground-based millimeter, MGS TES, and Viking atmospheric temperature measurements: Seasonal and interannual variability of temperatures and dust loading in the global Mars atmosphere, *Journal of Geophysical Research*, *105*, 9553, 2000.

Clancy, R. T., M. J. Wolff, B. A. Whitney, B. A. Cantor, M. D. Smith, and T. H. McConnochie, Extension of atmospheric dust loading to high altitudes during the 2001 Mars dust storm: MGS TES limb observations, *Icarus*, *207*, 98–109, 2010.

Claudin, P., and B. Andreotti, A scaling law for aeolian dunes on Mars, Venus, Earth, and for subaqueous ripples, *Earth and Planetary Science Letters*, *252*, 30–44, 2006.

Colburn, D. S., J. B. Pollack, and R. M. Haberle, Diurnal variations in optical depth at Mars, *Icarus*, *79*, 159–189, 1989.

Conrath, B. J., Thermal structure of the Martian atmosphere during the dissipation of the dust storm of 1971, *Icarus*, *24*, 36–46, 1975.

Daerden, F., J. A. Whiteway, L. Neary, L. Komguem, M. T. Lemmon, N. G. Heavens, B. A. Cantor, E. Hébrard, and M. D. Smith, A solar escalator on

Mars: Self-lifting of dust layers by radiative heating, *Geophysical Research Letters*, *42*, 7319–7326, 2015.

de Vaucouleurs, G., M. E. Davies, and F. M. Sturms, Mariner 9 Areographic Coordinate System, *Journal of Geophysical Research*, *78*, 4395–4404, 1973.

Ellehoj, M. D., et al., Convective vortices and dust devils at the Phoenix Mars mission landing site, *Journal of Geophysical Research*, *115*, E00E16, 2010.

Engelstaedter, S., and R. Washington, Atmospheric controls on the annual cycle of North African dust, *Journal of Geophysical Research*, *112*, D03,103, 2007.

Esau, I. N., Parameterization of a surface drag coefficient in conventionally neutral planetary boundary layer, *Annales Geophysicae*, *22*, 3353–3362, 2004.

Esposito, F., et al., The DREAMS experiment on the ExoMars 2016 mission for the study of Martian environment during the dust storm season, in *Fifth International Workshop on the Mars Atmosphere: Modelling and Observations*, 2014.

Fenton, L. K., and R. D. Lorenz, Dust devil height and spacing with relation to the martian planetary boundary layer thickness, *Icarus*, *260*, 246–262, 2015.

Fenton, L. K., P. E. Geissler, and R. M. Haberle, Global warming and climate forcing by recent albedo changes on Mars., *Nature*, *446*, 646–9, 2007.

Fenton, L. K., D. Reiss, M. T. Lemmon, B. Marticorena, S. R. Lewis, and B. A. Cantor, Orbital Observations of Dust Lofted by Daytime Convective Turbulence, *Space Science Reviews*, pp. 1–54, 2016.

Ferri, F., P. H. Smith, M. T. Lemmon, and N. O. Rennó, Dust devils as observed by Mars Pathfinder, *Journal of Geophysical Research*, *108*, 5133, 2003.

Ferri, F., F. Forget, S. R. Lewis, and O. Karatekin, ExoMars Atmospheric Mars Entry and Landing Investigations and Analysis (AMELIA), in *9th International Planetary Probe Workshop (IPPW9)*, 2012.

Ferri, F., et al., Atmospheric Mars Entry and Landing Investigations & Analysis (AMELIA) by ExoMars 2016 Schiaparelli Entry Descent Module, in *2017 IEEE International Workshop on Metrology for AeroSpace*, 2017.

Fisher, J. A., M. I. Richardson, C. E. Newman, M. A. Szwast, C. Graf, S. Basu, S. P. Ewald, A. D. Toigo, and R. J. Wilson, A survey of Martian dust devil activity using Mars Global Surveyor Mars Orbiter Camera images, *Journal of Geophysical Research*, *110*, E03,004, 2005.

Fitzjarrald, D. E., A Field Investigation of Dust Devils, *Journal of Applied Meteorology*, *12*, 808–813, 1973.

Forget, F., F. Hourdin, and O. Talagrand, CO2 Snowfall on Mars: Simulation with a General Circulation Model, *Icarus*, *131*, 302–316, 1998.

Forget, F., F. Hourdin, R. Fournier, C. Hourdin, O. Talagrand, M. Collins, S. R. Lewis, P. L. Read, and J. P. Huot, Improved general circulation models of the Martian atmosphere from the surface to above 80 km, *Journal of Geophysical Research*, *104*, 24,155–24,175, 1999.

Forget, F., A. Spiga, L. Montabone, E. Millour, A. Colaïtis, and V. Bourrier, Characterizing the Martian atmosphere for the ExoMars 2016 lander, in *Fourth International Workshop on the Mars Atmosphere: Modeling and Observations*, 2011.

Forget, F., E. Millour, and S. R. Lewis, Mars Climate Database v5.1 Detailed Design Document, *Tech. rep.*, 2015.

Gierasch, P. J., and R. M. Goody, The Effect of Dust on the Temperature of the Martian Atmosphere, *Journal of the Atmospheric Sciences*, *29*, 400–402, 1971.

Gierasch, P. J., and R. M. Goody, A Model of a Martian Great Dust Storm, *Journal of the Atmospheric Sciences*, *30*, 169–179, 1973.

Greeley, R., Saltation impact as a means for raising dust on Mars, *Planetary and Space Science*, *50*, 151–155, 2002.

Greeley, R., M. R. Balme, J. Iversen, S. M. Metzger, R. Mickelson, J. Phoreman, and B. White, Martian dust devils: Laboratory simulations of particle threshold, *Journal of Geophysical Research*, *108*, 5041, 2003.

Greeley, R., D. A. Waller, N. A. Cabrol, G. A. Landis, M. T. Lemmon, L. D. V. Neakrase, M. Pendleton Hoffer, S. D. Thompson, and P. L. Whelley, Gusev Crater, Mars: Observations of three dust devil seasons, *Journal of Geophysical Research*, *115*, E00F02, 2010.

Greeley, R., et al., Active dust devils in Gusev crater, Mars: Observations from the Mars Exploration Rover Spirit, *Journal of Geophysical Research*, *111*, E12S09, 2006.

Guzewich, S. D., E. R. Talaat, A. D. Toigo, D. W. Waugh, and T. H. McConnochie, High-altitude dust layers on Mars: Observations with the Thermal Emission Spectrometer, *Journal of Geophysical Research: Planets*, *118*, 1177–1194, 2013a.

Guzewich, S. D., A. D. Toigo, M. I. Richardson, C. E. Newman, E. R. Talaat, D. W. Waugh, and T. H. McConnochie, The impact of a realistic vertical dust distribution on the simulation of the Martian General Circulation, *Journal of Geophysical Research: Planets*, *118*, 980–993, 2013b.

Guzewich, S. D., A. D. Toigo, and D. W. Waugh, The effect of dust on the martian polar vortices, *Icarus*, *278*, 100–118, 2016.

Haberle, R. M., Planetary Atmospheres: Mars, *Encyclopedia of Atmospheric Sciences*, *5*, 1745–1755, 2003.

Haberle, R. M., C. B. Leovy, and J. B. Pollack, Some effects of global dust storms on the atmospheric circulation of Mars, *Icarus*, *50*, 322–367, 1982.

Haberle, R. M., R. T. Clancy, F. Forget, M. D. Smith, and R. W. Zurek (Eds.), *The Atmosphere and Climate of Mars*, Cambridge University Press, Cambridge, 2017.

Hanel, R. A., B. J. Conrath, W. A. Hovis, V. G. Kunde, P. D. Lowman, J. C. Pearl, C. Prabhakara, B. Schlachman, and G. V. Levin, Infrared Spectroscopy Experiment on the Mariner 9 Mission: Preliminary Results, *Science*, *175*, 305–308, 1972.

Hansen, J. E., and L. D. Travis, Light scattering in planetary atmospheres, *Space Science Reviews*, *16*, 527–610, 1974.

Heavens, N. G., Textured Dust Storm Activity in Northeast Amazonis–Southwest Arcadia, Mars: Phenomenology and Dynamical Interpretation, *Journal of the Atmospheric Sciences*, *74*, 1011–1037, 2017.

Heavens, N. G., D. J. McCleese, M. I. Richardson, D. M. Kass, A. Kleinböhl, and J. T. Schofield, Structure and dynamics of the Martian lower and middle atmosphere as observed by the Mars Climate Sounder: 2. Implications of the thermal structure and aerosol distributions for the mean meridional circulation, *Journal of Geophysical Research*, *116*, E01,010, 2011a.

Heavens, N. G., M. S. Johnson, W. A. Abdou, D. M. Kass, A. Kleinböhl, D. J. McCleese, J. H. Shirley, and R. J. Wilson, Seasonal and diurnal variability of detached dust layers in the tropical Martian atmosphere, *Journal of Geophysical Research: Planets*, *119*, 1748–1774, 2014.

Heavens, N. G., et al., The vertical distribution of dust in the Martian atmosphere during northern spring and summer: Observations by the Mars Climate Sounder and analysis of zonal average vertical dust profiles, *Journal of Geophysical Research*, *116*, E04,003, 2011b.

Hébrard, E., C. Listowski, P. Coll, B. Marticorena, G. Bergametti, A. Määttänen, F. Montmessin, and F. Forget, An aerodynamic roughness length map derived from extended Martian rock abundance data, *Journal of Geophysical Research: Planets*, *117*, 2012.

Heintzenberg, J., Properties of the Log-Normal Particle Size Distribution, *Aerosol Science and Technology*, *21*, 46–48, 1994.

Held, I. M., and M. J. Suarez, A Proposal for the Intercomparison of the Dynamical Cores of Atmospheric General Circulation Models, *Bulletin of the American Meteorological Society*, *75*, 1825–1830, 1994.

Hess, S. L., Some Aspects of the Meteorology of Mars, *Journal of Meteorology*, *7*, 1–13, 1950.

Hinson, D. P., and H. Wang, Further observations of regional dust storms and baroclinic eddies in the northern hemisphere of Mars, *Icarus*, *206*, 290–305, 2010.

Hinson, D. P., M. Pätzold, S. Tellmann, B. Häusler, and G. L. Tyler, The depth of the convective boundary layer on Mars, *Icarus*, *198*, 57–66, 2008.

Hollingsworth, J. L., R. M. Haberle, J. R. Barnes, A. F. C. Bridger, J. B. Pollack, H. Lee, and J. Schaeffer, Orographic control of storm zones on Mars, *Nature*, *380*, 413–416, 1996.

Hoskins, B. J., and A. J. Simmons, A multi-layer spectral model and the semi-implicit method, *Quarterly Journal of the Royal Meteorological Society*, *101*, 637–655, 1975.

Hourdin, F., A new representation of the absorption by the CO 2 15-μm band for a Martian general circulation model, *Journal of Geophysical Research*, *97*, 18,319, 1992.

Hourdin, F., P. Le Van, F. Forget, and O. Talagrand, Meteorological Variability and the Annual Surface Pressure Cycle on Mars, *Journal of the Atmospheric Sciences*, *50*, 3625–3640, 1993.

IEEE, *IEEE Standard Glossary of Software Engineering Terminology*, 2002 ed., IEEE, 1990.

Jemmett-Smith, B. C., J. H. Marsham, P. Knippertz, and C. A. Gilkeson, Quantifying global dust devil occurrence from meteorological analyses, *Geophysical research letters*, *42*, 1275–1282, 2015.

JPL, Opportunity's Devilish View from on High.

Kahanpää, H., et al., Convective vortices and dust devils at the MSL landing site: Annual variability, *Journal of Geophysical Research: Planets*, 2016.

Kahn, R., T. Z. Martin, R. W. Zurek, and S. W. Lee, The Martian Dust Cycle, in *Mars*, edited by H. H. Kieffer, B. M. Jakosky, C. W. Snyder, and M. S. Matthews, chap. 29, pp. 1017–1053, The University of Arizona Press, Tucson, 1992.

Kahre, M. A., J. R. Murphy, R. M. Haberle, F. Montmessin, and J. Schaeffer, Simulating the Martian dust cycle with a finite surface dust reservoir, *Geophysical Research Letters*, *32*, L20,204, 2005.

Kahre, M. A., J. R. Murphy, and R. M. Haberle, Modeling the Martian dust cycle and surface dust reservoirs with the NASA Ames general circulation model, *Journal of Geophysical Research*, *111*, E06,008, 2006.

Kahre, M. A., J. L. Hollingsworth, R. M. Haberle, and J. R. Murphy, Investigations of the variability of dust particle sizes in the martian atmosphere using the NASA Ames General Circulation Model, *Icarus*, *195*, 576–597, 2008.

Kahre, M. A., J. R. Murphy, C. E. Newman, R. J. Wilson, B. A. Cantor, M. T. Lemmon, and M. J. Wolff, The Mars Dust Cycle, in *The Atmosphere and Climate of Mars*, edited by R. M. Haberle, R. T. Clancy, F. Forget, M. D. Smith, and R. W. Zurek, pp. 295–337, Cambridge University Press, Cambridge, 2017.

Kalnay, E., *Atmospheric Modelling, Data Assimilation and Predictability*, Cambridge University Press, 2003.

Kanak, K. M., D. K. Lilly, and J. T. Snow, The formation of vertical Vortices in the convective boundary layer, *Quarterly Journal of the Royal Meteorological Society*, *126*, 2789–2810, 2000.

Kass, D. M., J. T. Schofield, T. I. Michaels, S. C. R. Rafkin, M. I. Richardson, and A. D. Toigo, Analysis of atmospheric mesoscale models for entry, descent, and landing, *Journal of Geophysical Research*, *108*, 8090, 2003.

Kass, D. M., A. Kleinböhl, D. J. McCleese, J. T. Schofield, and M. D. Smith, Interannual similarity in the Martian atmosphere during the dust storm season, *Geophysical Research Letters*, *43*, 6111–6118, 2016.

Keating, G. M., et al., The structure of the upper atmosphere of mars: In situ accelerometer measurements from mars global surveyor, *Science (New York, N.Y.)*, *279*, 1672–6, 1998.

Kinch, K. M., J. F. Bell, and M. B. Madsen, Dust deposition and removal at the MER landing sites from observations of the Panoramic Camera (Pancam) calibration targets, in *American Geophysical Union, Fall Meeting 2012*, 2012.

Kleinböhl, A., J. T. Schofield, D. M. Kass, W. A. Abdou, and D. J. McCleese, No widespread dust in the middle atmosphere of Mars from Mars Climate Sounder observations, 2015.

Klose, M., and Y. Shao, Large-eddy simulation of turbulent dust emission, *Aeolian Research*, *8*, 49–58, 2013.

Klose, M., Y. Shao, X. Li, H. Zhang, M. Ishizuka, M. Mikami, and J. F. Leys, Further development of a parameterization for convective turbulent dust emission and evaluation based on field observations, *Journal of Geophysical Research: Atmospheres*, *119*, 10,441–10,457, 2014.

Knutti, R., and J. Sedláček, Robustness and uncertainties in the new CMIP5 climate model projections, *Nature Climate Change*, *3*, 369–373, 2013.

Koch, J., and N. O. Rennó, The role of convective plumes and vortices on the global aerosol budget, *Geophysical Research Letters*, *32*, 2005.

Kok, J. F., Difference in the Wind Speeds Required for Initiation versus Continuation of Sand Transport on Mars: Implications for Dunes and Dust Storms, *Physical Review Letters*, *104*, 2010.

Kok, J. F., and N. O. Rennó, Enhancement of the emission of mineral dust aerosols by electric forces, *Geophysical Research Letters*, *33*, L19S10, 2006.

Kok, J. F., and N. O. Rennó, Electrostatics in Wind-Blown Sand, *Physical Review Letters*, *100*, 014,501, 2008.

Komguem, L., J. A. Whiteway, C. Dickinson, M. Daly, and M. T. Lemmon, Phoenix LIDAR measurements of Mars atmospheric dust, *Icarus*, *223*, 649–653, 2013.

Kurgansky, M. V., A. Montecinos, V. Villagran, and S. M. Metzger, Micrometeorological conditions for dust-devil occurrence in the Atacama Desert, *Boundary-Layer Meteorology*, *138*, 285–298, 2010.

Landis, G. A., and P. P. Jenkins, Measurement of the settling rate of atmospheric dust on Mars by the MAE instrument on Mars Pathfinder, *Journal of Geophysical Research: Planets*, *105*, 1855–1857, 2000.

Larsen, S. E., H. E. Jørgensen, L. Landberg, and J. E. Tillman, Aspects of the atmospheric surface layers on Mars and Earth, *Boundary-Layer Meteorology*, *105*, 451–470, 2002.

Lemmon, M. T., M. J. Wolff, J. F. Bell III, M. D. Smith, B. A. Cantor, and P. H. Smith, Dust aerosol, clouds, and the atmospheric optical depth record over 5 Mars years of the Mars Exploration Rover mission, *Icarus*, *251*, 96–111, 2015.

Leovy, C. B., R. W. Zurek, and J. B. Pollack, Mechanisms for Mars Dust Storms, *Journal of the Atmospheric Sciences*, *30*, 749–762, 1973.

Lewis, S. R., M. Collins, P. L. Read, F. Forget, F. Hourdin, R. Fournier, C. Hourdin, O. Talagrand, and J. P. Huot, A climate database for Mars, *Journal of Geophysical Research*, *104*, 24,177, 1999.

Lewis, S. R., D. P. Mulholland, P. L. Read, L. Montabone, R. J. Wilson, and M. D. Smith, The solsticial pause on Mars: 1. A planetary wave reanalysis, *Icarus*, *264*, 456–464, 2016.

Liu, J., M. I. Richardson, and R. J. Wilson, An assessment of the global, seasonal, and interannual spacecraft record of Martian climate in the thermal infrared, *Journal of Geophysical Research*, *108*, 5089, 2003.

López-Valverde, M. A., D. P. Edwards, M. López-Puertas, and C. Roldán, Nonlocal thermodynamic equilibrium in general circulation models of the Martian atmosphere 1. Effects of the local thermodynamic equilibrium approximation on thermal cooling and solar heating, *Journal of Geophysical Research: Planets*, *103*, 16,799–16,811, 1998.

Lorenz, R. D., and P. D. Lanagan, A barometric survey of dust-devil vortices on a desert playa, *Boundary-Layer Meteorology*, *153*, 555–568, 2014.

Lorenz, R. D., and J. Radebaugh, Dust devils in thin air: Vortex observations at a high elevation Mars analog site in the Argentinian Puna, *Geophysical Research Letters*, 2016.

Lorenz, R. D., and D. Reiss, Solar panel clearing events, dust devil tracks, and in-situ vortex detections on Mars, *Icarus*, *248*, 162–164, 2015.

3774 Lott, F., and M. J. Miller, A new subgrid-scale orographic drag parametrization:
3775 Its formulation and testing, *Quarterly Journal of the Royal Meteorological*
3776 *Society*, *123*, 101–127, 1997.

3777 Lowell, P., Mars in 1907, *Nature*, *76*, 446–446, 1907.

3778 Lyons, T. J., U. S. Nair, and I. J. Foster, Clearing enhances dust devil formation,
3779 *Journal of Arid Environments*, *72*, 1918–1928, 2008.

3780 Määttänen, A., H. Vehkamäki, A. Lauri, S. Merikallio, J. Kauhanen,
3781 H. Savijärvi, and M. Kulmala, Nucleation studies in the Martian atmosphere,
3782 *Journal of Geophysical Research*, *110*, E02,002, 2005.

3783 Määttänen, A., C. Listowski, F. Montmessin, L. Maltagliati, A. Reberac, L. Joly,
3784 and J.-L. Bertaux, A complete climatology of the aerosol vertical distribution
3785 on Mars from MEx/SPICAM UV solar occultations, *Icarus*, *223*, 892–941,
3786 2013.

3787 Madeleine, J.-B., F. Forget, E. Millour, T. Navarro, and A. Spiga, The influence
3788 of radiatively active water ice clouds on the Martian climate, *Geophysical*
3789 *Research Letters*, *39*, n/a–n/a, 2012.

3790 Malin, M. C., J. F. Bell III, W. M. Calvin, R. T. Clancy, R. M. Haberle, P. B.
3791 James, S. W. Lee, P. C. Thomas, and M. A. Caplinger, Mars Color Imager
3792 (MARCI) on the Mars Climate Orbiter, *Journal of Geophysical Research E:*
3793 *Planets*, *106*, 17,651–17,672, 2001.

3794 Malin, M. C., B. A. Cantor, and A. W. Britton, MRO MARCI Weather Report
3795 for the week of 17 October 2016 – 23 October 2016, Malin Space Science
3796 Systems Captioned Image Release, MSSS-449, 2016.

3797 Martin, T. Z., Thermal infrared opacity of the Mars atmosphere, *Icarus*, *66*,
3798 2–21, 1986.

3799 McCleese, D. J., et al., Mars Climate Sounder: An investigation of thermal and
3800 water vapor structure, dust and condensate distributions in the atmosphere,
3801 and energy balance of the polar regions, *Journal of Geophysical Research*,
3802 *112*, E05S06, 2007.

McCleese, D. J., et al., Structure and dynamics of the Martian lower and middle atmosphere as observed by the Mars Climate Sounder: Seasonal variations in zonal mean temperature, dust, and water ice aerosols, *Journal of Geophysical Research*, *115*, E12,016, 2010.

McGuffie, K., and A. Henderson-Sellers, *A Climate Modelling Primer*, third ed., John Wiley & Sons, Ltd, 2005.

McSween, H. Y., and K. Keil, Mixing relationships in the Martian regolith and the composition of globally homogeneous dust, *Geochimica et Cosmochimica Acta*, *64*, 2155–2166, 2000.

Merrison, J., J. Jensen, K. Kinch, R. Mugford, and P. Nornberg, The electrical properties of Mars analogue dust, *Planetary and Space Science*, *52*, 279–290, 2004.

Michaels, T. I., A. Colaprete, and S. C. R. Rafkin, Significant vertical water transport by mountain-induced circulations on Mars, *Geophysical Research Letters*, *33*, L16,201, 2006.

Millour, E., et al., The Mars Climate Database (MCD version 5.2), in *European Planetary Science Congress*, 2015.

Mishchenko, M. I., Light scattering by randomly oriented axially symmetric particles, *Journal of the Optical Society of America A*, *8*, 871, 1991.

Montabone, L., and F. Forget, Forecasting Dust Storms on Mars: A Short Review, in *Dust in the Atmosphere of Mars*, 2017.

Montabone, L., F. Forget, E. Millour, and T. Navarro, Technical note: Mars weather forecast for the Exomars 2016 EDL, *Tech. rep.*, Laboratoire de Météorologie Dynamique, Université Pierre et Marie Curie, Paris, France, 2015a.

Montabone, L., B. A. Cantor, F. Forget, D. Kass, A. Kleinböhl, M. D. Smith, and M. J. Wolff, On the Dustiest Locations on Mars from Observations, in *Fifth International Workshop on the Mars Atmosphere: Modelling and Observations*, 2017.

3832 Montabone, L., et al., Eight-year climatology of dust optical depth on Mars,
3833 *Icarus*, *251*, 65–95, 2015b.

3834 Morris, R. V., et al., Mineralogy, composition, and alteration of Mars Pathfinder
3835 rocks and soils: Evidence from multispectral, elemental, and magnetic data
3836 on terrestrial analogue, SNC meteorite, and Pathfinder samples, *Journal of*
3837 *Geophysical Research: Planets*, *105*, 1757–1817, 2000.

3838 Mulholland, D. P., Martian dust lifting, transport and associated processes,
3839 Ph.D. thesis, St. Anne's College, University of Oxford, 2012.

3840 Mulholland, D. P., P. L. Read, and S. R. Lewis, Simulating the interannual
3841 variability of major dust storms on Mars using variable lifting thresholds,
3842 *Icarus*, *223*, 344–358, 2013.

3843 Mulholland, D. P., A. Spiga, C. Listowski, and P. L. Read, An assessment of the
3844 impact of local processes on dust lifting in Martian climate models, *Icarus*,
3845 2015.

3846 Murphy, J. R., and S. Nelli, Mars Pathfinder convective vortices: Frequency of
3847 occurrence, *Geophysical Research Letters*, *29*, 2103, 2002.

3848 National Center for Atmospheric Research Staff (Eds.), The Climate Data
3849 Guide: Common Spectral Model Grid Resolutions.

3850 Neakrase, L. D. V., and R. Greeley, Dust devil sediment flux on Earth and
3851 Mars: Laboratory simulations, *Icarus*, *206*, 306–318, 2010.

3852 Newman, C. E., Modelling the dust cycle in the Martian atmosphere, Ph.D.
3853 thesis, St. Anne's College, University of Oxford, 2001.

3854 Newman, C. E., and M. I. Richardson, The impact of surface dust source ex-
3855 haustion on the martian dust cycle, dust storms and interannual variability, as
3856 simulated by the MarsWRF General Circulation Model, *Icarus*, *257*, 47–87,
3857 2015.

3858 Newman, C. E., S. R. Lewis, P. L. Read, and F. Forget, Modeling the Mar-
3859 tian dust cycle 1. Representations of dust transport processes, *Journal of*
3860 *Geophysical Research*, *107*, 5123, 2002a.

Newman, C. E., S. R. Lewis, P. L. Read, and F. Forget, Modeling the Martian dust cycle 2. Multiannual radiatively active dust transport simulations, *Journal of Geophysical Research*, *107*, 5124, 2002b.

Newman, C. E., S. R. Lewis, and P. L. Read, The atmospheric circulation and dust activity in different orbital epochs on Mars, *Icarus*, *174*, 135–160, 2005.

Nishizawa, S., et al., Martian dust devil statistics from high-resolution large-eddy simulations, *Geophysical Research Letters*, *43*, 2016.

Ockert-Bell, M. E., J. F. Bell III, J. B. Pollack, C. P. McKay, and F. Forget, Absorption and scattering properties of the Martian dust in the solar wavelengths, *Journal of Geophysical Research*, *102*, 9039, 1997.

Oke, A. M. C., N. J. Tapper, and D. Dunkerley, Willy-willies in the Australian landscape: The role of key meteorological variables and surface conditions in defining frequency and spatial characteristics, *Journal of Arid Environments*, *71*, 201–215, 2007.

Pacifici, A., G. G. Ori, F. Cannarsa, A. Murana, A. Aboudan, S. Portigliotti, A. Marcer, and L. Lorenzoni, Geological and Geomorphological Map of ExoMars 2016 Landing Site, *45th Lunar and Planetary Science Conference*, 2014.

Palmer, T. N., G. J. Shutts, and R. Swinbank, Alleviation of a systematic westerly bias in general circulation and numerical weather prediction models through an orographic gravity wave drag parametrization, *Quarterly Journal of the Royal Meteorological Society*, *112*, 1001–1039, 1986.

Pankine, A. A., and A. Ingersoll, Interannual variability of Mars global dust storms: an example of self-organized criticality?, *Icarus*, *170*, 514–518, 2004.

Pearl, J. C., M. D. Smith, B. J. Conrath, J. L. Bandfield, and P. R. Christensen, Observations of Martian ice clouds by the Mars Global Surveyor Thermal Emission Spectrometer: The first Martian year, *Journal of Geophysical Research: Planets*, *106*, 12,325–12,338, 2001.

Peterfreund, A. R., Visual and infrared observations of wind streaks on Mars, *Icarus*, *45*, 447–467, 1981.

Petrosyan, A., et al., The Martian atmospheric boundary layer, *Reviews of Geophysics*, *49*, RG3005, 2011.

Philpotts, A. R., and J. J. Ague, *Principles of igneous and metamorphic petrology*, Cambridge University Press, 2009.

Pike, W. T., U. Staufer, M. H. Hecht, W. Goetz, D. Parrat, H. Sykulska-Lawrence, S. Vijendran, and M. B. Madsen, Quantification of the dry history of the Martian soil inferred from in situ microscopy, *Geophysical Research Letters*, *38*, L24,201, 2011.

Pollack, J. B., D. S. Colburn, R. Kahn, J. Hunter, W. Van Camp, C. E. Carlston, and M. R. Wolf, Properties of aerosols in the Martian atmosphere, as inferred from Viking Lander imaging data, *Journal of Geophysical Research*, *82*, 4479–4496, 1977.

Pollack, J. B., D. S. Colburn, F. M. Flasar, R. Kahn, C. E. Carlston, and D. Pidek, Properties and effects of dust particles suspended in the Martian atmosphere, *Journal of Geophysical Research*, *84*, 2929, 1979.

Pollack, J. B., M. E. Ockert-Bell, and M. K. Shepard, Viking Lander image analysis of Martian atmospheric dust, *Journal of Geophysical Research*, *100*, 5235, 1995.

Priestley, A., A Quasi-Conservative Version of the Semi-Lagrangian Advection Scheme, *Monthly Weather Review*, *121*, 621–629, 1993.

Qi, J., C. Chen, and R. C. Beardsley, FVCOM one-way and two-way nesting using ESMF: Development and validation, *Ocean Modelling*, *124*, 94–110, 2018.

Rafkin, S. C. R., A positive radiative-dynamic feedback mechanism for the maintenance and growth of Martian dust storms, *Journal of Geophysical Research*, *114*, E01,009, 2009.

Rafkin, S. C. R., and T. I. Michaels, Meteorological predictions for 2003 Mars Exploration Rover high-priority landing sites, *Journal of Geophysical Research: Planets*, *108*, 2003.

Rafkin, S. C. R., R. M. Haberle, and T. I. Michaels, The Mars Regional Atmospheric Modeling System: Model Description and Selected Simulations, *Icarus*, *151*, 228–256, 2001.

Rafkin, S. C. R., J. Pla-Garcia, M. A. Kahre, J. Gomez-Elvira, V. E. Hamilton, M. Marin, S. Navarro, J. Torres, and A. R. Vasavada, The meteorology of Gale Crater as determined from Rover Environmental Monitoring Station observations and numerical modeling. Part II: Interpretation, *Icarus*, *280*, 114–138, 2016.

Read, P. L., and S. R. Lewis, *The Martian Climate Revisited*, Springer, Praxis Publishing, 2004.

Read, P. L., S. R. Lewis, and D. P. Mulholland, The physics of Martian weather and climate: a review, *Reports on Progress in Physics*, *78*, 125,901, 2015.

Reiss, D., M. Zanetti, and G. Neukum, Multitemporal observations of identical active dust devils on Mars with the High Resolution Stereo Camera (HRSC) and Mars Orbiter Camera (MOC), *Icarus*, *215*, 358–369, 2011.

Reiss, D., N. M. Hoekzema, and O. J. Stenzel, Dust deflation by dust devils on Mars derived from optical depth measurements using the shadow method in HiRISE images, *Planetary and Space Science*, *93-94*, 54–64, 2014a.

Reiss, D., A. Spiga, and G. Erkeling, The horizontal motion of dust devils on Mars derived from CRISM and CTX/HiRISE observations, *Icarus*, *227*, 8–20, 2014b.

Rennó, N. O., M. L. Burkett, and M. P. Larkin, A simple thermodynamical theory for dust devils, *Journal of the Atmospheric Sciences*, *55*, 3244–3252, 1998.

Rennó, N. O., A.-S. Wong, S. K. Atreya, I. de Pater, and M. Roos-Serote, Electrical discharges and broadband radio emission by Martian dust devils and dust storms, *Geophysical Research Letters*, *30*, 2140, 2003.

Richardson, M. I., and R. J. Wilson, Investigation of the nature and stability of the Martian seasonal water cycle with a general circulation model, *Journal of Geophysical Research*, *107*, 5031, 2002.

Ringrose, T. J., M. C. Towner, and J. C. Zarnecki, Convective vortices on Mars: a reanalysis of Viking Lander 2 meteorological data, sols 1–60, *Icarus*, *163*, 78–87, 2003.

Rossow, W. B., Cloud microphysics: Analysis of the clouds of Earth, Venus, Mars and Jupiter, *Icarus*, *36*, 1–50, 1978.

Ruff, S. W., and P. R. Christensen, Bright and dark regions on Mars: Particle size and mineralogical characteristics based on Thermal Emission Spectrometer data, *Journal of Geophysical Research*, *107*, 5127, 2002.

Ryan, J. A., Notes on the Martian yellow clouds, *Journal of Geophysical Research*, *69*, 3759–3770, 1964.

Ryan, J. A., and J. J. Carroll, Dust devil wind velocities: Mature state, *Journal of Geophysical Research*, *75*, 531–541, 1970.

Schiaparelli, G. V., On some observations of Saturn and Mars, *The Observatory*, *5*, 221–224, 1882.

Schwiesow, R. L., and R. E. Cupp, Remote Doppler velocity measurements of atmospheric dust devil vortices, *Applied Optics*, *15*, 1976.

Seidelmann, P. K., et al., Report of the IAU/IAG Working Group on Cartographic Coordinates and Rotational Elements of the Planets and Satellites: 2000, *Celestial Mechanics and Dynamical Astronomy*, *82*, 83–111, 2002.

Shao, Y., and H. Lu, A simple expression for wind erosion threshold friction velocity, *Journal of Geophysical Research*, *105*, 22,437, 2000.

Shirley, J. H., Solar System dynamics and global-scale dust storms on Mars, *Icarus*, *251*, 128–144, 2015.

Simmons, A. J., and D. M. Burridge, An Energy and Angular-Momentum Conserving Vertical Finite-Difference Scheme and Hybrid Vertical Coordinates, *Monthly Weather Review*, *109*, 758–766, 1981.

Sinclair, P. C., Some preliminary dust devil measurements, *Monthly Weather Review*, *92*, 363–367, 1964.

Sinclair, P. C., General characteristics of dust devils, *Journal of Applied Meteorology*, *8*, 32–45, 1969.

Skamarock, W. C., and J. B. Klemp, A time-split nonhydrostatic atmospheric model for weather research and forecasting applications, *Journal of Computational Physics*, *227*, 3465–3485, 2008.

Smith, D. E., et al., Mars Orbiter Laser Altimeter: Experiment summary after the first year of global mapping of Mars, *Journal of Geophysical Research: Planets*, *106*, 23,689–23,722, 2001.

Smith, M. D., Interannual variability in TES atmospheric observations of Mars during 1999–2003, *Icarus*, *167*, 148–165, 2004.

Smith, M. D., THEMIS observations of Mars aerosol optical depth from 2002–2008, *Icarus*, *202*, 444–452, 2009.

Smith, M. D., J. L. Bandfield, P. R. Christensen, and M. I. Richardson, Thermal Emission Imaging System (THEMIS) infrared observations of atmospheric dust and water ice cloud optical depth, *Journal of Geophysical Research*, *108*, 5115, 2003.

Smith, M. D., M. J. Wolff, R. T. Clancy, A. Kleinböhl, and S. L. Murchie, Vertical distribution of dust and water ice aerosols from CRISM limb-geometry observations, *Journal of Geophysical Research: Planets*, *118*, 321–334, 2013.

Smith, P. H., and M. T. Lemmon, Opacity of the Martian atmosphere measured by the Imager for Mars Pathfinder, *Journal of Geophysical Research*, *104*, 8975, 1999.

Snow, J. T., and T. M. McClelland, Dust devils at White Sands Missile Range, New Mexico: 1. Temporal and spatial distributions, *Journal of Geophysical Research*, *95*, 13,707, 1990.

Soriano, C., O. Jorba, and J. M. Baldasano, One-Way Nesting Versus Two-Way Nesting: Does It Really Make a Difference?, in *Air Pollution Modeling and Its Application XV*, edited by C. Borrego and G. Schayes, pp. 177–185, Springer, 2002.

Spiga, A., LMD Martian Mesoscale Model User Manual, *Tech. rep.*, Laboratoire de Meteorologie Dynamique Universite Pierre et Marie Curie, Paris, France, 2014.

Spiga, A., and F. Forget, A new model to simulate the Martian mesoscale and microscale atmospheric circulation: Validation and first results, *Journal of Geophysical Research*, *114*, E02,009, 2009.

Spiga, A., and S. R. Lewis, Martian mesoscale and microscale wind variability of relevance for dust lifting, *Mars*, *5*, 146–158, 2010.

Spiga, A., F. Forget, S. R. Lewis, and D. P. Hinson, Structure and dynamics of the convective boundary layer on Mars as inferred from large-eddy simulations and remote-sensing measurements, *Quarterly Journal of the Royal Meteorological Society*, *136*, 414–428, 2010.

Spiga, A., F. Forget, J.-B. Madeleine, L. Montabone, S. R. Lewis, and E. Millour, The impact of martian mesoscale winds on surface temperature and on the determination of thermal inertia, *Icarus*, *212*, 504–519, 2011.

Spiga, A., J. Faure, J.-B. Madeleine, A. Määttänen, and F. Forget, Rocket dust storms and detached dust layers in the Martian atmosphere, *Journal of Geophysical Research: Planets*, *118*, 746–767, 2013.

Stanzel, C., M. Pätzold, R. Greeley, E. Hauber, and G. Neukum, Dust devils on Mars observed by the High Resolution Stereo Camera, *Geophysical Research Letters*, *33*, L11,202, 2006.

Stanzel, C., M. Pätzold, D. Williams, P. L. Whelley, R. Greeley, and G. Neukum, Dust devil speeds, directions of motion and general characteristics observed by the Mars Express High Resolution Stereo Camera, *Icarus*, *197*, 39–51, 2008.

Steakley, K., and J. R. Murphy, A year of convective vortex activity at Gale Crater, *Icarus*, 2016.

Steele, L. J., A study of the martian water cycle and cloud radiative effects using data assimilation, Ph.D. thesis, The Open University, 2014.

4035 Steele, L. J., S. R. Lewis, M. R. Patel, F. Montmessin, F. Forget, and M. D.
4036 Smith, The seasonal cycle of water vapour on Mars from assimilation of Ther-
4037 mal Emission Spectrometer data, *Icarus*, *237*, 97–115, 2014.

4038 Steele, L. J., M. R. Balme, S. R. Lewis, and A. Spiga, The water cycle and
4039 regolith–atmosphere interaction at Gale crater, Mars, *Icarus*, *289*, 56–79,
4040 2017.

4041 Steele, L. J., E. S. Kite, and T. I. Michaels, Crater Mound Formation by Wind
4042 Erosion on Mars, *Journal of Geophysical Research: Planets*, *123*, 113–130,
4043 2018.

4044 Strausberg, M. J., H. Wang, M. I. Richardson, S. P. Ewald, and A. D. Toigo,
4045 Observations of the initiation and evolution of the 2001 Mars global dust
4046 storm, *Journal of Geophysical Research*, *110*, E02,006, 2005.

4047 Sullivan, R., et al., Wind-Driven Particle Mobility on Mars: Insights from MER
4048 Observations, in *American Geophysical Union, Fall Meeting 2007*, 2007.

4049 Szwast, M. A., M. I. Richardson, and A. R. Vasavada, Surface dust redistribu-
4050 tion on Mars as observed by the Mars Global Surveyor and Viking orbiters,
4051 *Journal of Geophysical Research*, *111*, E11,008, 2006.

4052 Takahashi, Y. O., Y.-Y. Hayashi, M. Odaka, and W. Ohfuchi, High Resolution
4053 Simulations of the General Circulation of the Martian Atmosphere: Small
4054 and Medium Scale Disturbances and Dust Lifting Processes, in *Third Inter-*
4055 *national Workshop on the Mars Atmosphere: Modeling and Observations*,
4056 2008.

4057 Takahashi, Y. O., Y.-Y. Hayashi, M. Odaka, and W. Ohfuchi, High resolution
4058 general circulation model experiments of the Martian atmosphere: resolution
4059 dependence of disturbance and surface stress, *Fourth International Workshop*
4060 *on the Mars Atmosphere: Modeling and Observations*, 2011a.

4061 Takahashi, Y. O., Y.-Y. Hayashi, M. Odaka, and W. Ohfuchi, High resolution
4062 general circulation model experiments of the Martian atmosphere: resolution
4063 dependence of disturbance and surface stress, in *Fourth International Work-*
4064 *shop on the Mars Atmosphere: Modeling and Observations*, 2011b.

Thomas, P., and P. J. Gierasch, Dust devils on Mars, *Science*, *230*, 175–7, 1985.

Toigo, A. D., and M. I. Richardson, Meteorology of proposed Mars Exploration Rover landing sites, *Journal of Geophysical Research*, *108*, 8092, 2003.

Toigo, A. D., M. I. Richardson, S. P. Ewald, and P. J. Gierasch, Numerical simulation of Martian dust devils, *Journal of Geophysical Research*, *108*, 5047, 2003.

Toigo, A. D., C. Lee, C. E. Newman, and M. I. Richardson, The impact of resolution on the dynamics of the martian global atmosphere: Varying resolution studies with the MarsWRF GCM, *Icarus*, *221*, 276–288, 2012.

Toigo, A. D., M. I. Richardson, H. Wang, S. D. Guzewich, and C. E. Newman, The cascade from local to global dust storms on Mars: Temporal and spatial thresholds on thermal and dynamical feedback, *Icarus*, *302*, 514–536, 2018.

Tomasko, M. G., L. R. Doose, M. T. Lemmon, P. H. Smith, and E. Wegryn, Properties of dust in the Martian atmosphere from the Imager on Mars Pathfinder, *Journal of Geophysical Research*, *104*, 8987–9007, 1999.

Toon, O. B., J. B. Pollack, and C. Sagan, Physical properties of the particles composing the Martian dust storm of 1971–1972, *Icarus*, *30*, 663–696, 1977.

Tyler, D., and J. R. Barnes, Atmospheric mesoscale modeling of water and clouds during northern summer on Mars, *Icarus*, *237*, 388–414, 2014.

Tyler, D., and J. R. Barnes, Convergent crater circulations on Mars: Influence on the surface pressure cycle and the depth of the convective boundary layer, *Geophysical Research Letters*, *42*, 7343–7350, 2015.

Tyler, D., J. R. Barnes, and R. M. Haberle, Simulation of surface meteorology at the Pathfinder and VL1 sites using a Mars mesoscale model, *Journal of Geophysical Research*, *107*, 5018, 2002.

Tyler, D., J. R. Barnes, and E. D. Skyllingstad, Mesoscale and large-eddy simulation model studies of the Martian atmosphere in support of Phoenix, *Journal of Geophysical Research*, *113*, 2008.

Urrego-Blanco, J., J. Sheng, and F. Dupont, Performance of One-Way and Two-Way Nesting Techniques Using the Shelf Circulation Modelling System for the Eastern Canadian Shelf, *Atmosphere-Ocean*, *54*, 75–92, 2016.

Vasavada, A. R., et al., Assessment of environments for Mars Science Laboratory entry, descent, and surface operations, *Space Science Reviews*, *170*, 793–835, 2012.

Vaughan, A. F., J. R. Johnson, K. E. Herkenhoff, R. Sullivan, G. A. Landis, W. Goetz, and M. B. Madsen, Pancam and Microscopic Imager observations of dust on the Spirit Rover: Cleaning events, spectral properties, and aggregates, *The Mars Journal*, *5*, 129–145, 2010.

Wallace, J. M., and P. V. Hobbs, *Atmospheric Science: An Introductory Survey*, second ed., Elsevier Inc., 2006.

Wang, H., Dust storms originating in the northern hemisphere during the third mapping year of Mars Global Surveyor, *Icarus*, *189*, 325–343, 2007.

Wang, H., and J. A. Fisher, North polar frontal clouds and dust storms on Mars during spring and summer, *Icarus*, *204*, 103–113, 2009.

Wang, H., and M. I. Richardson, The origin, evolution, and trajectory of large dust storms on Mars during Mars years 24–30 (1999–2011), *Icarus*, *251*, 112–127, 2015.

Wang, H., M. I. Richardson, R. J. Wilson, A. P. Ingersoll, A. D. Toigo, and R. W. Zurek, Cyclones, tides, and the origin of a cross-equatorial dust storm on Mars, *Geophysical Research Letters*, *30*, 1488, 2003.

Wang, H., R. W. Zurek, and M. I. Richardson, Relationship between frontal dust storms and transient eddy activity in the northern hemisphere of Mars as observed by Mars Global Surveyor, *Journal of Geophysical Research*, *110*, E07,005, 2005.

Waterman, P. C., Matrix formulation of electromagnetic scattering, *Proceedings of the IEEE*, *53*, 805–812, 1965.

White, A. A., and A. Staniforth, A generalized thermal wind equation and some non-separable exact solutions of the flow equations for three-dimensional spherical atmospheres, *Quarterly Journal of the Royal Meteorological Society*, *134*, 1931–1939, 2008.

Whiteway, J. A., et al., Mars water-ice clouds and precipitation., *Science (New York, N.Y.)*, *325*, 68–70, 2009.

Wilson, R. J., A general circulation model simulation of the Martian polar warming, *Geophysical Research Letters*, *24*, 123–126, 1997.

Wilson, R. J., Dust cycle modeling with the GFDL Mars General Circulation Model, in *Fourth International Workshop on the Mars Atmosphere: Modeling and Observations*, 2011.

Wilson, R. J., and K. Hamilton, Comprehensive Model Simulation of Thermal Tides in the Martian Atmosphere, *Journal of the Atmospheric Sciences*, *53*, 1290–1325, 1996.

Wilson, R. J., S. R. Lewis, L. Montabone, and M. D. Smith, Influence of water ice clouds on Martian tropical atmospheric temperatures, *Geophysical Research Letters*, *35*, 2008.

Withers, P., and R. Pratt, An observational study of the response of the upper atmosphere of Mars to lower atmospheric dust storms, *Icarus*, *225*, 378–389, 2013.

Withers, P., and M. D. Smith, Atmospheric entry profiles from the Mars Exploration Rovers Spirit and Opportunity, *Icarus*, *185*, 133–142, 2006.

Wolff, M. J., and R. T. Clancy, Constraints on the size of Martian aerosols from Thermal Emission Spectrometer observations, *Journal of Geophysical Research*, *108*, 5097, 2003.

Wolff, M. J., M. D. Smith, R. T. Clancy, R. Arvidson, M. A. Kahre, F. Seelos, S. L. Murchie, and H. Savijärvi, Wavelength dependence of dust aerosol single scattering albedo as observed by the Compact Reconnaissance Imaging Spectrometer, *Journal of Geophysical Research*, *114*, E00D04, 2009.

Wolff, M. J., R. T. Clancy, J. D. Goguen, M. C. Malin, and B. A. Cantor, Ultraviolet dust aerosol properties as observed by MARCI, *Icarus*, *208*, 143–155, 2010.

Wolff, M. J., et al., Constraints on dust aerosols from the Mars Exploration Rovers using MGS overflights and Mini-TES, *Journal of Geophysical Research*, *111*, E12S17, 2006.

Wurm, G., and O. Krauss, Dust Eruptions by Photophoresis and Solid State Greenhouse Effects, *Physical Review Letters*, *96*, 134,301, 2006.

Wurm, G., J. Teiser, and D. Reiss, Greenhouse and thermophoretic effects in dust layers: The missing link for lifting of dust on Mars, *Geophysical Research Letters*, *35*, L10,201, 2008.

Zalucha, A. M., The effect of dust on the Martian Hadley cells, in *Fifth International Workshop on the Mars Atmosphere: Modelling and Observations*, 2014.

Zurek, R. W., Solar heating of the Martian dusty atmosphere, *Icarus*, *35*, 196–208, 1978.

Zurek, R. W., The Spatial and Temporal Distribution of Dust in the Atmosphere of Mars, in *Dust in the Atmosphere of Mars*, 2017.

Zurek, R. W., and L. J. Martin, Interannual variability of planet-encircling dust storms on Mars, *Journal of Geophysical Research*, *98*, 3247–3259, 1993.

Zurek, R. W., J. R. Barnes, R. M. Haberle, J. B. Pollack, J. E. Tillman, and C. B. Leovy, Dynamics of the Atmosphere of Mars, in *Mars*, edited by H. H. Kieffer, B. M. Jakosky, C. W. Snyder, and M. S. Matthews, chap. 26, pp. 835–933, The University of Arizona Press, Tucson, 1992.